Technische Universität München

Max-Planck-Institut für Physik

Search for Dark Matter with the CRESST Experiment

Dissertation an der Fakultät für Physik
der Technischen Universität München
vorgelegt von

Rafael Florian Lang

Technische Universität München

Max-Planck-Institut für Physik
(Werner-Heisenberg-Institut)

Search for Dark Matter with the CRESST Experiment

Rafael Florian Lang

Vollständiger Abdruck der von der Fakultät für Physik der Technischen Universität München zur Erlangung des akademischen Grades eines Doktors der Naturwissenschaften genehmigten Dissertation.

Vorsitzender:	Univ.-Prof. Dr. Alejandro Ibarra
Prüfer der Dissertation:	
	1. Univ.-Prof. Dr. Lothar Oberauer
	2. Hon.-Prof. Allen C. Caldwell, Ph.D

Die Dissertation wurde am 28. Oktober 2008 bei der Technischen Universität München eingereicht und durch die Fakultät für Physik am 4. Dezember 2008 angenommen.

Abstract

In recent years cosmology became a quantitative science, predicting large quantities of Dark Matter (chapter 1). Astrophysical measurements also point toward such a dark component of our universe, being distributed on all scales from galaxy clusters to our own Milky Way (chapter 2). However, Dark Matter could so far not be observed directly (chapter 3).

The CRESST Experiment aims at the detection of Dark Matter particles on a laboratory scale. To this end, scintillating crystals are equipped with superconducting thermometers and cooled to a few millkelvin only. Hence particles can be detected calorimetrically. Using the information given by the scintillation allows to distinguish different kinds of particles, which in turn allows to suppress common radioactive backgrounds (chapter 4).

This work deals with the analysis of data attained. As a start, the employed methods are explained (chapter 5). Detailed investigations of the recorded spectra below a few 100 keV allow the identification of a variety of background sources (chapter 6).

The energy dependence of the scintillation light yield is of much relevance for the discrimination power of the experiment. For the first time a scintillator non-proportionality was shown to exist in CRESST detectors, as well as a differing behavior for electron and gamma events (chapter 7).

The possibility to use the light detectors themselves as an absorber in a Dark Matter search is briefly examined (chapter 8). The analysis of data to search for Dark Matter is exhaustively reported. Employing new parameters allows to isolate classes of relevant backgrounds (chapter 9).

The calculation of a limit on the Dark Matter scattering cross section is explained. An algorithm is developed that allows to make use of the data in an optimal way. Moreover, a new method to combine data from differing detectors is presented. Finally, a limit on the coherent WIMP-nucleus scattering cross section from data taken during 2007 is given (chapter 10).

Überblick

Die Kosmologie konnte sich in den letzten Jahren verstärkt zu einer quantitativen Wissenschaft entwickeln und sagt eine große Menge der sogenannten Dunklen Materie voraus (Kapitel 1). Auch astrophysikalische Messungen deuten auf große Mengen einer solchen dunklen Komponente unseres Universums hin, auf Skalen von Galaxienhaufen bis zu unserer Milchstraße (Kapitel 2). Allerdings entzieht sich die Dunkle Materie bislang jeder direkten Beobachtung (Kapitel 3).

Mit dem CRESST Experiment wird versucht, Teilchen der Dunklen Materie im Labormaßstab nachzuweisen. Dazu werden szintillierende Kristalle mit supraleitenden Thermometern versehen und auf wenige tausendstel Kelvin abgekühlt. Im Falle einer Wechselwirkung können so Teilchen kalorimetrisch nachgewiesen werden. Der Nachweis des Szintillationslichtes erlaubt Rückschlüsse über die Teilchenart, was eine wesentliche Unterdrückung allgemeiner radioaktiver Untergründe ermöglicht (Kapitel 4).

Diese Arbeit beschäftigt sich mit der Auswertung der im Experiment gewonnenen Daten. Die eingesetzte Methodik wird zunächst erläutert (Kapitel 5). Ausführliche Untersuchungen der gewonnenen Spektren im Energiebereich unterhalb weniger 100 keV erlauben die Identifizierung einer Vielzahl verschiedener Quellen (Kapitel 6).

Die Energieabhängigkeit der Lichtausbeute ist für das Diskriminierungspotential von großer Bedeutung. In diesem Zusammenhang kann erstmals eine nichtproportionale Energieabhängigkeit der Lichtausbeute ebenso wie unterschiedliche Reaktionen auf Elektronen- und Gammaereignisse in den CRESST Detektoren nachgewiesen werden (Kapitel 7).

Die Möglichkeit, die eingesetzten Lichtdetektoren selbst als Absorber für die Dunkle Materie einzusetzen, wird kurz behandelt (Kapitel 8). Die Verwertung der Daten zur Suche nach Dunkler Materie wird ausführlich dargestellt. Dabei können unter Einsatz neuer Parameter Klassen von relevanten Untergründen isoliert werden (Kapitel 9).

Die Berechnung einer oberen Schranke auf den Wirkungsquerschnitt der Dunklen Materie wird ausführlich dargelegt. Insbesondere wird ein Algorithmus entwickelt, mit welchem die gewonnenen Daten im Hinblick auf Ihre Aussagekraft optimal verwertet werden können. Desweiteren wird eine Methode zur Kombination der Daten verschiedener Detektoren vorgestellt. Schließlich wird mit den 2007 gewonnenen Daten eine obere Schranke für den kohärenten WIMP-Nukleon Wirkungsquerschnitt angegeben (Kapitel 10).

Contents

O flaumenleichte Zeit der dunkeln Frühe!
Welch neue Welt bewegest du in mir?
Was ists, daß ich nun in dir
Von sanfter Wollust meines Daseins glühe?

Einem Kristall gleicht meine Seele nun,
Den noch kein falscher Strahl des Lichts getroffen;
Zu fluten scheint mein Geist, er scheint zu ruhn,
Dem Eindruck naher Wunderkräfte offen,
Die aus dem klaren Gürtel blauer Luft
Zuletzt ein Zauberwort vor meine Sinne ruft.

Eduard Mörike

Part I

Dark Matter

Chapter 1

The Need for Non-Baryonic Matter

Intent: The work done within the framework of this thesis is devoted to the search for a new form of matter. This chapter introduces the need for such non-baryonic matter from various cosmological observations. In particular, Big Bang nucleosynthesis and observations of the cosmic microwave background radiation independently lead to the same conclusion: All the atoms make up only 4% of the energy density of the universe. We will see that five times more mass is hidden in the universe in an unknown form: the Dark Matter.

Organization: Section 1.1 gives an overview over contemporary cosmology, and introduces the notion of energy densities. Based on measurements of the abundances of light elements as well as the cosmic microwave background radiation, the following sections 1.2 and 1.3 respectively explain why baryonic matter can only contribute a small fraction to the total matter density. Finally, in section 1.4, other measurements are remarked at, and the findings are summarized in a coherent picture.

1.1 The Friedman Universe

1.1.1 An Introductory Comment

In cosmology, one usually works in the so-called **comoving coordinate system**. We are familiar with this peculiar concept of coordinates when we think of the latitudes and longitudes on the earth globe (radius $R_\oplus$). Almost at the north pole, for example, moving in longitude ϕ by one degree to the east implies traversing a much smaller distance than moving one degree to the east from München. The physical distance $\mathrm{d}s$ traversed is related to the coordinate distance $(\mathrm{d}\theta, \mathrm{d}\phi)$ by a **metric**

$$\mathrm{d}s^2 \quad = \quad R_\oplus^2 \left(\mathrm{d}\theta^2 + \sin^2\theta \, \mathrm{d}\phi^2\right) \tag{1.1}$$

which tells us how to calculate physical distances from our coordinates (θ, ϕ). In the example, we have $\sin^2\theta \to 0$ on the north pole, so the physical distance $\mathrm{d}s$ traversed becomes very small.

1.1.2 The Friedman-Lemaître-Robertson-Walker Metric

The **cosmological principle** states that the universe is everywhere the same, a very appealing postulate indeed in the light of the copernican history of science. More precisely, the principle assumes homogeneity and isotropy of the universe at scales $l \gg 100\,\mathrm{Mpc}$, which is the typical scale of clusters of galaxies such as our Local Group. We will see in section 1.3 that this indeed agrees very well with observations. The generic metric for such a universe is the **Friedman-Lemaître-Robertson-Walker metric** (labeled also using any subset of these four names, depending on regional preferences):

$$\mathrm{d}s^2 = c^2\mathrm{d}t^2 - a(t)^2\left(\frac{\mathrm{d}r^2}{1-kr^2} + r^2\mathrm{d}\theta^2 + r^2\sin^2\theta\,\mathrm{d}\phi^2\right). \tag{1.2}$$

For constant $r = R_\oplus$ this metric compares nicely to equation 1.1. In addition, it contains a free function $a(t)$ called the **scale factor**, and a free parameter k, describing the **curvature** of space-time. In section 1.3 we will also see that all observations point toward our universe being spatially flat (unless warped by gravitating bodies like galaxies), in which case $k = 0$. Thus, the metric describing our universe is very simply

$$\mathrm{d}s^2 = c^2\mathrm{d}t^2 - a(t)^2\left(\mathrm{d}x^2 + \mathrm{d}y^2 + \mathrm{d}z^2\right) \tag{1.3}$$

which is almost the Minkovsky metric, except that the spatial component has the scale factor in. We set the value $a_0 \equiv a(t = \text{today}) := 1$.

It was already in 1912 that Slipher discovered the apparent receding radial movement of the galaxies [1, 2], but only in 1929 that Hubble claimed his now famous law [3] of the expansion of the universe. Today, what we mean with the notion that **the universe is expanding** simply means that the scale factor $a(t)$ is increasing with time. For a nice review on this matter see reference [4].

1.1.3 General Relativity

Within the framework of General Relativity, the time evolution of the scale factor $a(t)$ is determined by the ten fundamental **Einstein equations** [5]

$$G_{\mu\nu} - \Lambda g_{\mu\nu} = \frac{8\pi G}{3}T_{\mu\nu} \tag{1.4}$$

with the **Einstein tensor** $G_{\mu\nu}$ describing the curvature of space-time, a **cosmological constant** Λ, the metric tensor $g_{\mu\nu}$ as defined in equation 1.3, Newton's constant G, and the **stress-energy tensor** $T_{\mu\nu}$ describing the density and flux of energy and momentum in space-time.

Inserting our metric 1.3 into these equations decouples the individual components, since the metric is diagonal. Solving the time-time-component ($\mu = \nu = 0$) of equations 1.4 yields the first **Friedman equation**, derived already in 1922 [6]:

$$H^2(t) := \left(\frac{\dot{a}(t)}{a(t)}\right)^2 = \frac{8\pi G}{3c^2}\varrho + \frac{c^2\Lambda}{3} - \frac{c^2k}{a^2(t)}. \tag{1.5}$$

Here, $\varrho \equiv T_{00}$ is the energy density of the universe, and H is called the **Hubble parameter**, with $H_0 \equiv H(t = \text{today}) = (70.1 \pm 1.3)\,\text{km}\,\text{s}^{-1}\,\text{Mpc}^{-1}$ [7] called the **Hubble constant** for historic reasons. It is this simple equation 1.5 that describes the evolution of the expansion of the universe.

1.1.4 Various Densities

With the Friedman equation 1.5 at hand, it is enough to measure the terms on the right hand side today to know the past and future evolution of the universe. To this end, it is customary to divide the equation by H_0 to get

$$\frac{8\pi G}{3c^2 H_0^2}\varrho + \frac{c^2\Lambda}{3H_0^2} - \frac{c^2 k}{a^2 H_0^2} = 1. \tag{1.6}$$

We define the **critical density**

$$\varrho_{\text{critical}} := \frac{3c^2 H^2(t)}{8\pi G} \tag{1.7}$$

which today has a value of $\varrho_{\text{critical},0} \approx 5\,\text{keV}/\text{cm}^3$, corresponding to about $5\,\text{protons}/\text{m}^3$. In cosmology it is customary to express the density of a species i not in g/cm^3 or the like, but as fraction of the critical density $\Omega_\text{i} := \varrho_{\text{i},0}/\varrho_{\text{critical},0}$. The Friedman equation is then simply

$$\Omega_{\text{matter}} + \Omega_\Lambda - \Omega_{\text{curvature}} = 1 \tag{1.8}$$

or, if we allow a more detailed division of species, such as Ω_{baryons} or $\Omega_{\text{neutrinos}}$, it reads

$$\sum_i \Omega_\text{i} = 1. \tag{1.9}$$

The following sections summarize the most important measurements of the various energy densities Ω_i, based on the four fields of nucleosynthesis, cosmic microwave radiation, structure formation, and supernovae.

1.2 Nucleosynthesis

After the Big Bang, neutrons and protons interact and form deuterium, which is again photodissociated by the ambient cosmic background radiation. After about 4 minutes, the temperature of the universe drops below $T \approx 80\,\text{keV}/\text{k}_\text{B} \approx 10^9\,\text{K}$, and photodissociation is no longer significant. This is when **Big Bang nucleosynthesis** starts: Deuterium can now be fused into tritium, helium, and even lithium. Once the neutrons are all used up, we are left with charged particles only (the nuclei), so the coulomb barrier puts an end to nucleosynthesis at temperatures of $T \approx 30\,\text{keV}/\text{k}_\text{B}$, at about 24 minutes after the Big Bang.

For the fraction of baryons that end up in helium (called the **helium mass fraction**), the situation is very simple: Helium is energetically very

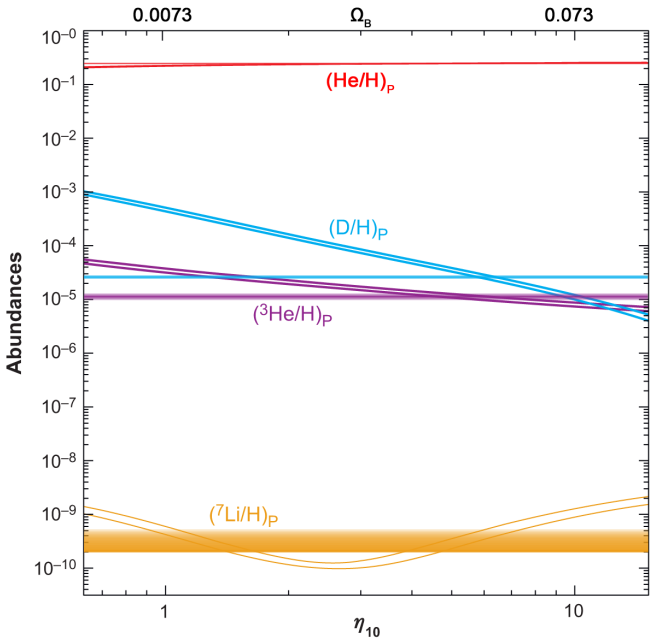

Figure 1.1: The abundances of light elements during Big Bang nucleosynthesis, as function of the baryon-to-photon ratio η_{10}, or directly the baryon density $\Omega_{\text{baryons}} = \eta_{10}/137$ [8]. Curves are shown for the four lightest elements. The double lines represent the uncertainties due to nuclear physics processes, while the strictly horizontal bars are measurements including statistical errors. This points toward a baryon density of only $\Omega_{\text{baryons}} \approx 0.04$. Tritium is not shown since it decays with a half-live time of only 12 years into ^3He. Plot based on data from [9].

favored, so to first order, all neutrons end up in ^{4}He. This means that the helium mass fraction is rather insensitive to the baryon density, but depends mainly on the initial ratio n/p at the time nucleosynthesis starts [9]. More precisely, with an initial $n/p \approx 1/7$ (from Boltzmann statistics given the different masses of protons and neutrons), this allows for one helium nucleus per 12 hydrogen nuclei, so we expect to end up with about 25% of the mass of baryons in the form of ^{4}He, and the rest in hydrogen (figure 1.1).

For higher order effects, we can have a look at deuterium, where things are different. The higher the baryon density, the faster deuterium is fused into more heavy elements, so that after nucleosynthesis, we end up with a lower deuterium abundance. In fact, the deuterium abundance is a very sensitive measure of the baryon density at the time of nucleosynthesis, and consequently, the deuterium curve in figure 1.1 is rather steep. Deuterium is the baryometer of choice since it is only destroyed in the course of the evolution of the universe, or the evolution of a star, but never enduringly created. This is due to the low binding energy of deuterium, and it keeps systematic uncertainties small: One can get a handle on the chemical evolution of stars or nebulae by probing higher mass elements, and in regions where there was

hardly any chemical evolution at all, the deuterium abundance will be very close to the primordial one.

Also, observations of the abundances of ^{3}He and ^{7}Li can be used to get a handle on the baryon density as indicated in the figure. The values for Ω_{baryons} derived from the deuterium abundance ($\Omega_{\text{baryons}} = 0.047 \pm 0.003$) and from helium-3 ($\Omega_{\text{baryons}} = 0.041^{+0.016}_{-0.010}$) agree very well, with higher uncertainties and a tendency toward lower baryon densities for the abundances derived from helium-4 and lithium [9]. This is our first glimpse of what is to come, namely that the matter we know so dearly makes up only a small fraction of the energy content of the universe, as we have seen from the Friedman equation 1.8 that $\sum \Omega_i$ needs to add up to one.

1.3 The Cosmic Microwave Background

The **cosmic microwave background** (CMB) was discovered by Penzias and Wilson in 1964 [10] and quickly interpreted to be the echo of the Big Bang [11]. It was emitted when the universe was about 380,000 years old, when, at a temperature of $T \approx 0.3\,\text{eV}/k_B$, electrons and protons combined to form neutral hydrogen. Thereafter, the primordial plasma became transparent for the photons to travel freely, so the apparent cosmic microwave background sphere is sometimes called the **surface of last scattering**. What we can observe as the cosmic microwave background is only those photons that reach us precisely today, so we can see neither beyond the surface of last scattering, nor see the whole universe, but only a (possibly very small) slice of it.

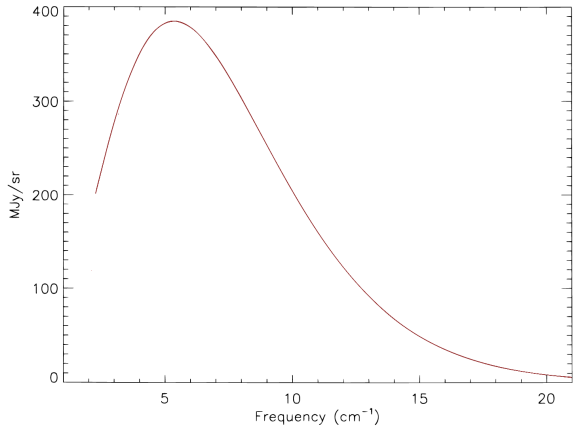

Figure 1.2: The most perfect black body spectrum ever observed: The cosmic microwave background. Shown are data together with a fit to a black body spectrum with $T = 2.728\,\text{K}$: The error bars are incredibly small. Plot from [12].

Figure 1.2 shows the spectrum of the cosmic microwave background, as measured by the FIRAS instrument on board the COBE satellite [12].

The cosmic microwave background is the most perfect Planck radiator we know, with its temperature today being pinned down to $T_{\mathrm{CMB}} = (2.725 \pm 0.001)K = 2 \times 10^{-4}\,\mathrm{eV/k_B}$. From this, the energy density of photons today follows directly as $\Omega_\gamma = (5.026 \pm 0.001) \times 10^{-5}$ [8].

More information can be gained by looking very closely at this spectrum [14], and one can see temperature fluctuations at the level of $\approx 10^{-5}$, see figure 1.3. What we see [15] as the structure in the cosmic microwave background is gravitational redshifting of the photons (**Sachs-Wolfe effect** [16]) as they decouple from matter at the surface of last scattering. This is an accurate probe of the matter distribution at that time. Thus by analyzing the structure in the cosmic microwave background, one can infer the distribution of gravitating matter in the early universe. To this end, one decomposes the observed picture into spherical harmonics in order to do some quantitative analysis on it, see figure 1.4. Some thoughts on why we can observe these variations at all, given that each multipole is an average over many modes, and given the universe is not bounded, are elaborated in appendix A.

Various parameters can be extracted from a combined fit to the cosmic microwave background spectrum. The densities that the microwave background is most sensitive to are:

The curvature $\Omega_{\mathrm{curvature}}$: In an open universe, the peaks would appear on smaller angular scales, since the geodesics pointing from us to the surface of last scattering are bent together (they are convex). By 2000, it was clear from BOOMERANG data that the universe is flat [19], and with the precision measurements of WMAP we can now put a tight limit of $-0.0175 < \Omega_{\mathrm{curvature}} < +0.0085$ [15]. So, as promised in section 1.1.2, the universe really is flat.

The total matter density Ω_{matter}: As one decreases the matter density, gravitational wells are more easily decaying. Then photons traveling on the way to us can gain more energy falling in these wells than they loose climbing out again (**integrated Sachs-Wolfe effect**). This decay might happen due to the presence of Dark Energy, massive neutrinos, or something involving lots of radiation and little mass close to the time of last scattering. As observable, the effect increases all odd peaks in the power spectrum. So by looking at the relative size of the peaks one can get an excellent handle on the matter density. The five year data from WMAP constrains $\Omega_{\mathrm{matter}} = 0.257 \pm 0.013$ [17].

The baryon density $\Omega_{\mathrm{baryons}}$: Gravity pull baryons together, but radiation pressure drives them apart. This causes so-called **baryon-acoustic oscillations** which leave their imprint in the cosmic microwave background's power spectrum. Raising the baryon density increases the peak height of the first peak but decreases the height of the second peak, very much like in the case of a driven harmonic oscillator when reducing the frequency of the driving force. Indeed,

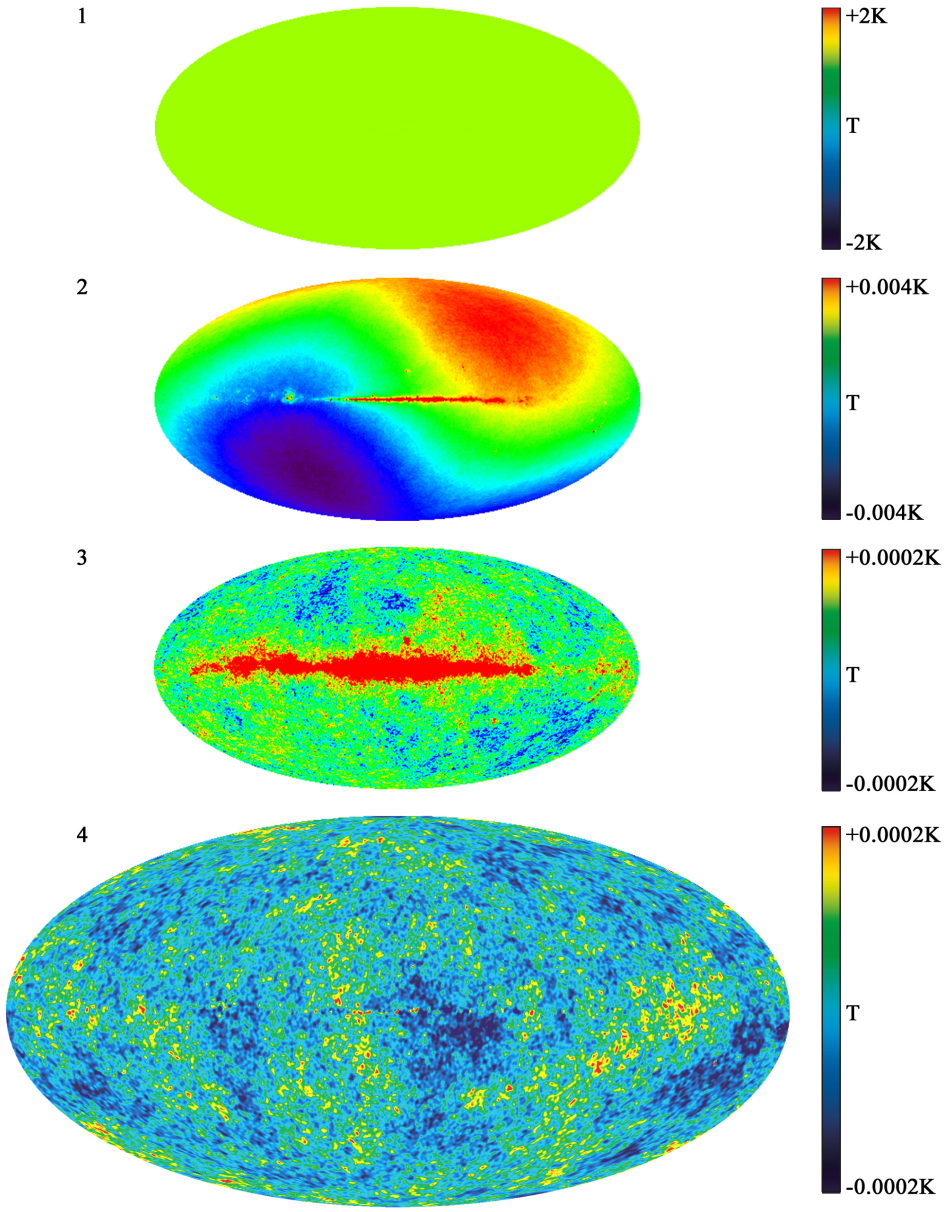

Figure 1.3: 5 year WMAP observation of the cosmic background temperature, in galactic coordinates. (1) The radiation is highly uniform over the whole sky. (2) A dipole structure emerges at a much finer temperature scale (shown on the right). It is caused by the dipole from the movement of the sun through the rest frame of the background radiation, and in galactic coordinates shows up as this yin-yang-like pattern. (3) Subtracting the dipole (and going to a finer temperature scale) the emission from the Milky Way becomes visible. (4) Subtracting this emission (based on estimates from the side bands of the radiation as well as on results of extensive modeling) the cosmic microwave background anisotropy emerges. Figure with pictures taken from [13].

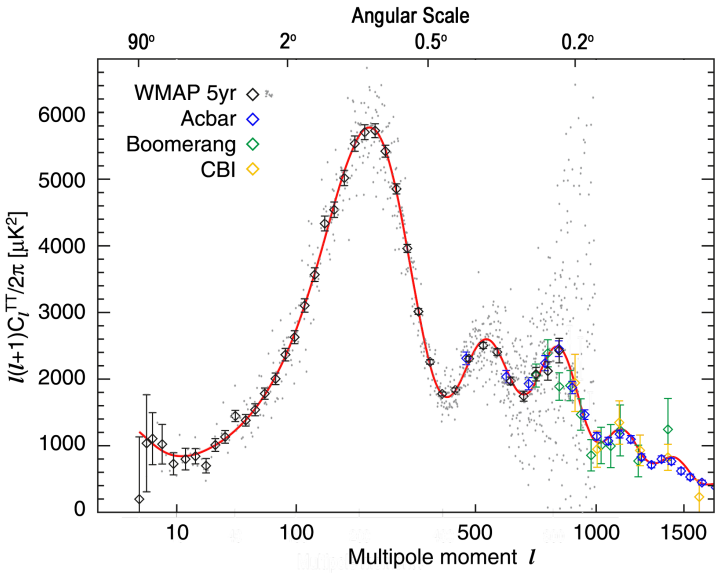

Figure 1.4: The angular power spectrum of the cosmic microwave background radiation. Shown are both binned data points from WMAP and other experiments (with error bars including cosmic variance), as well as unbinned data points from WMAP in gray. The simple cosmological model described here is capable of reproducing all observed features to very high accuracy, as shown by the best fit curve. Figure based on plots in [17] and [18].

in the plasma, a large baryon density corresponds to a small speed of sound and thus small frequencies, so the analogy really holds. Today, the best way to measure the baryon density is to measure the speed of sound by means of the cosmic microwave background, and from the five year WMAP data one gets $\Omega_{\text{baryons}} = 0.0463 \pm 0.0013$ [17].

Also the Dark Energy density can be inferred from observations of the cosmic microwave background [17] to be about $\Omega_\Lambda = 0.74 \pm 0.03$, and the neutrino density is at most $\Omega_\nu < 0.028$. Now, these densities do indeed add up to unity as required by the Friedman equation, and an independent calculation in which the total density is allowed to deviate from unity (thus violating either General Relativity or the copernican assumption of homogeneity and isotropy) also shows that $\sum_i \Omega_i = 1.0052 \pm 0.0064$ [15], another confirmation of our universe obeying the simple laws described. But we see again that a substantial fraction $\Omega_{\text{matter}} - \Omega_{\text{baryons}} - \Omega_\nu \approx 0.18$ of the universe is made from a form of matter we do not yet know.

1.4 Additional Observations

Taking the cosmic microwave background data alone to constrain the cosmological parameters leads to some degeneracies. Adding other indepen-

dent data sets can help to measure these parameters with even higher accuracy [20, 21].

The structure we live in today evolved from the tiny fluctuations in the cosmic background. Modeling this **evolution** is obviously highly nonlinear at later times and thus requires large computational efforts. But the combination of both such computer simulations (e.g. the Millennium Simulation [22]) as well as observations of the **large scale structure** of the universe today (e.g. from the Sloan Digital Sky Survey [23]) allows to independently constrain the cosmic parameters to $\Omega_{\text{matter}} = 0.26 \pm 0.03$ and $\Omega_{\text{baryons}} = 0.041 \pm 0.008$ [24, 25].

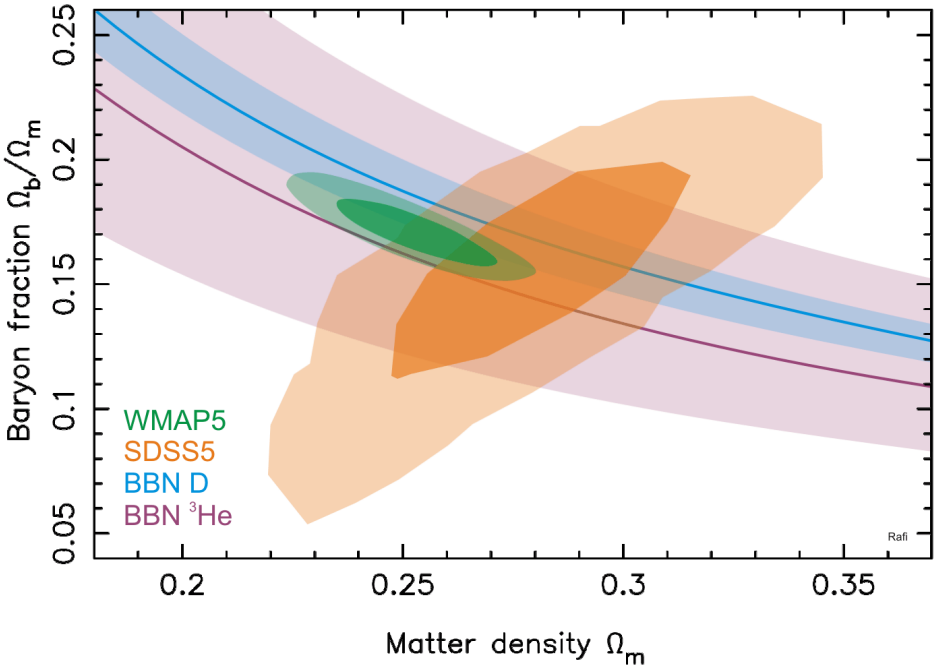

Figure 1.5: Combined constraints on the baryon fraction $\Omega_{\text{baryons}}/\Omega_{\text{matter}}$ as function of the total mass density Ω_{matter} from the various observations discussed here: Deuterium and ^{3}He abundance and Big Bang nucleosynthesis in cyan and violet, respectively [9] (central line and 1σ contour), the WMAP 5 year observation of the cosmic microwave background [17] in green and the Sloan Digital Sky Survey in orange [24, 26], both with their 1σ and 2σ contours.

Today, the accepted model is that of **hierarchical structure formation**, in which small structures merge to form larger and larger structures [27]. It is known since early times of observational cosmology [28] that structure formation requires large amounts of matter to be made from heavy particles that do not interact with photons, a component dubbed **cold Dark Matter**. In contrast, the density of light particles (e.g. neutrinos) is restricted to $\Omega_\nu < 0.01$ and by far not enough to explain all of the matter content of the universe.

For completeness, observations of **Supernovae of type IA** shall be noted. These objects are believed to have intrinsically the same true magnitude. From their observations one can infer the Hubble diagram to high distances, yielding a good handle especially on the Dark Energy parameter Ω_Λ, which is very useful given the degeneracy of measurements of the cosmic microwave background alone.

Figure 1.5 summarizes the deduced parameters of the different observations discussed above, in the $\Omega_{\text{baryons}}/\Omega_{\text{matter}}$ versus Ω_{matter} plane. The observations are all independent from one another, but they are all consistent in their outcome [7]: Baryonic matter is only a small fraction $\Omega_{\text{baryons}} = 0.0462 \pm 0.0015$ of a larger part $\Omega_{\text{matter}} = 0.233 \pm 0.013$ which consists mainly of matter in an unknown form! This non-baryonic matter must not interact with photons, or else we would have seen it in some wavelength or another, so we call it the **Dark Matter**.

At this stage, a warning is advisable. Astronomers sometimes call things like planets, dust, or black holes also by the name of Dark Matter. However, in this thesis, the term is used in the more restrictive meaning, referring to non-baryonic matter only. It is the central goal of this work to get closer to the answer of what this Dark Matter is made of.

Chapter 2

What and Where to Search

Intent: Now that we have seen that most of the matter in the universe is of unknown form, we should set out to explore this new frontier. This chapter will introduce ideas about what this Dark Matter might be made of, and we will see where we can hope to find it. In particular, there is evidence for a significant component of non-baryonic Dark Matter in our own Milky Way, so laboratory searches on Earth may unravel this mystery. Key parameters of the local Dark Matter distribution are presented.

Organization: After a quick motivation from an historical perspective in section 2.1, section 2.2 introduces the idea of Weakly Interacting Massive Particles to explain non-baryonic Dark Matter. In the remainder of this chapter, sections 2.3 to 2.7 discuss what we know about Dark Matter, starting from megaparsec galaxy cluster scales down to the $10\,\mu$pc scale of our Solar System.

2.1 A Historical Perspective

We have seen that a large fraction $\Omega_{\text{darkmatter}} \approx 0.18$ of the content of the universe is matter in a form not yet known to us. This leaves us with the daunting task of searching for something Out There that remains invisible. But this is not an impossible thing to do at all, as a historical remark might help to realize. The first predictions of non-luminous matter from observations of gravitating systems were made already in the 19th century. From detailed observations of Sirius, F. Bessel predicted in 1844 the existence of an unobserved companion [29, 30], which was then discovered as Sirius B in 1862 by A. Clark [31]. From perturbation calculations on the orbit of Uranus, J. Adams in 1845 and U. Leverrier in 1846 predicted the existence of an eighth planet. Thus Neptune was discovered by J. Galle in 1846 already during the first night he had looked for it, and on the very spot predicted by theory [32, 33]. And of course one could continue with this story, perhaps mentioning the experimental detection of the neutrino [34, 35], and eventually coming to a point where we know of having a black hole at the center of the Milky Way [36]. This should encourage us to go on with the quest for non-baryonic Dark Matter.

2.2 Weakly Interacting Massive Particles

Following reference [37], let us assume this non-baryonic Dark Matter is made from a new particle species χ. Constraints are placed on these particles by various experiments and observations; see reference [38] for a review rich in primary references.

From structure formation (section 1.4) we know that these particles have to be much more massive than neutrinos. In the early universe, when $T \gg m_\chi$, these particles will be in **thermal equilibrium**. This means that they are present in some number density n_χ, but constantly produced and destroyed in reactions $\chi\bar{\chi} \leftrightarrow f\bar{f}$, where f is some other particle. The annihilation reaction will take place with some characteristic reaction rate $\Gamma = \langle\sigma_\mathrm{A} v\rangle\, n_\chi$ where $\langle\sigma_\mathrm{A} v\rangle$ is the thermally averaged annihilation cross section σ_A given a relative velocity v.

Another time scale is set by the Hubble expansion of the universe, namely the expansion rate $H(t) \equiv \dot{a}(t)/a(t)$. As the universe expands, the χ particles will encounter themselves less and less often, so at some point, the annihilation reactions will no longer be possible. We say the particle will **freeze out**. After freeze out, the number density n_χ in a comoving volume will stay constant, provided only the particle is stable and no other significant production or destruction processes exist. The results from a more detailed numerical analysis, solving the Boltzmann equation in the early universe for n_χ, leads to the prediction shown in figure 2.1.

Given the abundance of particles Ω_χ, one can now predict the mass and cross section for these new Dark Matter particles χ as thermal relics of the early universe (e.g. [39]):

$$\Omega_\chi \equiv \frac{n_\chi\, m_\chi c^2}{\varrho_{\mathrm{critical},0}} \approx \frac{6 \times 10^4\,\mathrm{pb\,km/s}}{\langle\sigma_\mathrm{A} v\rangle}. \tag{2.1}$$

Given today's value for $\Omega_\mathrm{darkmatter}$, and setting $\Omega_\chi \approx \Omega_\mathrm{darkmatter}$, we then get

$$\langle\sigma_\mathrm{A} v\rangle \approx 3 \times 10^5\,\mathrm{pb\,km/s} \tag{2.2}$$

from purely cosmological arguments.

If we turn to particle physics for a moment, the probability for the annihilation is given by Fermi's Golden Rule,

$$\langle\sigma_\mathrm{A} v\rangle = \frac{2\pi}{\hbar} \left|\left\langle f\bar{f}\right| \hat{H} \left|\chi\bar{\chi}\right\rangle\right|^2 \varrho_\mathrm{f} \tag{2.3}$$

with matrix element $\left\langle f\bar{f}\right| \hat{H} \left|\chi\bar{\chi}\right\rangle$ and density of final states ϱ_f. Let the χ particles decay into N relativistic particle species. The energy E_f available in the final state is then simply $E_\mathrm{f} = m_\chi c^2$, and the density of final states is

$$\varrho_\mathrm{f} = N \frac{8\pi\sqrt{2}}{(2\pi\hbar c)^3} E_\mathrm{f}^2. \tag{2.4}$$

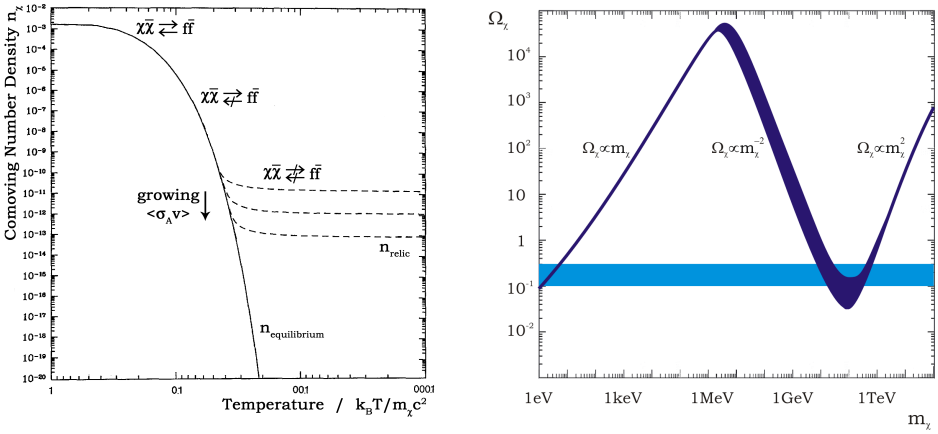

Figure 2.1: Left: The primordial number density n_χ as function of the temperature of the universe T, scaled to the mass m_χ of the particle; hence time progresses to the right. At first, the density follows the Boltzman-suppressed solid line. But at some point annihilation is no longer possible, the number density per comoving volume remains constant, and the particle is said to be frozen out. The higher the value for the thermally averaged annihilation cross section $\langle \sigma_\mathrm{A} v \rangle$, the longer χ particles can annihilate, and the lower the relic abundance n_relic. Figure based on the one from [39]. Right: Taking this production mechanism into account (results in dark blue), the observed Dark Matter density $\Omega_\mathrm{darkmatter}$ (in light blue) can be used to loosely constrain the allowed mass range for the new particles, if they are to be a dominant component. In particular, a large window around masses typical for the weak interaction remains. Figure based on similar plots in [37, 40]. Note that loopholes exist that may modify this simple picture, see e.g. [41].

For a hypothetical new particle χ that is typical for the weak interaction, we would expect $m_\chi \sim \mathcal{O}(10\,\mathrm{GeV/c^2})$ like for the gauge bosons, and for the matrix element we can estimate $\left\langle f\bar{f}\right| \hat{H} \left|\chi\bar{\chi}\right\rangle \sim G_\mathrm{Fermi} = (\hbar c)^3 \times 1.2 \times 10^{-5}\,\mathrm{GeV}^{-2}$. Plugging this in equation 2.3 ($\hbar c = 197\,\mathrm{MeV\,fm}$), we would expect

$$\langle \sigma_\mathrm{A} v \rangle \sim 1 \times 10^6\,\mathrm{pb\,km/s} \tag{2.5}$$

if our new electroweak particles are the dominant component of Dark Matter.

This is a very curious number, and it came as a big surprise [42] that it is close to the cosmological number, equation 2.2. It is by no means clear why those completely independent estimates, one purely cosmological, the other coming from particle physics, should have anything to do with each other. What is more, many models exist as extension to the standard model of particle physics, that do predict particles with such properties. Since these models are motivated by completely independent thoughts, this

makes this connection an intriguing argument in favor of this new particle. Of course all this might just be a coincidence, but it is often taken as a hint on what to search for: **thermal relic particles**. They have a large mass and a cross section that is typical for the electroweak interaction, and are therefore called **Weakly Interacting Massive Particles**, or WIMPs for short. The CRESST experiment aims to detect such particles.

Let us examine in the following chapters, in a few examples from large to small scales, where in the universe we may expect Dark Matter, possibly in the form of WIMPs.

2.3 Galaxy Clusters

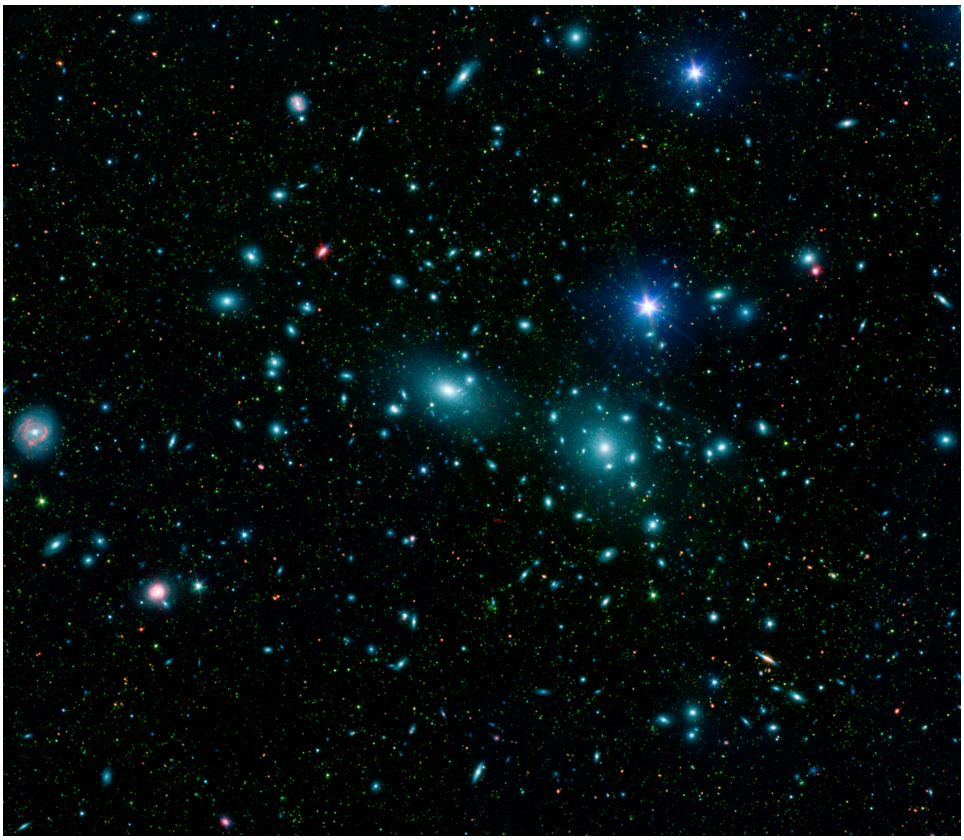

Figure 2.2: A Sloan/Spitzer image of the Coma cluster (Abell 1656), extending many Mpc in space [43]. Almost everything on this picture is a galaxy, including the faint green dots. The few stars in the image can be told by the faint rays they have, caused by interference on the telescope's secondary mirror support structure.

In a stable system of galaxies, kinetic energy T and potential energy V balance and are related via the virial theorem

$$2T = -V. \tag{2.6}$$

One can thus infer the total mass m e.g. of a galaxy cluster by measuring the velocities of the galaxies in the cluster, yielding T and hence V with the radius of the cluster, and therefore m. From such observations of the coma cluster (see figure 2.2), F. Zwicky argued already in 1933 that there had to be 400 times more mass than is seen as luminous and coined the term **Dunkle Materie** to describe this discrepancy [44]. Denoting the mass of the sun as $M_\odot$, modern values for the Coma cluster are a total mass of $1.6 \times 10^{15}\,\mathrm{M}_\odot$ [45], but the total mass of the gas and stars only adds up to about $2.4 \times 10^{14}\,\mathrm{M}_\odot$ [46]. This ratio is rather typical, most clusters have 50 to 100 times more mass than inferred from their luminosity alone [47].

In 2006, a direct observational evidence for Dark Matter was found by observations of the galaxy cluster 1E0657-558, the **Bullet Cluster** [48]. The Bullet Cluster consists of two Clusters of galaxies which passed through each other some time in the past, as can be inferred from their proper motions. Picture 2.3 shows the cluster as seen by three different data sets.

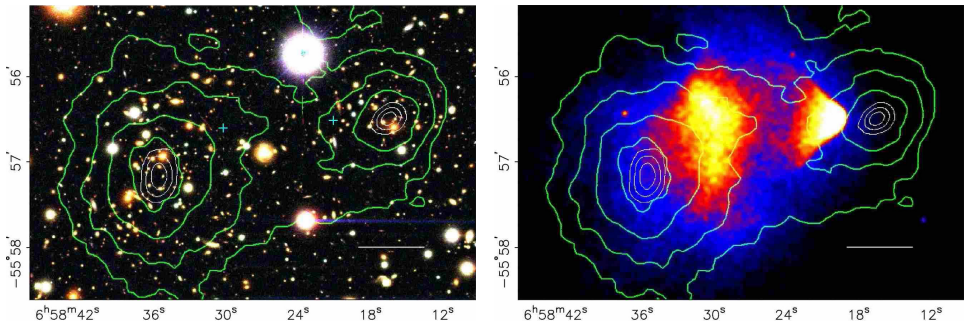

Figure 2.3: The Bullet Cluster, from [48]. Left: Black and white is an optical image, showing the galaxies. Weak lensing of background galaxies allows to map out the gravitational potential of the cluster, shown as the green contour lines. The individual galaxies are centered around the gravitational centers of the two clusters. Right: The gas in the clusters is offset from these gravitational centers as can be seen from this X-ray image. Also, the two gas clouds show clear signs of friction, the right one giving the cluster its name. But since gas is more massive than stars, but offset from both stars and gravitational centers, there has to be an additional mass component, obviously invisible, but also hardly interacting.

The gas is seen to be smoothly distributed around the cluster by its hot X-ray emission. When the clusters where passing each other, the gas was left behind due to friction. And indeed, this can be seen on the right hand side of figure 2.3, where the gas (color representation) is offset from the two clusters. In addition, one can also see a shock front that formed while the clusters passed each other. But since there is about 5 times more mass in the form of gas than in stars, then why are the two centers of gravity as inferred from weak lensing not coincident with the gas? Clearly, there has to be an even more massive component in the clusters, a component that has to be unseen and hardly interacting: Dark Matter again.

2.4 The Local Group

Our local galaxy cluster is the Local Group, where the Milky Way as well as the Andromeda galaxy M31 are the two most massive members. Together they contain about 95% of all Local Group stars, and are about 740 kpc apart. Kahn and Woltjer in 1959 [49] put forward the following **timing argument**: The universe as a whole is expanding linearly. But the Milky Way and the Andromeda galaxy are approaching each other with a velocity of about 123 km/s. Hence, in the absence of any other relevant gravitating body, the mass of these two galaxies needs to be enough to overcome the expansion of the universe. Then, from simple two-body mechanics, one can derive estimates for the total mass of the Milky Way and M31 to be $M_{\mathrm{MW+M31}} = 5 \times 10^{12}\,\mathrm{M}_\odot$ [50]. This needs to be compared to the luminous masses of the two galaxies which are only $M_{\mathrm{luminous}}(\mathrm{MW}) \approx M_{\mathrm{luminous}}(\mathrm{M31}) \approx 10^{11}\,\mathrm{M}_\odot$. Thus in these systems there needs to be an order of magnitude more mass than we can see.

2.5 Spiral Galaxies

An important area of study are **rotation curves of galaxies**, i.e. plots of the circular velocity $v_{\mathrm{rot}}(r)$ of stars in a galaxy. For the purpose of illustration, let us use the simple calculation for a spherically symmetric density distribution $\varrho(\vec{r}) = \varrho(r)$ as an approximation to a galaxy, the basic results of which will remain the same even for a proper treatment [51]. From Newtonian mechanics we know that *within* such a sphere the resulting gravitational force vanishes, and that *outside* of it, we can simply write

$$\frac{m v_{\mathrm{rot}}^2}{r} = \frac{GM(r)m}{r^2} \tag{2.7}$$

$$\Rightarrow v_{\mathrm{rot}} = \sqrt{\frac{GM(r)}{r}} \tag{2.8}$$

where

$$M(r) = \int_0^r 4\pi \varrho(r')\, r'^2\, \mathrm{d}r' \tag{2.9}$$

and the symbols have their usual meanings.

In the center of a galaxy, we have a roughly constant density ϱ_0, so the mass is increasing with the cube of the radius $M(r) \propto r^3$, which implies $v_{\mathrm{rot}} \propto r$. This approximates the observed situation at the very core of the galaxy (barely visible in figure 2.6 on page 34).

In the outskirts of a galaxy, the light typically falls off as a simple exponential with radius. Thus, as one gets to larger radii, basically all the luminous mass is inside a given radius and we can approximate $M(r)$ as point mass M at $r = 0$, so one would naively expect $v_{\mathrm{rot}} \propto r^{-1/2}$. In other words, one would expect the orbits of the stars to be Keplerian, in particular $v_{\mathrm{rot}}(r) \to 0$ as $r \to \infty$.

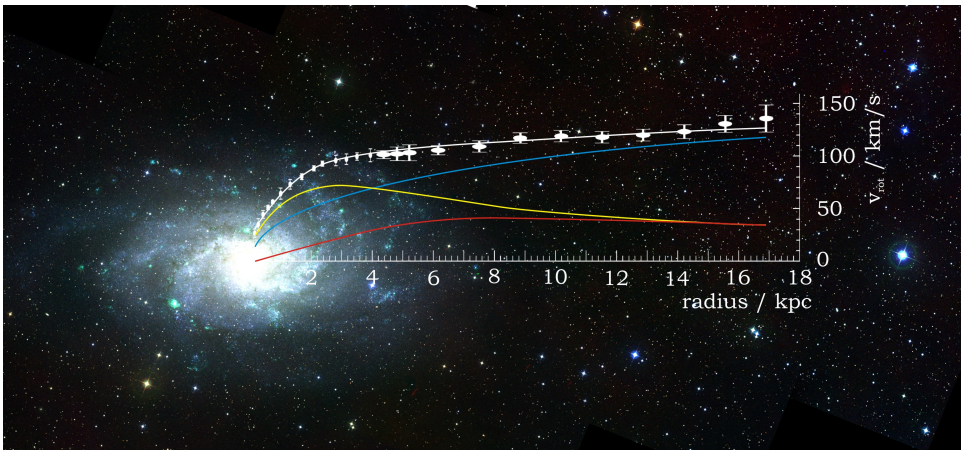

Figure 2.4: The spiral galaxy M33, from images of the Digitized Sky Survey [52]. Overlay is the measured rotation curve [53] (in white) with the best fit curve [54] (also white) and the major components that sum up to the grand total: The contribution of the stellar disc and the nucleus (yellow), the gas (red) and the dark halo (blue).

Rotation curves can be measured to high radial distances from the center of the galaxies, by observing the emission lines of neutral hydrogen (HI) and even some molecules. The overall record holder is the nearby dwarf galaxy NGC3741 for which the rotation curve was recently measured out to 40 times the exponential scale length of the luminous disc [55]. As a typical example for an observed rotation curve, figure 2.4 shows that of the Triangulum galaxy M33. This galaxy is part of our Local Group (only $\approx 900\,\mathrm{kpc}$ away) and makes a good candidate to study, since accurate observations are possible.

For the vast majority of galaxies the observation is the same as that for M33: The rotational velocities remain constant even at high radii and do not fall off as expected. What is more, as seen from figure 2.4, the visible matter is by far not sufficient to explain the high rotational velocities. For the Andromeda galaxy this behavior was known since the work of H. Babcock in 1938 [56]. V. Rubin and W. Ford measured the rotation curves of many more galaxies [57, 58], all showing a similar behavior, never reaching the expected Keplerian behavior. With statistics going in the thousands today, this feature is well established [59, 60].

A robust feature of rotating disks of stars that is observed in simulations is that a bar in the center of the disk forms once the rotational velocity exceeds a certain small value. But only a few observed galaxies do show a bar (our Milky Way is one such example [61]), and given the huge rotational velocities observed, basically all galaxies should be barred. J. Ostiker and P. Peebles found already in 1973 that to prevent a bar from forming, one needs to introduce a spherical halo of additional matter [62].

What can we take for the phase space distribution of such a Dark Matter

halo? Galaxies contract in a process called **violent relaxation** [63], where fluctuations in the gravitational potential during contraction of the galaxy are so large that they change the statistics of the system (hence the name). This suggests that the velocities of Dark Matter particles are thermalized, so they should follow a Maxwell-Boltzmann distribution in the galactic rest frame, an important result for the calculation of expected rates in direct detection experiments (section 3.3.5). For such an **isothermal sphere** (see e.g. [64] or chapter 4.4 in [51]), one has

$$\varrho(r) = \frac{\text{const}}{2\pi G r^2} \tag{2.10}$$

or, for finite densities ϱ_c at $r = 0$,

$$\varrho(r) \quad = \quad \frac{\varrho_c}{1 + (r/r_\text{c})^2}, \tag{2.11}$$

where

$$r_\text{c} \quad := \quad \sqrt{\frac{9\,\text{const}}{4\pi G \varrho_c}} \tag{2.12}$$

is called the **core radius** or **King radius**. This gives $M(r) \propto r$ (equation 2.9), so we can indeed expect a flat rotation curve from such an isothermal sphere.

More generally, measured rotation curves can be fitted with the phenomenological halo form

$$\varrho(r) \quad = \quad \frac{\varrho_c}{(r/r_\text{c})^\gamma \left(1 + (r/r_\text{c})^\alpha\right)^{(\beta-\gamma)/\alpha}}. \tag{2.13}$$

Common choices for the parameters (α, β, γ) that are discussed in the literature are the cored isothermal sphere from above which has $(\alpha, \beta, \gamma) = (2, 2, 0)$, the Navarro-Frenk-White (NFW) profile with $(\alpha, \beta, \gamma) = (1, 3, 1)$ [65, 66], the profile from Moore et al. with $(\alpha, \beta, \gamma) = (1.5, 0, 1.5)$ [67], or sometimes those from Kravtsov et al. with $(\alpha, \beta, \gamma) = (2, 3, 0.2 - 0.4)$ [68]. Predictions from such profiles for the local Dark Matter density ϱ_0 in our own galaxy at the position of the Sun are shown in figure 2.5.

Particles in an isothermal sphere have a constant RMS value throughout (hence the name). From the virial theorem it can be deduced (e.g. [70]) that the RMS velocity of Dark Matter particles at a given radius is the same as the orbital speed around the galactic center of gas and stars at this radius.

2.6 The Milky Way

Also our Milky Way as a whole must contain about 10 times more mass as Dark Matter than is expected from the visible component alone, a robust picture that emerges from a variety of independent measurements [76], and of course also from the rotation curve, figure 2.6.

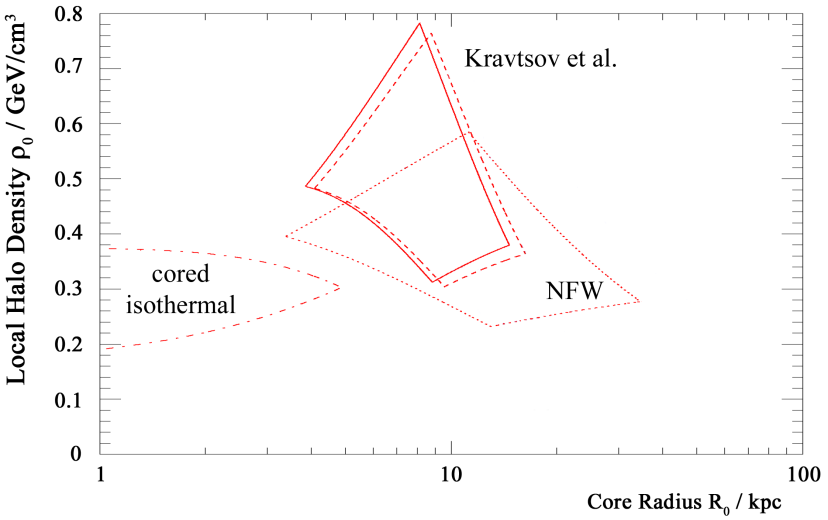

Figure 2.5: Predictions for the local halo density ϱ_0 for a few halo profiles described in the text, based on a figure in [69]. The distance of the sun from the galactic center is taken to be $r_\odot = 8.5\,\mathrm{kpc}$, and the halo mass within a radius of 100 kpc as $(6.3 \pm 2.5)\,\mathrm{M}_\odot$.

It is more difficult to estimate the Dark Matter density ϱ_0 at our position. From a combination of Poisson's equation with the first moment of the Boltzmann Equation in z for an infinite disk one can derive an equation relating the number density $n(z)$ and the velocity dispersion $\bar{v}_z$ of tracer stars (which are both measurable quantities) with the *total* mass density ϱ_{oort} of our galaxy, today called the **Oort limit**:

$$\frac{\mathrm{d}}{\mathrm{d}z}\left[\frac{1}{n(z)}\frac{\mathrm{d}}{\mathrm{d}z}n(z)\bar{v}_z^2\right] = 4\pi G\varrho_{\mathrm{oort}}. \tag{2.14}$$

Oort found that in the Milky Way we observe three times too little mass than expected from this Oort limit. However, todays estimates using the Oort limit [77, 78, 79] are also consistent with the local density being completely dominated by baryonic matter. Hence from the Oort limit we cannot learn much about the Dark Matter.

Hipparcos data on the other hand fits a total local mass density of $(0.076 \pm 0.015)\,\mathrm{M}_\odot/\mathrm{pc}^3$ [80], and requires locally an additional contribution from the Dark Matter halo of $0.007\,\mathrm{M}_\odot/\mathrm{pc}^3 < \varrho_0 < 0.008\,\mathrm{M}_\odot/\mathrm{pc}^3$. For comparison it is useful to note that the mean distance between stars in the vicinity of the Sun is about a parsec, and $1\,\mathrm{M}_\odot/\mathrm{pc}^3 = 38\,\mathrm{GeV/cm}^3$, so this corresponds to a local Dark Matter density of $0.27\,\mathrm{GeV/cm}^3 < \varrho_0 < 0.31\,\mathrm{GeV/cm}^3$, derived under the assumption that the Dark Matter is distributed in a strictly spherical halo. Other references give values e.g. as $0.18\,\mathrm{GeV/cm}^3 < \varrho_0 < 0.30\,\mathrm{GeV/cm}^3$ [81] or $0.3\,\mathrm{GeV/cm}^3 < \varrho_0 < 0.43\,\mathrm{GeV/cm}^3$ [82], see also figure 2.5. A value of $\varrho_0 := 0.3\,\mathrm{GeV/cm}^3$ is generally adopted to simplify comparison between experiments [39]. Most of this Dark Matter density ϱ_0 needs to be non-baryonic, since known com-

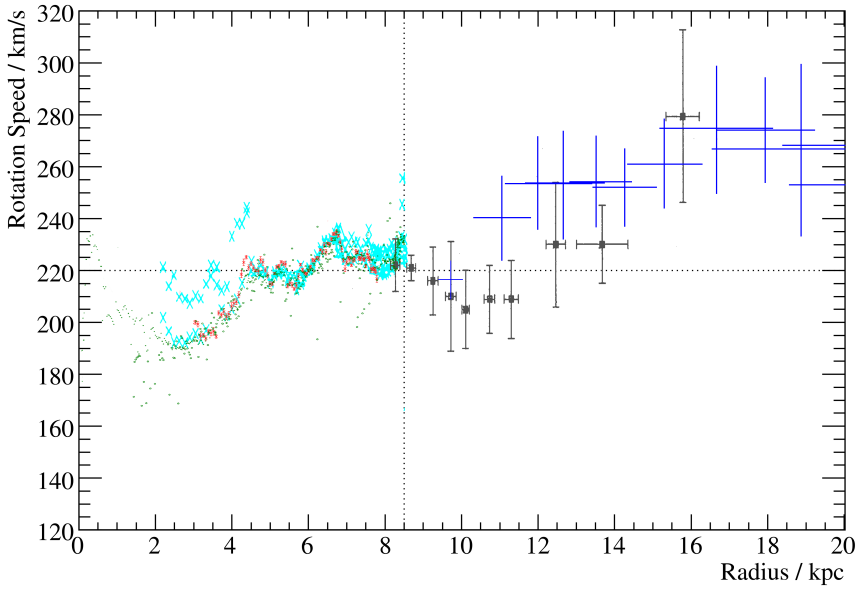

Figure 2.6: Rotation curve of our galaxy, from various data sets: From neutral hydrogen absorption (HI) in cyan [71] and blue [72], from ionized hydrogen (HII) emission in gray [73], red from a recent 21 cm line observations [74] (note that these points include the error bars), and from carbon monoxide emission in green [75] which was rescaled so that the HI data from the same publication match that of [74]. Clearly, the Milky Way needs to be Dark Matter dominated, too. The local ($r_\odot = 8.5\,\mathrm{kpc}$) rotational velocity is estimated to be 220 km/s.

ponents such as e.g. faint white dwarfs contribute less than 1% to the halo density [83].

The circular velocity in the disk near the Solar radius (at a distance of 8.5 kpc from the Galactic center) is $v_\odot = (220 \pm 30)\,\mathrm{km/s}$ [50]. Reference [39] gives a simple model for the Dark Matter distribution in the Milky Way which leads to the equation

$$\varrho_0 = 0.47\,\mathrm{GeV/cm^3}\,\frac{\left(\frac{v_\infty}{220\,\mathrm{km/s}}\right)^2}{\left(\frac{r_0}{8.5\,\mathrm{kpc}}\right)^2\left(1+(\frac{r_\mathrm{c}}{r_0})^2\right)} \tag{2.15}$$

relating the local Dark Matter density ϱ_0 with the rotation speed at large radii v_∞, the local radius r_0, and the core radius r_c of the Dark Matter halo. Therefore, one should keep in mind that these parameters are not independent from one another.

2.7 The Solar System

The smooth gravitational potential of our galaxy will not alter the orbits of our Solar System's planets, since the solar system is small compared to the galaxy. However, an **additional heliocentric distribution** of Dark Matter can introduce observable effects. In particular, such an additional matter distribution, typically taken to be spherically symmetric, would introduce a secular precession on the longitude of the perihelia. However, this effect is weak, and from current precision data on the planets, one cannot limit this *additional* Dark Matter density very much: $\Delta\varrho_0 \lesssim 10^4\,\mathrm{GeV/cm^3}$ [84, 85].

Nevertheless, this limit is already strong enough to exclude that the Pioneer anomaly [86, 87] might be caused by such a halo, since this would require $\Delta\varrho_0 \approx 8\times10^9\,\mathrm{GeV/cm^3}$, far above the allowed value [88]. Also, Dark Matter explanations for the recently discovered Earth flyby anomalies [89] seem highly unlikely [90].

As the Sun goes around the Milky Way, it encounters the halo of Dark Matter. The conservative gravitational potential of the Sun cannot capture such particles. But once the planets are taken into account, the potential becomes time-dependent, so Dark Matter may loose energy and be captured by the Sun's gravitational potential in a process similar to that of spacecraft swing-by maneuvers. Many ideas in this direction have been put forward in the 1990s, see e.g. references [91, 92]. Very recently this effect of **gravitational capture** was calculated to increase the Dark Matter density in the Solar System by up to five orders of magnitude [93], although this is probably rather an upper limit and seems to be in contrast to some simulations [94]. In particular, the authors find a local Dark Matter density of $\varrho_\oplus \approx 5500\,\mathrm{GeV/cm^3}$, four orders of magnitude higher than the generic Galactic halo density.

Part II

Detection Experiments

Chapter 3

Hunting Dark Matter

Intent: How can we hope to get hold of Dark Matter particles? Three main fields are available: Production of new particles at collider experiments, the search for signals from Dark Matter annihilation, and the search for direct interactions of Dark Matter particles in a laboratory environment. This chapter gives a brief overview over the status of other experiments, and presents the theory behind the expected direct detection signal, before we come to the CRESST experiment in the next chapter.

Organization: Section 3.1 briefly comments on Dark Matter production in colliders. Section 3.2 reports on the status of current experiments to search for indirect Dark Matter annihilation signals. Section 3.3 provides the theory necessary for direct Dark Matter detection, and section 3.4 gives an overview over direct search experiments other than CRESST.

3.1 Collider Experiments

Of course new particles are commonly found by collider experiments. Since Dark Matter particles hardly interact, their typical signature in such an experiment is missing energy in the detector. Thorough understanding of the experiment is therefore an indispensable prerequisite. Taking into account that the **LHC** will start operation in 2009, this translates in a vanishing discovery potential for collider experiments in the next few years, until the systematics of these very complicated devices are under control [95, 96]. However, in case of a discovery, it is rather easy to determine the mass of the new particles from their collider signature (e.g. [97]). Current **mass lower limits** come from the LEP collider and are $m_\chi \gtrsim 42$ to $50\,\mathrm{GeV/c^2}$ [98] with mild variations depending on specific model assumptions. Of course, even if new particles are discovered at collider experiments, that does not mean that they are the Dark Matter. Collider experiments are a complementary way to gain insight in the nature of Dark Matter.

3.2 Annihilation Searches

We saw already in section 2.2 that WIMPs can annihilate in the early universe, so one way to search for them is to search for their annihilation prod-

ucts, often called **indirect searches**. Basically any annihilation product is possible, and various channels, each with its own peculiarities, are available. Typically dubbed a **smoking gun** signal would be a line in the spectrum of the annihilation products, but a continuous spectrum is also possible.

Generally, the **annihilation rate** involves two WIMP particles which have to collide, so the rate is $\Gamma_{\text{indirect}} \propto n_\chi^2 \, \sigma_\text{A} v$ where n_χ is the number density of WIMPs and σ_A their annihilation cross section. While from cosmology one can get an idea about $\langle \sigma_\text{A} v \rangle$ (section 2.2), for a given v this can still lead to order-of-magnitude uncertainties. The Dark Matter density n_χ is taken from astrophysical observations, but, as we have seen in section 2.5, this requires some modeling. Due to the quadratic dependence, this also leads to large uncertainties. Very often the Dark Matter profile near the center of galaxies is taken to be $\varrho(r) \propto r^{-1}$ (Navarro-Frenk-White [65, 66]) or $\varrho(r) \propto r^{-1.5}$ (Moore et al. [67]).

An important question arises about the **clumpiness** of Dark Matter. Simulations of structure formation show structure on all scales, with no cut-off even at the smallest modeled scales. Recently, high resolution simulations ($M_\text{min} = 4100\,\text{M}_\odot$) of the structure formation of a Milky Way sized Dark Matter halo (the Via Lactea II simulation [99]) have shown that small scale structures remain from the hierarchical merging of structures even today. This would allow sub-structure to exist which could significantly boost the annihilation signal, leading to the name **boost factor** for the enhancement of a signal that is attributed to the clumpiness of Dark Matter. However, recent analysis tends to disfavor high boost factors [100], and from the Via Lactea II simulation one expects boost factor between 2 and 30 at most [99]. As for other galaxies, such subhalos of Dark Matter might one day be detectable due to strong gravitational lensing of background quasars, but with current or upcoming technology prospects seem rather dim [101].

In the following, various annihilation products are introduced: Photons of various energies, antiparticles, and neutrinos. The interested reader should have a look at the nicely written overview by D. Hooper [102] or the more complete review [103].

3.2.1 meV Photons

The WMAP satellite not only measures the cosmic microwave background, but naturally also any foreground emission in this frequency range. About 20° around the center of the Milky Way an excess microwave emission is observed in addition to the known contributions [104]. This excess emission became known as the **WMAP Haze**, and is shown in figure 3.1.

No standard processes are known that could create such a signal, and it could well stem from synchrotron radiation from Dark Matter annihilation products [105]: A WIMP annihilation could produce relativistic electrons and positrons, which travel through the galactic magnetic field. Modeling the resulting synchrotron radiation fits nicely to a Dark Matter density profile $\varrho(r) \propto r^{-1.2}$ just as expected, does not require any boost factor, and

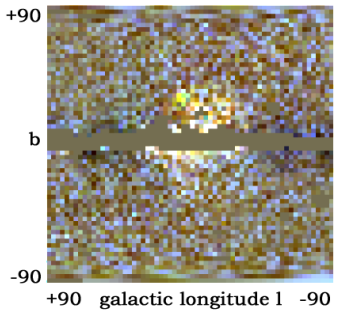

Figure 3.1: An image of the WMAP haze. Since the WMAP haze is roughly independent of energy, it shows up as white structure in this false color picture. Image created from data in [104]

fits within a factor of two or so to a cross section of $\sigma_A v \approx 3 \times 10^5\,\mathrm{pb\,km/s}$ required by thermal WIMP synthesis (equation 2.1 on page 26). From this hypothesis, a prediction for a gamma ray flux from the center of the Milky Way was derived that should be observable by the FGST/GLAST satellite [106].

3.2.2 511 keV Gammas

With the INTEGRAL satellite, a very bright 511 keV pair annihilation emission from the center of our galaxy was observed [107]. Since the signal was orders of magnitude stronger than expected, and distributed spherically around the center of the galaxy, Dark Matter was soon at hand to explain this signal [108]: WIMPs might **pair annihilate** into electron-positron-pairs $\chi\bar{\chi} \to e^- e^+$, giving rise to such a line signal. However, this would require Dark Matter with $m_\chi \sim \mathcal{O}(\mathrm{MeV/c^2})$, disfavored by particle physics. Alternatively, $m_\chi \approx 500\,\mathrm{GeV/c^2}$ WIMPs could be excited through collisions, and the de-excitation might yield an electron-positron pair, a model going under the name of *exciting Dark Matter* [109].

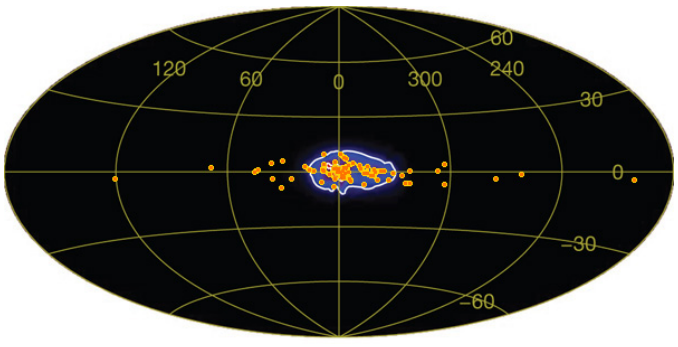

Figure 3.2: The INTEGRAL 511 keV emission (color map) is aligned with the distribution of hard low mass X-ray binaries (orange dots) and not spherical as expected for a Dark Matter annihilation signal.

However, with much more statistics today, the signal is distributed rather

lopsided around the galactic center, and coincides with the distribution of a certain class of **X-ray binaries** [110] (see figure 3.2). This suggests these binary stars as sources of the 511 keV signal, rendering the Dark Matter explanation dispensable.

3.2.3 Galactic GeV Gamma Rays

The EGRET instrument on board the COBE satellite has measured the diffuse galactic gamma ray spectrum to be higher than expected from conventional models. This excess can be explained to be due to gamma rays from π^0 decay which are produced during hadronization of the WIMP decay products [111] and fits a supersymmetric WIMP with masses of $\approx 100\,\mathrm{GeV/c^2}$ [112], see figure 3.3. Fitting the spectrum in different directions even allows to reconstruct a variation of the intensity of the signal that is consistent with features in the rotation curve of the Milky Way.

On the other hand, such strong substructures are not expected for the Dark Matter halo, and the excess signal is rather pronounced, requiring a boost factor of about 100. In addition, we will see shortly (section 3.2.7) that such a strong signal leads to tensions with other observable channels. Not surprisingly, other authors provide alternative explanations of the excess in terms of mildly modified cosmic ray propagation models [113].

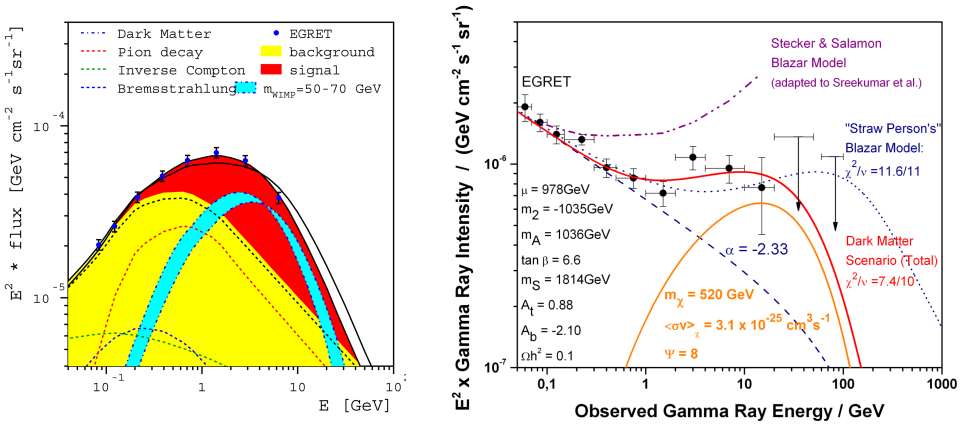

Figure 3.3: Left: The EGRET gamma ray spectrum (from [111]) shows an excess (red) over the expected backgrounds (yellow) for its diffuse flux from our galaxy. This excess can be fitted assuming gammas from Dark Matter annihilation (cyan). Right: The extragalactic gamma ray flux might also contain a Dark Matter annihilation signal (from [114]).

More recently, a careful investigation of **instrumental effects** leads one to conclude that systematic errors in the EGRET calibration can give rise to this effect [115]. The authors show that the excess appears uniformly over the whole sky, easily explainable by a mis-calibration of EGRET's sensitivity in this energy range. This uniformity is very different from the spatial flux distribution expected for Dark Matter annihilation. It has thus been argued

that the angular distribution of gamma rays rather than their spectral shape should be taken as signature for Dark Matter annihilation [116].

3.2.4 Extragalactic GeV Gamma Rays

After the subtraction of 271 EGRET point sources, the diffuse extragalactic gamma-ray emission remains, which, again, can be described by scenarios both with and without Dark Matter, see figure 3.3. The Dark Matter explanation fits a WIMP with mass $\approx 500\,\mathrm{GeV/c^2}$ [114], but requires high boost factors of up to 100. However, to be consistent with the galactic flux, this explanation implies that the Dark Matter profile of our galaxy is much less cusped than that of other galaxies [117].

Alternatively, the data can be nicely explained without Dark Matter to originate in **blazars** [118]. And of course this data is subject to the EGRET calibration issues as well, so the Dark Matter indication stands on shaky grounds.

3.2.5 TeV Gamma Rays

The story repeats for TeV gamma rays coming from the galactic center. Shortly after measurements of the gamma ray spectrum at these energies, ideas where put forward to explain the observed flux as a Dark Matter annihilation signal of heavy particles [119, 120] or, alternatively, by more conventional mechanisms such as particle acceleration near the black hole Sgr A* [121] or in the supernova remnant Sgr A East [122]. With more data available today [123] the Dark Matter explanations became incompatible with the data, see figure 3.4, instead favoring an astrophysical source with a constant spectral slope.

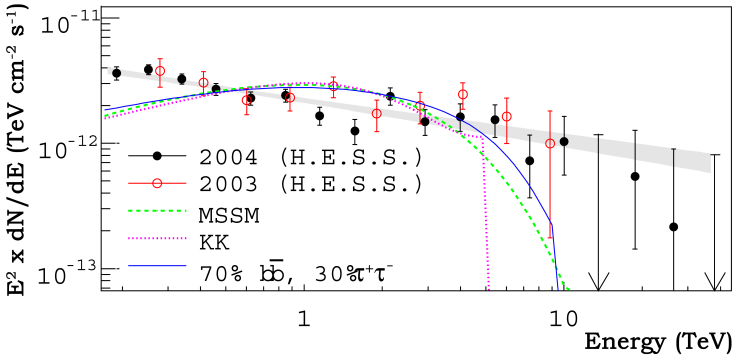

Figure 3.4: Spectrum of high energy gamma rays coming from the galactic center (multiplied by E^2 as is customary in this field), from [123]. While various $m \sim \mathcal{O}(\mathrm{TeV/c^2})$ Dark Matter explanations (green, violet, blue) were compatible with early data (red), more data (black) renders these explanations unlikely. In gray a simple power-law fit to the data, expected from conventional cosmic ray models.

3.2.6 Positrons

Generally, one expects antiparticles from WIMP annihilations, and since there are much less **antiparticles in the cosmic rays** than particles, one has a very favorable signal to noise ratio in antiparticle signatures to search for Dark Matter. One possibility are positrons from WIMP annihilations. Indeed, during its balloon flights in the 1990s, the HEAT experiment has observed an excess signal [124] over the expected flux from standard galactic propagation models [125], see figure 3.5. To explain this in terms of WIMPs, large boost factors are required [126]. Whether this excess flux of positrons is statistically significant, and if so, whether it can stem from Dark Matter annihilation will become much clearer once the PAMELA experiment releases its data so eagerly anticipated.

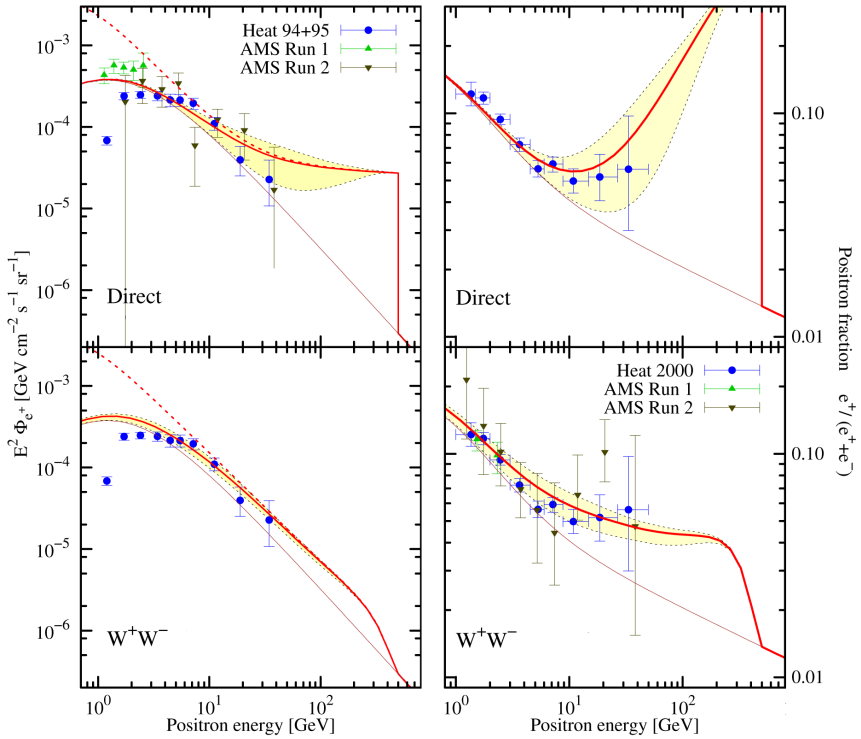

Figure 3.5: The positron excess explained in terms of a WIMP annihilation signal, here with $m_\chi = 500\,\mathrm{GeV/c^2}$, from [126]. The total measured and expected positron flux (scaled by E^2) on the left, and the positron fraction on the right. The top two figures show the signal from a direct $\chi\bar{\chi} \to e^+e^-$ annihilation, which has a very clear cutoff at the WIMP mass. The bottom two figures are smeared out due to the annihilation going into two W bosons. The authors assume a Navarro-Frenk-White halo, and a boost factor of 300 with respect to the thermal annihilation cross section.

3.2.7 Antiprotons

The first measurements of the antiproton flux also showed some excess over the expected signal, but once secondary antiproton-production by cosmic rays interacting with the galaxy were taken into account, the measured antiproton flux agreed well with the background estimates, see figure 3.6. Generally speaking, propagation effects are a source of major uncertainty [127], with the effects of the 11 year solar cycle being just one factor, but also, the expected rates are not very optimistic for a discovery of Dark Matter annihilation [128].

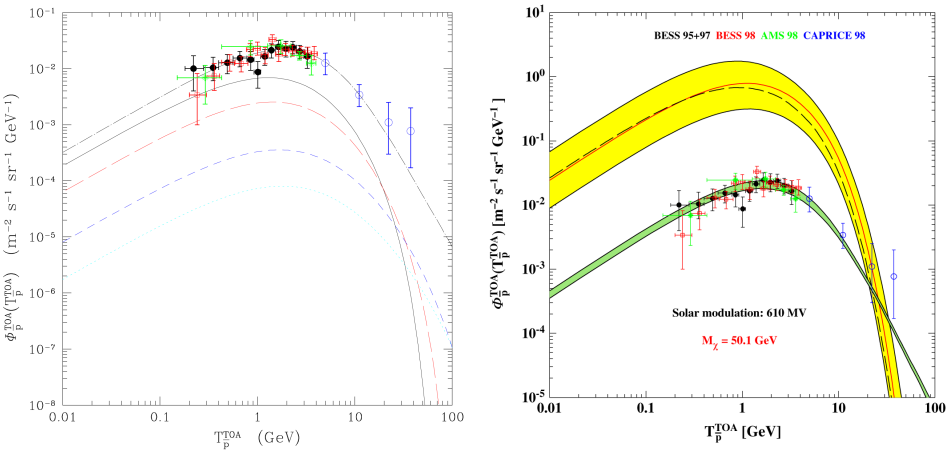

Figure 3.6: Left: The measured antiproton flux with data from BESS (black, red), AMS (green) and CAPRICE (blue), together with the expected background (uppermost black dashed line), from [127]. No excess is seen in the antiproton flux. The other curves are various expectations from Dark Matter annihilation. Right: The model that explains the EGRET gamma ray excess in terms of Dark Matter annihilation would lead to a flux of antiprotons orders of magnitude above the observed flux [129].

Earlier we saw that the EGRET excess of gamma rays may be explained by WIMP annihilations. But from the same jets that produce the gamma rays, one would also expect antiprotons. In fact, in standard halo models, the expected antiproton flux from such jets is orders of magnitude higher than observed [129], see figure 3.6. Needless to say, tweaked propagation models are available that reconcile the data with the Dark Matter interpretation [130].

3.2.8 Antideuterons

Work done in recent years suggest that antideuterons are a very clean channel for the detection of Dark Matter annihilation: The dominant background comes from spallation, but is at low energies ($<$ GeV) and orders of magnitude below the expected annihilation signal [133], see figure 3.7. Thus with

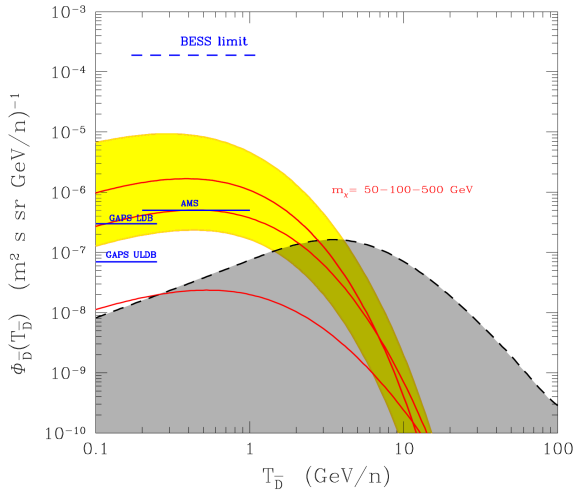

Figure 3.7: Expected antideuteron fluxes, based on figures in [131]. The gray area is the expected background from cosmic ray spallation processes. In red three curves for WIMPs with masses of, from top to bottom, 50, 100 and 500 $\mathrm{GeV/c^2}$. Clearly the discovery potential in this low energy range is highest for low mass WIMPs. Yellow is the uncertainty of the 50 $\mathrm{GeV/c^2}$ WIMP prediction due to uncertainties in antideuteron propagation models. In blue the existing limit from the BESS experiment [132] and some expected sensitivities of upcoming experiments.

antideuterons one could probe very significant portions of the parameter space in many Dark Matter models, and in terms of theoretical expectations and uncertainties, it might be the best indirect channel to find e.g. the supersymmetric neutralino, or to constrain mSUGRA [134]. However, current experiments are not yet sensitive enough.

3.2.9 Neutrinos

We will see in the next section 3.3 that Dark Matter particles might interact with standard nuclei. This interaction may be independent of the spin, in which case it favors heavy target materials, or it may be spin dependent, favoring light target nuclei with spin. Thus Dark Matter particles may be captured in the Sun (via spin-dependent interaction) or Earth (via spin-independent interaction). If the Dark Matter density is at or close to equilibrium between capture and annihilation, then the annihilations in the center of the Sun and Earth may produce a detectable flux of high energy neutrinos [128]. Given current technology, namely the cubic kilometer neutrino telescope IceCube at South Pole, the neutrino channel has somewhat better detection prospects for annihilations in the sun, since direct detection experiments already highly constrain the spin-independent interaction cross section [135], as we will see in the following section. No neutrino signal from Dark Matter annihilation has yet been observed.

3.3 Direct Scattering

If WIMPs are thermally produced in the early universe, Feynman graphs for their annihilation must exist. But then we may also expect the WIMPs to scatter from baryonic matter, so direct scattering experiments are a complementary mean to search for Dark Matter.

3.3.1 Astro- and Geophysical Constraints

Gravitational lensing on the extended dark halo of the galaxy cluster Abell 2218 allows to constrain the direct WIMP-nucleon scattering cross section to $\sigma < 7 \times 10^{13}\,\mathrm{pb} \times m_\chi/(\mathrm{GeV/c^2})$ [136]. In addition, if the halo of our Milky Way is to be stable, the infall time for a Dark Matter particle onto the disk must be large compared to the Hubble time. Given the known parameters of the Milky Way, this places an upper limit on the scattering cross section as $\sigma < 5 \times 10^{11}\,\mathrm{pb} \times m_\chi/(\mathrm{GeV/c^2})$ [137]. Even more stringent limits come from cosmic rays: If high energy protons from cosmic rays interact with a WIMP, this interaction would likely take place with a single quark only, thus destroying the proton, eventually leading to a readily detectable flux of gamma rays. From this, the limit $\sigma < 9 \times 10^{9}\,\mathrm{pb} \times m_\chi/(\mathrm{GeV/c^2})$ can be imposed [138].

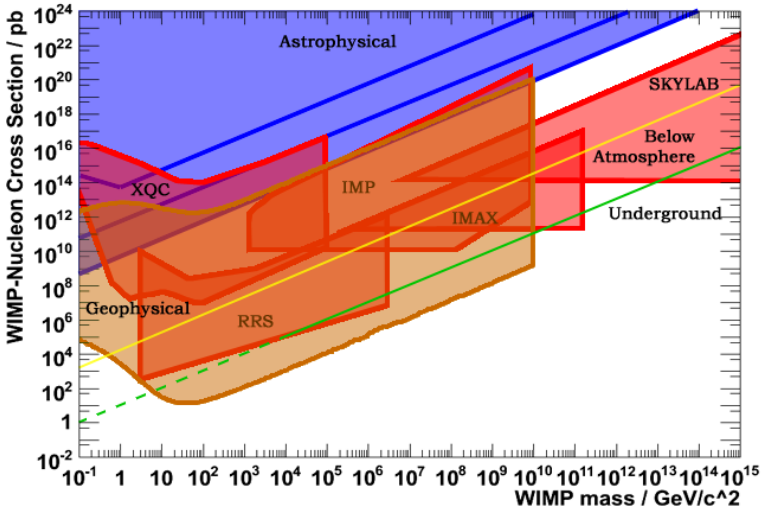

Figure 3.8: Constraints on the WIMP-nucleon scattering cross section from astrophysical observations [136, 137, 138] in blue, from geophysical considerations [139] in brown, and some high-altitude experiments (as quoted in [139]) in red. Yellow is an estimate of the maximum cross section accessible to detectors on Earth ($\sigma < 4 \times 10^{4}\,\mathrm{pb} \times m_\chi/(\mathrm{GeV/c^2})$), since WIMPs need to be able to penetrate the atmosphere [140]. Green is the maximum cross section accessible to typical underground detectors [141], extrapolated to lower masses (dashed).

Recently, much more stringent limits could be derived from Earth's heat

flow [139]. If the WIMP-nucleon scattering cross section is high, WIMPs are captured by Earth, settle to her core, and eventually annihilate. This would lead to an heat flow from the center of Earth, which is restricted by geophysical measurements to less than 44 TW. A summary of these and a few other constraints is shown in figure 3.8.

From what we saw in section 2.2 we should not be surprised to find much lower WIMP-baryon scattering cross sections. To discover such interactions, dedicated experiments are required. But can weakly interacting massive Dark Matter particles be detected directly by their interactions with a laboratory scaled apparatus at all? Two important features dominate the experiments that aim to do so: The low energies anticipated from an interaction, and the low expected rates.

3.3.2 Low Energies

The energies that may be expected can be quickly estimated: If a halo particle with momentum p_χ scatters from a target nucleus in an Earth bound detector, the transferred momentum will be at most $2p_\chi$, so the recoil energy of the target nucleus is at most

$$E_{\mathrm{r,max}} = (2p_\chi)^2/2m_\mathrm{N}. \tag{3.1}$$

For simplicity, put $v = 300\,\mathrm{km/s} = 10^{-3}c$ and $m_\chi = m_\mathrm{N} = 100\,\mathrm{GeV/c^2}$, so the maximum energy that we can hope for from such an interaction is

$$E_{\mathrm{r,max}} = \frac{\left(2 \times 100\,\mathrm{GeV/c^2} \times 10^{-3}\mathrm{c}\right)^2}{2 \times 100\,\mathrm{GeV/c^2}} = 200\,\mathrm{keV}. \tag{3.2}$$

Nuclear physics and astrophysics reduce the energies to the $\mathcal{O}(10\,\mathrm{keV})$ range, so this calls for low energy detectors. It was only in the mid 80s, when two seminal papers triggered work on Dark Matter detectors: In 1984, A. Drukier and L. Stodolsky proposed a neutral-current detector for neutrino physics [142] that should be able to detect these low energies. Their idea was to use small superconducting grains: Following the energy deposit of a neutrino interaction, these would go normal conducting, and the change of resistance could be measured. Quickly thereafter, M. Goodman and E. Witten adopted the idea to the search for Dark Matter, and estimated the prospects of such a detector [143]. Today, after 20 years of research in the field, technologies are refined and discovery prospects better than ever. The main players in the field are discussed toward the end of this chapter in section 3.4.

3.3.3 Low Rates

As a first approximation, the event rate Γ for a detector with n_target nuclei, given a WIMP Flux Φ and the elastic scattering cross section σ is

$$\Gamma = n_\mathrm{target} \Phi\, \sigma \tag{3.3}$$

or, with the target mass M_{target} of a material with mass number A and nucleon mass m_{N}, the WIMP mass m_χ and density ϱ_χ, and the average WIMP speed onto the target $\langle v \rangle$:

$$\Gamma = \frac{M_{\text{target}}}{m_{\text{N}}} \frac{\varrho_\chi}{m_\chi} \langle v \rangle \, \sigma. \tag{3.4}$$

With some typical values this is equivalent to

$$\Gamma = 0.03/\text{day} \; \frac{\frac{M_{\text{target}}}{1\,\text{kg}}}{\frac{A}{100}} \frac{\frac{\varrho_\chi}{0.3\,\text{GeV/cm}^3}}{\frac{m_\chi}{100\,\text{GeV/c}^2}} \frac{\langle v \rangle}{230\,\text{km/s}} \frac{\sigma}{1\,\text{pb}}, \tag{3.5}$$

a very low rate indeed. Together with the low energies anticipated, this sets the challenge for any direct Dark Matter detection experiment.

3.3.4 Interaction Modes

How might Dark Matter particles interact with ordinary matter? On the one hand, the WIMP may couple to the net spin of the target nucleus. For a detection experiment this suggests light nuclei with odd proton and/or neutron numbers to detect this **spin-dependent** interaction.

But let us estimate the de Broglie wavelength λ of our aforementioned WIMP:

$$\frac{\lambda}{2\pi} = \frac{\hbar}{p} = \frac{\hbar c}{mc^2 \, v/c} = \frac{197\,\text{MeV fm}}{100\,\text{GeV}\;10^{-3}} = 1.97\,\text{fm} \approx r_{\text{nucleus}} \tag{3.6}$$

where r_{nucleus} is the length scale of an atomic nucleus. Hence it is reasonable to assume that the WIMP is not able to resolve individual nucleons but instead interacts **coherently** with all the A target nucleons at the same time. Then, for such a **spin-independent** interaction, the A individual WIMP-nucleon scattering amplitudes will add up in phase. This increases the WIMP-nucleus scattering probability by a factor A^2, so equation 3.4 is modified to read

$$\Gamma = \frac{M_{\text{target}}}{m_{\text{N}}} \frac{\varrho_\chi}{m_\chi} \langle v \rangle \, \sigma_{\chi\text{N}} A^2 \tag{3.7}$$

$$= 300/\text{day} \; \frac{\frac{M_{\text{target}}}{1\,\text{kg}}}{\frac{A}{100}} \frac{\frac{\varrho_\chi}{0.3\,\text{GeV/cm}^3}}{\frac{m_\chi}{100\,\text{GeV/c}^2}} \frac{\langle v \rangle}{230\,\text{km/s}} \frac{\sigma_{\chi\text{N}}}{1\,\text{pb}} \frac{A^2}{100^2}. \tag{3.8}$$

In light of the rather pessimistic estimate of equation 3.5, this brightens the prospects somewhat for experiments that use heavy target nuclei. Therefore, this coherent detection channel is generally expected to have the better cards for a discovery.

Once the theoretically possible dependence of the interaction on the isospin of the target (i.e. the difference between protons and neutrons) [144] is neglected, the total scattering cross section σ_{tot} is just the sum of the two cases, $\sigma_{\text{tot}} = \sigma_{\text{spin-independent}} + \sigma_{\text{spin-dependent}}$. Although limits on the

cross section are given assuming either pure spin-dependent or pure spin-independent interactions, in reality, the truth may lie somewhere in between. In the CRESST-II experiment, we use $CaWO_4$ crystals as target material. In these crystals, only 2.4% of the nuclei have a net spin, so the experiment is not sensitive to spin-dependent interactions, and we will only consider the spin-independent case in what follows.

3.3.5 Expected Recoil Spectrum

Following the notation of reference [145], let us consider a few additional effects beyond the simple picture of equation 3.4.

The Form Factor: The cross section σ depends on the recoil energy $E_\mathrm{r} = q^2/(2m_\mathrm{N})$, since it is reduced by the **form factor** $F(q)$ for large momentum transfers q. Often the form factor is defined via $\mathrm{d}\sigma/\,\mathrm{d}\Omega$, but let us conveniently define it directly in dependence of the recoil energy:

$$\frac{\mathrm{d}\sigma}{\mathrm{d}E_r} = \frac{\sigma_0}{E_{\mathrm{r,max}}(v)} F^2(q) \tag{3.9}$$

where σ_0 is the **total, point-like WIMP-nucleus scattering cross section**, and $E_{\mathrm{r,max}}(v)$ is the highest possible energy transfer (which happens when the scattering angle θ gives $\cos\theta = 0$). For the form factor that describes the elastic scattering of WIMPs on a target nucleus, we use the parametrization put forward by R. Helm [146]. This **Helm form factor** is the Fourier transform of a box potential convolved by a Gaussian:

$$F(q) = 3\,\frac{j_1(qr_0)}{qr_0} \exp\left(-\frac{1}{2}(qs)^2\right) \tag{3.10}$$

where $j_1(qr_0)$ is the first spherical Bessel function, $s \approx 1\,\mathrm{fm}$ is the thickness of the nucleus surface, and $r_0 \equiv \sqrt{r^2 - 5s^2}$ where $r = 1.2A^{1/3}$, see figure 3.9. The Helm form factor is a standard parametrization, in use for spin-independent Dark Matter searches since it was proposed adequate by J. Engel [147]. Its parameters are adopted from data of electron scattering experiments, so an implicit assumption is that the WIMP scatters are distributed as the charge in the nucleus [148].

Halo Velocities: Instead of just using the average $\langle v \rangle$ in equation 3.4, we have to properly take into account the velocity distribution $f(v)$ of WIMPs. This will be the distribution of WIMPs in the Galactic halo, modulated by the motion of Earth and Sun through the galaxy, and transformed to the Earth frame. Hence we calculate with a differential rate $\mathrm{d}\Gamma/\,\mathrm{d}E_\mathrm{r}$ and replace the average velocity by the integral

$$\langle v \rangle \to \int_{v_\mathrm{min}}^{\infty} v f(\vec{v})\,\mathrm{d}\vec{v} \tag{3.11}$$

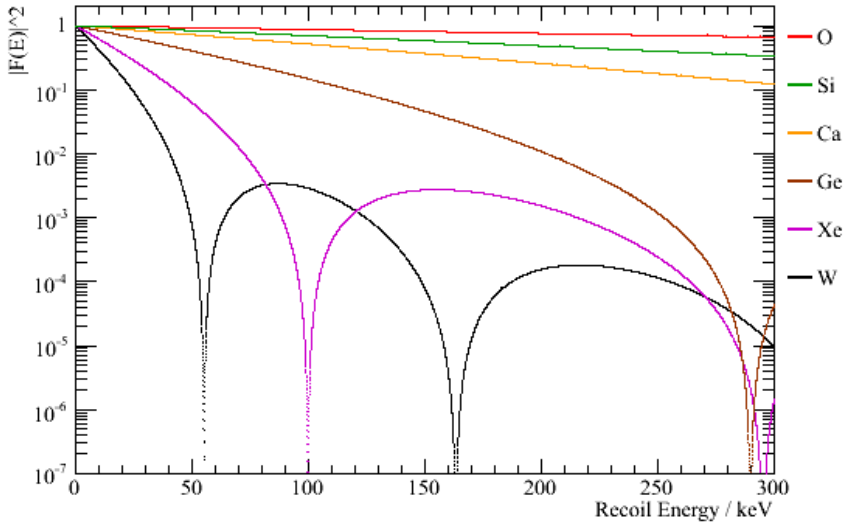

Figure 3.9: The Helm form factor with the parameter values given in the text, for various nuclei used in Dark Matter searches. Note that for tungsten, the form factor causes a complete suppression of the recoil spectrum at transferred momenta corresponding to a recoil energy of about 50 keV.

over the velocity density function $f(v)$, defined in the galactic coordinate system. Here, we integrate from the minimum velocity for given recoil energy E_r to infinity, with

$$v_\mathrm{min} = \sqrt{\frac{E_\mathrm{r} m_\mathrm{N}}{2\mu^2}} \tag{3.12}$$

and the reduced WIMP-nucleus mass

$$\mu = \frac{m_\chi m_\mathrm{N}}{m_\chi + m_\mathrm{N}}. \tag{3.13}$$

We have already seen in section 2.5 (page 32) that we may expect the Dark Matter in the Milky Way to be distributed in an isothermal sphere, where the particles are thermalized and follow the Maxwell-Boltzmann distribution. This Maxwell-Boltzmann distribution is slightly modified by a truncation above the escape velocity v_esc of the galaxy and then reads

$$f(v) = \frac{1}{\mathcal{N}} \left(\frac{3}{2\pi w^2}\right)^{3/2} \exp\left(-\frac{3v^2}{2w^2}\right) \tag{3.14}$$

with the root mean square velocity w and a normalization factor

$$\mathcal{N} = \mathrm{erf}(z) - \frac{2}{\sqrt{\pi}} z \exp(-z^2), \tag{3.15}$$

$$z^2 = \frac{3v_\mathrm{esc}^2}{2w^2}, \tag{3.16}$$

which would be absent for the untruncated distribution. The value of the escape velocity is somewhat uncertain, $v_{\rm esc} = 550 \pm 100\,{\rm km/s}$ [149], but the effect due to this truncation is small when compared to other theoretical uncertainties. We adopt as a reference value $v_{\rm esc} = 650\,{\rm km/s}$ [145] at the upper end of this range.

For the isothermal sphere, the **root mean square velocity** w is $w = \sqrt{3/2}v_\infty$, where v_∞ is the asymptotic value of the rotational velocities (e.g. [150]). We take the standard IAU values [151] $v_\infty = v_\odot = (220 \pm 20)\,{\rm km/s}$ despite figure 2.6 suggesting a somewhat larger value of v_∞, so $w \equiv \bar{v} \equiv \sqrt{\langle v^2 \rangle} := 270\,{\rm km/s}$ [39].

Other corrections arise to the isothermal sphere but are generally neglected due to the small effects they introduce, of order one percent or so: One is the anisotropy of the local gravitational potential due to the baryonic disk [152], and another one from the gravitational potential of the Sun which also modifies the velocity distribution of Dark Matter particles [153]. If the Dark Matter halo is rotating, this can have some effect, scaling the expected rates up or down for counter- or co-rotating halos [145]. Usually results of direct Dark Matter searches are given for a non-rotating halo.

At this point we can get a rough feeling about the expected signal spectrum. In the simplest case of a pure Maxwell-Boltzmann distribution, the integral 3.11 is proportional to the exponential $\exp\left(-v_{\rm min}^2/w^2\right)$, and with the definition of $v_{\rm min}$ in equation 3.12, this is proportional to $\exp\left(-E_{\rm r}\right)$. So in direct Dark Matter experiments we expect to find a roughly **exponential recoil spectrum**. Of course, the form factor effect as well as the other effects discussed in this section modify this simple picture.

Coordinate Change: We still have to perform the **Galilei transformation** $\vec{v}' = \vec{v} + \vec{v}_\oplus$ of $f(v)$ defined in the Galactic rest frame into the rest frame of Earth [154]. The circular velocity of the local standard of rest about the galactic center is 220 km/s, and adding the motion of the Sun with respect to the local standard of rest gives the net speed of the Sun with respect to the galactic rest frame of $(232 \pm 20\,{\rm km/s})$.

The orbital speed of Earth around the Sun is 30 km/s, with the angle between the ecliptic and the velocity vector of the Sun of about $\delta = 30.7°$. Roughly,

$$v_\oplus = \left(244 + 15\sin(2\pi t)\right)\,{\rm km/s} \tag{3.17}$$

when t is the time since March 2nd in years. This results in a seasonal variation of the expected recoil spectrum, an effect at the few-percent level [152, 39]. In addition to modifying the expected rate above threshold, it results in a pivot point in the observed spectrum which can help to clarify the modulation's nature. Moreover, the angular distribution of WIMPs impinging on the detector is anisotropic, so a directional information of the WIMP induced nuclear recoil would be a powerful way to clarify the nature of the recoils.

Eventually, the average velocity $\langle v \rangle$ in equation 3.4 turns into an expression in the differential rate that takes into account the velocity distribution of WIMPs in the galactic halo and the motion of Sun and Earth [148]:

$$\begin{aligned}\frac{\mathrm{d}\Gamma}{\mathrm{d}E_\mathrm{r}}(E_\mathrm{r}) &= \frac{\Gamma_0 m_\chi m_\mathrm{N}}{E_0 4\mu^2} \\ &\times \left(\mathrm{erf}\left(\frac{v_\mathrm{esc}}{w}\right) - \frac{2}{\sqrt{\pi}}\frac{v_\mathrm{esc}}{w}\exp\left(-v_\mathrm{esc}^2/w^2\right)\right)^{-1} \\ &\times \left[\frac{\sqrt{\pi}}{4}\frac{w}{v_\oplus}\left(\mathrm{erf}\left(\frac{v_\mathrm{min}+v_\oplus}{w}\right) - \mathrm{erf}\left(\frac{v_\mathrm{min}-v_\oplus}{w}\right)\right)\right. \\ &\left. - \exp\left(-v_\mathrm{esc}^2/w^2\right)\right] \end{aligned} \tag{3.18}$$

The dependence on E_r comes through equation 3.12, $v_\mathrm{min} \propto \sqrt{E_\mathrm{r}}$.

Detector Effects: The detector may, as is the case in the CRESST-II experiment, consist of **multiple target nuclei** i. This extension is rather trivial, the event rate will be simply the sum over the rates of the individual target materials.

The **energy resolution** ΔE of the detector also has to be taken into account. For this, the *observed* energy E_ee in the detector is the important parameter, where ee stands for **electron equivalent**, so $\Delta E = \Delta E(E_\mathrm{ee})$. E_ee is related to the recoil energy E_r by the **quenching factor** Q, $E_\mathrm{ee} = QE_\mathrm{r}$. In CRESST, the energy parameter is deduced from the phonon channel (see section 5.4), and since most of the energy of an interaction is transferred into phonons, we can set $Q = 1$ for the phonon channel. Nevertheless, for the time being we will stick with the clean notation involving E_ee.

To take the energy resolution into account, we convolve the spectrum $\mathrm{d}\Gamma/\mathrm{d}E_\mathrm{ee}$ with a Gaussian that has a width corresponding to the energy resolution:

$$\left.\frac{\mathrm{d}\Gamma}{\mathrm{d}E_\mathrm{ee}}\right|_\mathrm{obs} = \frac{\mathcal{C}}{\Delta E}\int_0^\infty \exp\left(-\frac{(E_\mathrm{ee}-E_\mathrm{r})^2}{2\Delta E^2(E_\mathrm{ee})}\right)\frac{\mathrm{d}\Gamma}{\mathrm{d}E_\mathrm{r}}\,\mathrm{d}E_\mathrm{r} \tag{3.19}$$

with the normalization constant

$$\mathcal{C} = \frac{\sqrt{2}}{\sqrt{\pi}}\left(1 + \mathrm{erf}\left(\frac{E_\mathrm{ee}}{\sqrt{2}\Delta E(E_\mathrm{ee})}\right)\right)^{-1}. \tag{3.20}$$

In the following we will neglect the small difference between E_ee and E_r in the case of the CRESST phonon detectors.

The **acceptance** of the detector has of course to be taken into account. Most importantly, this includes the energy threshold E_t, but more generally affects the observed spectrum through an energy-dependent acceptance $A(E_\mathrm{r})$, and so we write for the differential rate

$$\left.\frac{\mathrm{d}\Gamma}{\mathrm{d}E_\mathrm{r}}\right|_\mathrm{acc} = A(E_\mathrm{r})\left.\frac{\mathrm{d}\Gamma}{\mathrm{d}E_\mathrm{r}}\right|_\mathrm{obs} \tag{3.21}$$

where E_r is the **recoil energy**,

$$E_\mathrm{r} = \frac{\mu^2}{m_\mathrm{N}} v^2 (1 - \cos\theta) \tag{3.22}$$

with the reduced mass $\mu = (m_\chi m_\mathrm{N})/(m_\chi + m_\mathrm{N})$ and the scattering angle in the WIMP-nucleus center-of-mass frame θ. If only the energy threshold E_t is to be considered, one would have

$$A(E_\mathrm{r}) = \begin{cases} 0 & E_\mathrm{r} < E_\mathrm{t} \\ 1 & E_\mathrm{r} \geq E_\mathrm{t} \end{cases} \tag{3.23}$$

but we will encounter a more involved case in chapter 10.

Normalization per Nucleon: Direct detection experiments always only measure the product $\varrho_\chi \sigma_0$, and the individual local WIMP density ϱ_χ cannot be disentangled from the cross section σ_0. Results are customarily quoted assuming that $\varrho_\chi = 0.3\,\mathrm{GeV/c^2}$, which might only be a fraction of the local Dark Matter density $\varrho_\mathrm{DarkMatter}$ if there are other components to it.

To facilitate the comparison between different experiments, the cross section is not quoted for the particular nucleus, since different experiments use different targets. Instead, we assume a coherent interaction of the WIMP with the target nucleus, and following reference [145] rescale the WIMP-nucleus cross section to a WIMP-nucleon cross section as

$$\sigma_\mathrm{scalar,nucleon} = \frac{\mu_p^2}{\mu_\mathrm{N}^2} \frac{\varrho_\chi}{A^2} = \left(\frac{1 + m_\chi/m_\mathrm{N}}{1 + m_\chi/m_\mathrm{p}} \right)^2 \frac{\varrho_\chi}{A^2} \tag{3.24}$$

where m_N and m_p are the mass of the target nucleus and of the proton, respectively. Note that some older references, e.g. [155], used other normalizations.

To conclude, let us have a look at the spectra we get from this discussion. Figure 3.10 shows the spectra expected for $100\,\mathrm{GeV/c^2}$ WIMPs, coherently scattering from a few target materials relevant to the field. As the target becomes heavier, the expected spectrum becomes more significant, but also, the form factor further suppresses high recoil energies. Perhaps more interestingly for the experimentalist, at least as long as no signal has been found, the integrated event rates above some energy threshold are shown in figure 3.11 for these target materials. In CRESST, we use tungsten in $CaWO_4$ crystals as target material, so figure 3.12 shows the expected spectra for various WIMP masses. Clearly, above about $100\,\mathrm{GeV/c^2}$, the form factor totally dominates the spectral shape. Since the number density of WIMPs decreases as their mass increases, the spectra only become less and less significant.

3.3.6 Signal Identification

It was clear since the early days of direct Dark Matter detection experiments that a claim of discovery would be very difficult. As we have seen, the signal

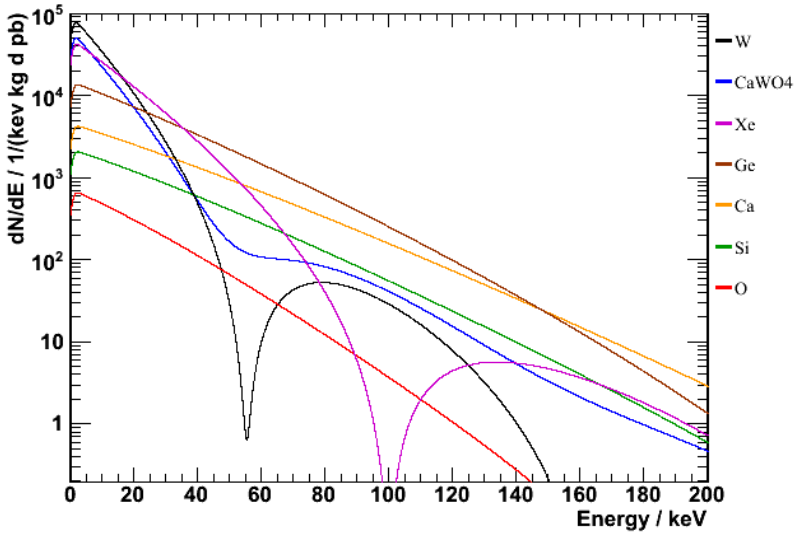

Figure 3.10: $\mathrm{d}\Gamma/\mathrm{d}E_\mathrm{r}$ for various target materials, given a $100\,\mathrm{GeV/c^2}$ heavy WIMP in an isothermal halo, scattering coherently off the target. The units are number of events per kilogram of detector, per day of measuring time, per 1 keV bin and assuming a cross section of 1 pb. The reduction of the spectra around zero energy is due to an assumed energy resolution of 1 keV. Note the logarithmic scale: basically the complete spectra are confined below $\approx 40\,\mathrm{keV}$ for heavy targets.

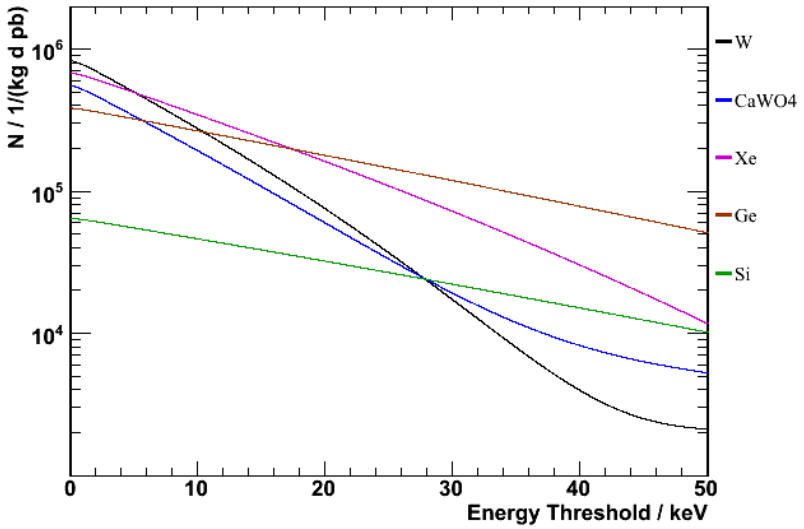

Figure 3.11: The integral of the spectra of figure 3.10 from a given energy threshold to infinity, as function of this energy threshold. Units are events per kilogram of target, day of measuring time, and assuming a cross section of 1 pb.

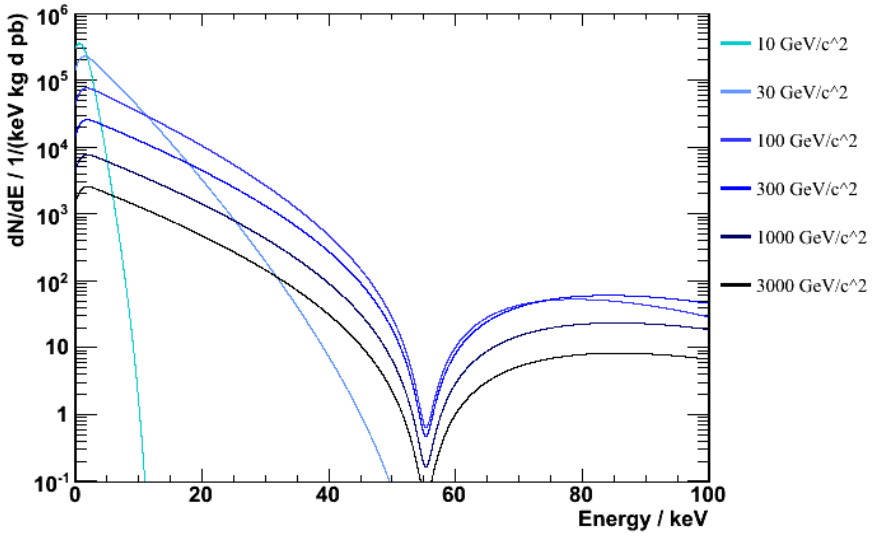

Figure 3.12: The expected recoil spectrum $\mathrm{d}\Gamma/\,\mathrm{d}E_\mathrm{r}$ in a tungsten target for WIMPs with different masses as indicated, again in units of kg d of exposure for a cross section of 1 pb and per keV bin. For heavy target materials like tungsten, the recoil spectrum for heavy WIMPs is completely dominated by the form factor.

is featureless, and at these low energies, the backgrounds are very poorly understood even today. With current experiments we are searching for less than one nuclear recoil per kilogram of target and month of exposure. So how can one make that claim of discovery at this level?

Of course a necessary prerequisite is that no obvious sources of background exist that could mimic the measured signal, so very generally, the background level has to be extremely low. As experiments become more and more sensitive, new backgrounds can appear. Cryogenic calorimeters for example can suffer from stress relaxations, providing a nice example of scientific serendipity: Initially in the CRESST experiment, the observed count rate was orders of magnitude above the expected level. A statistical analysis of the events showed that they were not Poissonian, and eventually they were identified as being due to cracks developing in the crystals due to a too strong clamping [156, 157]. This is a nice example of how unexpected backgrounds can show up, but it is also a showcase for serendipitous science, since it turned out that with this tight clamping, CRESST had the most sensitive device to measure stress relaxation in solids, or even earthquakes [158]. Today, a group in Finland is specializing in using this technique to study crack formation in unprecedented detail [159].

More generally, the problem occurs since often the best available measurement of backgrounds is at the same time the best available exposure for the signal. It is the challenge to the experimenter to gain enough confidence that observed events can not be due to background effects. To this end, it is

important to realize that the expected signal has quite a few peculiarities, despite having no particularly distinct energy spectrum.

- The signal spectrum and rate depend in a known way on the target nucleus. Once different experiments see a signal with consistent behavior with respect to the target nuclei employed, this will be a very strong point for the discovery claim, and is known as the **multi-target-approach**. It is therefore widely believed that an observation based on one target alone is not enough for a discovery claim. In CRESST, such multi-targets are intrinsic to the crystals, and can in addition be realized e.g. by the use of a $CaMoO_4$ target.

- WIMPs will cause nuclear recoils in the target, which can often be discriminated from electron recoils that are caused by electrons or gammas. The CRESST experiment allows even to disentangle neutron induced oxygen recoils from WIMP induced tungsten recoils, see section 7.1.1.

- For large detectors which can somehow spatially resolve the particle interaction point, this provides valuable information, since WIMPs are expected to scatter uniformly throughout the detector, in contrast to the dominant background sources: Electrons, alphas, or more exotic particle interactions like the one discussed in section 9.8 will be confined to the surface of the detector.

- Due to the low interaction probability, WIMPs will only scatter once in a detector. Neutrons on the other hand have short interaction lengths and may be discriminated against since they scatter multiply within a large detector volume or a segmented detector. The powerful capabilities available through such a coincidence technique become evident in section 6.2.9.

- WIMPs are expected to show an annual modulation effect, caused by the motion of Earth around the Sun [152]. This was examined as means of signal identification already in the early days [160], since for such a variation, the amplitude, phase and period can be predicted.

- The signal has to be site-independent.

- If it were possible to record the direction of the recoiling nucleus, this would be a very powerful discrimination against all other backgrounds.

3.4 Scattering Experiments

Before describing the CRESST experiment in some detail in the next chapter, let us quickly summarize some key technologies in the field. This will be done by means of a few examples, and in no way exhaustive of the estimated $\approx$ 30 or so experiments in operation or under development. For

a more complete summary the reader is directed to the literature, e.g. the reviews [161, 162].

3.4.1 Ionization Detectors: Si/Ge

Historically the first detectors to seriously search for Dark Matter interactions were Ge or Si ionization detectors, which could rule out **Dirac neutrinos** [163] and **cosmions** [164] as Dark Matter candidates. Since these devices are not able to discriminate between the different types of interacting particles, shielding and radiopurity of the crystals are particularly important. Improvements in the layout of these crystals by the **CoGeNT** collaboration have recently lead to a reduction of threshold [165] and important limits for low mass WIMPs [166].

3.4.2 Common Scintillators: NaI/CsI

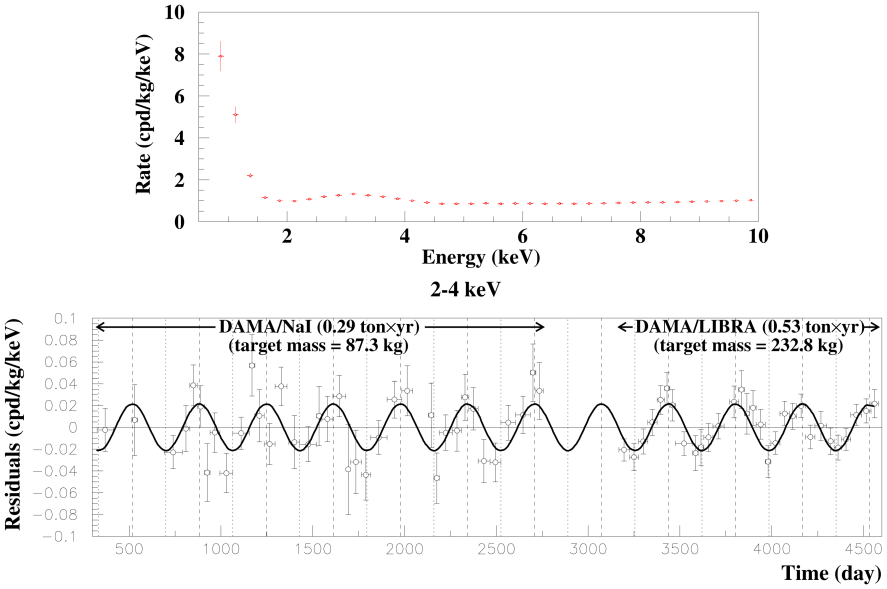

Figure 3.13: Results from the DAMA/LIBRA experiment [167]. The origin of the low energy spectrum shown here remains unexplained (top) but in the energy interval between $2-4\,\mathrm{keV}$, the signal amplitude shows a clear annual modulation as expected for Dark Matter (bottom).

The **DAMA/LIBRA** experiment [168], situated in the Laboratori Nazionali del Gran Sasso, uses 25 ultra pure Tl doped NaI crystal scintillators that are read out by two photomultipliers each, amounting to a total mass of $250\,\mathrm{kg}$. After a total exposure of $300000\,\mathrm{kg\,d}$ they observed for single hits in one of the crystals the spectrum shown in figure 3.13 [167]. The background rate of $\approx 1.2\,\mathrm{counts/keV/kg/d}$ in the low energy region above threshold remains unexplained. In the energy region between $2-4\,\mathrm{keV}$, the rate shows an annual modulation with am-

plitude $A = (0.022 \pm 0.003)$ counts/keV/kg/d and the maximum of the signal occurring at June 2nd. On the other hand, the rate is flat for energies above 6 keV. We have seen in section 3.3.6 that this is consistent with the expectation from scatterings due to the Earth going through a WIMP wind. Indeed, the collaboration claims the discovery of light weight ($m_\chi \approx 1 - 10\,\mathrm{GeV/c^2}$ [169, 170]) Dark Matter.

Claiming the discovery of Dark Matter based on a 2% variation of an unknown background is a rather bold thing. Clearly, other experiments and careful investigations on possible systematic effects are needed to clarify this point. In any case, constraints from other experiments have meanwhile ruled out completely the explanation with a standard halo WIMP with either spin-independent [166] or spin-dependent [171] interactions. Independent experiments such as that of the **KIMS** collaboration using CsI(Tl) crystals [172] are also starting to test the claim.

3.4.3 Cryogenic Ionization Detectors

The **EDELWEISS** experiment [173] is located in the Laboratoire Souterrain de Modane (in the Fréjus tunnel). They employ neutron transmutation doped (NTD) thermistors that are glued on germanium absorbers, operated at cryogenic temperatures of ≈ 25 mK. For each particle interaction, a *thermal* phonon signal as well as an ionization signal is detected. This allows to further reduce the background, since WIMPs will scatter from the heavy nuclei, while electrons or gammas will cause electron recoils in the crystals. The collaboration has upgraded their setup to hold more than 7 kg of Ge and is taking Dark Matter data again [174].

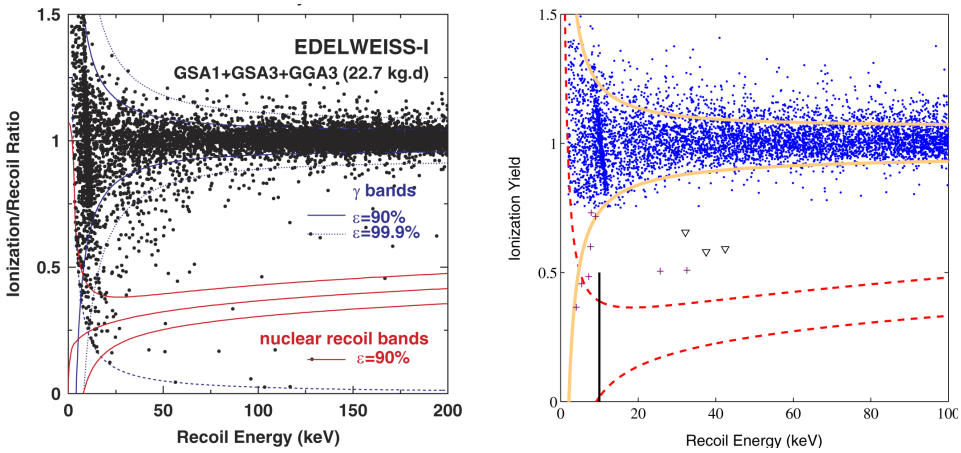

Figure 3.14: Scatter plots of the *yield*, the ionization signal per recoil energy, versus recoil energy. Left for EDELWEISS from [173], and on the right for CDMS from [175], both for comparable exposures (19.4 kg d in the case of this CDMS plot). Having the ionization as a second signal allows to discriminate electron recoils from nuclear recoils.

In the Soudan Underground Laboratory, the **CDMS** experiment [176]

uses cryogenic Ge and Si targets, allowing them to search for both spin-dependent and spin-independent interactions. They operate Z-dependent ionization and phonon (ZIP) detectors, with superconducting transition edge sensors to detect *non-thermal* phonons (see section 4.3.7). Collecting the charge signal of an interaction allows active background discrimination. Some of the most stringent exclusion limits on the WIMP-nucleon-scattering cross section are placed by this experiment [175, 177, 178, 179]. Typical **charge yield plots** of these two experiments are shown in figure 3.14.

3.4.4 Liquid Noble Elements

Liquid Xenon and Argon are also used as targets in Dark Matter searches. The **XENON** experiment uses a dual phase Xenon time projection chamber. Following an interaction in the liquid target, a scintillation signal is read out by an array of photomultipliers that are immersed in the liquid. An electric field is used to drift the ionization signal to the surface of the liquid, where it is extracted and registered by a second photomultiplier array. Both the scintillation and the ionization signals are quenched, but by different amounts, so their ratio can be used to discriminate electrons from nuclear recoils [180, 181], see figure 3.15. Very stringent limits on the WIMP cross section have been placed by this experiment [182].

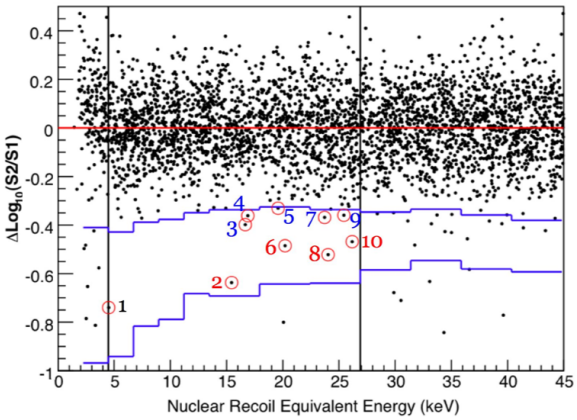

Figure 3.15: Scatter plot of an exposure of 316 kg d in liquid Xenon, from [182]. The events around the red line are electron and gamma events, and the area confined by the blue lines mark $\approx 50\%$ of the nuclear recoil band which is used as the acceptance region for Dark Matter induced nuclear recoils.

3.4.5 Bubble Chambers

The **COUPP** collaboration has revived the Bubble chamber technology for the direct search for Dark Matter interactions [171]. Discrimination against otherwise dominant backgrounds from electrons and gammas can be achieved by adjusting the operating temperature of the chamber. This

prevents such particles to generate bubbles at all, in contrast to nuclear recoils (or alpha events). This allowed some of the most stringent limits in the case of spin-dependent WIMP-nucleon interactions. In case of detection of signal candidates, the ability of COUPP to use target materials both with spin and without, such as e.g. CF_3 and C_4F_{10}, subsequently in the same detector, will allow to gain much information about the nature of the signal [183].

3.4.6 Gaseous Detectors

The directional information of the recoiling nucleus following a WIMP interaction would be the most direct evidence for the astrophysical origin of a signal. Hence, **Time Projection Chambers** (TPCs), filled with gaseous CF_4 [184, 185] and CS_2 [186] are under development. Concerning their applicability to Dark Matter searches, this is probably a long-term effort, since the recoil energies anticipated are low, corresponding to short track lengths. But given the scientific prospects, these technologies are for sure worth pursuing.

Chapter 4

CRESST

Intent: The CRESST experiment uses scintillating crystals as a target for coherent Dark Matter interactions, operated as calorimeters at cryogenic temperatures of only a few millikelvin. For each target crystal there are two detectors, one for the calorimetric measurement of the deposited energy, and another one to measure of the scintillation light. Together, such a detector module is the essence of the experiment. This chapter discusses the shielding required for operating such a Dark Matter detector, and presents the setup of the CRESST experiment.

Organization: In section 4.1 the most important radioactive backgrounds are discussed together with means of shielding them, and the particular shield implemented in CRESST. Section 4.2 introduces the cryostat and overall setup of the experiment. Special emphasis is given to the crystals, detectors, and pulse formation in section 4.3. Details of the data acquisition are given in section 4.4.

4.1 Shielding

Given the low expected event rates in a Dark Matter detector, a substantial reduction of radioactive backgrounds is a key requirement to the experiment. Primary source of free particles at the surface of the Earth are **Cosmic Rays** (see e.g. [187]). At sea level, their composition is given in table 4.1. Cosmic rays are of course a direct background to the experiment, but in addition can **activate** the material by the production of radionuclides.

Another important background source is **environmental radioactivity**, such as that from the ^{238}U and ^{232}Th decay chains, or that from ^{40}K. All materials contain primordial radionuclides at some level, that is, isotopes with half-lives of the order of the age of the solar system, 4.5×10^9 y. Man made radioactivity can also be an important background, coming from explosions of nuclear weapons or nuclear plants accidents. This adds mainly ^{137}Cs and ^{90}Sr to the environmental radioactivity.

Hence in designing a low background experiment, one has to consider radioactive impurities in the materials used in the vicinity of the detectors, or impurities in the detectors themselves. Measures have to be taken to reduce all these backgrounds as far as possible.

species	flux / $\mathrm{m^{-2}\,s^{-1}}$
muons	≈ 400
gammas	≈ 300
electrons, positrons	≈ 200
protons	≈ 6

Table 4.1: Approximate flux of various components of the cosmic rays at sea level, estimated from data in [188].

4.1.1 Muons

The most penetrating component of the Cosmic Rays are muons, which can induce backgrounds in various ways:

- Directly by traversing the detector
- Through the production of electrons (delta rays) which will cause secondary particle showers
- Through interaction and spallation in the surrounding material, producing gamma rays, neutrons, or nuclei.

Shielding muons is therefore indispensable but requires an experiment in locations deep underground. Figure 4.1 shows a list of available underground laboratories together with the measured muon flux.

The **Cryogenic Rare Event Search with Superconducting Thermometers CRESST** [191, 192] is located in the Laboratori Nazionali del Gran Sasso. These underground laboratories, operated by the Instituto Nazionale di Fisica Nucleare, are the largest in the world, with a total underground area of $18000\,\mathrm{m^2}$ [193]. They have a minimum rock overburden (mean mass per unit area) of 1400 m of dolomite rock, which reduces the cosmic muon flux by six orders of magnitude to about $2\,\mathrm{m^{-2}\,h^{-1}}$ [194]. A sketch of the underground area with the location of the CRESST experiment is shown in figure 4.2.

To shield the detector against prompt muon backgrounds, a **muon veto** can be installed. If a muon triggers such a veto, events recorded in the detector are rejected. Direct muon induced backgrounds as well as secondary particles with short (as defined by the veto window) delays to the traversing muon can be rejected. In CRESST, a system of 20 plastic scintillator panels with a solid angle coverage of 98.7% is installed. Each panel is read our by one photomultiplier, and the summed signal is used as veto signal.

4.1.2 Radon

Radon gas is produced in the ^{238}U decay chain. ^{222}Rn alpha decays into ^{218}Po with a half-life of 3.8 d (see e.g. [195]). Hence radon gas is long lived enough to be washed out of the rock by ground water, or diffuse out of it, with subsequent diffusion into the shielding of the detector. In the radon

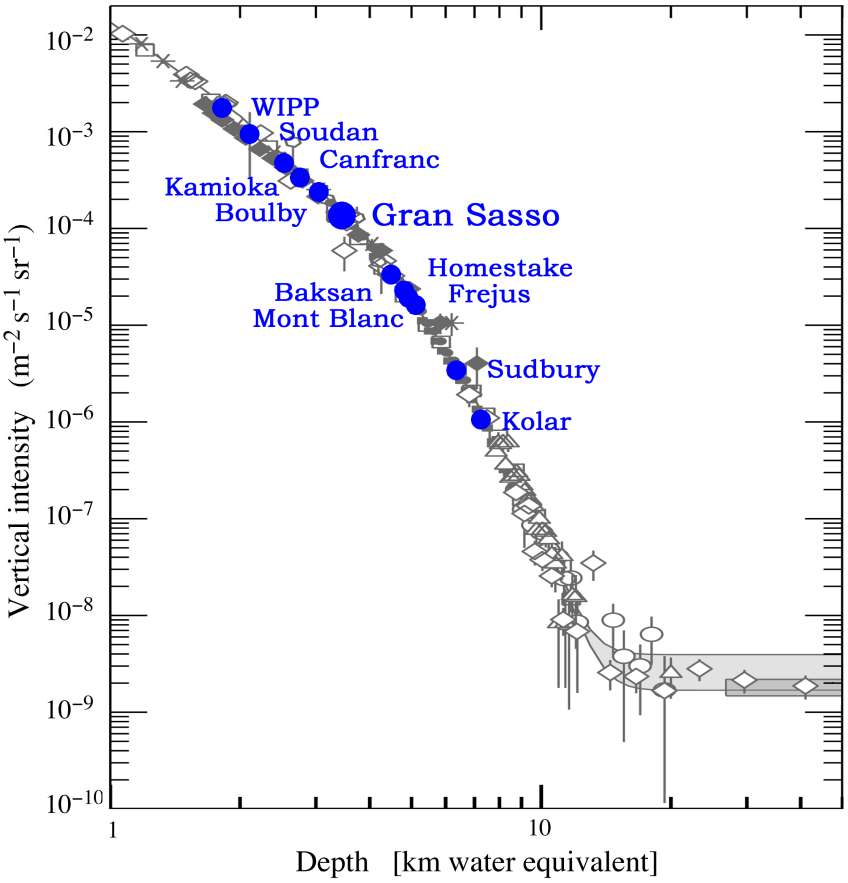

Figure 4.1: The muon flux versus depth, from [188]. Superimposed are the minimum overburdens of a few underground laboratories, from [189] and [190]. At depths greater than $\approx 10\,\mathrm{km}$ water equivalent $= 10^6\,\mathrm{g\,cm^{-2}}$ of standard rock (about 3 km), the flux levels off due to neutrino induced muons. CRESST is located in the Gran Sasso laboratories.

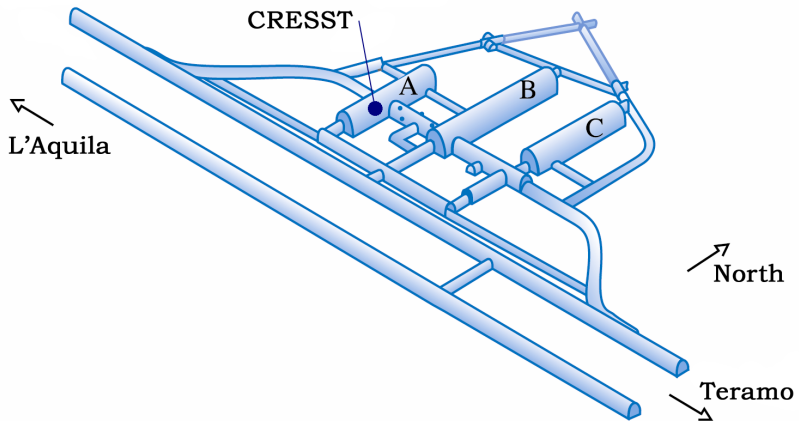

Figure 4.2: Sketch of the Gran Sasso underground laboratories. Two separate, 10 km long highway tunnels connect the east and west side of the Abruzzo mountain range. About halfway in, the laboratories are excavated, shown here with the three main experimental halls (depicted hall A, B and C). The lab hosts almost 20 different experiments, with the CRESST experiment located at the position indicated.

and the following decays, a variety of α and β particles are produced, which in turn can produce gammas through bremsstrahlung and other nuclear reactions. In the Gran Sasso laboratories, the radon level can be reduced by adequate ventilation from about $300\,\mathrm{Bq\,m^{-3}}$ to $20 - 50\,\mathrm{Bq\,m^{-3}}$ [196, 197], but is generally monitored at higher values of $50-100\,\mathrm{Bq\,m^{-3}}$ [198, 199, 200].

To shield the CRESST detector from radon, it is enclosed in an air tight container, the **radon box**. This container is constantly flushed with vapor from liquid nitrogen and kept at a small overpressure. Hence the inner parts of the setup are radon free within a few days after activating the radon box. Care is taken to minimize the deposition of radon progenies on surfaces (plate-out effect, see appendix B).

4.1.3 Gammas and Electrons

Gammas mainly come from the natural decay chains of ^{238}U, ^{232}Th and ^{40}K, evaluated in more detail in table 4.2. The energies range up to 2.6 MeV (from the ^{232}Th chain), with the integral gamma flux in the Gran Sasso laboratories measured to be about $1\,\mathrm{cm^{-2}\,s^{-1}}$ [201].

Due to Compton scattering, even monoenergetic, high energy gammas can induce a low energy background. Shielding of the detector against gammas is of course done by a high density, large atomic number shield, typically a **lead** barrier. In CRESST, we have a 20 cm thick lead shield (weighting about 24 t) which surrounds the detectors. This shield is mounted on movable wagons to allow access to the detectors.

However, ^{210}Pb can be produced by cosmic rays in the lead, and it is also

sample	^{238}U	^{232}Th	^{40}K
Hall A rock	116	12	307
Hall B rock	7	0.3	7
Hall C rock	11	0.4	4
concrete 1	52	41	303
concrete 2	26	15	164
concrete 3	17	9	182
concrete 4	69	15	260

Table 4.2: Measured gamma activities in (Bq/kg) for different samples of rock and concrete in the Gran Sasso laboratories, from [202], where the errors are quoted also (they are in the range of 1%). There are strong variations from sample to sample, and in particular, the rock of Hall A has an order of magnitude higher contaminations with ^{238}U and ^{232}Th.

present naturally since it is a step in the decay chain of ^{238}U. ^{210}Pb β-decays with a half-life of 22.3 y in ^{210}Bi, producing 46.5 keV gamma radiation, which in turn decays with $t_{1/2} = 5$ d in ^{210}Po and eventually with $t_{1/2} = 138$ d in ^{206}Pb, each time producing α, β and/or γ radiation [203]. From these processes, bremsstrahlung and lead X-rays contribute to the low energy background. In addition, ^{210}Po diffuses to the surface of the lead, increasing the activity over the one expected from the bulk activity [204].

To avoid this source of background, Swedish **Boliden lead** can be used, where the activity is reduced by a factor ≈ 50 over conventional lead [205]. If only small quantities are required, **Roman lead** can be used, for example from ships such as the freighter which sank ≈ 70 a.c. off the coast of Sardinia [206, 207], where the radioactivity is reduced by another factor of $\approx 10^4$.

Alternatively, one can place an additional shielding layer within the lead shield to reduce the ^{210}Pb induced background. Electrolytically refined copper such as **oxygen free high conductivity (OFHC)** copper is a very pure material. Hence, such copper can make a very clean shielding. Due to the large cross section for neutron capture, one has to take care to keep exposure to cosmic radiation to a minimum after production.

In CRESST, an additional 14 cm thick (and 10 t heavy) copper shield is installed within the lead shield. It is made from very clean OF01 copper from the Norddeutsche Affinerie [208]. Until installation in Gran Sasso, it was stored underground after production in the Weihenstephan brewery cellar [209] at a depth of more than 10 m water equivalent, where the hadronic component of the cosmic rays is reduced by more than two orders of magnitude. Total time above ground was less than 10 weeks [210, 211].

4.1.4 Neutrons

Neutrons are a very dangerous background in direct Dark Matter searches, since they can mimic WIMP interactions. The surface neutron flux is reduced in the Gran Sasso underground laboratories due to the low activity dolomite rock [193]. The dominant flux of low energy neutrons (of a few MeV) comes from (α, n) reactions on light elements, and from fission of nuclei in the rock or concrete in the halls. In addition, high energy neutrons ($\gtrsim 10\,\mathrm{MeV}$) can be induced by muons in the rock or shielding material of the experiment, but as we have seen, this background is reduced by six orders of magnitude. Fast neutrons can in turn produce additional neutrons through spallation reactions.

Neutrons from (α, n) reactions or from fission are produced at depths of $\mathcal{O}(10\,\mathrm{cm})$ within the walls. In the Gran Sasso laboratories, the walls are covered with concrete of about this thickness, so it is this layer that will be the dominant source of neutrons. Since the concrete is roughly the same throughout the laboratories, one can expect the neutron flux in the various Halls to be roughly equal [212]. The expected flux in Hall A from simulations is about $9-26\,\mathrm{m}^{-2}\,\mathrm{h}^{-1}$ [212], which agrees with measurements of $19-30\,\mathrm{m}^{-2}\,\mathrm{h}^{-1}$ [213], although it should be noted that variations between different measurements (e.g. [214]) can be larger than expected from the quoted errors (see [212] for a discussion of possible systematics).

If such neutrons scatter from light nuclei in the target, this can induce an observable recoil in the crystal. To prevent this source of background, the CRESST setup has an additional **neutron shield**. This barrier is a 45 cm thick (and 10 t heavy) structure from Polyethylene (PE) which moderates neutrons to thermal energies below eV, which can then no longer trigger the CRESST detectors.

This additional shielding was installed after run 28. Due to the surprisingly complex geometry of the shielding (mainly owing to the necessity of allowing access to the cryostat and detectors), the shield was not everywhere as close as desired, so after run 30, the neutron shield was improved in some upper regions with additional Polyethylene as well as water.

Simulations of the expected neutron recoil spectra in the CRESST setup have been performed [216]. These backgrounds are shown in figure 4.3 for a geometry that resembles the actual setup. After the installation of the neutron moderator, the dominant neutron flux is muon induced in the lead (and copper) shield. Hence, one would like to have the moderator *within* the gamma shield, not outside of it. However, this was not possible for the current CRESST setup, which is shown in figure 4.4.

With the shielding opened, the trigger rate of a CRESST detector module is about 2 Hz. This is reduced by two orders of magnitude with the shielding closed. Most of the remaining activity comes from radioactivity intrinsic to the detectors (chapter 6), a much less dangerous background due to the calorimetric nature and active discrimination capabilities of the CRESST detectors.

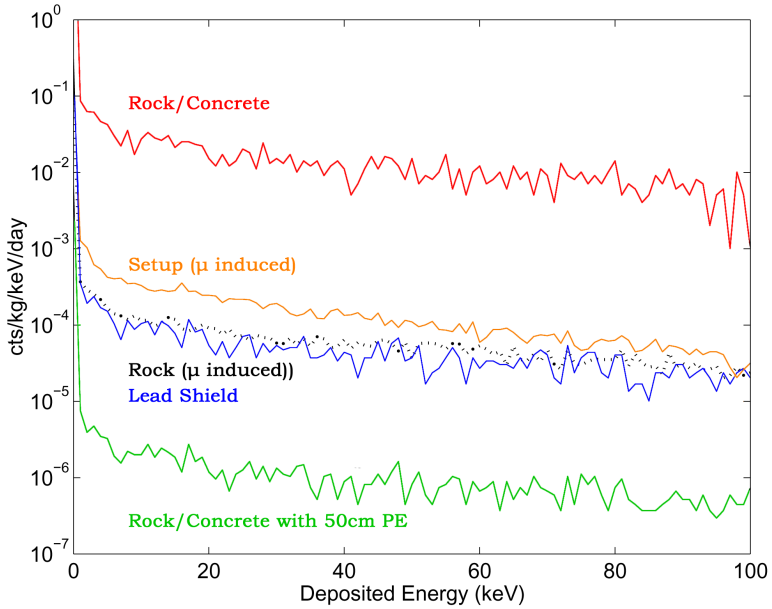

Figure 4.3: Simulated recoil spectra of various neutron sources in a $CaWO_4$ crystal within the CRESST setup, from [215]. The dominant source (red) comes from low energy neutrons produced in the rock or concrete, which can be moderated away, shown in green for a 50 cm thick Polyethylene shield. Other sources of background are neutrons from muon interactions in the setup (orange) or rock (black), and from fission of an assumed 0.1 ppb ^{238}U contamination in the lead shield (blue).

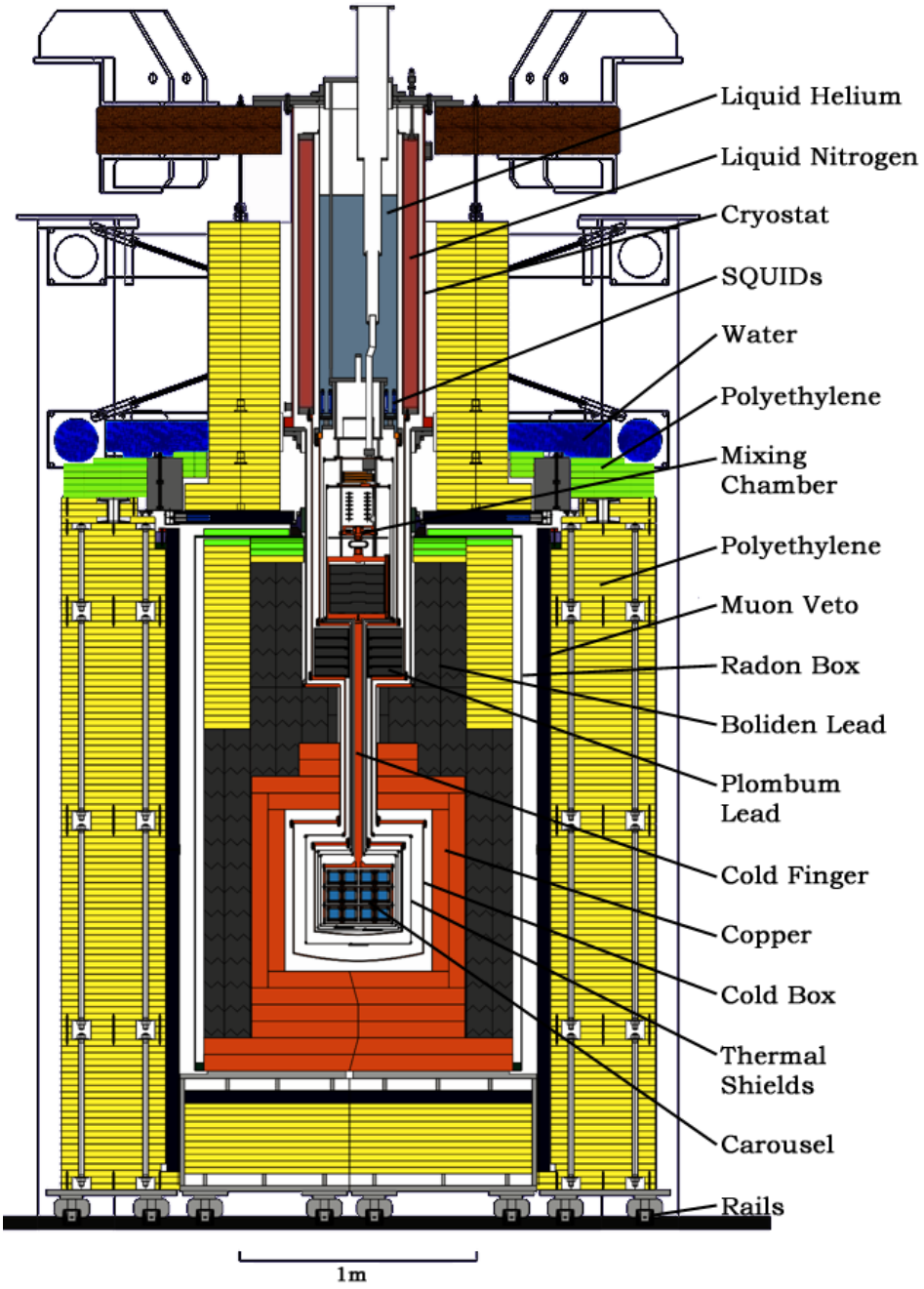

Figure 4.4: The CRESST setup. The cryostat, in the upper half of the picture, is kept away from the detectors since it is made from standard, i.e. non-radiopure, materials. The shielding consists of copper (orange), lead (gray), the radon box (thin line), the muon veto (blue), the neutron moderator (polyethylene in yellow as well as the helium and nitrogen in the cans of the cryostat), and the neutron moderator as patched after run 30 with more polyethylene (green) and water (blue). The whole shielding is mounted on wagons movable on rails to allow access to the detectors.

4.2 Layout of the Experiment

4.2.1 The Cryostat

The CRESST detectors are operated at temperatures in the millikelvin range, requiring a dilution refrigerator. Such ^{3}He/^{4}He cryostats are commercially available but contain various materials that are not suited for low background applications. This gives the CRESST setup its peculiar arrangement, shown in figure 4.4. In this setup, the cryostat is kept away from the shielded detectors, and the cooling power is transferred into the shielded volume via a 1.3 m long copper rod, the **cold finger**.

The cryostat is an Oxford Instruments 1000S dilution refrigerator, reaching a base temperature of ≈ 6 mK. Its operation requires refilling of liquid helium and nitrogen every 3 1/2 days, interrupting measurements for three hours or so. Shown in figure 4.4 are the helium- and nitrogen bath and the pumping line as well as the five thermal shields of the cryostat at temperatures of 80 mK, 600 mK, 4 K, 77 K and room temperature, together constituting a total thickness around the detectors of 1.2 cm of copper. Hence there is always a minimum separation between the detectors and the outside of the cryostat; this is to be kept in mind for the discussion of calibrating the detectors with sources from the outside. Just like the copper shield, these thermal shields are made from radiopure copper with minimized exposure to comic rays (see section 4.1.3). Also, this **cold box** was electropolished (see appendix B) to reduce and suppress surface contaminations. Typically, indium is used to seal flanges in millikelvin applications, but due to its radioactivity, it is replaced with high purity lead seals instead.

To prevent any line of sight from the detectors to the cryostat, there is a shield of 98 kg of Boliden lead (35 Bq/kg ^{210}Pb [217]) directly below the mixing chamber, thermally anchored not to the mixing chamber but to the 80 mK shield. Below this, another 232 kg of Boliden lead are installed, thermally anchored only to the 77 K thermal shield. The lowest layers of these shields are made from **Plombum lead**, which has an activity of only 3.6 Bq/kg ^{210}Pb.

Mechanical vibrations can limit the operativity of cryogenic detectors. Hence, in CRESST, the whole cryostat rests on air dampers and has no touch with the shielding. The pumping line is decoupled by a delicate design from the setup. In addition, the structure holding the detectors at the bottom of the cold finger (section 4.2.3), is decoupled from the cold finger by springs.

4.2.2 Setup

A two-storey **Faraday cage** protects the sensitive electronics from electromagnetic interference, see figure 4.5. The lower half of the Faraday cage is equipped as a clean room to reduce the contamination with radioactive isotopes such as those contained in exhaust and cigarette smoke. Human skin contact with parts inside the shielding is forbidden to prevent contamination with ^{40}K. Care should be taken to prevent contamination with ^{60}Co

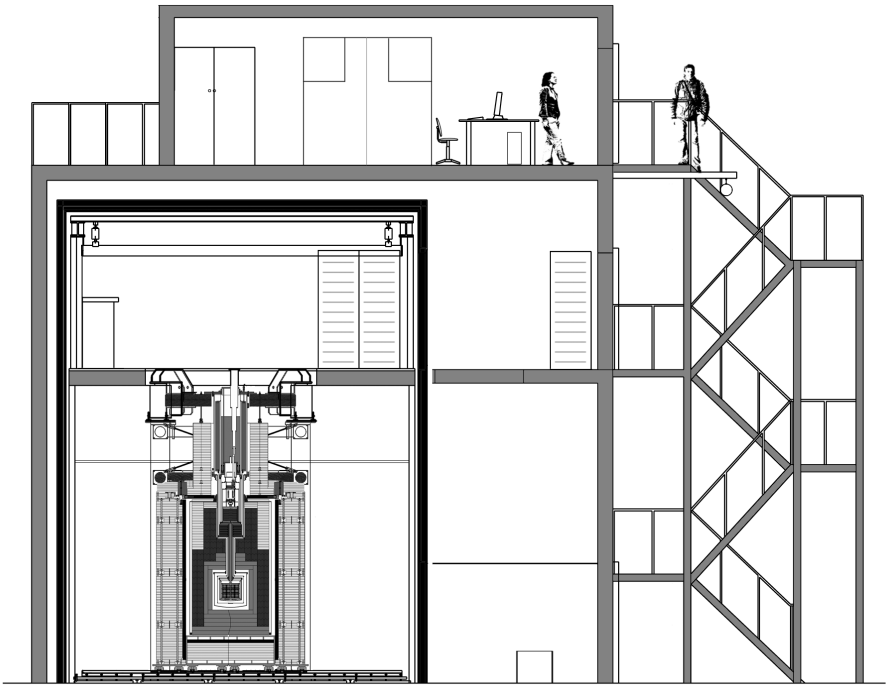

Figure 4.5: Sketch of the CRESST hut in hall A of the Gran Sasso underground laboratories. The cryostat is shown on the lower left and is surrounded by the shielding. The cryostat is placed in a Faraday cage, whose lower half is equipped as a clean room. On the top floor of the building there is room for workplaces as well as a small clean room for servicing of the detectors.

from the use of tools unsuited.

Only the ground level is a clean room, so the cryostat can be serviced from the second floor without the need of entering the clean experimental area. Gas-handling, pumping systems as well as the data acquisition electronics are located outside the Faraday cage. Finally, the top floor of the CRESST hut contains workspaces and a workbench, and a small clean room with a bonding machine to work on the detectors.

4.2.3 Experimental Volume

The current 80 mK shield encloses 24 liters which are available as experimental volume. A support structure, dubbed the **carousel**, has been constructed to hold up to 33 detector modules. This structure allows modular access to the individual modules, as shown in figure 4.6. Equipped with all 33 detectors, it weighs 38 kg and with the current crystals allows a target mass of 10 kg. The carousel is decoupled from mechanical vibrations of the cryostat with springs, custom made from copper with an addition of 6% 99.9999% pure tin to be fit for the radiopure requirements [218]. These springs are thermally anchored only to the cold finger side. The detector part

of the carousel is thermally coupled to the cold finger only via six 1.5 mm copper wires, giving a measured cooling time constant of about 30 min.

Great care has to be taken that the materials in the vicinity of the detectors are both radiopure and suitable for the millikelvin temperature range. The copper employed for the detector holders and the support structure is so-called **NOSV** copper [208], produced by the Norddeutsche Affinerie AG and stored underground only a few days after production. NOSV copper is very pure and oxygen rich but contains no hydrogen, which is crucial for low temperature applications: Hydrogen shows the spin excitation which is known from the 21 cm line in radio astronomy. At around 70 mK one can hardly cool any further because the ortho-para transition of this excitation acts as a heat leak [219]. Thus one has to implement copper with no hydrogen, such as NOSV, which has a measured heat leak of $< 0.9\,\mathrm{pW/g}$ ([211], chapter 2.3).

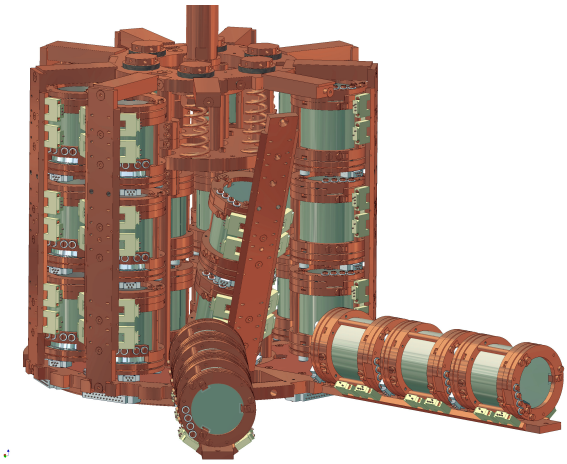

Figure 4.6: Drawing of the detector support structure hanging from the cold finger. Detector modules are mounted together on a **wing** which can then be handled as a whole. If no detector is placed at a certain position, a copper weight with the same mass as a detector is put in its place to balance the springs.

All parts below the mixing chamber are custom made, including each screw or plug. For the fabrication of the individual copper parts no lubrication is used where possible. The pieces are then pickled in Piranha acid ($H_2SO_4 + H_2O_2$) to remove surface contaminations. Subsequent electropolishing reduces the surface area, inhibiting re-contamination. Assembly is then done in clean room conditions. Appendix B gives some hands-on information on this process of surface treatment.

4.3 CRESST Detectors

4.3.1 Cryogenic Calorimeters

CRESST detectors are cryogenic calorimeters, the principle of which is quickly illustrated, with the details discussed in the subsequent sections. As a first estimate, the change of temperature ΔT of a calorimeter following an energy deposit ΔE is

$$\Delta T = \frac{\Delta E}{C} \tag{4.1}$$

where C is the heat capacity of the absorber. Hence the temperature rise is proportional to the deposited energy. For particle interactions of $\mathcal{O}(\mathrm{keV})$, on needs small C. At low temperatures, the heat capacities of dielectric crystals and semiconductors are dominated by the phonon system, and $C \propto (T/\Theta_\mathrm{D})^3$ where Θ_D is the Debye temperature. In CRESST we use dielectric crystals at millikelvin temperatures, since such temperatures can be obtained with commercially available dilution refrigerators.

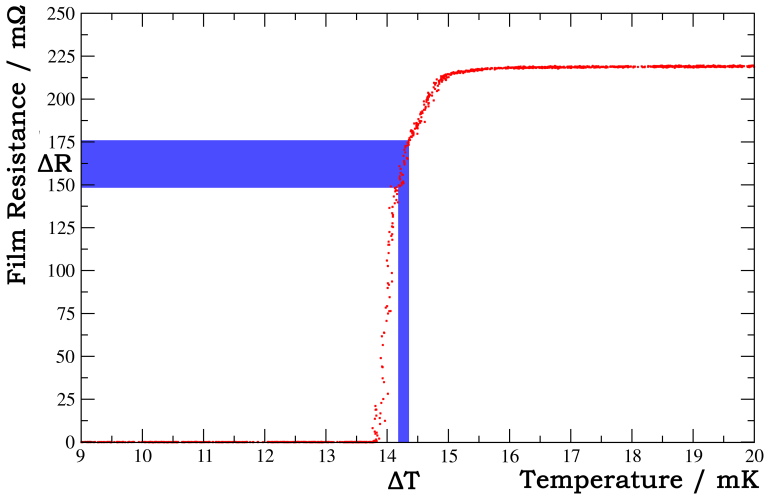

Figure 4.7: Principle of a Transition Edge Sensor. It is stabilized in its operating point by means of an additional heater structure. The small change of temperature following a particle interaction leads to a measurable change of resistance of the thermometer film.

To measure small temperature changes at such low temperatures, one needs a suitable thermometer. Materials that come into question having a significant change of resistance $\mathrm{d}R/\mathrm{d}T$ are superconductors that have their phase transition from the normal to the superconducting phase in the temperature range of the experiment. In CRESST, we use thin films of tungsten (in its α-phase), which shows superconductivity at temperatures below $\approx 15\,\mathrm{mK}$ [220]. Figure 4.7 clarifies the operating principle of these **Superconducting Phase Transition thermometers** SPT, also called **Transition Edge Sensors** TES. The superconducting material is in strong

thermal contact with the target material. It is stabilized at an operating point in the phase transition by means of an additional heater structure that is evaporated on the film. Then a small change of temperature in the thermometer, such as one induced by a particle interaction in the target, leads to a measurable change in resistance.

4.3.2 CRESST-I

Originally the CRESST experiment was located in Hall B of the Gran Sasso underground laboratories, using the same cryostat and inner shielding [210, 221]. **Sapphire crystals** (Al_2O_3) measuring $4 \times 4 \times 4.1\,cm^3$ and weighting 262 g each were used as a target. Each crystal was equipped with a $3 \times 5\,mm^2$ tungsten SPT, the **phonon detector**.

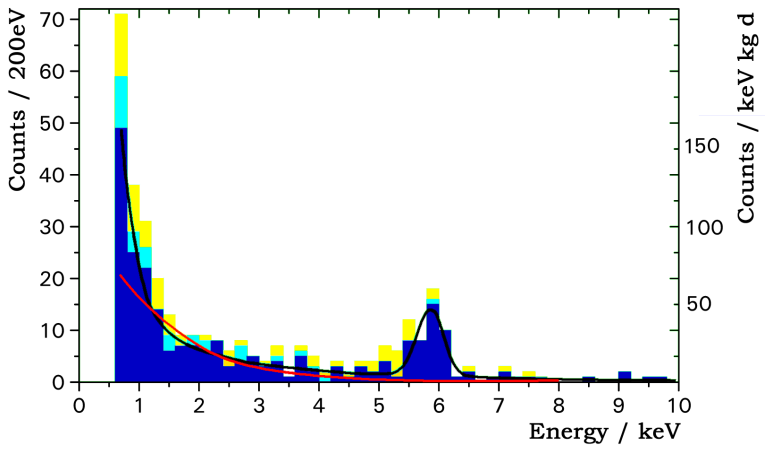

Figure 4.8: Spectrum measured in a 1.51 kg d background run with a 261 g Al_2O_3 target, from [221]. In orange the uncut spectrum. Light blue the spectrum after a coincidence cut, and dark blue the final spectrum after a pulse shape cut. The black line is an empirical fit to the spectrum needed to extract a limit, and the red line is the expectation from a $5\,GeV/c^2$ WIMP with a cross section that is excluded at 90% confidence.

These detectors had a very low energy threshold of 580 eV (100% trigger efficiency), allowing to constrain very low mass WIMPs. In runs with exposure only to background radiation, these detectors have proven to be very clean, see figure 4.8, having a count rate after a veto cut and a pulse shape cut of only 0.3/keV kg d. In fact, 17% of all events were in coincidence with one detector of similar make that was placed immediately next to the target. This suggests a very efficient discrimination against background if all six sides of the cubic detector were equipped with a veto; however, operation of such detectors has ceased in 2002.

4.3.3 Scintillating Crystals

Another way of discriminating residual backgrounds is possible if scintillating targets are used [222]. Inside the shielding as described, most of the relevant background comes from low energy electrons and gammas. It is well known (e.g. [223]) that such particles yield more light in a scintillator than interacting alpha particles, or even heavy nuclei. Hence if a scintillating target is used and the scintillation light is measured, this allows for a discrimination of dominant background sources.

The peculiarities of the CRESST experiment constrain the choice of scintillator. Most importantly, a scintillator with possibly heavy nuclei is desired to make use of the $\propto A^2$ scaling of the coherent WIMP-nucleus cross section. In addition, the material needs to be suitable for cryogenic environments, and with sufficient scintillation efficiency. Finally, the material must not be too radioactive to prevent operation of the slow cryogenic detectors.

Thus, in the second phase of the CRESST experiment [224, 225], we use mainly **calcium tungstate** $CaWO_4$ **crystals** as target. This material is to mineralogists also known as Scheelite, and was discovered as a scintillator by Edison only in 1896 [226]. With tungsten ($A = 186$) it contains very heavy nuclei, favorable due to the expected $\propto A^2$ dependence of the WIMP-nucleus cross section. In contrast to the more commonly used (see e.g. [227]) Lead Tungstate $PbWO_4$ it has no intrinsic radioactive isotopes. Other scintillators currently investigated for the use in CRESST-II include Ti doped Al_2O_3 [228], $ZnWO_4$ which promises better radiopurity [229], and $CaMoO_4$ for systematic studies [229].

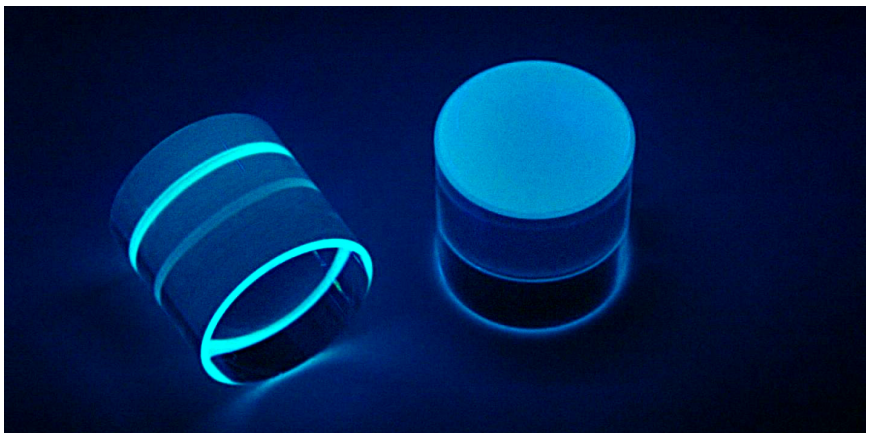

Figure 4.9: Two $CaWO_4$ crystals under UV light irradiation. Concerning the light output along the axis, the plane surface facing the light detector is roughened (right) to homogenize the otherwise very inhomogeneous light emission of the crystals, focused at the baffled edges (left).

The optimum shape of a crystal with high refractive index like $CaWO_4$ ($n = 1.92$) is a (possibly clipped) pyramid with side angles of 60°, since with this geometry, any light ray escapes the crystal after at most three

internal reflections [230]. However, $CaWO_4$ crystals are produced with the Czochralski process [231]. It is still a technological challenge to produce large, optically clean specimen [232]. Also, we will see in chapter 6 that this process can introduce significant amounts of radioactive isotopes in the crystal.

Hence, to have the largest possible target, CRESST employs cylindrical crystals with a diameter achievable from standard crucibles used for Czochralski crystal pulling. They are cut to a diameter and height of 4 cm, respectively. As a drawback of such cylindrical crystals, light may be trapped in infinite paths. However, tests have shown that scattering dominates over absorption, and so the cylindrical shape was accepted [230]. Figure 4.9 is a photograph of scintillating $CaWO_4$ crystals as used in CRESST-II.

4.3.4 Light Detector

To detect the scintillating light, the operation of photomultiplier tubes is not feasible, because at these low temperatures, the photocathode becomes non-conductive. In addition, photomultipliers are generally rather dirty, and the required high voltage causes problems in millikelvin applications. Hence a dedicated cryogenic light detector is used in addition to the phonon detector. This **light detector** consists of a light absorbing substrate, equipped with another phase transition thermometer. Following a particle interaction in the crystal, the scintillation light is absorbed in the wafer, creates phonons there, and can hence be detected with a similar phonon detector.

This allows to discriminate electron or gamma events from nuclear recoils, and the original proof-of-principle of this technique to the application of the Dark Matter search is illustrated in figure 4.10. Details on the light detectors and their fabrication can be found in dedicated theses [233, 234].

Just as in the case of ionizing detectors (section 3.4.3), this second channel allows a significant discrimination of background. In addition, the technique used in CRESST has distinct advantages: The light signal is not degraded significantly for events that happen close to the surface, which in an ionizing detector may lead to a misidentification of an electron recoil as a nuclear recoil. Since only a few percent of the signal are emitted as light, the quenching of the phonon signal can be neglected, giving a direct measurement of the energy from this channel.

In a compound material like $CaWO_4$, neutrons will be seen in the detector mainly if they scatter from light elements (like oxygen) due to the kinematics of the scattering. On the other hand, we saw that we can expect WIMPs to scatter mainly from heavy elements (like tungsten) due to the $\propto A^2$ enhancement of the coherent scattering cross section. With the scintillators used in CRESST, different recoiling nuclei can be discriminated by their different light yield. This even opens the possibility to discriminate the neutron background from WIMP induced events, a feature unique to this method.

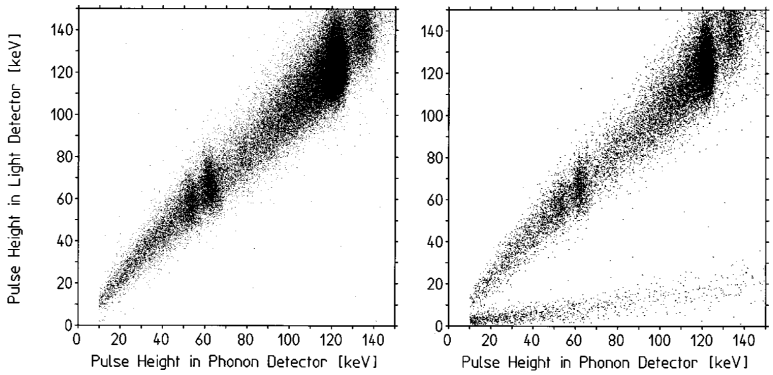

Figure 4.10: Operating a macroscopic, scintillating crystal as cryogenic target together with an appropriate light detector allows the discrimination of electron and nuclear recoils at low energies relevant for a Dark Matter search. Shown is a scatter plot of the energy in the light detector versus the energy in the phonon detector, on the left with a ^{57}Co gamma source and a ^{90}Sr beta source, and on the right with an additional Am/Be neutron source. Clearly, electron and gamma events are separated from neutron induced events. Plot from [235].

4.3.5 Detector Modules

The target crystal with its phonon detector and the light absorber with *its* phonon detector are paired together in a housing and then referred to as **detector module**. Figure 4.11 illustrates the concept, and 4.12 is a picture of an opened detector module.

The design of the detector module has been subject to some optimization [230, 233]. The main structure is manufactured from low background NOSV copper. Surface treatment is done as described in appendix B. The modules are assembled in a clean room and are brought as a whole to the experiment in Gran Sasso. Soldering is to be avoided in low background environments due to the radioactive isotopes abundant in solder and flux. Hence, thermal and electrical contact is given by screw contacts [233].

Mechanical crabbing of the crystal and the light absorber is subject to two main requirements. On the one hand, the clamping should be tight to prevent thermal signals induced by microphonics of the cryostat. On the other hand, strong thermal contact needs to be avoided to prevent spurious relaxation of phonons in the heat bath rather than in the detector film. During an early phase of CRESST, a too strong clamping of the crystals resulted in cracks forming with a rate of $\mathcal{O}$(Hz) (section 3.3.6 on page 54). Cracks in $CaWO_4$ do not emit any light and thus are, the high counting rate aside, a dangerous background for the Dark Matter search. Hence we now use custom made $CuSn_6$ bronze clamps [218]. These clamps were originally silver coated for better reflectivity, and since run 29 are covered by the same scintillating foil that is also used to enclose the whole module.

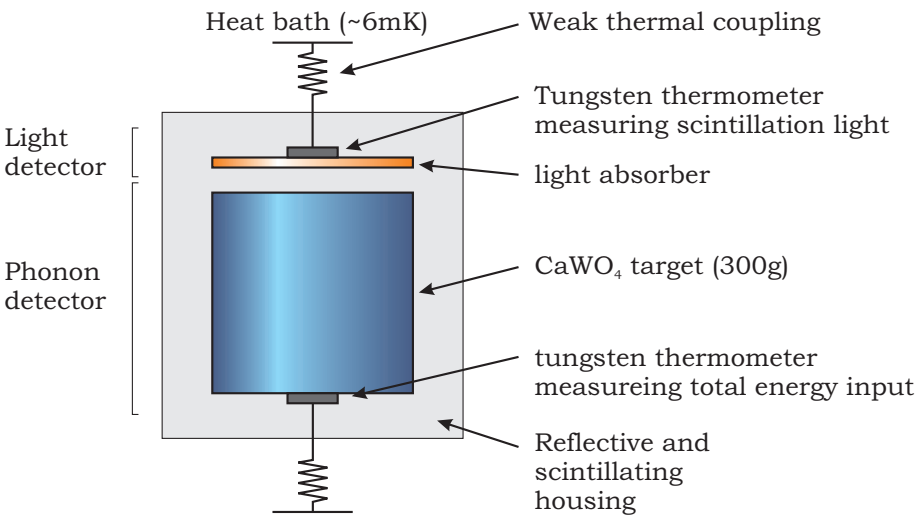

Figure 4.11: Concept of a CRESST detector module. Each module contains two separate tungsten thermometers. One is evaporated directly onto the $CaWO_4$ crystal, measuring the total deposited energy. To measure the scintillation light, a thin light absorber with the second thermometer is placed in the vicinity of the crystal. The structure is encapsulated in a reflective housing, which since run 27 also scintillates.

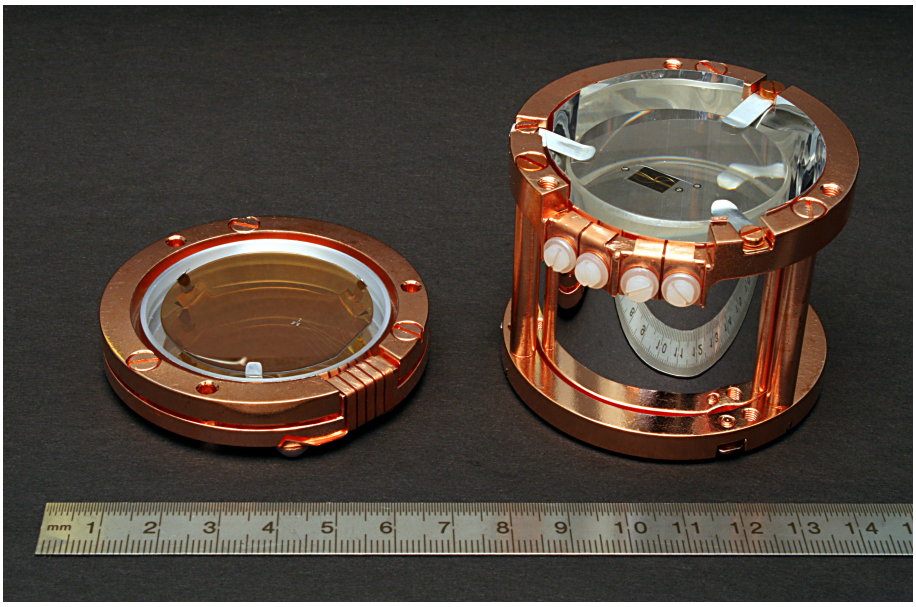

Figure 4.12: Picture of an opened module as used in CRESST-II. On the left, the orange wafer is the silicon-on-sapphire light absorber, the transition edge sensor is the tiny structure on it. On the right, the crystal can be seen with the phonon detector, a transition edge sensor with larger geometry, evaporated on it. The crystal is encircled by the scintillating reflective foil and hold by custom made springs. Bonding wires for thermal and electrical contact are barely visible also.

4.3.6 Reflective Foil

To increase the light collected in the light absorber, the module is encapsulated with a reflector. Due to the cylindrical geometry of the holder, light may undergo many reflections before it hits the light absorber, so a highly effective reflector is mandatory. Teflon can not be used as it prevents the structure from cooling. In run 27, a silver reflector has been used with a reflectivity above 95% for wavelengths $\lambda > 400\,\text{nm}$ [233] but was found to be not suitable. In run 28, the detectors were encapsulated with a **3M Radiant Mirror Film VM2000**, and after that, with **VM2002** film. These polymeric foils achieve a high reflectivity through a multilayer structure which is optimized for photomultiplier operation, but suitable also for the $CaWO_4$ emission spectrum. Table 4.3 shows the influence of the foils on light collection and resolution.

Reflector	Pulse Height (arbitrary normalization)	Resolution at 662 keV in %
Electropolished Al	0.65	17.8
Al metal foil	0.80	15.8
Teflon	0.88	14.2
Al polymeric foil	0.92	13.4
Ag foil	0.97	14.3
VM2000 R	1.00	12.5
VM2000 S	1.12	12.3
VM2002 R	1.12	12.5
VM2002 S	1.21	12.4

Table 4.3: Pulse height and energy resolution in the light detector for various reflectors, from [236]. R and S refers to whether the reflective layer or the support layer of the multilayer foils is facing the crystal.

An dangerous background for the search for Dark Matter comes from alpha decays in the vicinity of the crystal. If the alpha escapes, the recoiling daughter nucleus may impinge on the crystal and mimic a heavy nuclear recoil. Some details on such processes are discussed in detail in section 9.8.

In order to be able to distinguish such events from Dark Matter induced tungsten recoils, the reflective foil is made scintillating. Then the escaping alpha will produce additional scintillation light, allowing to reject this background. All VM type foils scintillate. In runs 29 and 30 the clamps that hold the crystals are covered with this foil also.

4.3.7 Model of Pulse Formation

The thermodynamical picture of equation 4.1, $\Delta T = \Delta E/C$, is oversimplified. Instead, let us get a more detailed insight into the formation of a pulse following a particle interaction in the absorber. This will be done without

giving too much details of the model; A nice overview on this subject can be found in [211], and [237] gives the details to this discussion.

Within less than a nanosecond, an energy deposition in the absorber leads to a spectrum of high frequency phonons. Ionizing radiation releases its energy mainly in the electron branch, which results in an almost monoenergetic population of acoustic phonons with about half the Debye frequency. For $CaWO_4$, the Debye temperature is $\Theta_{\text{Debye}} = 250\,\text{K}$ [238], so $\nu_{\text{Debye}}/2 = k_\text{B}\Theta_{\text{Debye}}/2h \approx 2\,\text{THz}$. Interactions that deposit their energy directly in the nuclear branch, such as elastic scatterings on nuclei, result in a continuous spectrum of acoustic phonons up to ν_{Debye}.

THz phonons have energies of a few meV, which is large compared to thermal energies of interest, $E = k_\text{B}T = 8.6 \times 10^{-5}\,\text{eV/K} \times 15\,\text{mK} = 1\,\mu\text{eV}$. Hence such THz phonons are called **non-thermal phonons**. They decay due to crystal lattice anharmonicities with a decay rate that is proportional to ν^5 [239]. This strong frequency dependence means that the initial high frequency is quickly reduced, but remains almost constant at a few 100 GHz, still above thermal energies, on a time scale of a few milliseconds [237]. During this time the phonons spread ballistically throughout the absorber and fill it uniformly after a few reflections on the surface.

Such non-thermal phonons are readily absorbed by the free electrons of the metal film in the thermometer. This absorption is mediated by a strong coupling due to space charge variations of the phonon oscillation. The strong interaction among the electrons in the thermometer then quickly shares and thus thermalizes the phonon energy, which results in a heating of the thermometer. With superconducting phase transition thermometers, this temperature change is then measurable as a change in resistance. Since phonons are mostly absorbed in the thermometer alone, this allows to scale up the targets to the large dimensions used in the CRESST experiment.

To come to a quantitative description of the pulse shape in the thermometer, we model the absorber and thermometer as shown in figure 4.13. According to the above discussion, we can model a particle interaction as resulting in a sudden time dependent power input in the electron system of the thermometer, $P_\text{e}(t)$, and also, a power input in the thermalized phonon system of the absorber, $P_\text{a}(t)$. Given a fraction ϵ of phonons that are thermalized in the thermometer, and $(1-\epsilon)$ in the absorber, we have

$$P_\text{e}(t) = \Theta(t)\,\epsilon\,\frac{\Delta E}{\tau_\text{n}} \text{e}^{-t/\tau_\text{n}} \tag{4.2}$$

$$P_\text{a}(t) = \Theta(t)\,(1-\epsilon)\,\frac{\Delta E}{\tau_\text{n}} \text{e}^{-t/\tau_\text{n}} \tag{4.3}$$

where Θ is the step function, and ΔE is the energy deposited by the incident particle. The time constant τ_n for the thermalization of the non-thermal phonon population is given as

$$\tau_\text{n} = \left(\frac{1}{\tau_\text{e}} + \frac{1}{\tau_\text{a}}\right)^{-1} \tag{4.4}$$

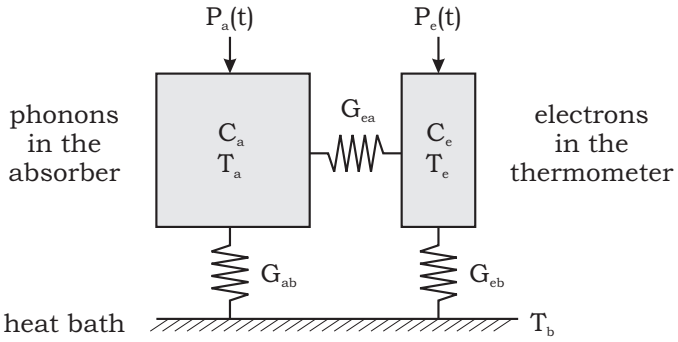

Figure 4.13: Thermal model of the detector. T_e and T_a are the temperatures of the electron system in the thermometer and of the phonon system in the absorber, respectively, and C_e and C_a are their heat capacities. T_b is the temperature of the heat bath. $P_\mathrm{e}(t)$ and $P_\mathrm{a}(t)$ are energy flows from non-thermal phonons into the thermalized systems. The various G are thermal conductances.

where τ_e and τ_a are the time constants for the thermalization in the thermometer and absorber, respectively. The fraction ϵ of phonons thermalized in the thermometer is

$$\epsilon\tau_\mathrm{e} = (1-\epsilon)\tau_\mathrm{a}. \tag{4.5}$$

The change of temperature of the thermometer and absorber, $C_\mathrm{e}\,\mathrm{d}T_\mathrm{e}/\,\mathrm{d}t$ and $C_\mathrm{a}\,\mathrm{d}T_\mathrm{a}/\,\mathrm{d}t$ is equal to the power input minus the power transferred through various channels out of the system. Taking into account energy losses to the heat bath, as well as a coupling between thermometer and absorber (see figure 4.13), this leads to two coupled differential equations for the temperatures:

$$C_\mathrm{e}\frac{\mathrm{d}T_\mathrm{e}}{\mathrm{d}t} = P_\mathrm{e}(t) - (T_\mathrm{e}-T_\mathrm{a})G_\mathrm{ea} - (T_\mathrm{e}-T_\mathrm{b})G_\mathrm{eb} \tag{4.6}$$

$$C_\mathrm{a}\frac{\mathrm{d}T_\mathrm{a}}{\mathrm{d}t} = P_\mathrm{a}(t) - (T_\mathrm{a}-T_\mathrm{e})G_\mathrm{ea} - (T_\mathrm{a}-T_\mathrm{b})G_\mathrm{ab}. \tag{4.7}$$

With the initial condition $T_\mathrm{a}(t=0) = T_\mathrm{e}(t=0) = T_\mathrm{b}$ these equations have the solution for the thermometer signal $\Delta T_\mathrm{e}(t) \equiv T_\mathrm{e}(t) - T_\mathrm{b}$:

$$\Delta T_\mathrm{e}(t) = \Theta(t)\left[A_\mathrm{n}\left(\mathrm{e}^{-t/\tau_\mathrm{n}} - \mathrm{e}^{-t/\tau_\mathrm{intr}}\right) + A_\mathrm{t}\left(\mathrm{e}^{-t/\tau_\mathrm{t}} - \mathrm{e}^{-t/\tau_\mathrm{n}}\right)\right] \tag{4.8}$$

where the constants expressed in terms of the original quantities can be found e.g. in [237]. τ_intr is the intrinsic thermal relaxation time constant of the thermometer, τ_t the thermal relaxation time of the absorber, and τ_n the life-time of the non-thermal phonon population.

This solution consists of two components. One is a non-thermal component with amplitude A_n, the other a thermal component with amplitude A_t. Three time constants appear as observed in a typical pulse of the CRESST detectors, and this model suffices to explain the observed pulse shapes.

The ratio of τ_{intr} and τ_{n} controls the sign of the non-thermal parameter A_{n}, so two different modes of operation of the thermometer can be discussed. A thermometer for which $\tau_{\mathrm{n}} \ll \tau_{\mathrm{intr}}$ integrates the power input $P_{\mathrm{e}}(t)$: The phonons flow into the thermometer more quickly than out of it. The amplitude of the non-thermal component measures the total energy of the high-frequency phonons absorbed in the thermometer and is given by $A_{\mathrm{n}} \approx -\epsilon\Delta E/C_{\mathrm{e}}$. Hence, for a given energy deposition, the heat capacity C_{e} of the electron system of the thermometer determines the amplitude A_{n}. This operating mode of the thermometer is referred to as **calorimetric mode**. In this mode, τ_{n} defines the rise time of both the non-thermal and the thermal signal component, τ_{intr} defines the decay time of the non-thermal component, and τ_{t} determines the decay time of the thermal component. The light detectors used in the CRESST experiment are optimized to work in the calorimetric mode.

In a thermometer with $\tau_{\mathrm{n}} \gg \tau_{\mathrm{intr}}$ phonons flow out of the thermometer more quickly than in. Hence it measures the flux of non-thermal phonons and is said to operate in the **bolometric mode**. Also in this mode, the pulse height is proportional to the deposited energy. For an observed pulse, the rise time of the non-thermal component is then determined by τ_{intr} and its decay time by τ_{n}. The rise time of the thermal component on the other hand is defined by τ_{n}, and its decay time is defined by τ_{t}. The phonon detectors used in the CRESST experiment work in the bolometric mode due to the long time needed for the thermalization of the high frequency phonons.

To avoid confusion, let it be mentioned that the distinction as bolometric or calorimetric mode refers to the processing of the incoming flux of non-thermal phonons. With respect to the incoming flux of particles, the CRESST detectors of course still work as calorimeters, measuring the energy of each individual particle.

4.4 Data Taking

4.4.1 SQUID Based Readout

To measure the change in resistance that is caused by the change of temperature of the thermometer, **Superconducting Quantum Interference Devices**, SQUIDs for short, are ideal devices. They are extremely sensitive indeed and measure (and amplify) the magnetic flux Φ_{in} produced by an input coil, and hence the current in this coil. In our case the input coil is connected in parallel to the superconducting phase transition thermometer $R_{\mathrm{t}}(T)$, see figure 4.14, which matches the impedance of the low ohmic thermometer. In the new setup, two shunt resistors $1/2R_{\mathrm{s}} = 20\,\mathrm{m}\Omega$ are used to symmetrize the circuit [240] as shown in the figure, where the **bias current** I_0 is split in the two branches.

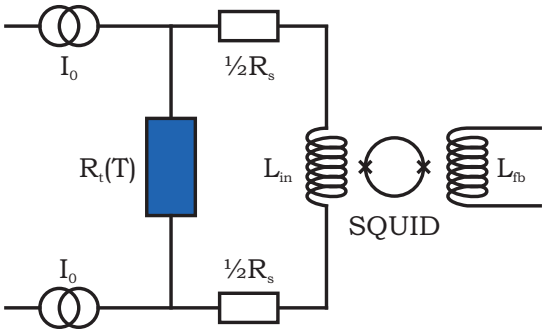

Figure 4.14: The basic readout scheme.

The current through the SQUID input coil is

$$I_\mathrm{s} = \frac{I_0 R_\mathrm{t}(T)}{R_\mathrm{t}(T) + R_\mathrm{s}}. \tag{4.9}$$

Given a small change of thermometer resistance $\Delta R_\mathrm{t} \ll R_\mathrm{t}$, this changes as

$$\begin{aligned} \Delta I_\mathrm{s} &= \frac{\mathrm{d}I_\mathrm{s}}{\mathrm{d}R_\mathrm{t}} \Delta R_\mathrm{t} && (4.10)\\ &= \frac{I_0 R_\mathrm{s}}{(R_\mathrm{t} + R_\mathrm{s})^2} \Delta R_\mathrm{t} && (4.11)\\ &= \frac{I_0 R_\mathrm{s}}{(R_\mathrm{t} + R_\mathrm{s})^2} \frac{\mathrm{d}R_\mathrm{t}}{\mathrm{d}T} \Delta T && (4.12) \end{aligned}$$

which is proportional to ΔT for small enough ΔR_t.

The SQUIDs employed in Gran Sasso are commercially available dc-SQUIDS from Supracon. The amplified output signal is given as

$$V_\mathrm{squid} = \gamma(\Phi_\mathrm{in} + n\Phi_0) \tag{4.13}$$

where γ is the gain of the system, n an unknown integer number and $\Phi_0 = \hbar/2e$ is the flux quantum. The ambiguity represented by the last term is due to the periodicity of the SQUID response. The SQUIDs are therefore operated in flux-locked mode by means of a feedback circuit, and the output signal is the current in this feedback loop. In this way the relationship between the magnetic flux Φ_in and the output voltage V_squid is linearized over a wide range. The feedback mechanism requires the change of resistance ΔR_t to be slow compared to its slew rate. Otherwise the flux lock can be lost, which results in a so-called **flux quantum loss**, changing n to a new value. In practice, this results in events after which the baseline is shifted by an amount $\gamma n \Phi_0$. Another case in which the baseline can change to a new value is when the input flux of the SQUID causes V_squid to exceed 10 V, so the SQUID resets. Therefore it is required that the dynamical range of the SQUID can encompass the full difference from the operating point of the detector up to the top of the transition. Since the baseline of the pulses carries no information, pulses are typically shown with their baseline subtracted.

4.4.2 Data Acquisition

A block diagram of the main data acquisition components is shown in figure 4.15. The thermometers are connected electrically with bond wires to pads on the detector holder. From there, contact is made through superconducting NbTi wires which first run to a connector at the bottom of the carousel, and then up along the cold finger. These wires are twisted in pairs and woven with an insulating thread [240]. To reduce crosstalk, the pairs are twisted in alternate directions, and ground carrying single wires are woven between the pairs. Being a superconductor, the NbTi have a bad thermal conductance. Therefore they are clad with a thin layer of CuNi to allow cryostat and detectors to reach base temperature. Thermal anchoring is provided on various places in the cryostat.

The bias current is supplied by a floating current source. High frequency noise is reduced with 10 kHz low pass filters. To minimize Johnson-Nyquist noise [241, 242], the shunt resistors are thermally anchored to the mixing chamber, the coldest point in the cryostat. The SQUIDs are located in the liquid helium bath at 4 K. After a differential amplification step, the signals are transferred through 50 kHz low pass Faraday cage filters and 10 kHz anti-aliasing filter. One branch of the signal is then fed through an 8 Hz high pass filter and amplified $\times 20$, low pass shaped, and reaches the trigger unit.

A trigger signal can then be sent to the 16 bit transient digitizer, which samples 8 channels simultaneously. In runs 28 through 30, pulses were sampled with 25 kHz (40 μs time base), the record length was chosen as 4096 samples (164 ms). Detectors Zora and Verena with their light detectors were served by one such digitizer module. The first quarter of the record length (1024 samples) is called the **pre-trigger region** and is used to evaluate the baseline. The remaining 3/4 hold the pulse information.

Once one channel of the digitizer module receives a trigger, this channel is read out together with its associated channel, i.e., both detectors in a module are always read out together. During read out of the digitizer module, digitalization of all channels has to pause. Hence, the trigger for other channels on the same 8 channel digitizer module are blocked for the second half of the post-trigger time, $1/2 \times 3/4$ times the record length. This guarantees that pulses that triggered are recorded long enough so that a proper pulse height evaluation is possible. Pulses are recorded together with the `trigger delay` parameter set with respect to the first channel on the digitizer module that triggered.

The digitized data is then written to hard disk. Under normal running conditions, this adds up to only ≈ 100 MB of data per detector module and day, which is easily transferred out of the Gran Sasso tunnel and distributed via internet throughout the collaboration.

4.4.3 Heater Pulses

Each tungsten thermometer film has an additional heater structure evaporated to it. This film heater is used to stabilize the thermometer in its op-

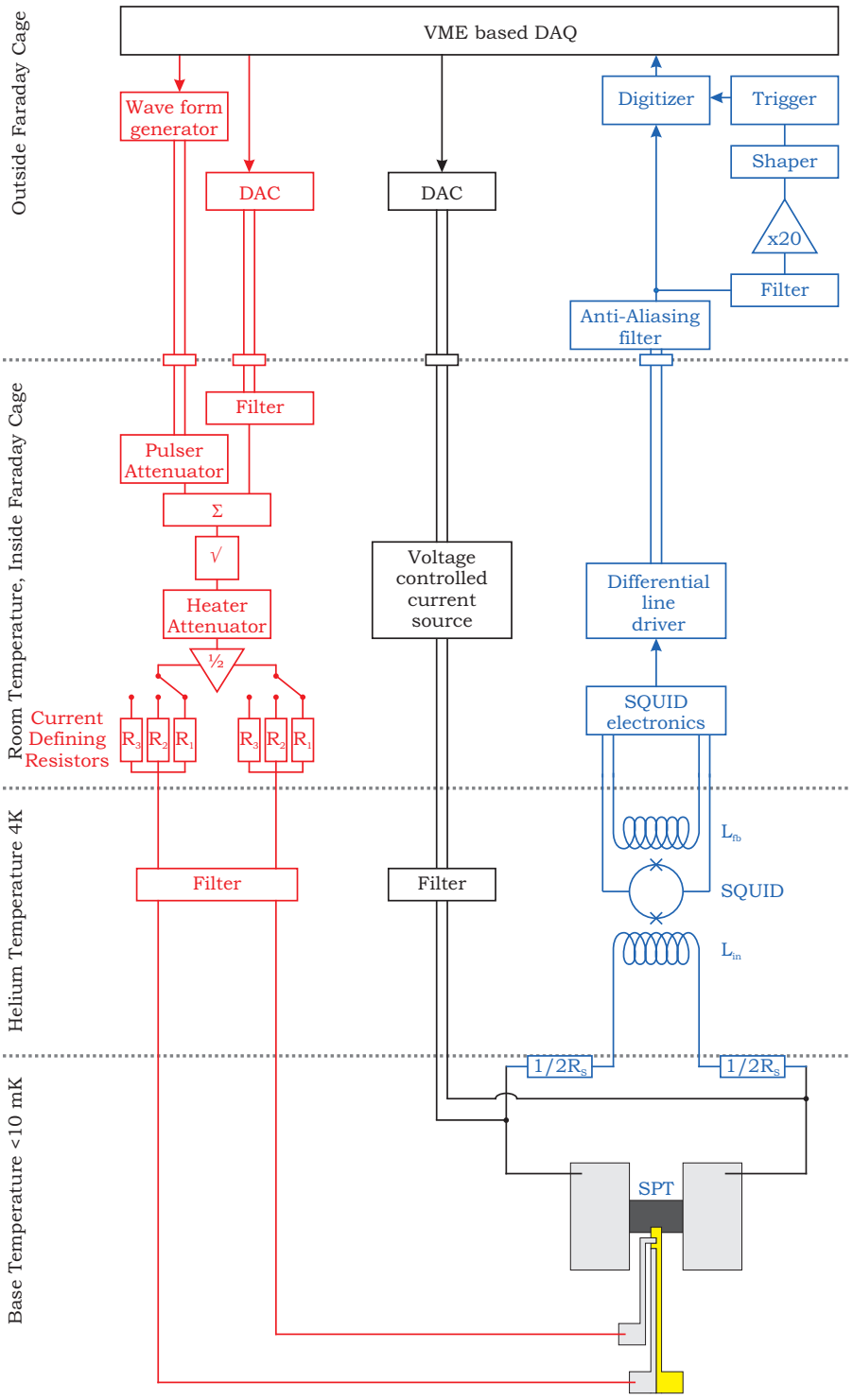

Figure 4.15: Block diagram of essential electronics components. The readout circuit with SQUID and trigger is shown in blue. Shown in black the bias circuit. Red the heater system for stabilization in the operating point and injection of heater pulses.

erating point (section 4.3.1), and to inject heater pulses for operation point control and calibration (section 5.4.2). The wires are woven to twisted pairs in the same making as the bias cables, however they are separated from the bias lines as much as possible; for example, at the bottom of the carousel, they are separated by a copper plate to reduce cross-talk, and they run up the cold finger on opposite sides.

Figure 4.15 also shows the main electronics parts of the heater circuit. Two arbitrary wave form generators produce the heater pulses for all the light and phonon detectors, respectively. This requires attenuators to adjust the pulse height individually for each detector. The attenuated pulser signal is then added to the constant current needed for stabilization of the operating point. An analog square-rooter is needed to linearize the dependence of the heating power with respect to the input voltage, since otherwise the energy of a heater pulse would depend on the heating power needed to stabilize the detector in its operating point. An additional heater attenuator allows continuous adjustment of the heating, and a set of different ohmic resistors (kΩ to MΩ) is installed to adjust the dynamical range of the available heating power. This is required since phonon and light detectors as well as detectors of different design have significantly different heaters, requiring heating powers of varying strength.

Part III

Data Analysis

Chapter 5

Detector Operation and Data Analysis

Intent: How are CRESST detectors operated, and how does one analyze the data? This chapter gives some information on the setting up of the detectors in their operating point. It explains how the stability in the operating point is monitored, and how small deviations are corrected for. Parameters extracted from the thermometer pulses are introduced, and the process of energy calibration is explained.

Organization: Section 5.1 explains how to set up the detectors in their transition to the superconducting state. Primary parameters extracted from the pulses are defined in section 5.2. Before explaining the procedure for energy calibration in section 5.4, section 5.3 explains the method for proper pulse height evaluation.

5.1 Detector Operation

5.1.1 Transition Curve Measurement

The central characterization of a superconducting phase transition thermometer is its transition curve. The lower the transition temperature, the smaller the heat capacity of the film, and hence the larger the signal for a given interaction. The steeper the transition, the better the sensitivity of the film. Conversely, the wider the transition, the larger the dynamical range of the thermometer.

One way to measure the transition curve of the detector is to regulate the temperature of the mixing chamber of the cryostat, only slowly varying its temperature. The temperature of the (weakly coupled) thermometers will then follow, changing the resistance of the film, which can be measured.

Another way, closer to the actual operating conditions, is to ramp the current through the heater and record the thermometer resistance. Since the bias current needed for readout also heats the tungsten film, the shape of the transition depends on this current, see figure 5.1. Criteria for the optimum transition curve are its steepness, linearity, and temperature.

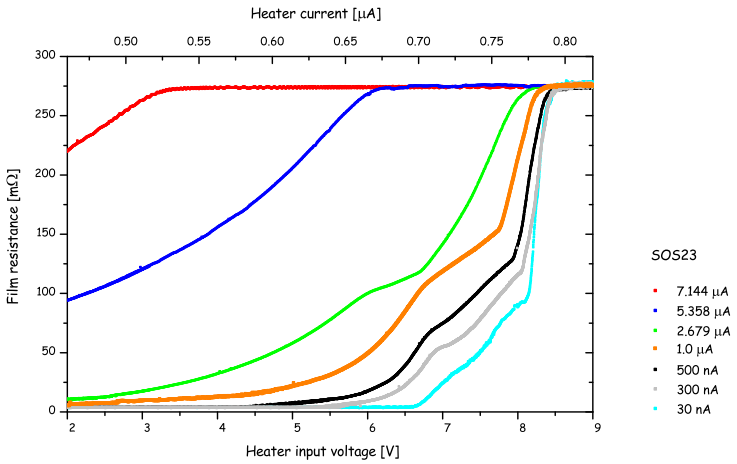

Figure 5.1: The shape of the transition curve depends on the bias current: Higher currents tend to smoothen the transition. This is data from the light detector SOS23 [234]. The temperature range shown corresponds to approximately $10 - 17\,\mathrm{mK}$, and the bias current is shown on the right.

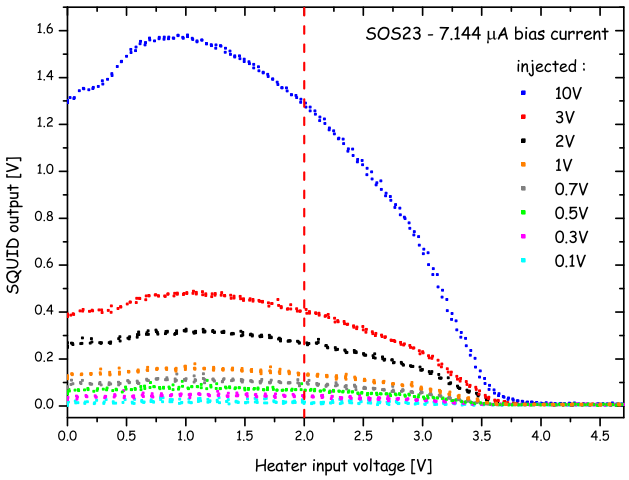

Figure 5.2: One chooses an operating point where the response is possibly linear with increasing injected heater pulse energy and shows little variation with respect to changes in the operating point for energies of interest. Shown are data from the light detector SOS23 after cooldown to run 29, with constant bias current for varying heater pulse amplitude.

5.1.2 Operating Point

The detectors are usually set up at the top half of the transition since the noise is generally smaller in this region of the transitions, see [234] for a detailed discussion. An additional benefit is that it is easier to approach this operating point after refilling cryogenic liquids (which is necessary about every third day) and thus makes operating the detectors more reliable.

For a fixed bias current, heater pulses of varying amplitude can be injected. This directly probes the relevant quantity, namely the response of the detector to various injected energies. Figure 5.2 shows this response for a given bias current, and different temperatures of the thermometer (that is, different DC heater input voltages). One chooses the operating point such that there is a possibly strong dependence of the control pulse on temperature, but a possibly weak dependence of the response to heater pulses (of relevant energies) on the temperature of the detector. In addition, one would like a possibly linear dependence of the response to the energy of the pulses. Details on the setting up of detectors for runs 29 and 30 can be found in [234]. In particular, considerations regarding different amounts of noise are discussed there.

5.1.3 Stability Control

The low energy interactions of interest here result in temperature changes of the thermometer film of a few μK. Hence it is necessary to stabilize the film temperature at least to this precision. As a necessary precondition, the detector modules are only weakly coupled thermally to the cryostat. In addition, active control is mandatory. To this end, **control pulses** are injected in the heater structure every 3 seconds, which is frequent enough to sample temperature fluctuations, but does not introduce too much dead time. These control pulses are heater pulses which drive the detector out of its transition. Their pulse height is evaluated online by software and serves as input variable for a PI control of the operating point through an adjustment of the steady heater current.

The baseline of the pulses can also be used for stabilization [211]. However, this method suffers from flux quantum losses and was not used during the data taking presented here.

Heater pulses of amplitudes other than that of the control pulses are injected in addition every 30 seconds. This serves the purpose of energy calibration down to lowest energies as is explained in section 5.4.2. Moreover, it can be used to monitor the stability of the detector, which is shown in figure 5.3, and to check the trigger efficiency at low energies.

5.2 Pulse Parameters

Figure 5.4 shows typical pulses recorded by the CRESST-II detectors. For the data sets presented here, the pulses are sampled with a time base of 40 μs (25 kHz). A record consists of 4096 samples, hence lasting 163.84 ms.

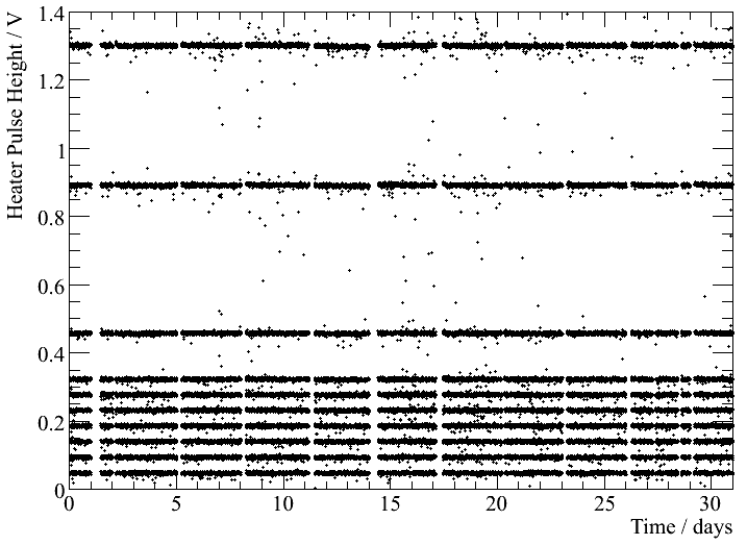

Figure 5.3: Pulse heights of the heater pulses versus time, here for detector ZORA during one month of data taking in run 30. No cuts where applied on the data. The detector response can be seen to be stable within resolution over the full time window. The small time gaps are when measurement is interrupted to refill cryogenic liquids for operation of the cryostat. This is necessary about every third day.

Following a trigger, the preceding 1024 samples are recorded for evaluation of the baseline; this region is called the **pre-trigger region**. The **post-trigger region** accordingly denotes the following 3072 samples.

5.2.1 Main Parameters

To prepare for off-line analysis, a set of fast and robust parameters is extracted from each pulse. They are described in detail in appendix C. Three parameters deserve mention here. The `baseline offset` parameter is the average level of the baseline, taken from the pre-trigger region. The `pulse height` parameter is the maximum of the pulse, extracted from a 50 sample moving average. This parameter is good for a first look at the data. However, since taking only the maximum of the pulse treats noise in a biased way, it cannot be used as a precise `amplitude` parameter. Finally, the average of the first 50 samples and the last 50 samples of a pulse are subtracted and give the `right - left baseline` parameter.

5.2.2 Life Time

Each pulse carries two cumulative parameters, `Dead Time` and `Life Time`. Both counters are reset only at the beginning of a new data file (a `Run Segment`).

Before the trigger electronic is activated, a pre-trigger region of $1/4 \times 4096 \times 40\,\mu\text{s} = 50.96\,\text{ms}$ is enforced. Hence each event increments its `Dead`

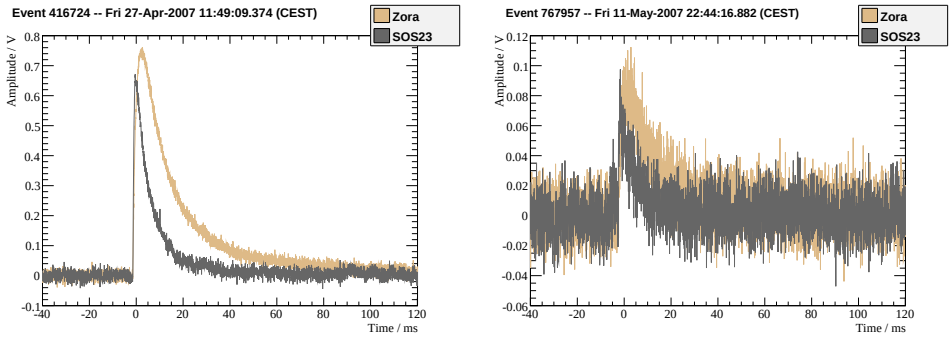

Figure 5.4: Typical pulses recorded by CRESST detectors, here from phonon detector Zora and its light detector SOS23. Shown are events from the electron/gamma band with energies of 100 keV (left) and 10 keV (right).

`Time` parameter by this time. Following a trigger, all channels on the same (8 channel) transient recorder are only allowed to trigger for half the post-trigger region ($1/2 \times 3/4 \times 4096 \times 40\,\mu$s $= 61.44$ ms). Hence, each event adds half the post-trigger time as dead time to other channels on the same recorder. Finally, for each event, the read out time of the DAQ is also added to the `Dead Time` parameter. The `Life Time` parameter on the other hand is the time in which a trigger may have occurred since the last event, that is, real time minus the dead time.

Each heater pulse, be it a control pulse or a calibration pulse, is flagged as such and not considered in the particle analysis. Therefore each such pulse has to be considered as additional dead time. Heater pulses are only shot if a time corresponding to the pre-trigger region is trigger free in all detectors. Therefore each heater pulse adds the post-trigger region $3/4 \times 4096 \times 40\,\mu$s $=$ 122.88 ms as dead time for all channels. Typically, for each calibration pulse, we shoot 10 control pulses which are not recorded to disk (only their pulse height is). This makes a total of 11 heater pulses that have to be considered for the dead time for each recorded heater pulse.

The full record length of 163.84 ms is added to the dead time for each cut event. The stability cut (section 9.2.2) removes whole time periods and has therefore to be considered fully as additional dead time. Given that the efficiency of the cuts employed is close to unity, this completes the discussion of the live time necessary to calculate the exposure. On the last point, however, it should be noted that a cross-check is required to make sure that the cut efficiency is not time dependent; in particular, one has to check whether a cut removes all events from a certain time period. In this case, one had to consider this full time period as dead time.

5.3 Pulse Height Evaluation

The `pulse height` parameter is good for a first look to the data, but not for further analysis. The reason is simply that it treats noise in a biased

way: By looking only for the maximum of the pulse, negative excursions due to noise are not taken into account. The pulse height will always tend to overestimate the true amplitude of the pulse. Therefore, in CRESST we use a **standard event fit** (or **template fit**) to derive the `amplitude` of a pulse.

To this end, an average pulse is constructed and then fitted to each event. This has two distinct advantages: It guarantees that noise is treated in an unbiased way, and it uses the complete available pulse information to derive the amplitude. The following will explain the procedure in some detail.

5.3.1 Creating a Standard Event

A preliminary **template pulse** or **standard event** is generated as the average of a set of pulses from an energy interval. Events from the 122 keV line of a Cobalt calibration are readily used. The energy interval should be chosen possibly narrow due to a dependence of the pulse onset on energy (trigger walk).

These events are added together and averaged, forming a first preliminary standard event. This standard event is then fitted to the individual events themselves. Free parameters in the fit are the `baseline offset` of the pulse, a possible time `shift` of the pulse and of course the `amplitude` of the pulse, see figure 5.5.

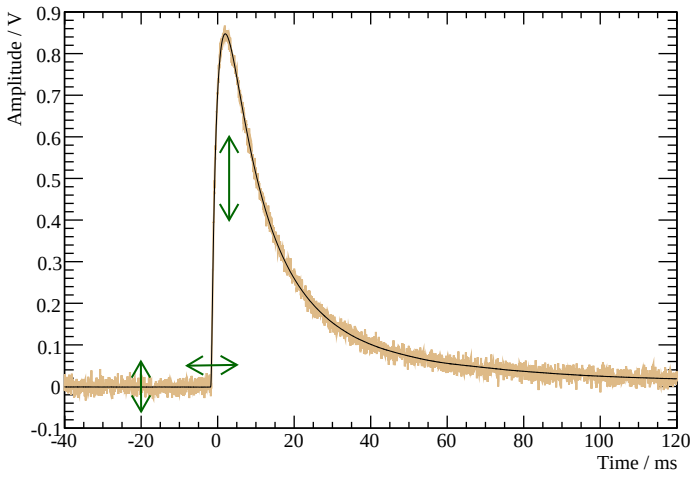

Figure 5.5: A typical event in the phonon detector ZORA with an energy of approximately 100 keV (light brown) together with a standard event fit (black line). The three free parameters in the fit are indicated by the arrows: the height of the baseline, a time shift of the standard pulse, and its amplitude.

Looking at distributions like the `RMS` value (or the χ^2) of the fit, the `onset channel`, and the fitted `amplitude` allows to reject events which are noisy, pile-up events, or events with pathological signatures. Thus one arrives at

a clean set of events that are used to create a second standard event which eventually can be used for further analysis.

5.3.2 How Many Events to Include

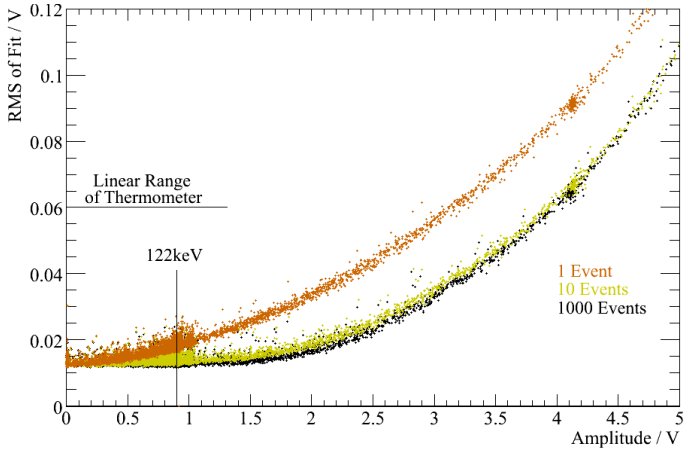

Figure 5.6: RMS of standard event fits versus amplitude, for pulses from a ^{57}Co calibration of phonon detector Zora. The standard event was created from clean samples of 1, 10, and 1000 events from the 122 keV line, as indicated by the different colors. Two reasons for an increase in the RMS value separate: For too few events, the quality of the fit decreases (the RMS value increases) with increasing energy due to the high noise in the standard event. For many events, the RMS value increases also, but at higher values, due to the non-linearity of the detectors. Already with 10 events in the standard event, the noise effect becomes negligible.

The pulse shape $P(t)$ of the standard event has two components: The signal pulse $S(t)$ and some noise contribution $N(t)$: $P(t) = S(t) + N(t)$. Fitting a standard event to a pulse implies scaling the amplitude to fit the sum $P(t)$ of these two contributions. If all matches up, and if the standard event has negligible noise, the RMS (or χ^2) of the fit will just be the RMS of the noise on the fitted pulse. But the noise on the standard event is also scaled, and if it is too high, it will eventually dominate the error of the fit. Figure 5.6 shows this effect. If only one event is used to create a standard event, the quality of the fit decreases rapidly with increasing energy. But already from 10 events in the standard event, the picture hardly changes anymore when adding more pulses to the standard event. Hence, given the usual noise conditions in Gran Sasso, already a few 10s of clean pulses are enough to create a standard event which is scalable to higher energies. Since long exposures are often available, typical values easily go in the hundreds.

The pulses in CRESST sample the transition curve of the thermometer. At the top of the transition the resistivity curve bends over to its normal-conducting value. Hence the remaining increase of the RMS value of the fit observed in figure 5.6 is due to the non-linearity of the transition. Of

course the standard event fit only works in the linear regime, where the pulse shape can be simply scaled with the amplitude parameter. Toward higher amplitudes, the transition curve of the detector will eventually cause a non-linear response. The pulse shape changes, and the quality of the standard event fit decreases.

5.3.3 The Truncated Fit

The RMS-versus-Amplitude plot of figure 5.6 is an important plot for the standard event fit indeed. Not only does it indicate the quality of a particular fit, but it also clearly indicates the linear regime of the detector.

In case the standard event is created from pulses beyond the linear regime, this would also show up in this plot. The quality of the fit would then show a bump at energies below the standard event energy, being best at zero energy and at the energy of the pulses that were used to construct the standard event. In this case, pulses with lower energies would have to be used to create the standard event. Most detectors are linear up to the 122 keV line from a ^{57}Co calibration. Only for phonon detector VERENA, lower energy pulses had to be used as standard event.

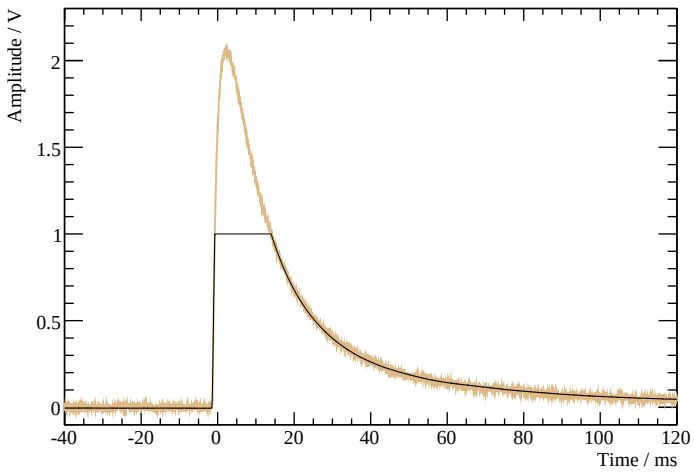

Figure 5.7: A typical event in the phonon detector ZORA with an energy of approximately 300 keV (light brown) together with a standard event fit (black line), truncated at 1 V. Pulse information above this value is not used for the fit. In this case, 20 samples are available for the rising part of the pulse.

If a pulse is large enough to sample the non-linear region of the transition, its shape will become nonlinear. But this affects only those parts of the pulse shape that are in or above this amplitude, while the parts of the pulse shape in the linear regime remain the same. One can therefore **truncate** the pulse shape of the standard event if it is scaled above the linear regime, and include only those parts of the pulse in the fit that are below the truncation,

see figure 5.7. The effect of this truncation is dramatic, as indicated by figure 5.8: The detectors are linearized up to highest energies.

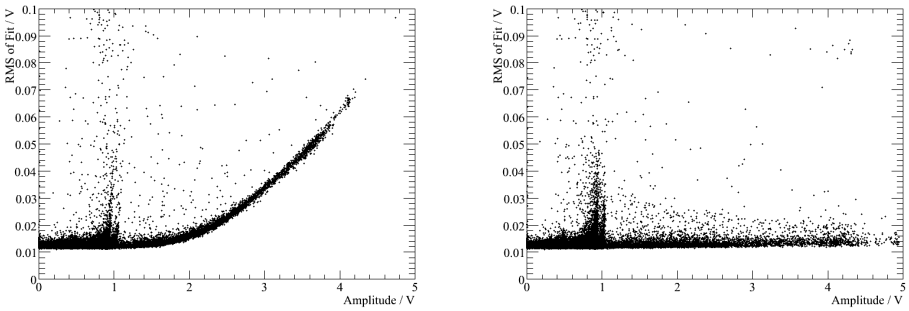

Figure 5.8: Left: The RMS-versus-amplitude plot, here from a standard event fit on phonon detector Zora from a ^{57}Co calibration. Above amplitudes of $\approx$ 1 V the fit quality decreases because the detector becomes nonlinear. Truncating the pulse at this value linearizes the detector up to highest amplitudes, as shown on the right; to set an energy scale, for Zora, 1 V corresponds to about 135 keV.

For simplicity, the term is used for both pulses with amplitude above and below the linear range. All fits done within this work are truncated standard event fits unless noted explicitly.

5.3.4 The Correlated Truncated Fit

The light detectors of CRESST are much more sensitive than the phonon detectors, which naturally makes them more sensitive to interference also. Especially for the small light pulses anticipated for the tungsten recoils in a WIMP search, this can render the standard event fit to a light pulse alone a difficult task at best. The **correlated truncated standard event fit** eliminates this problem: Instead of leaving the pulse onset for both the light detector and the phonon detector as independent free parameters, their relative timing is fixed. Both pulses are fitted at the same time, and the combined RMS is minimized. This dramatically improves the performance of the fit for pulses with low light yield. A necessary prerequisite is however that the standard events for both detectors are chosen from the same set of events. Otherwise trigger walk would render the procedure meaningless. If not otherwise mentioned, all pulses are fitted with a correlated truncated standard event fit.

5.4 Calibration

The CRESST experiment aims at detecting WIMP induced nuclear recoils in the 10 keV range. This requires a calibration procedure in this energy range. However, as already mentioned in section 4.2.1, the cold box poses a 12 mm thick barrier which cannot be penetrated by such low energy photons.

To nevertheless have an energy calibration at these energies, the heater structure on the CRESST thermometer is used, as described in the following.

5.4.1 Cobalt Calibration

A ^{57}Co calibration gives a calibration line at 122 keV, see figure 5.9. Details of the features seen in the calibration are discussed in detail in section 6.1; here, it suffices to note the 122 keV calibration peak.

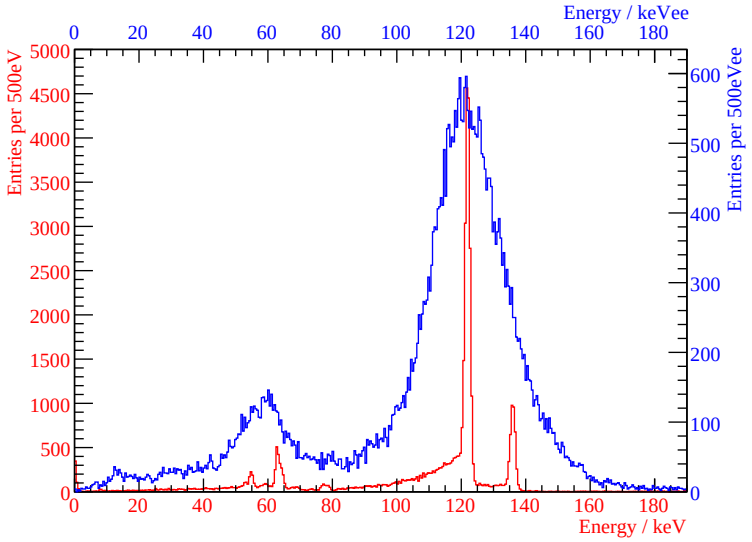

Figure 5.9: Data from 35 hours of ^{57}Co calibration of the phonon detector ZORA (red spectrum and scales) and its light detector SOS23 (blue spectrum and scales). The resolution of the phonon channel is an order of magnitude better than that of the light channel.

5.4.2 Calibration With Heater Pulses

The calibration at 122 keV is transferred to low energies with the help of heater pulses. These are injected at regular time intervals, distributed in a set of fixed energies. In runs 29 and 30, heater pulses were sent every 30 seconds, with injected voltages from $\{0.1, 0.2, 0.3, 0.4, 0.5, 0.6, 0.7, 1.0, 2.0, 3.0, 10.0\}$ V. Hence the thermometer response to a heater pulse of given energy is available about every 6 minutes. For noise investigations, empty baselines where partially recorded also, which prolongs the period a little.

In a purely ohmic heater circuit, the injected energy is proportional to the square of the voltage applied ($P = UI$ and $I = U/R$, so $E \propto P \propto U^2$). Hence the heater voltage is sent through an analog square root circuit (see figure 4.15). For a linear thermometer we can therefore expect a linear dependence for the reconstructed amplitude on the injected voltage.

The amplitude of the response to a heater pulse is evaluated using the truncated standard event fit with the template being chosen from heater pulses in the linear range. Since the pulse height probes the transition curve of the thermometer, this then gives a proper energy assessment independent of the particular pulse shape, which may hence be different from that of particle pulses.

Figure 5.10 shows the relation of injected voltage versus reconstructed amplitude of these heater pulses. The dependence can be seen to be indeed a rather linear one. A low-order polynomial is fitted to these pulses to give the transfer function between injected energy and amplitude.

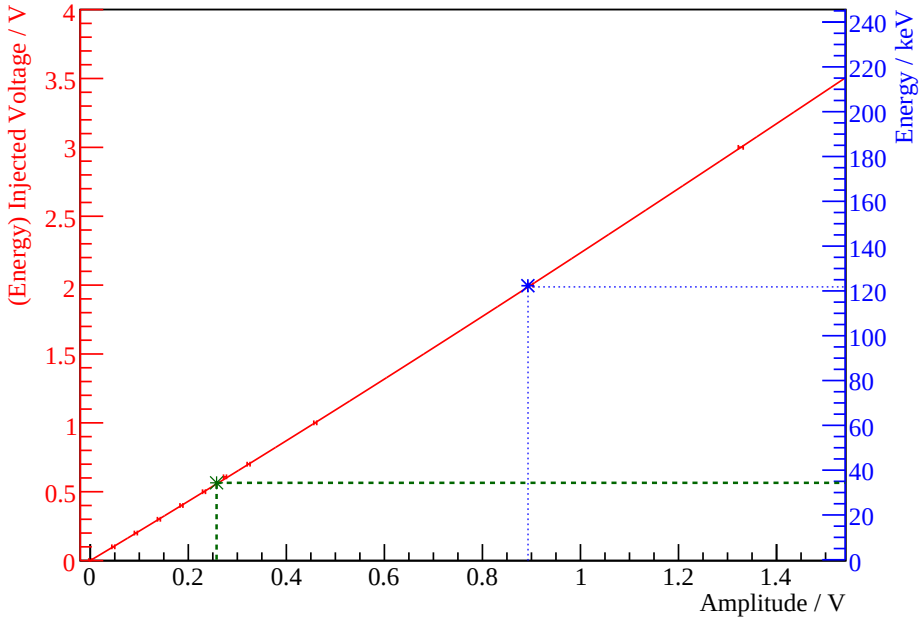

Figure 5.10: Heater pulses of varying energies are injected (red points, including error bars). Fitting a low order polynomial gives the transfer function (red line) between injected energy (red scale on the left) and reconstructed amplitude (scale on the bottom). The 122 keV peak gives a calibration point (blue), and sets the energy scale (in blue on the right). Then, for each particle pulse, the energy is found by evaluating the transfer function at the reconstructed amplitude (green).

The 122 keV gamma line is then used to calibrate the heater. To keep the errors from interpolation small, the heater can be adjusted (through the attenuators described in section 4.4.3) to have a heater pulse response close to the calibration reference point. The transfer function is then used to calibrate the amplitudes to lowest energies. This is explained again in the caption to figure 5.10.

5.4.3 Time Variations

Depending on the topology of the transition, pulses with some particular energy range can suffer more from operating point variations than others. For example, if the transition curve contains a part with a large $\mathrm{d}R/\mathrm{d}T$, pulses that warm the thermometer up to this part show larger variations in amplitude than pulses which warm the thermometer to temperatures where the $\mathrm{d}R/\mathrm{d}T$ of the transition is smaller. Using the heater pulses, such variations can be corrected for in an elegant way. Figure 5.11 shows the reconstructed `amplitude` of heater pulses which is seen to vary a little, mostly after refilling the cryostat, when the environment of the detectors still needs some time to approach base temperature again.

To correct for this effect, a **spline** is fitted through all heater pulses of given amplitude. Then, for each particle pulse, the energy is derived as described in the previous section. The only difference is that the polynomial transfer function is not fitted to some average value for the heater pulses' amplitude, but to the values of the splines, evaluated at the time of the particle pulse.

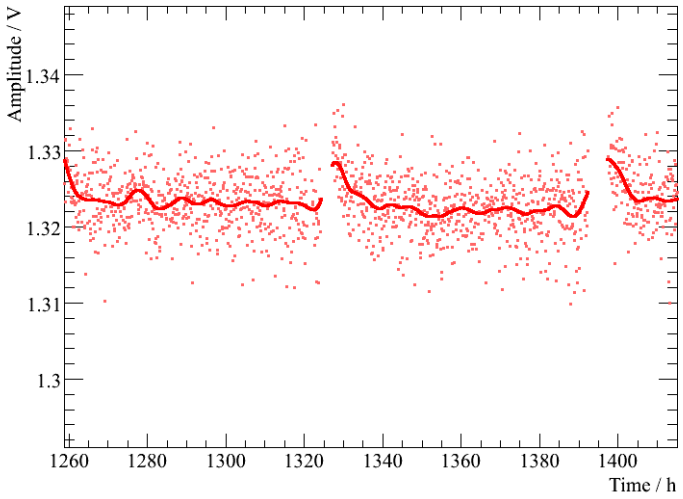

Figure 5.11: Slight variations in the operating point can cause variations for pulses with given energy, shown here for 3 V heater pulses of detector ZORA. A spline, shown as solid line, is fitted to correct for such variations.

This procedure results in an excellent energy resolution for the phonon detector, better than 1 keV over the full energy range of interest. The derived energy agrees within resolution with the literature energies of features seen in the spectra, as will be laid out in detail in the next chapter.

5.4.4 Light Detectors

For the light detectors, an absolute energy calibration requires a dedicated low energy (e.g. X-ray) source *within* the cold box. This was not available for the data presented here, and only in run 31 such (very weak) sources are installed. But an absolute energy calibration is not necessary for the discrimination capability of the detectors. Hence the detected scintillation light of the crystal is taken as a reference point. The unit of the energy scale is taken to be $\mathrm{keV_{ee}}$, short for electron-equivalent. It is defined such that 122 keV gamma radiation impinging on the crystal gives a signal in the light detector of $122\,\mathrm{keV_{ee}}$. Other than that, the calibration of the light detector follows the same procedure as explained above.

5.4.5 Amplitude Cut

When applying this method of energy calibration, for each pulse, one fits a polynomial to the values of the fitted splines at the time of the pulse. In particular if this polynomial is chosen of odd order, the transfer function that translates `amplitude` into `energy` can look like the one in figure 5.12. For particles beyond the region where the calibration is available, this may result in mis-calculated energies which are well within the region of interest. A simple cut on the `amplitude` easily rejects these events.

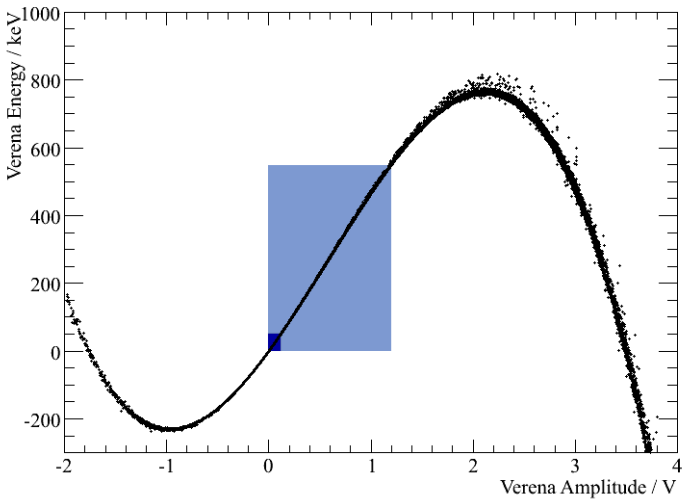

Figure 5.12: Since a polynomial is fitted within to the splines at a given time, this can result in smaller energies for higher amplitudes for events beyond the calibrated region (light blue region). This may lead to irritations in the analysis, so such events are discarded. In dark blue the region of interest for the Dark Matter analysis, $E < 50\,\mathrm{keV}$, is shown.

Chapter 6

Spectral Features

Intent: The phonon detectors of CRESST perform very well. The available exposure at low energies, the good energy resolution, and the stable environment call for a profound investigation of the recorded spectra. In addition, for the search for Dark Matter it is important to understand radioactive contaminations that are present in the crystals. This chapter explains the observed features in the spectra of phonon detectors.

Organization: In the first section 6.1 the spectra recorded during ^{57}Co calibrations are discussed; In particular, this includes the observation of escaping X-rays. In the second section 6.2 the various features that were discovered in the background spectra are presented.

6.1 Co-57 Calibration

6.1.1 The Plain Spectrum

Calibration sources are placed outside the cryostat. To place a source close to the detectors without the need of opening the radon box, a flexible tube is installed that goes from the outside into the radon box, spirals through the gamma shielding, winds twice around the cold box, and goes back out of shielding and radon box again. The calibration source is attached to a string and is blown through this tube by means of pressurized air, so its position can be adjusted to yield the desired trigger rates in the detectors.

The main purpose of the CRESST experiment is the search for Dark Matter, and we have seen in section 3.3.5 that this calls for energies of up to a few tens of keV. Hence, to calibrate the phonon channels and set the energy scale for the recoils, we use a ^{57}Co **source**, which decays via electron capture to the stable ^{57}Fe isotope, see figure 6.1. The particular source in use from run 29 on had an activity of 70 kBq as of early 2006.

Since the calibration source is outside the cold box, the thermal shield of the cryostat needs to be considered. It consists of five concentric copper cylinders with a total thickness of 12 mm. For the two main cobalt lines at 122 keV and 136 keV, the half-thickness $d_{1/2}$ of copper is about 2 mm (see appendix D), so the lines are attenuated to an intensity of $I = I_0\, 2^{-d/d_{1/2}} \approx 0.02 I_0$.

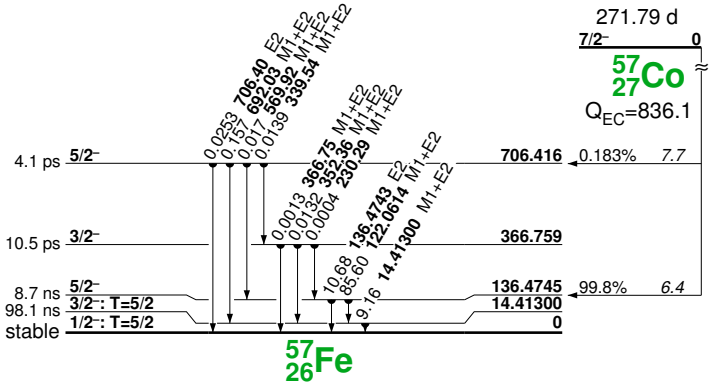

Figure 6.1: ^{57}Co decay scheme, from [195].

This also means that we can expect an additional contribution toward lower energies from Compton scattered gammas. Looking more closely at the absorption coefficients, one realizes that the cold box is 5 half-thicknesses for 122 keV gammas but only 4 for 136 keV gammas. Hence we can expect the Compton shoulder below 122 keV to be more pronounced than the one below 136 keV, since 122 keV gammas can interact more. This is indeed the case, as can be seen for example in the calibration spectrum of detector DAISY during run 31, figure 6.2.

With high enough statistics, the cobalt lines at higher energies can also be seen, most prominently the one at 692 keV. The 14 keV line on the other hand will be absorbed completely by the cold box, since at this energy, the half-thickness of copper is only 10 μm.

6.1.2 Escape Peaks

At the energies of interest, the photoelectric effect is the dominant gamma interaction mode. Hence, gammas interacting in the target mostly eject an electron from its shell, and the void will quickly be filled with electrons from other shells. In low Z targets, the energy difference will be converted mainly to Auger electrons [243]. High Z targets such as tungsten on the other hand will dominantly produce X-rays. If the original gamma interaction happens close to the surface of the target, the X-ray may escape from it. We then can expect tungsten **escape lines** from such processes. Table 6.1 shows the X-ray energies E_{esc} for the relevant materials.

Hence for each calibration line at an energy E_γ we can expect other lines at $E_\gamma - E_{\mathrm{esc}}$, as well as lines at E_{esc} due to interactions in neighboring crystals. Due to the excellent energy resolution of the detectors, for example the tungsten $K_{\alpha 1}$ and $K_{\alpha 2}$ escape peaks can readily be separated. Generally, the resolution of the CRESST phonon detectors is better than 1 keV. Given

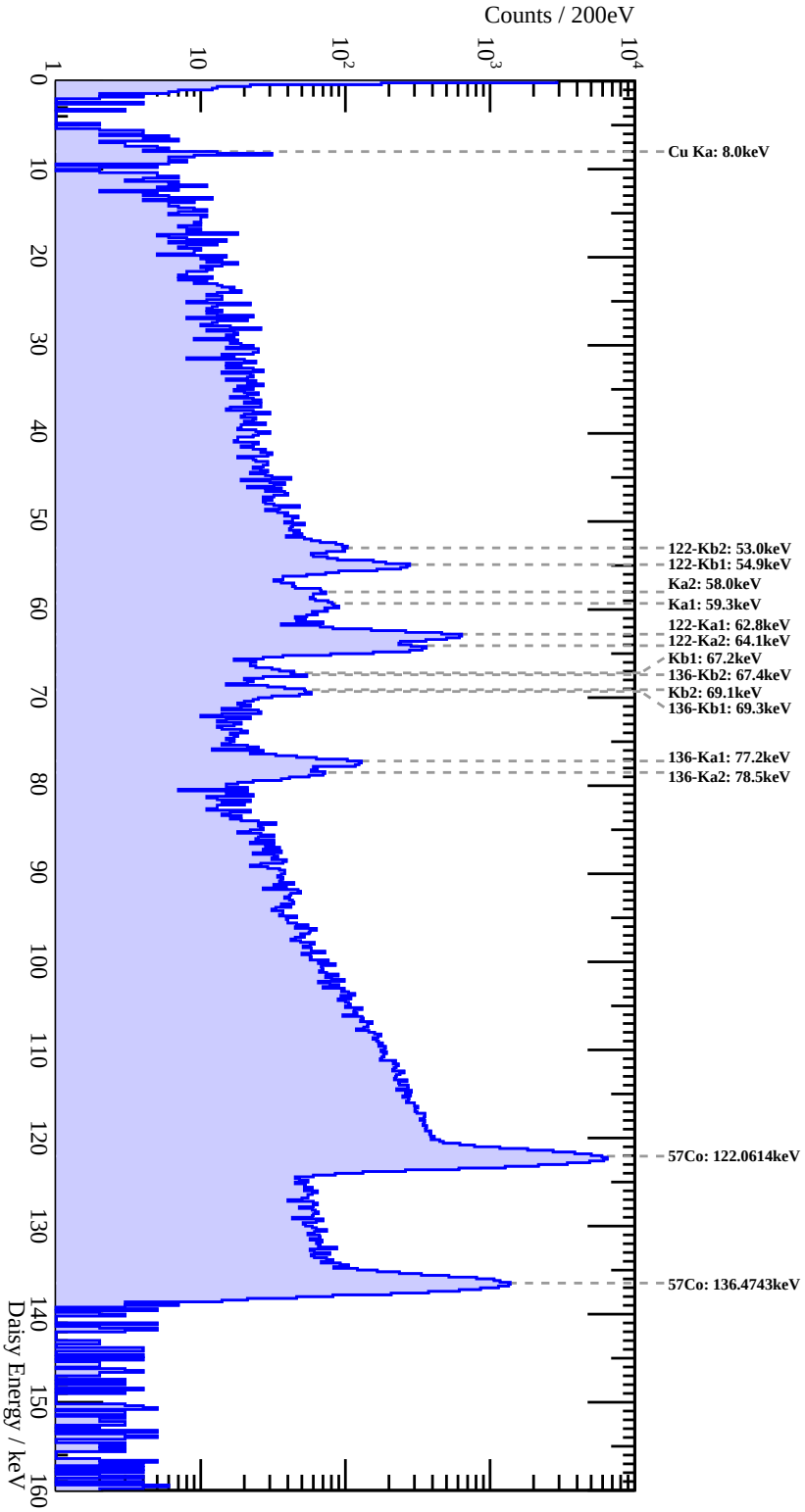

Figure 6.2: Energy Spectrum in detector Daisy from one week of ^{57}Co calibration. The lines are labeled according to their origin, see text for details.

element	transition (Siegbahn)	initial-final shell vacancies	intensity	energy
O	K_α	$K - L$	1	0.5 keV
Ca	K_α	$K - L$	15	3.7 keV
Cu	K_α	$K - L$	39	8.0 keV
W	$K_{\alpha 1}$	$K - L_3$	47	59.3 keV
W	$K_{\alpha 2}$	$K - L_2$	27	58.0 keV
W	$K_{\beta 1}$	$K - M_3$	10	67.2 keV
W	$K_{\beta 2}$	$K - N_2N_3$	4	69.1 keV
W	L_α	$L_3 - M$	11	8.4 keV

Table 6.1: Some X-rays from the de-excitation of shell electrons, from [195], with their Siegbahn designation, the corresponding electron transition, and the intensity for 100 primary vacancies in the K shell.

the high statistics calibration of figure 6.2, indeed all possible lines can be identified.

The detectors have mostly ultra pure copper around them. From this we get the copper fluorescence at the escape energy of a copper K electron, 8 keV, which is also visible in figure 6.2.

6.1.3 Coincident Events

During run 30, the detectors ZORA and VERENA were in immediate vicinity, see figure 6.3. Hence, the escaping X-rays from one detector had a good chance to hit the other one. The foil in between the detectors is only $70\mu m$ thick, and approximating its unknown attenuation coefficient (as being that of Mylar foil for which absorption data is available [244]), we can estimate the X-ray transmission through the two layers of foil as $I/I_0 \approx 1.00$ for $60 - 70$ keV X-rays and $I/I_0 \approx 0.81$ for 8 keV X-rays. Hence, we expect coincident events in the two detectors, where one detector sees the escape of energy, and the other this escaped energy quantum.

Indeed this is the case. Conveniently, both VERENA and ZORA happen to be read out by the same eight channel digitizer, so the correct timing of the events is trivial, since possible small differences between different digitizers do not have to be taken into account. Hence, to simply extract coincident events from the data, the fitted `onset channels` of the pulses are required to have a negligible time difference. This results in the events shown in figure 6.4.

Let us take some time to understand this plot. The largest population at the center of the scatter plot comes from 122 keV gammas that interact in VERENA, ejecting a tungsten $K_{\alpha 1}$ X-ray ($E = 59$ keV) from it, which in turn is absorbed in ZORA. Hence, in VERENA, we see the escape event at 122 keV − 59 keV = 63 keV and in ZORA the escaped X-ray at 59 keV. Other populations corresponding to the $K_{\alpha 2}$, $K_{\beta 1}$ and even $K_{\beta 2}$ X-rays can

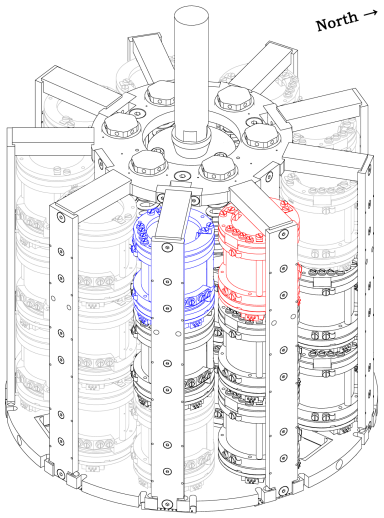

Figure 6.3: The position of Zora (blue) and Verena (red) during run 29 and 30. Modules drawn in black are other detectors that were not operational for a Dark Matter analysis. The positions in light gray were not filled with detectors but copper dummies.

easily be separated. They all lie on the solid diagonal line that marks a summed energy in both detectors of 122 keV. The events along this line are histogramed for clarity in figure 6.5. Fitting Gaussians with all parameters left free except the resolution which is required to be the same for all populations, one deduces an intensity according to table 6.2. Also in this table, the measured ratios are compared to ratios expected from the literature.

escape peak	energy	measured intensity	relative emittance
$K_{\alpha 2}$	58 keV	0.52 ± 0.02	0.583
$K_{\alpha 1}$	59 keV	1 (def.)	1.000
$K_{\beta 1}$	67 keV	0.39 ± 0.02	0.219
$K_{\beta 2}$	69 keV	0.14 ± 0.02	0.076

Table 6.2: A comparison of the relative measured intensities of the escape lines in figure 6.5 with the relative X-ray ratios per given K-shell vacancy from reference [195]. The possible effect of the reflective foil is less than 10^{-3} and can be neglected. Following the primary interaction, higher energy X-rays are more likely to escape the crystal. Hence the $K_{\alpha 2}$ is less abundant than expected naively, whereas the K_{β} events are more abundant.

Similar populations in figure 6.4 stem from impinging 136 keV gammas. They are simply shifted to the right by an energy of 136 keV − 122 keV = 14 keV, and lie on the line corresponding to a summed energy of 136 keV.

We have seen in figure 6.2 that the cobalt gamma lines have broad Compton shoulders toward lower energies. If such a gamma hits the crystal, it can of course lead to an escaping X-ray as well, so the populations men-

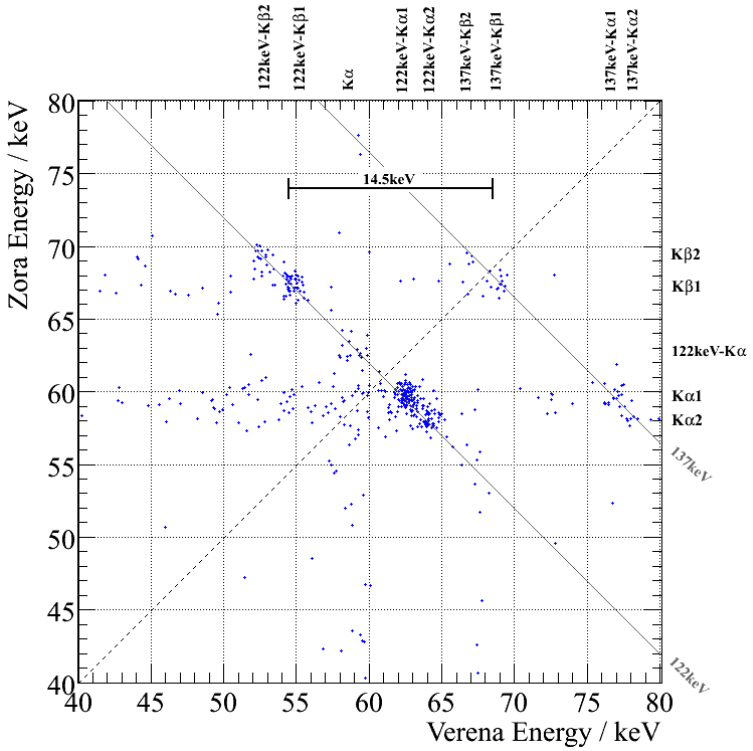

Figure 6.4: Events during the available ^{57}Co calibrations which are coincident in both VERENA and ZORA. Mainly, one recognizes events where the X-ray escapes from VERENA and is absorbed in ZORA (see text). The origins of various energies are labeled on the axes. The solid diagonal lines indicate a summed energy in both channels of 122 and 136 keV, hence originating from the ^{57}Co lines. The dashed angle bisector is only to guide the eye to the asymmetry of the distribution.

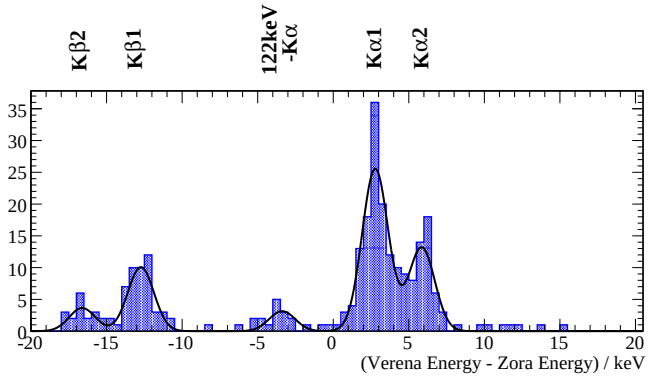

Figure 6.5: Projection of events within 2 keV along the line designated as "122 keV" in figure 6.4. Clearly the individual escape events from $K_{\alpha 1}$, $K_{\alpha 2}$, $K_{\beta 1}$ and even $K_{\beta 2}$ can be separated. Fitted are Gaussians with all parameters left free except the width which is required the same for all populations. On the top the corresponding energies of the events in ZORA are shown.

tioned above are smeared out toward lower energies in the detector with the primary interaction.

The process in which Zora emits an X-ray, which is then absorbed by Verena, is much rarer. This allows to deduce that Zora was closer to the cobalt source than Verena: If the interaction of a 122 keV gamma in Zora results in an X-ray, this can only be ejected from Zora in the half-space facing the source, since otherwise it would be absorbed by Zora itself. Hence if Zora is closer to the source than Verena, we will see less escaped X-rays from Zora in Verena.

On top of all this we can also see from figure 6.4 that the asymmetry between the two detectors is less pronounced for the populations from gammas which have interacted in the cold box before the first interaction in a crystal: The tail going down along the K_α energy of 59 keV in Verena is stronger than expected from the population where Zora sees exactly 122 keV − 59 keV. In light of what we have just discussed, this is easily appreciated, since gammas that are Compton scattered in the cylindrical thermal shielding have a broader angular distribution.

To finish the discussion of the ^{57}Co spectrum, we finally note that there is a line at 8 keV which is broader than expected from the energy resolution of the detectors, which is better than 400 eV (1σ) at this energy. This line comes from copper K_α (at 8.0 keV) and tungsten L_α (8.4 keV) X-rays. In the background data we will have a much cleaner probe of this energy range.

6.2 Background Spectra

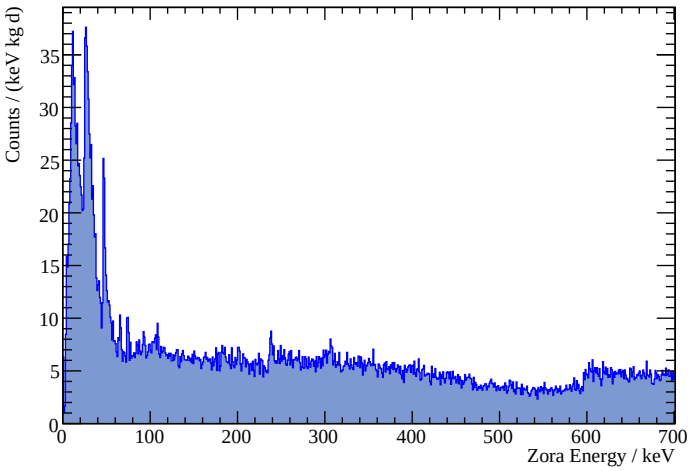

Figure 6.6: Spectrum recorded with Zora (m = 307.01 g) during run 30 with an exposure of 22.81 kg d to background radiation. The energy reconstruction is based on the truncated standard event fit, with the standard event from the 122 keV ^{57}Co line. Hence for this histogram the energies above 122 keV are only extrapolations, but good to 1% up to 600 keV, see section 6.2.9.

Figure 6.6 shows a spectrum recorded by detector ZORA during run 30 as a first example of a spectrum from exposure to background radiation alone. This remaining activity is mainly intrinsic to the crystals. On the one hand, this is a shortcoming of the employed crystals, but on the other hand, it allows to check the calibration of the detectors during exposure to background radiation down to lowest energies, as we will see shortly.

Generally, the spectra are rather featureless above $\approx 100\,\mathrm{keV}$. The broad background extending to $\approx 550\,\mathrm{keV}$ is conjectured to be due to a contamination of the crystals with strontium. Strontium belongs to the same chemical group as calcium and can easily be incorporated in the $CaWO_4$ crystals. ^{90}Sr is a well-known beta source with an endpoint of 546.2 keV and a half-life of 29 years, which can explain the general trend in the spectra. Crystals that have a reduced strontium content were grown and employed in the setup but not operational for this data taking period. Data from these crystals will clarify the significance of strontium to the background spectra. For other sources of background, the situation is clearer, and we will discuss them in the following.

6.2.1 Pb-210

Figure 6.7 shows a zoom on the spectrum of detector DAISY taken in run 27 with an exposure to background radiation of 12 kg d. The most prominent line appears at 46.5 keV and is attributed to a contamination with ^{210}Pb in the vicinity of the detector. ^{210}Pb is a step in the natural decay chain of ^{238}U after radon. It beta decays with a half-life of 22.3 years into ^{210}Bi, see the corresponding decay scheme in figure 6.8. Hence, if the vicinity of the detector was exposed to radon, this leads to the observed line.

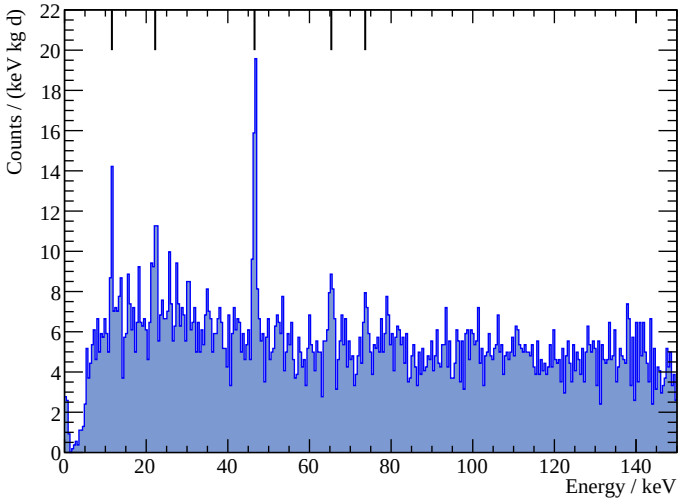

Figure 6.7: Spectrum of DAISY ($m = 306.77\,\mathrm{g}$) from an exposure to background radiation of 12.31 kg d during run 27.

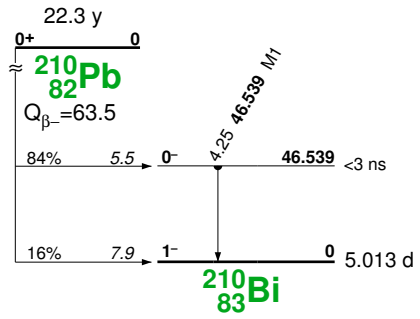

Figure 6.8: The beta decay of ^{210}Pb, from [195].

The activity is readily calculated from a Gaussian fit (over a linear background), yielding $(49 \pm 6)\,\mu$Bq (and a 1σ resolution of the detector at this energy of $(380 \pm 40)\,$eV). Run 27 took place late 2003. Back then, the reflective foil around the crystals was not scintillating. It was replaced by a VM2000 class foil early 2004, and a similar exposure was acquired during run 28. For Daisy, the spectrum obtained is shown in figure 6.9. The lead peak is still prominent, but with a reduced activity, now corresponding to an activity of $(31 \pm 5)\,\mu$Bq in the vicinity of the detectors.

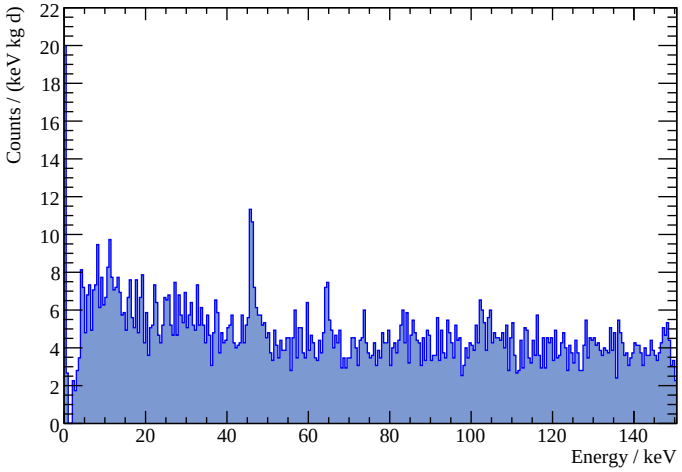

Figure 6.9: Spectrum of Daisy ($m = 306.77\,$g) from an exposure to background radiation of $15.00\,$kg d during run 28.

For Verena and Zora in run 30, the situation looks a bit different, and figures 6.10 and 6.11 show a zoom on the background spectra of these two detectors. Both show a rich structure in this energy range.

For the moment, let us focus on the ^{210}Pb feature at $46.5\,$keV. It is present in both crystals, but with a significant shoulder toward higher energies, in particular in Verena. This allows to deduce that in Verena, there is a significant contamination of ^{210}Pb *intrinsic* to the crystal: Not only do we see the energy of the $46.5\,$keV gamma, but in addition to it, we

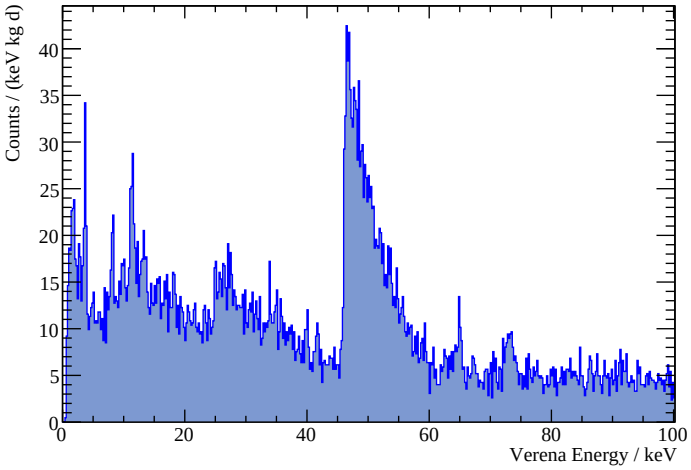

Figure 6.10: Background spectrum recorded with VERENA during an exposure of 21.20 kg d in run 30.

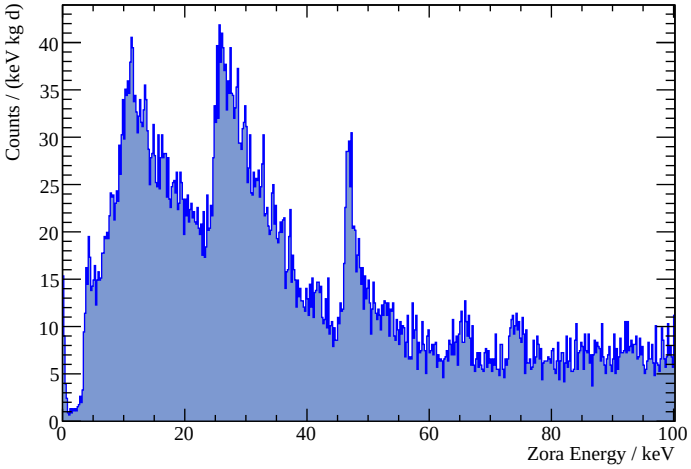

Figure 6.11: Also a background spectrum during run 30, but from detector ZORA, with a similar exposure of 22.81 kg d.

see the energy of the emitted electron from the beta decay. Since CRESST detectors are rather slow (rise time of the pulses is $\mathcal{O}(100\,\mu s)$), the two particles cannot be resolved, and the calorimetric measurement simply gives the summed energy of both particles. We therefore see the ^{210}Pb beta spectrum starting at 46.5 keV and extending up to the Q-value of the decay, 63.5 keV. The activity corresponds to $(672 \pm 28)\,\mu$Bq with the error being dominated by the background estimation. Since ^{210}Pb is part of the ^{238}U decay chain and uranium is known as contaminant in the crystals [245], the origin of this isotope is clear.

For Zora, the lead feature is less pronounced, and its shape may point to a combination of intrinsic and extrinsic contamination. Above background the cumulative rate from this contamination is $(241 \pm 25)\,\mu$Bq and hence about a third of that in Verena.

6.2.2 Ac-227

The two large features at energies below the lead feature in detector Zora (figure 6.11) can be recognized as being due to an internal contamination with a beta emitter. The energies very nicely match those from the ^{227}Ac decay which is shown in figure 6.12. This actinium isotope is a step in the natural decay chain of ^{235}U.

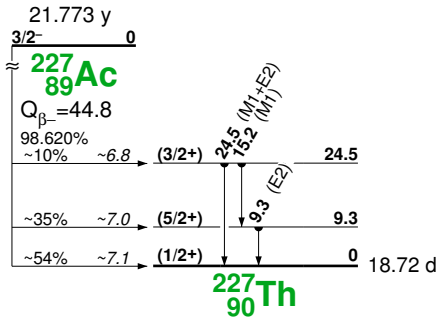

Figure 6.12: The level scheme of the ^{227}Ac decay, from [195].

According to the level diagram we would expect three dominant features in the spectra: One is a beta spectrum extending to the Q-value of the decay at 44.8 keV. In addition, we would expect a second beta spectrum starting at the energy of the first excited ^{227}Th state, namely 9.3 keV, and a third beta spectrum starting at the energy of the second excited daughter state, 24.5 keV. This perfectly matches the observed spectral features in both Zora and Verena. Since the decay time is 22 years and thus too long to wait for this background to disappear, this calls for the exclusive use of ultra pure chemicals for future crystal growth.

6.2.3 Pb-212

Most steps in the natural decay chains of ^{238}U, ^{235}U, and ^{232}Th are α-decays. They can be reconstructed as well [245], but the analysis is beyond the scope of this thesis. Yet another contamination from the natural decay chains is observable in the low energy ($\lesssim 0.5\,\mathrm{MeV}$) part of the spectra. Figure 6.6 on page 111 and figure 6.13 show this energy range, where a line at 238 keV is visible.

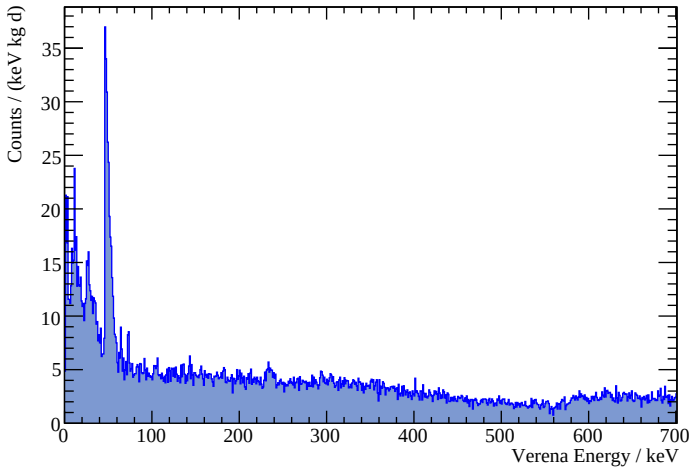

Figure 6.13: Spectrum of VERENA after an exposure of 21.20 kg d to background radiation during run 30. At low energies the ^{227}Ac features are visible, then the dominant ^{210}Pb feature above 46.5 keV and the ^{212}Pb line at 238.6 keV. The broad emission spectrum is conjectured to be due to ^{90}Sr up to $\approx 550\,\mathrm{keV}$ with a beta spectrum from ^{176}Lu (section 6.2.9) starting above.

This line can be attributed to the ^{212}Pb beta decay. ^{212}Pb is a step in the natural decay chain of ^{232}Th that decays within 11 h into ^{212}Bi following the decay scheme of figure 6.14. The activity seen in ZORA and VERENA from the ^{212}Pb contaminations in the vicinity of the detectors is readily calculated from a Gaussian fit above a linear background as $(37 \pm 6)\,\mu$Bq and $(93 \pm 2)\,\mu$Bq, respectively.

Contaminations outside the shielding of the experiment would lead to rates much more similar than observed. Therefore this source of contamination is probably within the cold box. However, then it is not clear what this source could be. One possibility is a Speer carbon resistor [246, 247] that was installed in the cold box for temperature measurements. It measures only a few mm^3 but is made from standard materials. Whether this really is a source of radioactivity will become clear with the data from run 31, where many detectors are taking data in a large variety of space angles to this thermometer.

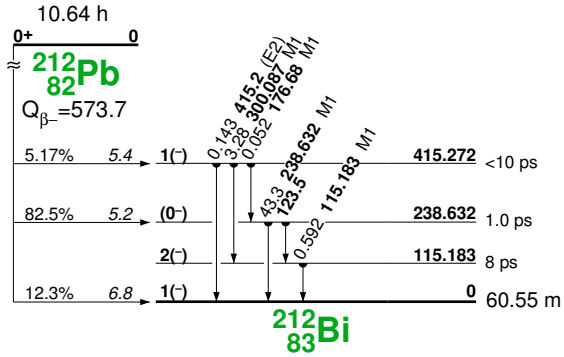

Figure 6.14: The level scheme of the ^{212}Pb beta decay, from [195]. Most decays will be accompanied by a 238.6 keV gamma which can readily be seen in the detectors.

6.2.4 Activated Tungsten

As discussed in section 4.1, exposure of materials to cosmic rays activates the material. This can result in long-lived isotopes which may decay during the low-background measurements. Having a look at the chart of nuclides, figure 6.15, one can search for relevant production and decay channels.

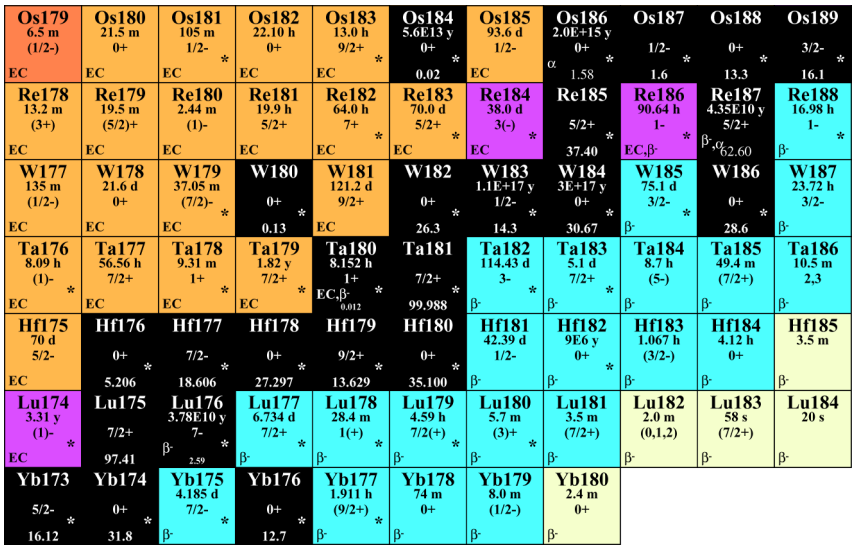

Figure 6.15: Excerpt of the chart of nuclides, from [195].

Neutron capture can result in ^{185}W, the decay of which yields a broad beta spectrum but no relevant gamma line. Neutron capture resulting in ^{187}W leads to a broad beta spectrum with a multitude of lines, but given the rather high background in the detectors these lines are not observable either.

Proton reactions on tungsten on the other hand do lead to observable decays. One is the (p, α) reaction on ^{182}W which results in ^{179}Ta [248, 249, 250]. This tantalum isotope will be present in the crystals from cosmogenic

activation either of the raw materials the crystals are grown from, or from activation of the crystals themselves. Since it decays with a half-life of two years into ^{179}Hf, this will remain a background in the measurement for quite some time. This decay is an electron-capture process, see figure 6.16. When a ^{179}Ta nucleus decays in the crystal, the energy of the decay will vanish with a neutrino. Subsequently we are left with a hafnium atom that lacks an electron in an inner shell. This void will be quickly filled in an electron cascade, and our calorimetric measurement will see the binding energy *of hafnium* for the captured electron. Mostly, a K-shell electron is converted, resulting in a total energy of 65.35 keV [195] that is seen in the detectors, see figures 6.10 and 6.11. The measured activity of this line for various detectors and runs is summarized in table 6.3.

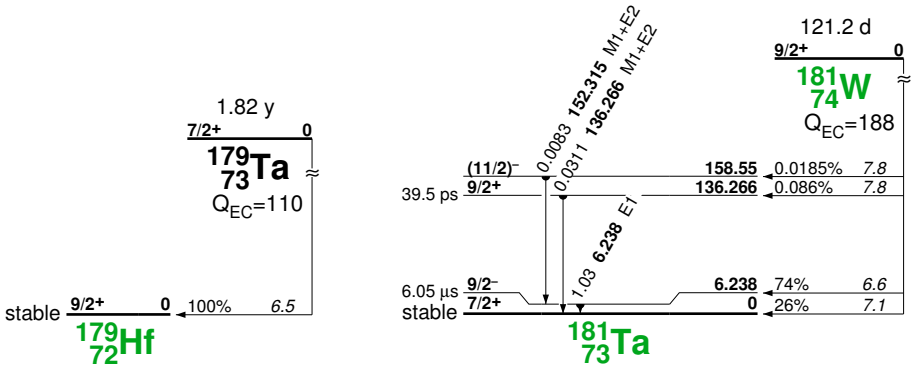

Figure 6.16: Level schema of the ^{179}Ta and ^{181}W electron capture processes, from [195]. While no gamma is associated with the ^{179}Ta capture process, most ^{181}W decays have a 6.2 keV gamma associated.

Origin	Detector, Run	Activity
^{179}Ta	DAISY, run 27	$(72 \pm 4)\,\mu$Bq
	DAISY, run 28	$(65 \pm 3)\,\mu$Bq
	VERENA, run 30	$(20 \pm 4)\,\mu$Bq
	ZORA, run 30	$(24 \pm 4)\,\mu$Bq
^{181}W	DAISY, run 27	$(12 \pm 4)\,\mu$Bq
	DAISY, run 28	$(5 \pm 3)\,\mu$Bq
	VERENA, run 30	$(25 \pm 4)\,\mu$Bq
	ZORA, run 30	$(33 \pm 5)\,\mu$Bq

Table 6.3: Overview over the activities of the two lines due to cosmogenic tungsten activation. DAISY was underground already for many months prior to run 27, so the ^{181}W line had time to decay already prior to the first measurement.

Another possible cosmogenic activation of tungsten goes through the reaction ^{183}W(p, t)^{181}W [251]. Hence ^{181}W is expected to be present in the crystals. It decays via electron capture with a half-life of about 4 months,

also shown in figure 6.16. However, in most cases this decay is accompanied by a 6 keV gamma, so the energy that will be seen in the crystals following a K-shell capture process is that of the K-shell binding energy of tantalum (67.4 keV [195]) plus that of the gamma (6.2 keV), namely 73.7 keV. Indeed there is a line at precisely this energy, see figures 6.10 and 6.11. This confirms the idea of cosmogenically activated tungsten.

The intensity of the line from the ^{181}W process should decrease with a half-life of 121 d. Only two data points with meaningful statistics could be extracted from run 27 and 28, collected over an exposure of a few weeks each. The data is as depicted in figure 6.17, indeed consistent with the expected half-lifes.

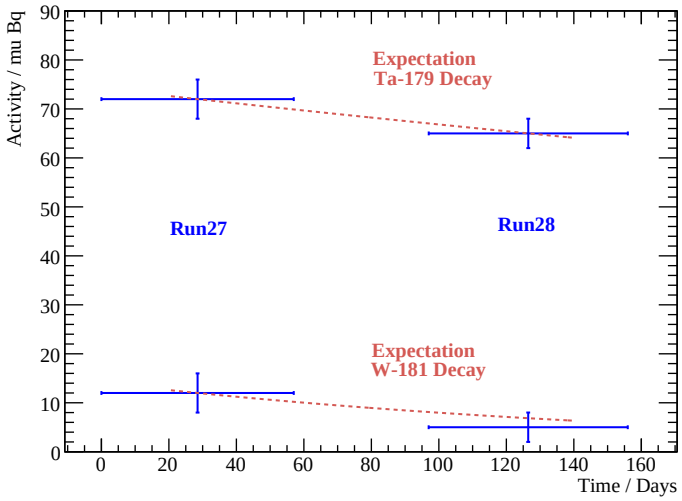

Figure 6.17: The two measurements of the ^{181}W and ^{179}Ta activity in Daisy during run 27 and run 28 are consistent with the expectation from a decay with $T_{1/2} = 121.2\,\mathrm{d}$ and $T_{1/2} = 665\,\mathrm{d}$, which are also drawn, normalized to the run 27 data points.

We can calculate the ratio of K-shell electron captures to **L-shell electron captures** for the two electron capture processes, following references [195] and [252]. This would result in lines at about 11 keV and 11 keV + 6 keV = 17 keV, and indeed there is a yet unidentified line observed at about 11 keV (section 6.2.8). As an example, consider the ratio of L1-shell captures λ_{L1} to K-shell captures λ_{K} in the ^{179}Ta decay. If energies are expressed in terms of the electron rest mass, for the case considered here, this ratio is given by

$$\frac{\lambda_{\mathrm{L1}}}{\lambda_{\mathrm{K}}} = \frac{\Big((Q_\epsilon - E_{\mathrm{level}}) + (1 - |E_{\mathrm{binding}}|_{\mathrm{L1}})\Big)^2 \beta'_{\mathrm{L1}}}{\Big((Q_\epsilon - E_{\mathrm{level}}) + (1 - |E_{\mathrm{binding}}|_{\mathrm{K}})\Big)^2 \beta'_{\mathrm{K}}} \tag{6.1}$$

where Q_ϵ is the electron-capture decay energy (the Q-value), E_{level} is the energy of the level populated in the daughter nucleus, E_{binding} is the electron

binding energy in the parent atom, and β_i' are values tabulated in the references given. One can calculate this ratio for all the available combinations and obtains that for 100 K-shell captures in the ^{179}Ta decay there are 18.8 L-shell captures, with higher order captures being negligible.

It was however not possible to identify these lines consistently at the corresponding energies, and with the corresponding activities. This is simply due to the rather high electron recoil background at these low energies. As an example, figure 6.18 shows the low energy spectrum of VERENA. Given the activity of the activated tungsten inferred above, we would expect only one L-shell capture per kg d, a vanishing small signal in the spectrum of figure 6.18.

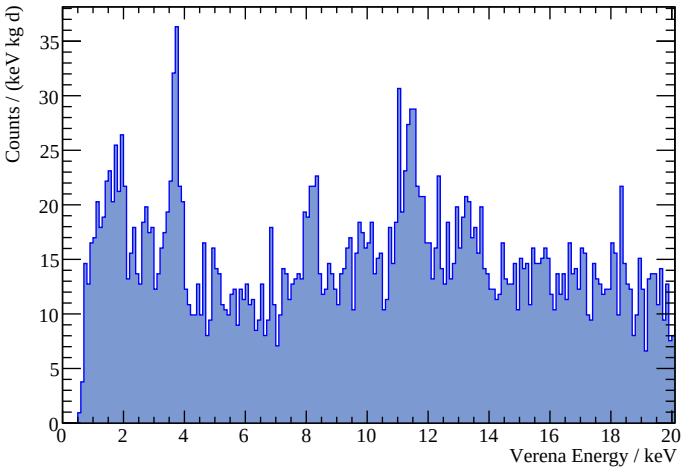

Figure 6.18: Spectrum of detector VERENA with an exposure of 21.20 kg d. The ^{227}Ac beta spectrum starting at ≈ 9 keV can be seen as well as lines at 3.7, 8, and 11.5 keV.

6.2.5 Ca-41

^{41}Ca can be produced by thermal neutron capture of ^{40}Ca [195]. It has a half-life of 10^5 years and decays via electron-capture in ^{41}K, see figure 6.19. In our detectors, this decay will deposit the K shell binding energy of potassium of $E = 3.61$ keV. It is a challenge to detect such low energies in a massive detector, but with CRESST detectors, this challenge can be met! Figure 6.18 shows a zoom to the low energy region of the spectrum of detector VERENA during run 30.

The lowest line that can be identified is at (3.71 ± 0.02) keV with a resolution at this energy of (0.13 ± 0.02) keV (1σ) and an intensity of $(25.9 \pm 0.4)\mu Bq$ (corresponding to 155 ± 24 counts). This is only 100 eV or 3% above the expected 3.61 keV, giving an independent confirmation of the energy calibration (section 5.4.2) down to lowest energies.

The activity of this line allows to calculate the number N_0 of ^{41}Ca atoms

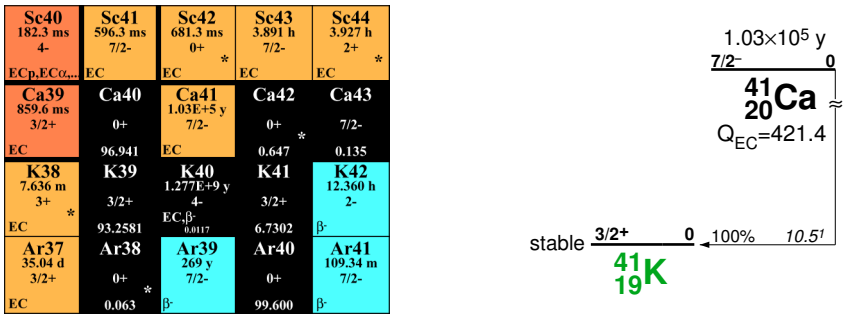

Figure 6.19: Excerpt of the chart of nuclides, and the level diagram of the ^{41}Ca decay, from [195].

in the crystal. Using standard notation we have:

$$\begin{aligned} N(t) &= N_0\, 2^{-t/T_{1/2}} \\ \Delta N &= N_0 \left(1 - 2^{-t_{\text{live}}/T_{1/2}}\right) = 1.10 \times 10^{-6} N_0 \stackrel{!}{=} 155 \\ \Rightarrow N_0 &= 1.41 \times 10^{8}. \end{aligned} \tag{6.2}$$

$CaWO_4$ has a molecular weight of $(40.078 + 183.84 + 4 \times 16)\,\text{g/mol} = 287.9\,\text{g/mol}$. Verena weights 305.49 g, so we have $1.06\,\text{mol} = 6.4 \times 10^{23}$ atoms of calcium in the crystal. Hence only every $1.4 \times 10^8 / 6.4 \times 10^{23} = 2.2 \times 10^{-16}$th calcium atom is ^{41}Ca. They decay with a half-life of 10^5 years and still they are readily visible as a line in the spectrum, demonstrating the extreme sensitivity of the CRESST experiment.

6.2.6 Ca-45

The ^{44}Ca isotope is naturally abundant to 2%. Neutron capture would lead to ^{45}Ca, which beta-decays into ^{45}Sc with a Q-value of 257 keV, and in 2×10^{-3}% of the cases ends in a metastable excited state of ^{45}Sc. This state has a long half-life of 318 ms and de-excites under emission of a 12.4 keV gamma. One can look for events that match this pattern, and a search was performed for run 30, but no significant amount of this rare ^{45}Ca/^{45}Sc* process could be identified.

6.2.7 Copper Fluorescence

Another feature in the low energy spectrum of Verena, figure 6.18, is visible at (8.17±0.04) keV, and we can attribute this peak to **copper fluorescence**. If the copper, abundant in the vicinity of the detectors, is hit by gamma rays, we can expect to see the K_α-escape line at 8.04 keV. Again, the energy calibration puts the line only 100 eV or 2% too high. The corresponding activity in the line is $(15 \pm 3)\,\mu$Bq, and the resolution of Verena at these energies is (0.17±0.04) keV (1σ). Copper K_β is only expected with a fraction of 12% and not visible above background.

6.2.8 11.5 keV

All detectors show a line at 11.5 keV which could not be attributed in a consistent way to a decay. Possible candidates are X-rays with the binding energy of an arsenic K-shell electron, or from L-shell electrons of hafnium or tantalum (but see the discussion in section 6.2.4). If the feature is due to an escape line, a possible candidate is bromine which gives K_α X-rays at 11.92 keV and K_β X-rays at 11.88 keV. Tungsten has L_γ escape lines at these energies, but then $L_{\alpha,\beta}$ lines at 8.4 keV and 9.9 keV should be more abundant by an order of magnitude. Finally, if the energy originally available is too low to excite a K-shell electron, radon is a possible candidate also, with an energy of 11.7 keV for $L_{\alpha 1}$ escape X-rays. It is however very unclear where such contaminations should come from. A search was also performed for primordial radioisotopes, as well as decays in which a combination of two energies adds up to the observed 11.5 keV, both with negative outcome. Table 6.4 shows the measured activities of this line for the different detectors and runs.

Detector, Run	Energy	Activity
DAISY, run 27	(11.59 ± 0.07) keV	$(18 \pm 4)\,\mu$Bq
DAISY, run 28	(11.1 ± 0.2) keV	$(26 \pm 7)\,\mu$Bq
VERENA, run 30	$(11.41 \pm 0.05_{\text{stat}} - 0.1_{\text{sys}})$ keV	$(74 \pm 11)\,\mu$Bq
ZORA, run 30		$< 9\,\mu$Bq

Table 6.4: Overview over the activities of the 11.5 keV line of unidentified origin. For ZORA, the ^{227}Ac background is too strong to positively identify a line at this particular energy. For Verena, there is a systematic effect of 100 eV in the energy calibration, see the previous sections.

6.2.9 Lu-176

ZORA's background spectrum of figure 6.6 on page 111 shows a small feature at ≈ 300 keV, which we take as starting point for another analysis of the spectra. A line at this energy can only come from an internal conversion process, or from a decay outside the crystal — otherwise one would see e.g. a broadened line such as the ^{210}Pb line.

The origin of this line can only be found when events are investigated that are coincident in both detectors; We have already seen in section 6.1.3 that this can be a powerful way of learning about physics in the detectors. To extract these coincident events, an additional requirement to the pulses is that there are pulses in both detectors at the same time (technically done by a Boolean `AND` operation on the `event list` of VERENA and ZORA). This requirement will keep random coincidences like the one in figure 6.20 (left), i.e. pulses in both detector modules which happen to be less than half a post-trigger region ($1/2 \times 3/4 \times 4096$ channels $\times\, 40\,\mu$s/channel $= 61.44$ ms) apart. These events have to be cut as well. Since both detectors are read

out by the same digitizer, this is simply done requiring the difference of the `shift`s of the standard event fits to be less than 1 ms, see figure 6.20 (right).

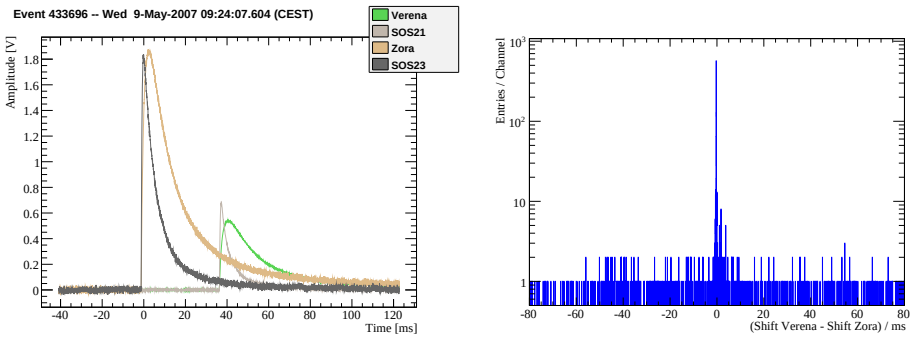

Figure 6.20: Left: Two events that are coincident in both the detector modules of Verena and Zora, although most likely not related to each other. After the first trigger (here from Zora), Verena, being read out by the same digitizer, is allowed to trigger as well for up to half the post-trigger region (here at 61.44 ms). Right: To retain only true coincidences, a cut on the difference of the `shift` parameter of the standard event fit, requiring $|\Delta t| < 1\,\text{ms}$, is done. Note the faint shoulder to the right of the coincidence peak which might hint at a decay with some time constant of $\mathcal{O}(\text{ms})$; however the statistics is too low to draw any conclusions on this particular issue.

The spectrum of such truly coincident events, shown in figure 6.21, looks very different from the individual spectra of the detectors. Indeed the line at 307 keV is now very prominent, with an additional line at 202 keV appearing, which helps a lot to identify the origin [253]. In addition, one can now easily recognize the tungsten K_α escape peak at 59 keV. We have seen this class of escape events already discussing the cobalt calibration, section 6.1.

The 307 keV and 202 keV lines together allow to identify their origin as being due to lutetium. Lutetium is a rare earth and as such common in scintillators such as LSO, LPS and others [254]. It has never been seen in CRESST crystals before, but since the crystal pullers that grow our $CaWO_4$ crystals also grow scintillating crystals containing lutetium, one can well imagine where such a contamination might come from.

^{176}Lu is a primordial isotope with an natural abundance of 2.6% [203] that beta decays with a half-life of 10^{10} years, following the level scheme of figure 6.22. When ^{176}Lu beta decays, it mostly emits an electron that follows a beta spectrum between $\approx 0\,\text{keV}$ and $E_{\text{e,max}} = 1191.7\,\text{keV} - 596.8\,\text{keV} = 594.9\,\text{keV}$. This results in an excited state of ^{176}Hf which will de-excite in a cascade of gamma transitions. If the lutetium contamination is intrinsic to the crystals, then, from most of these decays, we will see the full energy of the excited ^{176}Hf atom, 597 keV, plus the energy of the electron, and hence a beta spectrum starting at 597 keV in one of the detectors. Indeed this can be seen in figure 6.6 on page 111, although not fully reconstructed by the standard event fit.

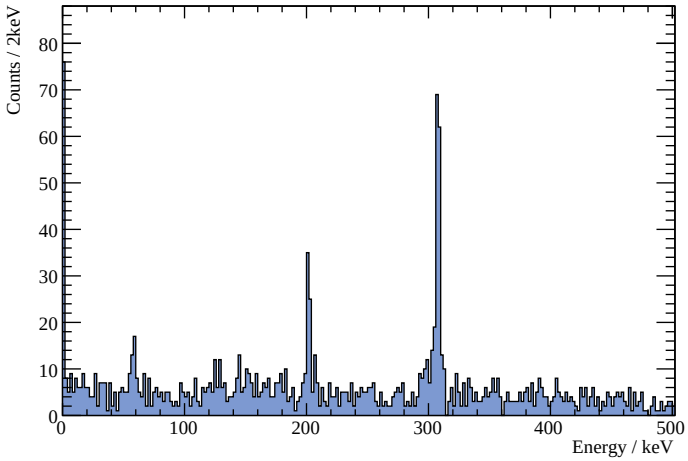

Figure 6.21: Spectrum of coincident events. To increase the statistics, the spectra of VERENA and ZORA have been added together. Clearly visible are lines at 307 keV, 202 keV and 59 keV as well as a smaller feature just to the left of the 307 keV line. Without the coincidence requirement, the added spectra have a count rate two orders of magnitude above the background shown here (i.e. $\mathcal{O}(500)$ counts per 2 keV bin).

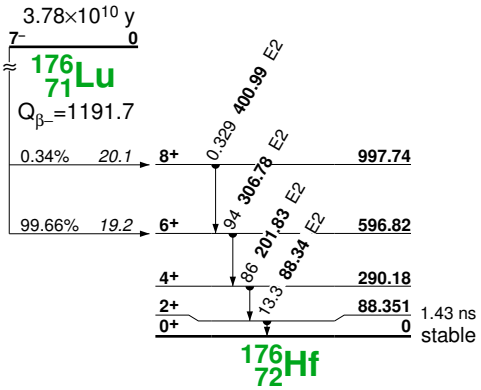

Figure 6.22: Level scheme of the ^{176}Lu beta decay, from [195].

If the lutetium decay happens not too deeply within the crystal, one of the gammas may escape the crystal and has a chance of hitting the neighboring detector. The absorption length of calcium tungstate at $\approx 300\,\mathrm{keV}$ is $d_{1/e} \approx 1\,\mathrm{cm}$ (see appendix D), but drops to $\approx 1/2\,\mathrm{mm}$ at $\approx 90\,\mathrm{keV}$. Hence for an assumed homogeneous contamination of lutetium in the crystals there is a fair chance for the high energy gammas to escape, but we do not expect to see an escaping 88 keV gamma.

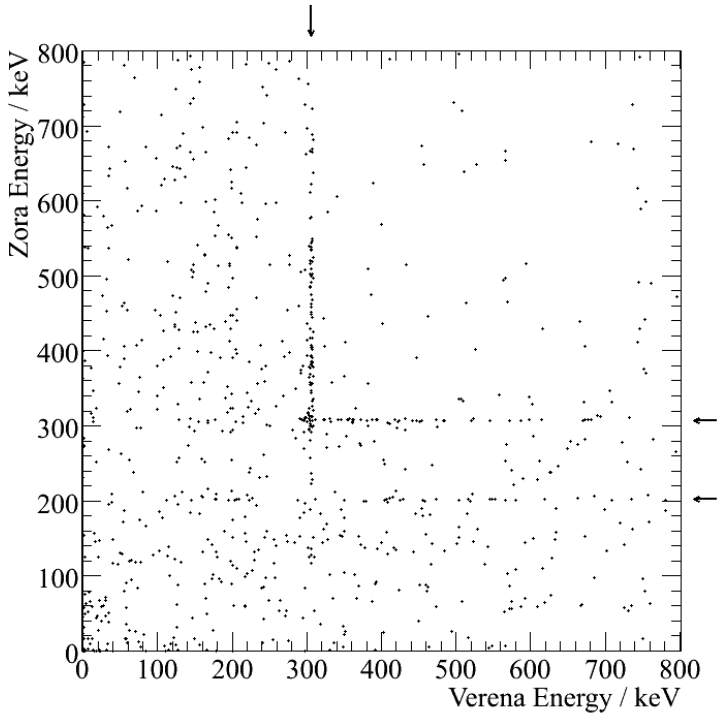

Figure 6.23: Scatter plot of the energies of coincident events in Verena and Zora. The two lines going up and to the right from ($\approx 300\,\mathrm{keV}$| $\approx 300\,\mathrm{keV}$) immediately catch the eye. Another horizontal line at 200 keV in Zora is also visible. See text for details.

Figure 6.23 shows the energy distribution of the events in the two detectors. Clearly visible in the figure are two lines that emerge from about 300 keV and extending to higher energies in one of the detectors. To discuss these lines in an example, consider the horizontal line at an energy of 307 keV in Zora. In the light of the above discussion, this is easily recognized as being a ^{176}Lu that decays in Verena, with the 307 keV gamma escaping and hitting Zora. Hence in Zora we see precisely this escaped energy, but in Verena, we see the two remaining gammas plus the electron, giving a beta spectrum that is offset by $202\,\mathrm{keV} + 88\,\mathrm{keV} = 290\,\mathrm{keV}$ and extends up to energies of $Q - E_\gamma = 1192\,\mathrm{keV} - 597\,\mathrm{keV} = 595\,\mathrm{keV}$. Of course the same argument holds the other way round, where the contamination is intrinsic to Zora. Figure 6.24 is a histogram of these events, nicely matching the expectations.

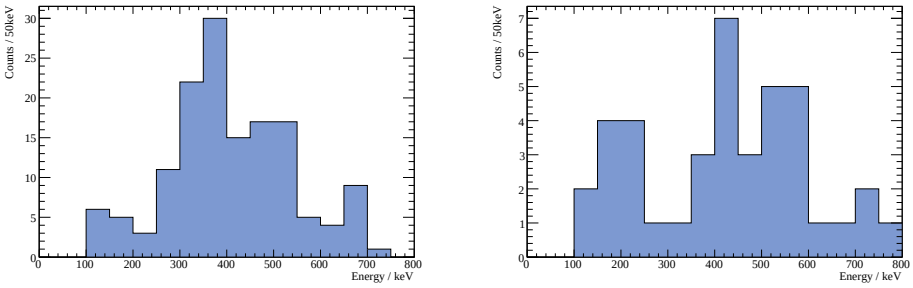

Figure 6.24: Left: Histogram of all coincident events in one detector that appear at (307±3) keV in the respective other detector: The ^{176}Lu beta spectrum starting at 290 keV is clearly visible despite the low statistics. Right: For an escaping 202 keV gamma the statistics are meager, nevertheless, this histogram shows events in VERENA that have a (202 ± 2) keV coincidence in ZORA.

In addition, if the 202 keV gamma escapes VERENA and hits ZORA, we expect to see in VERENA a beta spectrum between 307 keV + 88 keV = 395 keV and $Q - E_\gamma = 595$ keV. Figure 6.24 also shows a histogram of these events. Other combinations of escaping gammas are of course possible, but not significant given the available exposure.

Chapter 7

Quenching

Intent: The amount of light produced by different particles is the basis for the active background discrimination in the CRESST experiment. Here, the amount of light that can be expected from WIMP induced tungsten recoils is discussed. In addition, two effects were newly observed and are described here: One concerns a position dependence of the light output owing to the cylindrical shape of our crystals. A second, more subtle effect concerns a different light output from electron events with respect to gamma events.

Organization: In section 7.1 results are presented from different experiments measuring the light output anticipated for tungsten recoils. The newly observed position dependence of the light output is presented in section 7.2. In addition, there is a scintillator non-proportionality, which is discussed in section 7.3, with the consequences for gamma and electron events presented in section 7.4.

7.1 Quenching

7.1.1 Quenching of Various Nuclei

Active background discrimination in CRESST-II is based on the observed difference in the light yield produced by various impinging particles. To come to a quantitative description, we define the **quenching factor** Q for a particle species as

$$Q := \frac{\text{light signal from electrons of energy } E}{\text{light signal from particles with energy } E}. \tag{7.1}$$

Note that in the literature one also finds the inverse of this definition, which is simply the **light yield** if electrons have a light yield of unity. This is the case here, given our energy calibration of the light channel in terms of keV_{ee} (section 5.4.4).

Precise knowledge of the quenching factor for WIMP induced tungsten recoils is a prerequisite for the discrimination approach. The CRESST collaboration has put and still is putting much effort in the determination of this parameter.

One possibility to measure this value is of course to use the usual cryogenic setup with superconducting thermometers for both energy and light determination [255, 256]. However, the observed nuclear recoils induced by common neutron sources are dominantly oxygen recoils, and to a lesser degree, calcium recoils. Tungsten recoils become dominant only well below 10 keV due to simple two-body kinematics. Hence these methods cannot be used to find the quenching of tungsten recoils.

An alternative approach uses neutron scattering on a $CaWO_4$ target at room temperature [257, 258, 259]. The crystal is irradiated with neutrons of known energy from an accelerator, and the scintillation light is measured with a photomultiplier. The angle and the time of flight of the scattered neutrons are recorded. Hence the kinematics is fixed, and the energy transfer can be determined. This allows to identify which nucleus scattered, and hence derive the quenching factors for nuclei present in the crystal. However, above threshold, tungsten recoils are so rare and dark that only a limit on their light yield could be given.

Experiments combining both above variants are under way [260, 261]. Measuring the recoil energy via the cryogenic phonon detector as well as the angle of scattered neutron and the time-of-flight gives redundant information which will help to reduce systematic effects. The measurement at cryogenic temperatures makes an adoption of such results independent of the assumption of temperature independence. Despite promising first results [262], no estimates for the light yield of tungsten were available at the time of writing.

Finally, a third way to measure the quenching of various recoiling nuclei uses a mass spectrometer. Starting point for this method is the understanding that the scintillation light is not caused by the incident gamma, neutron, or WIMP, but by the recoiling nucleus. Hence different ions can be accelerated onto the $CaWO_4$ target. The only difference between such external nuclei and nuclear recoils is due to the binding energy of an atom within the crystal, but since this is of the order of eV, it can safely be neglected when dealing with keV nuclei. Hence, in the absence of surface effects, the light output of such a bombardment will just be the same as if the nucleus recoiled following a particle interaction.

This method has the major advantage that a large variety of different nuclei can be studied. In addition, the energy of the impinging nucleus can be freely adjusted in the range of interest. Measurements were done using a $5 \times 5 \times 5\,mm^3$ cubic $CaWO_4$ crystal at room temperature, and the scintillation light was read out with a photomultiplier [236, 263, 264].

Figure 7.1 shows the quenching factor Q for various recoiling nuclei, measured at different temperatures and using the above independent methods [265]. Two additional points from in situ measurements are shown in the graph. One comes from alpha events observed following decays of contaminations in the crystals [245]. This directly gives the quenching factor for recoiling helium nuclei. Another point comes from a background of impinging lead nuclei [233], which is discussed further in section 9.8.

A general trend is observable which can also be understood theoretically [265]. To summarize, we can expect alpha particles to have $Q = 5.7 \pm 0.01$, oxygen recoils $Q = 9.7 \pm 1.7$ and tungsten recoils at $Q = 40.1 \pm 2.7$.

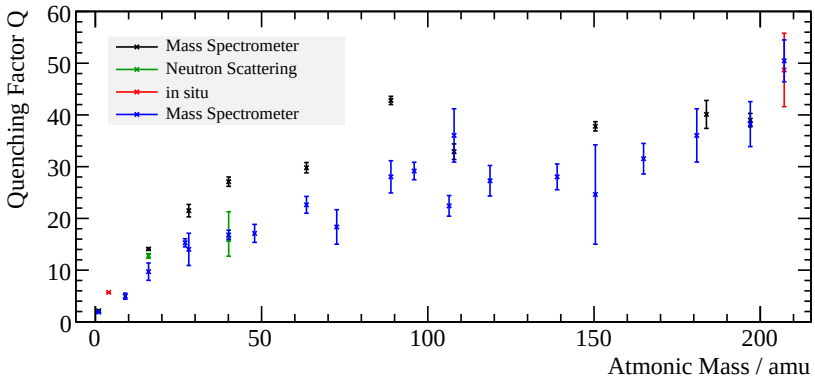

Figure 7.1: Assembly of various measurements of the quenching factor for different recoiling nuclei. In black measurements using the mass spectrometer technique at room temperature, where the error bars are only errors from a fit [263]. In blue refined measurements with the mass spectrometer technique at room temperature, also using a refined error estimation [264]. Green are measurements using neutron scattering at room temperature [257]. Red are points derived from in situ measurements at cryogenic temperatures [245, 233]. Tungsten is at $A = 184$.

7.1.2 Linearity

At energies above $\approx 100\,\mathrm{keV}$, the linearity of the light output of $CaWO_4$ crystals with energy is well established, see e.g. [236, 245, 266, 267]. Figure 7.2 shows one such measurement at room temperature with a standard crystal as they are used in the Gran Sasso setup. No deviations from a linear behavior can be found in this energy range.

7.2 Position Dependence

A dependence of the **scintillation efficiency** in a $CaWO_4$ crystal on the position of the interaction is not expected, since this efficiency only depends on the stoichiometry of the crystal (including the distribution of contaminations), which can be made very homogeneously. However, the **light collection efficiency** can very well depend on the position, as was already discussed in section 4.3.3. From simulations of cylindrical crystals as used in CRESST [230, 268], one would expect a position dependence, with decreasing light yield from events at high radial positions. This effect was however not observed previously [267].

To calibrate the detectors prior to the upgrade (run 28 and before), the lead and copper shield had a removable plug which was used to position

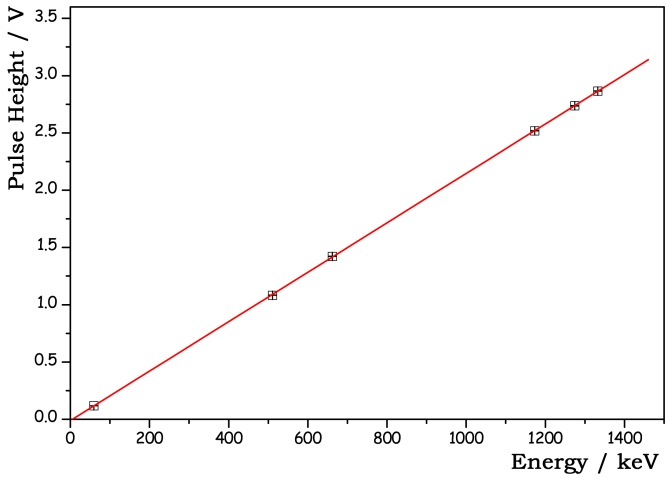

Figure 7.2: Linearity of the scintillation response of reference crystal BORIS ($CaWO_4$ crystal with standard dimensions), measured at room temperature with a photomultiplier setup. Figure taken from [236].

the source below the cold box. Hence the radiation hit the crystals from below, on the plane surface of the cylindrical crystals. After the upgrade, calibration sources are brought into the shielding by means of a plastic hose, which spirals through the shielding and around the cold box. Hence the radiation impinges on the cylindrical surface of the crystals. Since 122 keV gammas penetrate only the first few millimeters of a $CaWO_4$ crystal (see appendix D), a possible geometrical effect on the light collection efficiency may well be seen in this case.

Figure 7.3 shows such an effect. Presented are data from runs 28 and 31, both from the background run, where the events are mostly from radioactive contaminations intrinsic to the crystal, and overlaid with data from cobalt calibrations, where the events are confined to the first few millimeters of the crystal surface. One can see clearly that the calibration on the cylindrical surface yields less light than that on the flat face. Fitting first order polynomials through the origin, the slope is derived as given in table 7.1. The light yield of 122 keV gammas impinging on the cylindrical side is reduced by almost 20% of that of gammas impinging on the flat surface.

data set	slope	relative to background
run 28, calibration	1.016 keV_{ee}/keV	1.008
run 28, background	1.008 keV_{ee}/keV	1.000
run 31, calibration	1.001 keV_{ee}/keV	0.805
run 31, background	1.244 keV_{ee}/keV	1.000

Table 7.1: The fit of a linear function through zero to the data in figure 7.3 gives this slope. Errors of the fit are smaller than the stated precision.

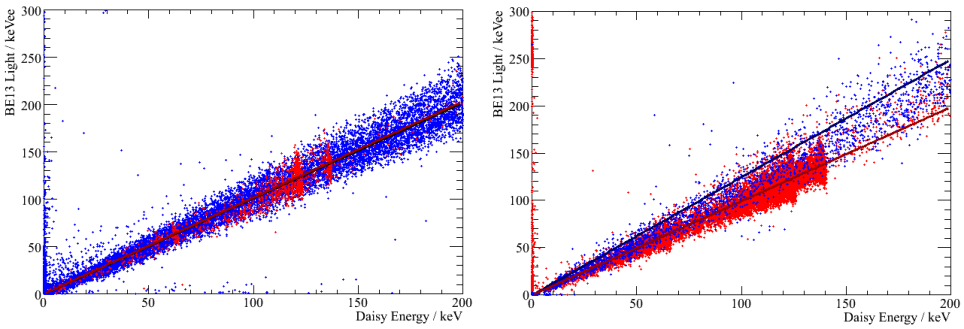

Figure 7.3: Data from detector module Daisy/BE13 from run 28 (left) and run 31 (right). Background data, mostly intrinsic in nature, is shown in blue together with a linear fit through zero in dark blue. Calibration data from a ^{57}Co source, interacting close to the surface, is shown in red together with the linear fit in dark red. In run 28, the source was placed below the cylindrical crystal and the two fitted lines almost coincide. In run 31, the source irradiates the side of the crystal, which results in a significantly reduced light yield.

Given the high statistics calibration available in run 31, a proof of the position dependence of the light output, even simpler and more clear, can be made. Figure 7.4 shows the data from 47.8 live hours of ^{57}Co calibration. The gamma lines at 122 keV and 136 keV can be seen as well as high energy lines at 570 keV and 692 keV (the decay scheme of ^{57}Co is given on page 106; other lines are present as well). Above 136 keV, the background contributes significantly, namely about 3 counts keV^{-1} kg^{-1} d^{-1} to the total rate of about 8 counts keV^{-1} kg^{-1} d^{-1}; the rest can be expected to be events from Compton scattering of the higher energy lines.

Two linear functions through the origin are fitted to this data set: One fitted in the energy range $[0, 140]$ keV has a slope of 0.988 keV$_{ee}$/keV, the other is fitted in $[150, 550]$ keV and has a slope of 1.115 keV$_{ee}$/keV. Hence it is clear again that gamma interactions close to the surface yield less light than events in the bulk of the crystal.

At even higher energies, events from the cobalt source become less and less important, and eventually, above 700 keV, all events are from background alone. At this stage, one should keep in mind that the energy reconstruction relies on the truncated standard event fit, with a truncation at 170 keV for Daisy and 240 keV$_{ee}$ for BE13 in this case. Hence we may expect inaccuracies to show up at the level of a few percent. Fitting a line through the origin in the energy interval $[710, 850]$ keV yields a slope of 1.186 keV$_{ee}$/keV which comes very close to the slope measured in the background data alone, but at lower energies (table 7.1).

The absorption length for 700 keV gammas is already 1.6 cm. Hence the interactions of such gammas will be distributed roughly uniformly in the crystal, at least in radius. Therefore this high energy line is not reduced in light yield but centered in the electron/gamma band, rounding off a coherent

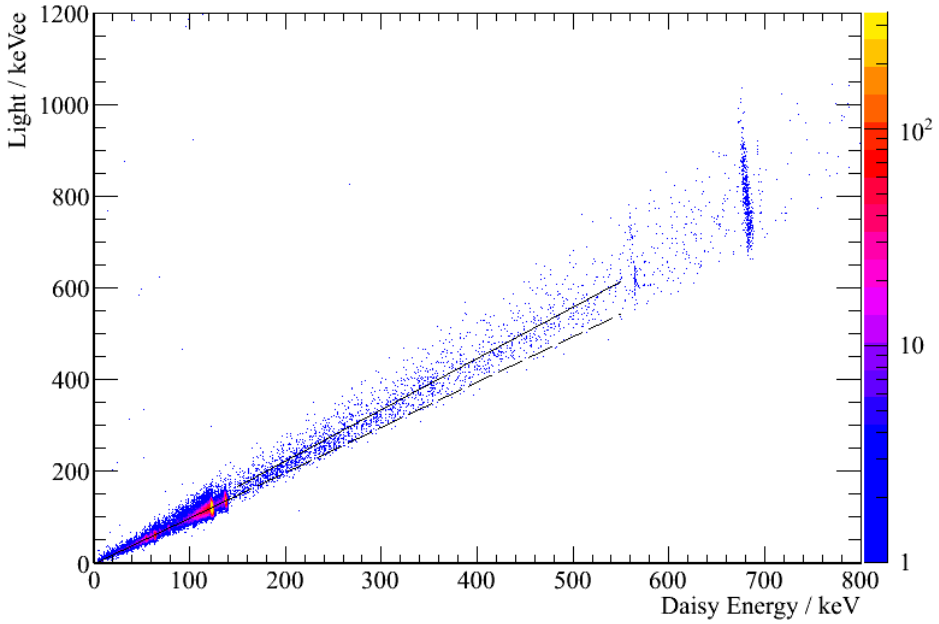

Figure 7.4: Data from a long ^{57}Co calibration of detector module DAISY/BE13 in run 31. Events from the cobalt source are dominant below 140 keV. Above that value, the events can be seen to be distributed in a broader band, and with a steeper slope.

picture of position dependence in cylindrical $CaWO_4$ crystals.

This position dependence has a strong effect of the resolution of the light channel. To give an example, consider the light detector SOS23 during run 30 at an energy of 122 keV. The resolution at this energy during the cobalt calibration is $(9.1 \pm 0.3)\%$ (1σ). During the background run however this worsens to (12.5 ± 0.7) since all radii of the crystal are probed equally. Cubic crystals could minimize this effect, but are difficult to implement given the current design of the carousel and the detector module holders (sections 4.2.3 and 4.3.5).

7.3 Scintillator Non-Proportionality

7.3.1 The Model of Rooney and Valentine

So far we have considered gamma and electron events to have the same light yield. But this need not necessarily be the case. Early works in the 1950s already hinted at a reduced light yield for gammas with respect to electrons in $CaWO_4$ but were somewhat inconclusive [269]. Today, a different quenching for electrons and gammas is established for some materials, see the review [270]. However, specifically for $CaWO_4$, the situation is less clear.

A possible difference in the light yield of electrons and gammas can be explained by the model of Rooney and Valentine [271]. Suppose a scintillator has a light yield as sketched in figure 7.5. An electron of a given energy E will simply produce the amount of light according to this light yield function. On the other hand, a gamma impinging on the crystal cannot directly produce scintillation light. Instead, it needs to interact first, via the photoelectric effect at the energies of interest. But all the available electrons are bound, so the scattered electron has less energy than the original gamma. The remaining energy is carried away either by Auger electrons, or by X-rays, in which case further electrons with even less energy can be produced. Eventually, a gamma event results in a distribution of electrons. Each will produce scintillation light according to the light yield function, but if this is not constant in energy, this will result in less scintillation light following the gamma interaction.

In addition, one also expects the *shapes* of the light yield functions to differ for electrons and gammas. Whereas the electron response should be monotonic, the gamma response should show a structure at energies where a transition in the scintillator becomes available as a channel to produce more X-rays or Auger-electrons. Figure 7.6 shows a particularly nice example for the scintillator LSO.

7.3.2 Observed Non-Proportionality

A scintillation non-proportionality of small $CaWO_4$ crystals has been demonstrated in dedicated experiments [266], but was so far not shown to exist in the data taken with the large crystals. To measure this effect in

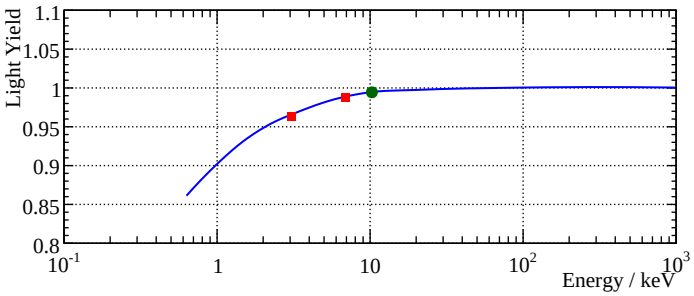

Figure 7.5: Sketch of scintillator non-proportionality. Electrons of a given energy produce the amount of light as indicated (blue line and green circle for a 10 keV electron). Gammas of the same energy first need to interact and produce electrons, which will have less energy than the original gamma (for example, resulting in two electrons as indicated by the red squares). Since the light yield is not proportional of energy, this results in a different quenching for electron and gamma events.

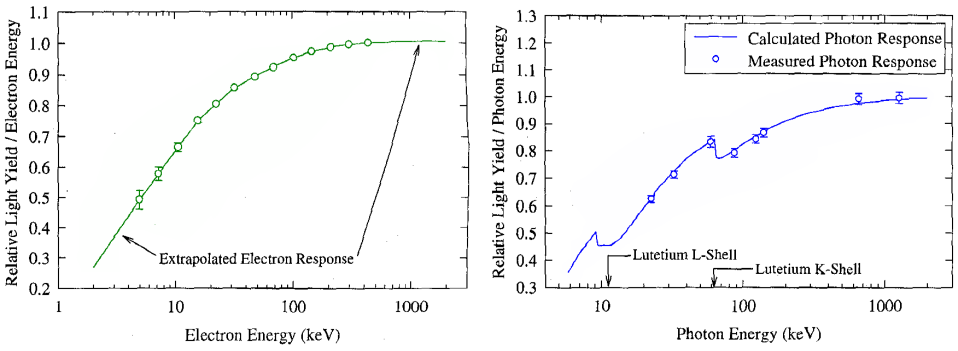

Figure 7.6: Left: The electron response of LSO(Ce) both measured (circles) and extrapolated in an empirical fit. Right: Measured photon response of the same crystal (circles) together with the prediction from the model of Rooney and Valentine. The gamma response shows jumps at energies of electron transitions. From [271].

the data from Gran Sasso, the difficulty arises in disentangling a possible non-proportionality from the position dependence, which seems difficult or even impossible as long as the events that constitute the spectrum are not known precisely. In addition, high counting statistics are required down to the lowest energy bins. In light of these uncertainties, the data is simply presented in figure 7.7 without an interpretation as being due to one or the other effect; most likely, it is a combination of both. Clearly, there is a strong scintillator non-proportionality toward lowest energies.

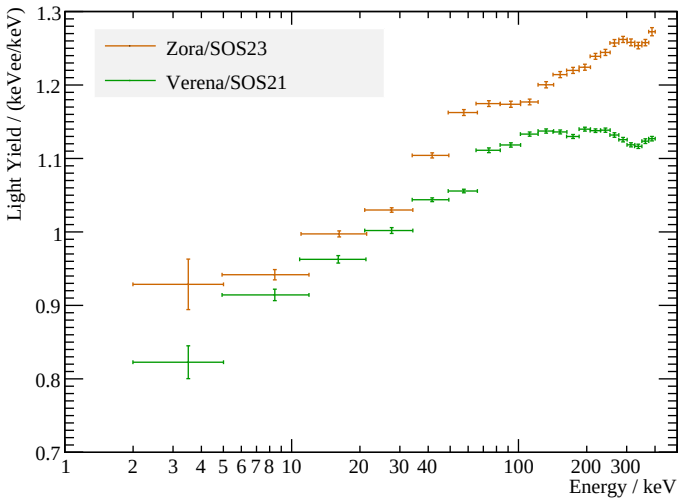

Figure 7.7: Light yield of detectors Zora (brown) and Verena (green) during background data taking in run 30. 100 events are taken together as one energy bin, a Gaussian is fitted, and shown here is the mean with the error of the fit. The indicated error in energy clasps around all events used for this data point. Clearly, the light yield is not a constant function of energy but decreases toward low energies.

7.4 Gamma and Electron Quenching

According to the model of Rooney and Valentine, we can therefore expect electron and gamma events to have a different quenching factor. Figure 7.8 shows again the spectrum of background radiation taken with Daisy during run 27. Let us investigate the light yield of three lines in more detail: The one from an external contamination with ^{210}Pb, and the two lines from cosmogenic tungsten activation.

As a first look, figure 7.9 shows this data as histogram in the light yield-energy plane. Already from this plot a reduced light yield for the ^{210}Pb line at 46.5 keV is evident. The energy binned mean is also shown in the figure, but given each gamma line sits on a considerable background, the mean itself is a bad measure of the quenching of the line alone. The background

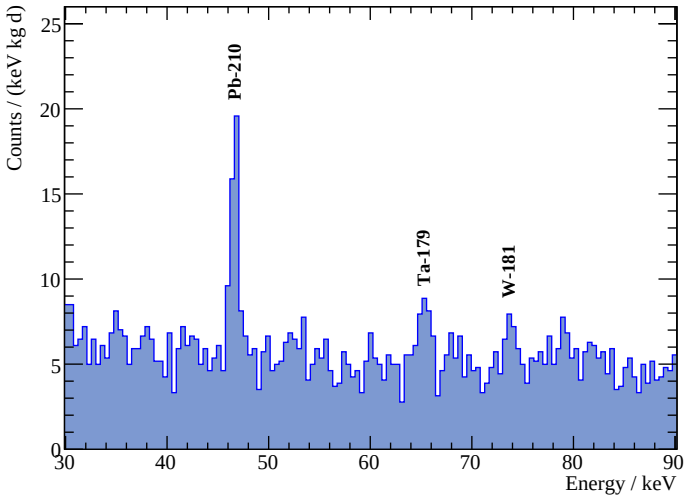

Figure 7.8: Spectrum of DAISY taken during run 27, marked with the three lines under special consideration here.

needs to be discarded for a proper assessment.

A technicality is quickly noted, namely that for this analysis a cut on the `light yield` as being in $[0.4, 1.6]\,\mathrm{keV_{ee}/keV}$ is done. This is necessary since in run 27 there was no neutron shield yet. At the energies considered here, this cut has no effect other than cutting nuclear recoil events away.

To investigate the light yield for the three lines without being sensitive to the background, two histograms of the light yield are formed for each of the three lines, at energy E_γ. One is an **on-peak** histogram, containing the events in the electron recoil band, which occur at energies $E_\gamma \pm 0.4\,\mathrm{keV}$. This corresponds to the resolution (1σ) of DAISY at these energies and gives a possibly pure sample of peak events. Another histogram is formed from **off-peak** events which occur at $E_\gamma \pm 5\,\mathrm{keV}$ but not within $E_\gamma \pm 1\,\mathrm{keV}$. These events are used to determine the behavior of the background. Hence, the on-peak distribution is $\Delta E = 0.8\,\mathrm{keV}$ wide and the off-peak distribution $\Delta E = 8\,\mathrm{keV}$.

7.4.1 Pb-210

The peak at 46.5 keV comes from an external contamination with ^{210}Pb (decay scheme on page 113). A Gaussian is fitted to the light-yield distribution of the off-peak events, resulting in a set of parameters, namely amplitude A_{off}, light yield y_{off}, and width σ_{off}, see figure 7.10. Then, the histogram of on-peak events is fitted with two Gaussians. One has all parameters fixed, taken from the off-peak fit, with the amplitude scaled by the energy bin width (1/10). For the second Gaussian, all parameters are left free. The result can be seen in figure 7.10.

Clearly, the light yield of gammas from the external ^{210}Pb decay is lower

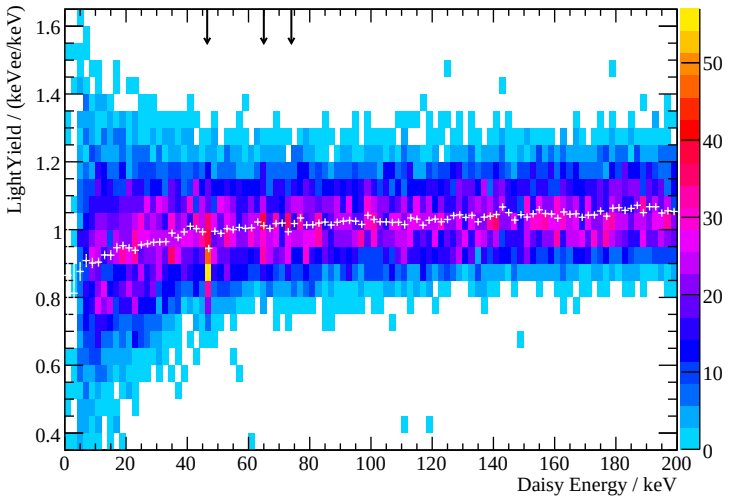

Figure 7.9: Histogram of the electron/gamma band in a light yield-energy histogram of background events from detector Daisy during run 27. The number of entries are given according to the color scale on the right. The white overlay is the mean in each 2 keV energy bin. For the ^{210}Pb line at 46.5 keV a reduced light yield is evident.

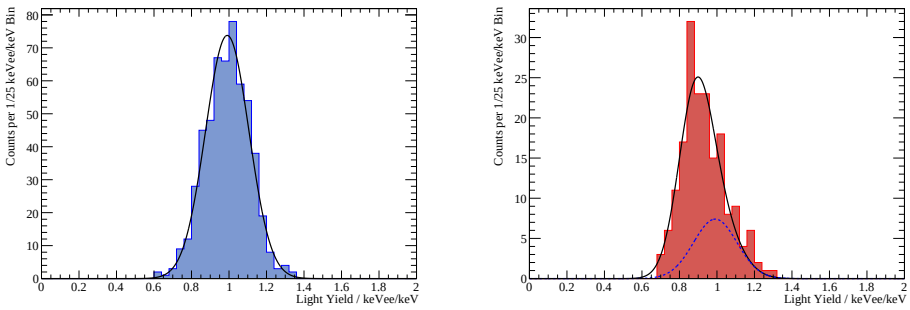

Figure 7.10: Left: Fit of a Gaussian to the off-peak events around the ^{210}Pb peak. The resulting parameters are $A_{\text{off}} = (74 \pm 4)$, $y_{\text{off}} = (0.991 \pm 0.005)\,\text{keV}_{\text{ee}}/\text{keV}$, and $\sigma_{\text{off}} = (0.116 \pm 0.004)\,\text{keV}_{\text{ee}}/\text{keV}$. Right: Fit of the sum of two Gaussians to the ^{210}Pb on-peak distribution. One Gaussian (shown dashed) has all parameters fixed according to the fit on the left: The amplitude is set to $A'_{\text{off}} = 7.4$ to scale for the different energy bin widths, and the light yield and width are the same as for the off-peak distribution. For the second Gaussian all parameters are left free, and the fit finds $A_{\text{on}} = (20 \pm 3)$, $y_{\text{on}} = (0.88 \pm 0.02)\,\text{keV}_{\text{ee}}/\text{keV}$, and $\sigma_{\text{on}} = (0.09 \pm 0.01)\,\text{keV}_{\text{ee}}/\text{keV}$. The errors are generally higher than in the off-peak case due to the lower statistics, but the result is unambiguous: The light yield of gammas from the ^{210}Pb decay is quenched relative to electrons of the same energy.

than that of the background of the same energy by about 10%. More precisely, the factor is $(0.991 \pm 0.005)/(0.88 \pm 0.02) = 1.13 \pm 0.02$.

However, the ^{210}Pb contamination of DAISY in run 27 had to be external, since we only see the gamma from the excited state of ^{210}Bi. But then, a 47 keV gamma in $CaWO_4$ will only penetrate the first millimeter (see appendix D). Hence this might well be a geometrical effect, caused by a reduced light yield at the cylindrical surface of the crystal.

7.4.2 Ta-179

The situation looks different for the ^{179}Ta line at 65 keV. ^{179}Ta stems from a (p, α) reaction on ^{182}W and is therefore intrinsic to the crystal. Let us follow the exact same procedure as in the previous section to find out in a quantitative way about the quenching of this line. Figure 7.11 shows the corresponding fits to the off-peak and on-peak distributions, respectively.

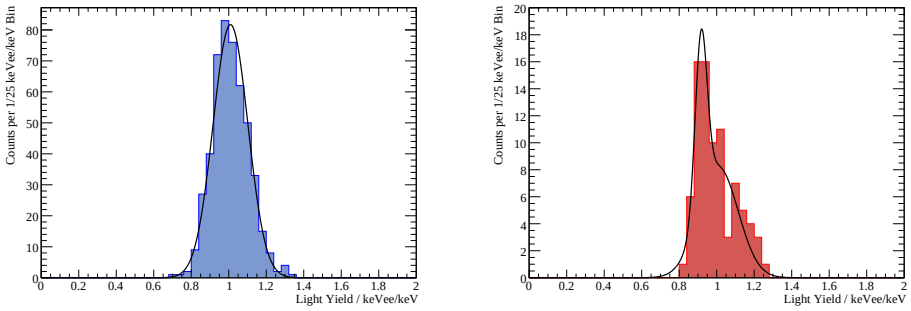

Figure 7.11: Left: The Gaussian fit to the off-peak events around the ^{179}Ta peak gives $A_{\text{off}} = (82 \pm 5)$, $y_{\text{off}} = (1.009 \pm 0.004)\,\text{keV}_{\text{ee}}/\text{keV}$, and $\sigma_{\text{off}} = (0.093 \pm 0.003)\,\text{keV}_{\text{ee}}/\text{keV}$. Right: Fit of the sum of two Gaussians to the ^{179}Ta on-peak distribution, the one completely fixed to $A'_{\text{off}} = 8.2$, $y'_{\text{off}} = 1.009\,\text{keV}_{\text{ee}}/\text{keV}$, and $\sigma'_{\text{off}} = 0.093\,\text{keV}_{\text{ee}}/\text{keV}$ and the other one left completely free, resulting in $A_{\text{on}} = (13 \pm 3)$, $y_{\text{on}} = (0.92 \pm 0.01)\,\text{keV}_{\text{ee}}/\text{keV}$, and $\sigma_{\text{on}} = (0.032 \pm 0.008)\,\text{keV}_{\text{ee}}/\text{keV}$.

The result is again very unambiguous to the existence of a different quenching for on-peak and off-peak events. But, one might plead, that the tantalum may be produced by cosmogenic activation prior to pulling the crystals. After all, the powders that the crystals are made from, either $CaCO_3$ and WO_3 or directly $CaWO_4$ powder, are standard albeit very pure materials. In this case, there might be an unknown effect during crystal growth that leads to an increased contamination from chemical elements in the melt toward the rim of the crystal, near the walls of the crucible. Then the ^{179}Ta decay might take place within the crystal, but nevertheless only close to its surface, hence giving the observed effect due to a dependence of the light yield on position.

7.4.3 W-181

This objection can be met. The cosmogenic activation $^{183}\mathrm{W}(\mathrm{p},\mathrm{t})^{181}\mathrm{W}$ yields tungsten again. If this happens prior to pulling of the crystal, still the $^{181}\mathrm{W}$ will be distributed uniformly throughout the crystal. If it happens after pulling, the source will be distributed homogeneously as well, since the hadronic component of the cosmic radiation is well known for its ability to penetrate a few centimeters of material (e.g. [217]). Hence, the above procedure is repeated for the 74 keV line from decaying $^{181}\mathrm{W}$. Figure 7.12 shows the results.

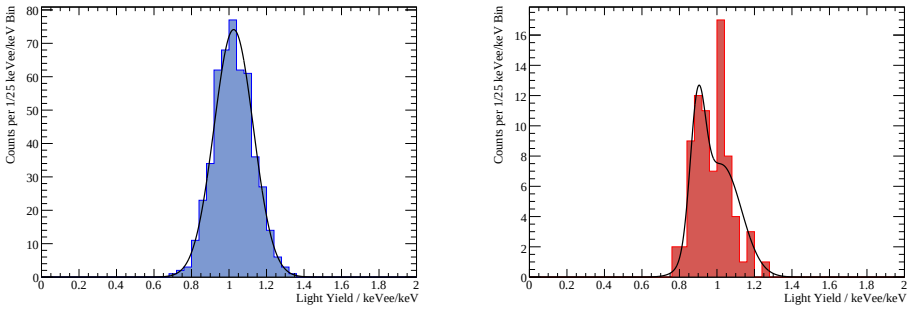

Figure 7.12: Whereas the fit of a Gaussian to the off-peak events around the $^{181}\mathrm{W}$ peak (left) gives $A_{\mathrm{off}} = (74 \pm 4)$, $y_{\mathrm{off}} = (1.025 \pm 0.005)\,\mathrm{keV_{ee}/keV}$, and $\sigma_{\mathrm{off}} = (0.105 \pm 0.004)\,\mathrm{keV_{ee}/keV}$, fitting the sum of two Gaussians (right) to the on-peak distribution, the one fixed, the other one free, gives for the second Gaussian $A_{\mathrm{on}} = (9 \pm 3)$, $y_{\mathrm{on}} = (0.90 \pm 0.01)\,\mathrm{keV_{ee}/keV}$, and $\sigma_{\mathrm{on}} = (0.04 \pm 0.01)\,\mathrm{keV_{ee}/keV}$.

Again it is shown unambiguously that on-peak events are quenched by a factor $(1.025 \pm 0.005)/(0.90 \pm 0.01) = 1.139 \pm 0.006$. We therefore have to abandon the explanation of the observed differences in quenching as being due to inefficient light collection for events that occur near the surface of the crystal.

7.4.4 More Physics in Run 30

There is an additional effect that can be examined in run 30, in particular with Verena. Recall Verena's background spectrum on page 114, where we have an intrinsic contamination of $^{210}\mathrm{Pb}$ which is visible as a beta spectrum that is offset by the gamma energy of a daughter level at 46.5 keV.

The light yield of these events is also quenched by about 10%. Now, at $\approx 47\,\mathrm{keV}$, all the visible energy of the decay comes from the gamma, and basically no energy from the electron. Toward higher energies, for example at $\approx 57\,\mathrm{keV}$, there is the same amount of energy coming from a gamma, and an additional amount of 10 keV from the electron which should contribute an unquenched fraction $10\,\mathrm{keV}/57\,\mathrm{keV} = 0.18$ to the light yield of these events. Hence, we would expect the light yield of the $^{210}\mathrm{Pb}$ events at 57 keV

to have a light yield not to 90% less than the background, but only to $(0.18 \times 100\% + 0.82 \times 90\%) = 92\%$.

If we bin the data in energy and follow the above procedure once more, we can fit to each bin the scaled off-peak Gaussian plus a second on-peak Gaussian. Since we have to work in the tail of the ^{210}Pb distribution with hardly any events above background, this time, the amplitude of the on-peak Gaussian is fixed such that its integral equals the additional number of events in the respective bin.

We might expect that, as the energy increases, the electron component becomes more and more important, dragging the mean of the additional Gaussian toward higher light yield values. Figure 7.13 shows the mean versus energy. However, the hoped-for effect is difficult to observe given the errors.

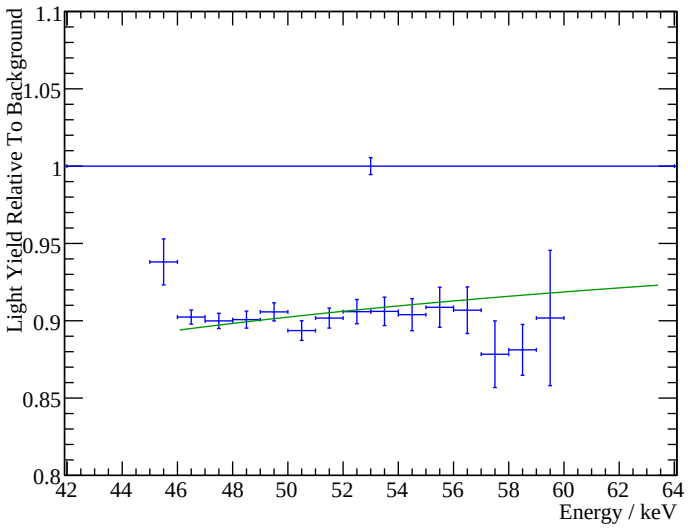

Figure 7.13: Light yield of the second fitted Gaussian in energy bins along the ^{210}Pb beta spectrum, normalized to the mean of the off-peak Gaussian, shown at unity. The green curve is a fit to the expected behavior, equation 7.2. The data point at 45.5 keV is excluded from the fit since this energy is below the onset of the beta spectrum.

More quantitatively, if the light yield of electrons is normalized to $1\,(\mathrm{keV_{ee}/keV})$, and that of gammas is ξ ($\approx 0.9\,(\mathrm{keV_{ee}/keV})$), then the expected dependence of the light yield y on energy E is

$$\begin{aligned} y(E) &= \frac{46.5\,\mathrm{keV} \times \xi \;+\; (E - 46.5\,\mathrm{keV}) \times 1\,(\mathrm{keV_{ee}/keV})}{E} \\ &= 1\,(\mathrm{keV_{ee}/keV}) - \frac{1\,(\mathrm{keV_{ee}/keV}) - \xi}{E/(46.5\,\mathrm{keV})}. \end{aligned} \tag{7.2}$$

Figure 7.13 also shows a fit of this dependence to the data, with ξ as free parameter. The result is $\xi = (0.895 \pm 0.002)\,(\mathrm{keV_{ee}/keV})$ with $\chi^2/\mathrm{ndf} =$

14.3/13. Fitting a constant value gives $y(E) = (0.901 \pm 0.002)\,(\mathrm{keV_{ee}/keV})$ with $\chi^2/\mathrm{ndf} = 5.9/13$. As is clear from the figure, the data is compatible with both hypotheses.

But perhaps the jump of the light yield at about 58 keV in figure 7.13 is not just statistical scattering, but a systematic effect. This energy happens to be that of tungsten K_α X-rays. Hence this reduction may be caused by additional X-rays from the neighboring crystals that hit Verena, deposit 59 keV with the light yield of photons, and therefore reduce the light yield in this energy bin. To test this, a cut on coincident events is done, or in other words, the neighboring detector Zora is used as a veto. Then the same procedure with fitting two Gaussians to each energy bin is repeated again. Figure 7.14 shows the result.

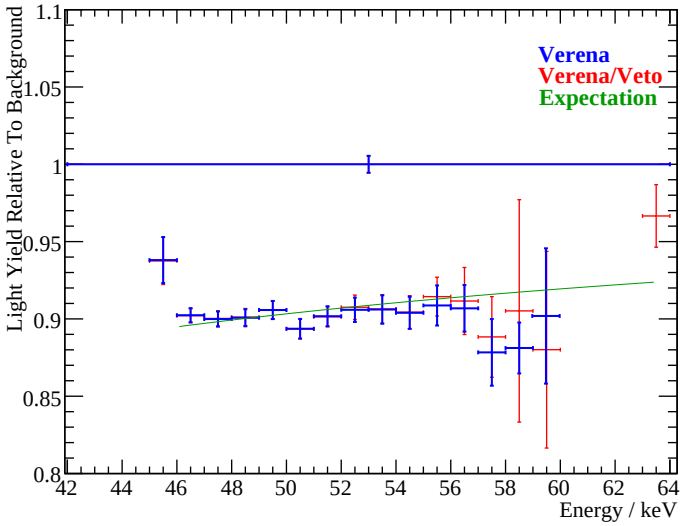

Figure 7.14: Same plot as figure 7.13 now with data after a veto cut on a neighboring crystal (red). One data point at 63.5 keV appears since in this energy bin the total number of counts now is higher than the scaled background, so the second Gaussian can be fitted. Clearly, coincident events contaminate the distribution at energies above 58 keV (the K_α energy of tungsten). However, since only one neighboring detector could be used as a veto, the data remains indefinite as to the nature of this dip.

At energies below ≈ 56 keV the veto cut has negligible effect. But above this energy, indeed the event sample is contaminated with coincident events, and the result changes a little. Fitting equation 7.2 now results in a better fit with $\chi^2/\mathrm{ndf} = 7.6/13$, resulting in $\xi = (0.896 \pm 0.002)\,(\mathrm{keV_{ee}/keV})$. Alternatively fitting a constant value gives $y(E) = (0.902 \pm 0.002)\,(\mathrm{keV_{ee}/keV})$ with $\chi^2/\mathrm{ndf} = 4.7/13$.

Other detectors in the vicinity of Verena were present but not operated during this run, so that it is not clear whether the region above 58 keV is still contaminated with escaped X-rays from these crystals. It will be

very interesting to see in upcoming runs, perhaps even with more exposure, whether one can really see the light yield and quenching change along the beta spectrum according to the energy splitting between electrons and gammas. This will then clarify whether the remaining observed dip at the K_α-transition is really due to scintillator effects, or due to coincident X-rays from neighboring detectors.

The same analysis was tried with the beta spectra of ^{227}Ac in ZORA during run 30, but for the lower energy actinium feature, the general non-proportionality of the light yield is already too strong to conclude. For the higher energy actinium feature, it is unclear how to normalize the background since this spectrum already sits on the lower energy beta spectrum, and in addition, there is a contamination from the ^{210}Pb line where a tungsten L_α X-rays escape the crystal.

Chapter 8

Light Detector as Target

Intent: The CRESST light detectors have an excellent energy threshold, well below 1 keV. This chapter gives some attention to the data collected with these detectors, answering the question whether they can be used to detect Dark Matter. In short, the answer is positive, but the high count rate renders the results by far not competitive.

Organization: In section 8.1 the search for very low energy interactions is motivated. Data taken with a light detector is described in section 8.2, and in section 8.3 limits on WIMP parameters are calculated from this data.

8.1 Low Energy Interactions

WIMPs are typically expected to have masses between 10 and 1000 $\mathrm{GeV/c^2}$, but this range can easily be too narrow. The more open-minded experimentalist will want to search a broader mass range. With increasing WIMP mass m_χ, the recoil energy $E_\mathrm{r} \propto p_\chi^2$ (see also page 48) will increase, but given a constant density ϱ_χ, the number density n_χ will decrease. Thus there seems little that one can do about this end of the mass scale, except for increasing the exposure in conventional low-background Dark Matter searches. Toward masses below $\mathcal{O}(10\,\mathrm{GeV/c^2})$, things are different. As the mass decreases, the number density increases, so the interaction rate goes up. But the recoil energy quickly goes down to energies well below 1 keV. Figure 8.1 shows a few expected recoil spectra. The challenge is to build detectors that can detect these low energies.

Another motivation to search for Dark Matter at very low recoil energies comes from possible enhancements of the Dark Matter density in the Solar System. Recently, the gravitational capture of Dark Matter particles due to three-body interactions with the Sun and the planets was estimated to enhance the local Dark Matter density by up to four orders of magnitude (reference [93] and section 2.7 on page 35). Hence it seems very natural to search for this possibly dominant component. If Dark Matter is gravitationally bound to the Sun, its halo parameters will change. Taking this local component to be distributed in an isothermal halo, this means one has

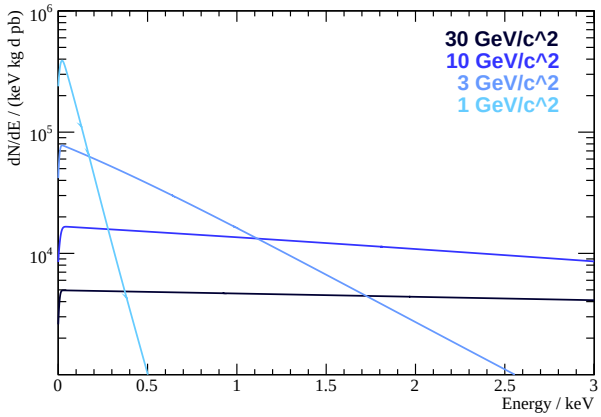

Figure 8.1: The expected recoil spectrum $\mathrm{d}\Gamma/\,\mathrm{d}E_\mathrm{r}$ for WIMPs interacting coherently on a sapphire target. The scaling assumes a cross section of 1 pb and a local halo density of $0.3\,\mathrm{GeV/cm^3}$. The reduction of the spectra around zero energy is due to an assumed energy resolution of 10 eV. The expected recoil spectra become very steeply falling toward lower WIMP masses even on this logarithmic scale.

to replace the velocity of the Sun through the Galaxy (232 km/s) by the velocity of Earth around the Sun (29.8 km/s). Hence the RMS velocity is reduced to about 30 km/s. Since $E_\mathrm{r} \propto p_\chi^2$, a reduction of v by one order of magnitude shifts the expected recoil spectrum from $\mathcal{O}(10\,\mathrm{keV})$ down to $\mathcal{O}(100\,\mathrm{eV})$.

Few detectors are available that can detect such low energy particle interactions, but the CRESST light detectors are among of them. In what follows, the possibility of using the light detectors as a target for such interactions is examined.

8.2 BE13 in Run 28

8.2.1 Data Reduction

In CRESST, both the phonon and the light detector trigger independently, but are always read out in pairs. The parameter `trigger delay` measures the time between the first and second trigger, and if there is no second trigger, this parameter is given a value larger than the record length. This allows to easily cut events that happen directly in the light detector: they will trigger there, but not in the phonon channel.

For this analysis, data from the module DAISY/BE13 from run 28 are used, where the trigger threshold of the light detector BE13 was set close to the noise level. In contrast to the silicon-on-sapphire-detectors (SOS type), BE13 has a $(30 \times 30 \times 0.45)\,\mathrm{mm^3}$ **cubic silicon absorber** substrate and weights only 1.00 g. Requiring the `trigger delay` of DAISY to be larger

than 125.51 ms (the post trigger time) leaves only events in the light detector that have no counterpart in the phonon detector.

For pulse height evaluation, a standard event is created from pulses in the light detector around a pulse height of 0.04 V, and fitted with a truncation at 3 V to these events. The conversion from `Amplitude` into electron-equivalent energy $\mathrm{keV_{ee}}$ is done with the standard procedure described in section 5.4.2. Cuts on an inclined baseline ($-0.02\,\mathrm{V} <$ `Right-Left Baseline` $< +0.02\,\mathrm{V}$) and the quality of the standard event fit (Polygon with (Energy/$\mathrm{keV_{ee}}$|RMS/V) coordinates (−11|0), (−11|0.008), (55|0.008), (999|0.032)) do not result in any significant reduction of the spectrum and thus do not influence the results of this discussion; hence these cuts may even be skipped.

8.2.2 Energy Estimation and Resolution

To know the absolute energy deposited in the light detector (in keV), one needs an independent energy calibration of the detector at low energies in order to translate the $\mathrm{keV_{ee}}$ energy scale. No such calibration was available for the detectors of run 27 through run 30: External calibration sources providing low energy gammas cannot penetrate the 12 mm thick copper of the thermal shield of the cryostat, and of course one is reluctant to build a calibration source *into* a low background experiment. This conversion factor will be known for sure with new data from Gran Sasso after run 30, where some light detectors have a very weak ($< 20\,\mathrm{mBq}$) ^{55}Fe source attached.

However, calibrations have been performed on detectors in München ([230, 255] and an earlier measurement in a less optimized setup [235]) giving the conversion factors in table 8.1. From these measurements we can expect that about $(1.3 \pm 0.2)\%$ of the energy of an interaction in the $CaWO_4$ crystal are deposited in the light detector. In what follows, we will take $1\,\mathrm{keV} = 0.013\,\mathrm{keV_{ee}}$.

In the case considered here, the energy resolution is readily estimated from the resolution of the heater pulse amplitudes, see figure 8.2 and table 8.2. For this analysis it easily suffices to use a central value of 8.6 eV for the energy resolution (1σ) of the detector, see figure 8.3.

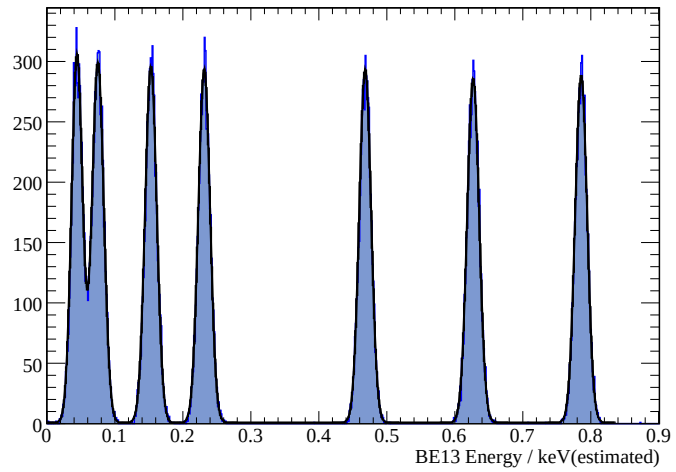

Figure 8.2: Reconstructed Amplitudes of the Heater Pulses of BE13 during run 28 together with a Gaussians fitted to each peak. The energy scale is set assuming $1\,\mathrm{keV} = 0.0131\,\mathrm{keV_{ee}}$. Table 8.2 gives the fitted resolutions, but it is already clear from this figure that the light detector has an excellent energy resolution for heater pulses which is constant over the energy range of interest.

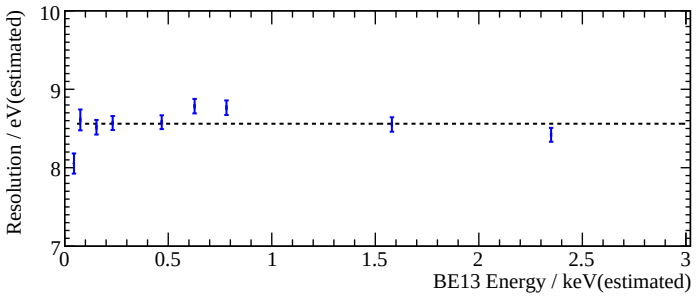

Figure 8.3: Resolution of the light detector BE13 as inferred from the fits on the heater pulses in figure 8.2 and at higher energies. Fitting a flat line gives $(8.56 \pm 0.03)\,\mathrm{eV}$ as the 1σ resolution of the detector.

setup	detected light
small crystal, $(20 \times 20)\,\mathrm{mm}^2$ Si detector	1.4%
small crystal, $(20 \times 20)\,\mathrm{mm}^2$ Ge detector	1.6%
small crystal, $(20 \times 20)\,\mathrm{mm}^2$ Si detector	0.7%
small crystal, $(20 \times 20)\,\mathrm{mm}^2$ Si detector	0.7%
teflon reflector, $(13 \times 10)\,\mathrm{mm}^2$ Al_2O_3 detector	0.33%
teflon reflector, $(20 \times 10)\,\mathrm{mm}^2$ Al_2O_3 detector	0.52%
teflon plus foil, $(20 \times 10)\,\mathrm{mm}^2$ Al_2O_3 detector	0.68%
foil bilayer, $(20 \times 20)\,\mathrm{mm}^2$ Al_2O_3 detector	0.5%
foil bilayer, $(20 \times 20)\,\mathrm{mm}^2$ Si detector	0.55%
foil bilayer, etched $(20 \times 20)\,\mathrm{mm}^2$ Si detector	0.7%
foil bilayer, $(30 \times 30)\,\mathrm{mm}^2$ Si detector	1.3%

Table 8.1: Measurements of the absolute energy deposited in the light detector following an interaction in the scintillating crystal. The top four measurements from reference [255] (chapter 5.2) used smaller crystals, the other measurements from reference [230] (chapter 5.1) the setup as it is used in Gran Sasso with 300 g $CaWO_4$ crystals. Taking into account the various setups of these measurements, we will consider the last in the list and estimate that 1.3% of the interaction energy are detected with BE13 in run 28.

injected voltage	reconstructed amplitude	resolution (1σ)
0.1 V	(0.0446 ± 0.0002) keV	(0.0081 ± 0.0001) keV
0.2 V	(0.0754 ± 0.0002) keV	(0.0086 ± 0.0001) keV
0.3 V	(0.1433 ± 0.0001) keV	(0.0085 ± 0.0001) keV
0.4 V	(0.2317 ± 0.0001) keV	(0.0086 ± 0.0001) keV
0.5 V	(0.4685 ± 0.0001) keV	(0.0086 ± 0.0001) keV
0.6 V	(0.6273 ± 0.0001) keV	(0.0088 ± 0.0001) keV
0.7 V	(0.7862 ± 0.0001) keV	(0.0088 ± 0.0001) keV
1.0 V	(1.5801 ± 0.0001) keV	(0.0086 ± 0.0001) keV
2.0 V	(2.3490 ± 0.0001) keV	(0.0084 ± 0.0001) keV
3.0 V	(5.4971 ± 0.0004) keV	(0.0264 ± 0.0003) keV
10 V	(7.8519 ± 0.0009) keV	(0.0550 ± 0.0006) keV

Table 8.2: Fit results from a Gaussian fit to the heater pulses in BE13.

8.2.3 Observed Spectrum

The accumulated spectrum of direct hits in the silicon light detector with an exposure of 0.998 kg d is shown in figure 8.2.2. Generally, one notes that the count rate is very high More precisely, we count about 10 $\mathrm{keV^{-1}g^{-1}d^{-1}}$ in the light detector at 1 keV, rapidly growing to higher values at lower energies. This count rate is indeed due to particle interactions and not due to noise, as can be inferred from figure 8.5. where the noise distribution is shown to be limited to the range below 50 eV. Figure 8.6 shows a typical pulse in the light detector from an estimated 100 eV interaction.

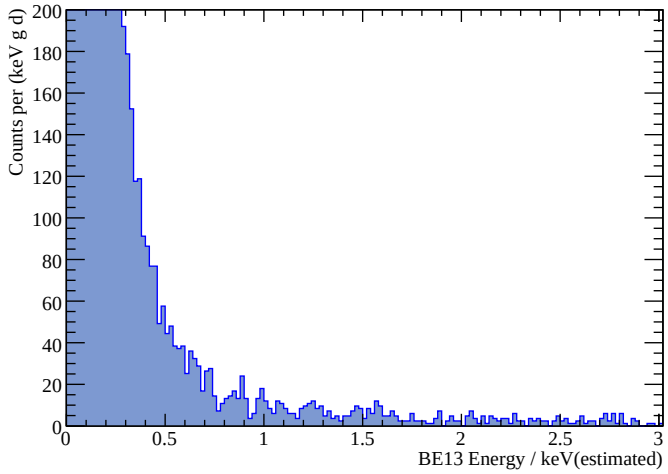

Figure 8.4: Spectrum of events in the light detector BE13 ($m = 1.00\,\mathrm{g}$) during run 28 after an exposure of 0.998 kg d, with the energy estimated assuming $1\,\mathrm{keV} = 0.013\,\mathrm{keV_{ee}}$.

With the large CRESST-I sapphire crystals (section 4.3.2 on page 75) a similar energy range was probed, but the count rate given per keV kg d was much lower, of order 100 $\mathrm{keV^{-1}kg^{-1}d^{-1}}$ at 1 keV. Those crystals weighted 262 g, but the light detector weights only 1 g. We have seen in section 4.3.2 that there is good reason to believe that the bulk of events at these energies happens at the surface of the detector, since in CRESST-I, more than a sixth of the events could be vetoed away with only one of the six sides of the crystal being guarded.

Then, per unit surface area (the CRESST-I crystals are $(40 \times 40 \times 41)\,\mathrm{mm^3}$ cubes), the count rate in CRESST-I at 1 keV was about 0.3 $\mathrm{keV^{-1}cm^{-2}d^{-1}}$. Here, with BE13 in run 28 (measuring $(30 \times 30 \times 0.45)\,\mathrm{mm^3}$), we have a count rate per unit surface area of the same magnitude, about 0.6 $\mathrm{keV^{-1}cm^{-2}d^{-1}}$ at 1 keV. In light of chapter 6 where we have seen the rich variety of radioactivity introduced into the Cold Box by the $CaWO_4$ target crystals themselves, it is no wonder that the rate is a little higher in run 28 than in the CRESST-I phase where this source of contamination was not present.

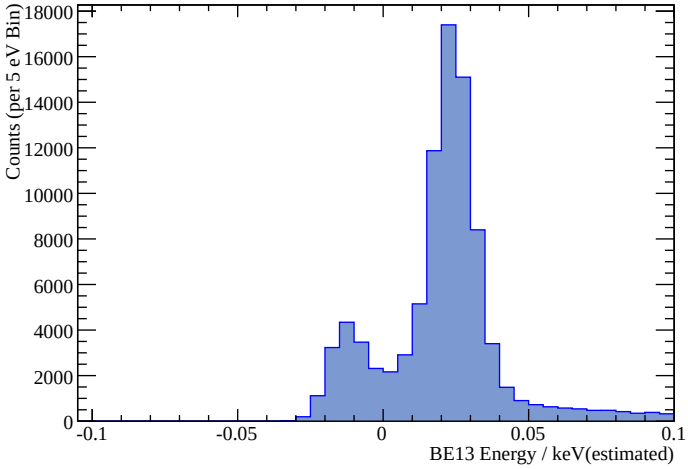

Figure 8.5: Spectrum of events in the light detector with the energy estimation as above. BE13 was setup with trigger close to noise, and this can nicely be seen in this figure. Two peaks appear symmetric to zero amplitude. This is expected from a standard event fit to empty baselines (the noise), since looks for the best fit without a bias toward positive amplitudes. Hence the position of the peaks gives a good estimate of the noise in the detector. The peak at positive values is stronger than that of negative amplitudes because for a trigger a necessary prerequisite is a positive excursion of the noise. At energies well above $\approx 50\,\mathrm{eV}$ however, the spectrum can be assumed to be noise free.

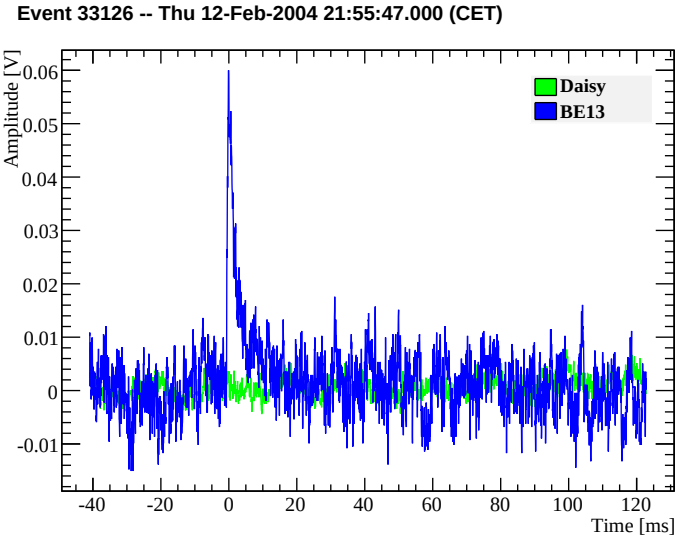

Figure 8.6: A typical pulse recorded following an interaction in the light detector with an estimated energy of only 100 eV. Already at this energies the pulses are well above the baseline noise.

Surface events at these energies are most likely due to electrons. $\mathcal{O}(10\%)$ of $\mathcal{O}(\text{keV})$ electrons impinging on a surface are not absorbed but scattered elastically [272, 273], and can hence induce further interactions. The observed spectra are very similar for BE13 in run 28 as well as SOS21 and SOS23 in run 30, both in rate and shape. This points toward a common origin of the interactions.

8.3 Calculating a Limit

To seriously search for Dark Matter, the possibility to veto surface events is indispensable. If one were to use the CRESST-II light detectors for this purpose, one would like to use a triple sandwich design of these detectors, so that for the detector in the middle, the two main surfaces could be vetoed. Whether this makes sense, given the small mass of these devices, shall be examined with an academic exercise: What limit on the Dark Matter scattering cross section can be placed given the above data?

8.3.1 Isothermal Milky Way Halo

To calculate a limit, we assume the WIMP halo parameters discussed in section 3.3.5, and calculate a signal expectation for a given WIMP-nucleon cross section σ. Now we need a measure of how large a σ is still compatible with the observed spectrum. Clearly, if the signal expectation for a given cross section σ is, say, an order of magnitude above the observed spectrum, we can reject this cross section as being too high. But to be more precise, there is no generally accepted method to calculate the limit on the cross section.

Here, we will adopt the following method, shown to yield similar results as do alternatives used in the field [210]. As a first step, an empirical function $B(E, \vec{p})$ is fitted to the experimental spectrum, figure 8.4, yielding a set of best-fit parameters $\vec{p}$. Here, we use the sum of three exponentials plus a constant to describe this background. Given the χ^2/ndf of the fit $\vec{p}$ one also has its likelihood $\mathcal{L}(B)$ which will serve as a measure to judge the quality of the signal fit.

As second step, for a given WIMP mass, the signal hypothesis $S(E, \sigma)$ is calculated with the cross section σ as scaling parameter. The function $f(E, \vec{p}, \sigma) := \max\{B(E, \vec{p}) + S(E, \sigma)\}$ is then fitted to the observed spectrum, yielding a likelihood $\mathcal{L}(f)$ of the fit. As long as σ is small enough, $S(E) < B(E)\ \forall\ E$, so $f(E) = B(E)$, and hence $\mathcal{L}(f) = \mathcal{L}(B)$. Then σ is increased until the fit of f becomes worse than the fit of B alone. A limit at 90% confidence is achieved once $\ln(\mathcal{L}(f)) = \ln(\mathcal{L}(B)) - 1.28^2/2$. The subtrahend is given since 1.28σ gives the one sided 90% confidence limit of a Gaussian distribution, and the factor of 2 is needed because we use likelihood rather than χ^2. Figure 8.7 shows the observed spectrum together with signal expectations that are excluded by this method.

The resulting limit is shown in figure 8.8 together with the 2002 limit

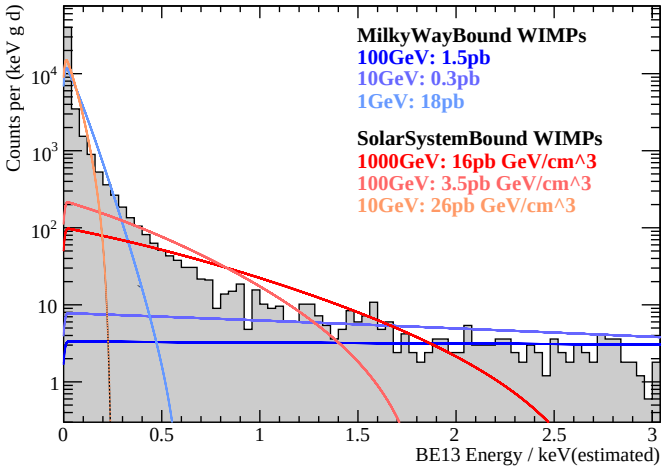

Figure 8.7: Observed spectrum in BE13 together with signal expectations that are excluded at 90% confidence, for both a standard isothermal Milky Way halo and the modified isothermal Solar System halo.

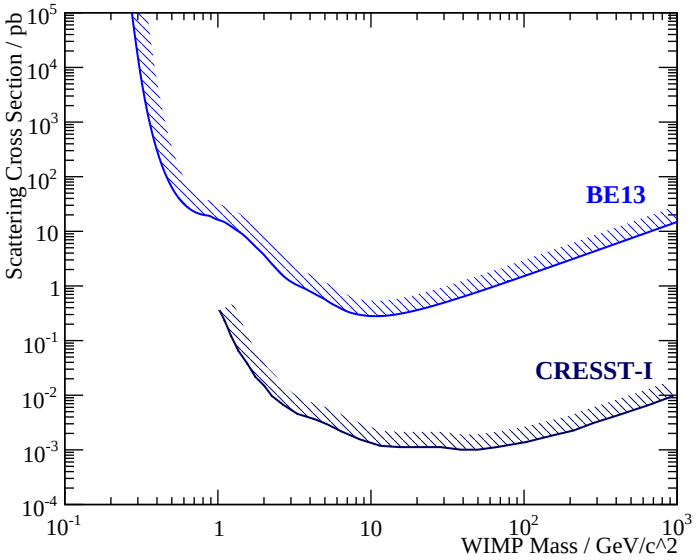

Figure 8.8: Upper limit on the coherent WIMP-nucleon scattering cross section from the light detector BE13 as target during run 28 (upper curve). The area above the line is excluded at 90% confidence since WIMPs with such a high cross section would induce more events than observed. For comparison, the 2002 CRESST-I limit [210] is also shown; other current experimental limits (typically for higher WIMP masses) are well below the limit from the light detector [274].

from CRESST-I. Of course the limit from the light weight light detector is worse than that from CRESST-I. This is expected since the limit is completely background dominated, and the background rate is two orders of magnitude higher (as the mass of the target is two orders of magnitude smaller). Curiously, for WIMP masses below $1\,\mathrm{GeV/c^2}$, one can extrapolate that the difference vanishes. Hence, one might really pursue the concept introduced above, using clean cryogenic low threshold detectors as target, with a complete surface veto, to seriously search for Dark Matter.

8.3.2 WIMPs in the Solar System

Another exercise, again rather academic given the high observed count rate in the light detectors, is to constrain an additional WIMP population in the Solar System. We will consider two cases as possible WIMP halos. One is a modified isothermal halo as discussed in the introductory section 8.1, where we take the escape velocity as being that of the Sun, 618 km/s [150].

The second WIMP population is the one put forward by J. I. Collar [275], where the WIMPs are assumed to be on Keplerian Earth-crossing orbits around the sun. The resulting expected recoil spectra differ only at low momentum transfers, see figure 8.9.

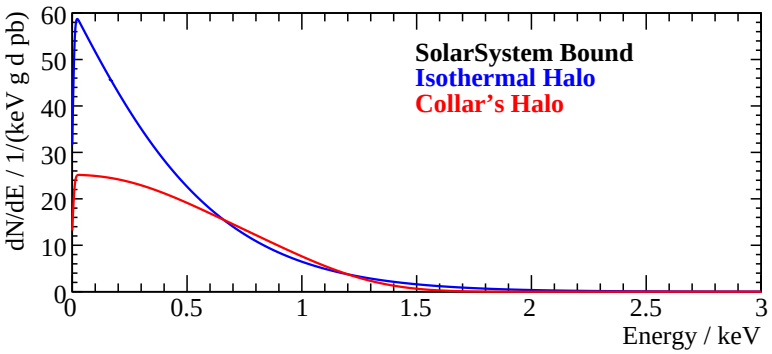

Figure 8.9: Expected recoil spectra $\mathrm{d}\Gamma/\mathrm{d}E$ in a silicon target with an exposure of 1 g d, for $100\,\mathrm{GeV/c^2}$ WIMPs with a WIMP-nucleon cross section of 1 pb. The WIMPs are assumed to be bound to the Sun in one of the two halo models discussed in the text.

Direct detection experiments always measure the product of density and cross section, $\varrho_\chi\sigma_0$ (section 3.3.5 on page 54). For the standard isothermal Milky Way halo, the assumption of $\varrho_\chi = 0.3\,\mathrm{GeV/cm^3}$ is well justified, but no such generally accepted reference value for the density $\varrho_{\chi,\mathrm{SSB}}$ of an additional local, solar bound WIMP population exists. Hence, for Solar System bound WIMPs, we do not give a limit on the cross section alone, but on the product $\sigma_0 \times \varrho_{\chi,\mathrm{SSB}}$. Using the same procedure as in the above case results in the limits shown in figure 8.10. Some spectra excluded at 90% confidence are also shown in figure 8.7.

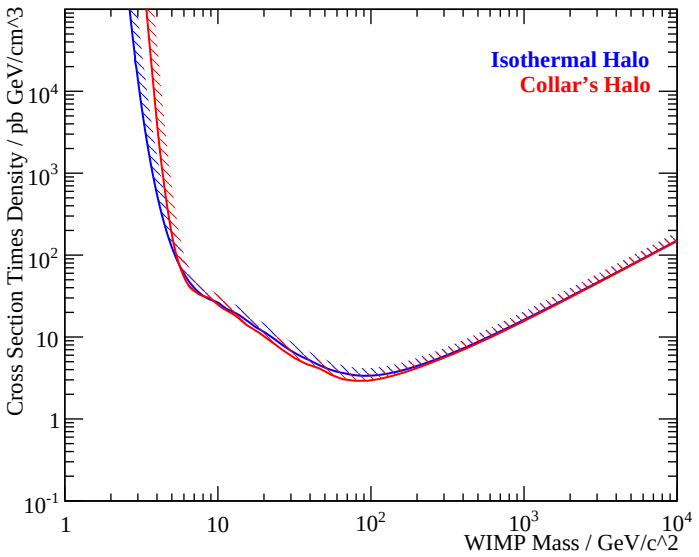

Figure 8.10: Upper limit on the product of coherent WIMP-nucleon cross section σ_0 and Solar System bound density $\varrho_{\chi,\mathrm{SSB}}$, using the light detector BE13 as a target during run 28. The blue line assumes an isothermal Solar System bound halo, the red line follows the distribution put forward in [275]. Both exclusion curves are seen to be similar except at very low WIMP masses.

Clearly, even for a density that is enhanced by four orders of magnitude as proposed in reference [93], this is not a competitive limit. Instead, it shows the necessity of large target masses and active background discrimination in the search for Dark Matter.

Chapter 9

Dark Matter Analysis

Intent: During 2007, background data was taken with two detector modules to search for Dark Matter interactions. The data is analyzed and discussed in this chapter. This includes the implementation of a blind analysis, description of employed cuts, and a discussion of observed events in the region where WIMP induced tungsten recoils are expected. A new way to determine the position and resolution of the electron/gamma band and the nuclear recoil band is applied. Innovative parameters are presented that allow to separate sources of background, which are discussed also.

Organization: Section 9.1 introduces the need for a blind analysis method, before cuts are applied to the data as discussed in section 9.2. Sections 9.3 and 9.4 present the data that is obtained by this analysis from two detector modules during data taking in 2007. In section 9.5 possible origins are given for a few events that appear in the region where WIMP induced events are expected. Resolution parameters required for further evaluation of the data are derived in sections 9.6 and 9.7. Before the calculation of the limit is discussed in the next chapter, section 9.8 describes a source of background that can now be isolated with new available parameters.

9.1 Blind Analysis

The influence of human perception on the outcome of an investigation is probably most well-known from the field of medicine, from which the buzzwords *double-blind analysis* and *placebo effect* are well known. The history of science is full of effects that were discovered but eventually turned out to be non-existent. There are well documented examples also from the field of particle physics. The Davis-Barnes effect, meaning electrons bound to alpha particles, which turned out to be misconception is particularly well documented [276]. The splitting of the A_2 meson resonance seemed clearly discovered but eventually vanished [277]. The Particle Data Group has compiled a noted selection of measured parameters versus time which are seen to jump from time to time by many standard deviations [278]. Even more effects from the field of particle physics alone can be found in the cited references.

This is not to say that any of these effects have deliberately been produced, and this section is not about fraud and methods to prevent it. An experimentalist may unintentionally or even unconsciously influence the outcome of a measurement to conform with his believes, feelings, or expectations. In the context of this section this is the experimenter's **bias**. This bias cannot be quantified and thus needs to be avoided [279]. Since it can be introduced in an unconscious way it is necessary to design an analysis such that bias is excluded by construction. Such studies are then called **blind** analysis.

Various standard techniques exist to do so. For the rare event search of interest here, the **hidden signal box** or simply the **hidden box** method is most appropriate [280, 281, 282]. In this method, the region where the signal is expected is hidden from the experimentalist, who is then free to design the analysis based on physical reasoning and distributions in the blinded data. Only once the analysis is finalized and the cuts that are to be performed are fixed, the signal region is **unblinded**.

Here, we define the hidden box in the light yield-energy plane by the energy interval $[0, 50]\,\mathrm{keV}$ well above the maximum expected recoil energy, and the light yield interval $[-0.5, +0.5]\,\mathrm{keV_{ee}/keV}$, much larger than the width of the nuclear recoil band above threshold.

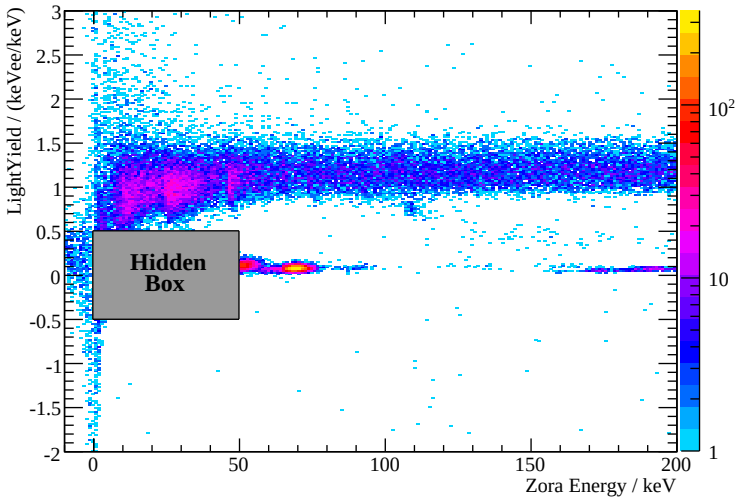

Figure 9.1: Histogram of events from module ZORA/SOS23 during run 30 in the light yield-energy plane. Color coded is the number of entries per bin according to the palette on the right. No cuts have yet been applied, and the signal region is blinded. The gamma band is clearly visible, but pathological events appear in the nuclear recoil region.

As an example, we will go through the analysis of detector ZORA during about half of the data of run 30. Figure 9.1 shows the raw sample of events in the light yield-energy plane. At this stage, the calibration of the two detectors is already performed as described in chapter 5. No cuts are applied

yet, and the signal region is hidden. The gamma and electron band with its spectral features, namely the ^{227}Ac and ^{210}Pb beta spectra, are already visible in this plot. However many pathological events appear in the nuclear recoil region. Hence we have to characterize these pathological events and design cuts to remove them whilst keeping events due to true particle interactions.

9.2 Cuts

The stable ($\Delta T \ll$ mK) and quiet (trigger rate $<$ Hz) environment for the CRESST detectors yields high quality data. In contrast to e.g. collider experiments, hardly any cuts have to be performed on the data to yield the signal sample of interest. Nevertheless, some cuts sill have to be in order to ensure the quality of the remaining data.

9.2.1 Pathological Pulses

Occasionally the SQUID system, being a very sensitive device in its own, can malfunction. Also, given data is taken over many months, other pathological events are recorded which stem from a variety of causes. Figure 9.2 shows a selection of pulses that disturb the measurement, or are of no interest for the Dark Matter search.

A standard event fit on such pulses can lead to surprising parameters. In particular, events like the ones shown in figure 9.2 (b,c,h,i) may lead to a positive `amplitude` for the phonon detector but zero `amplitude` in the light detector. Hence these events may show up in the WIMP acceptance region. In what follows, cuts are described that are necessary to guarantee the operational reliability of the detectors for the accepted events.

9.2.2 Stability Cut

In the end of the Dark Matter analysis there will be a scatter plot of particle interactions in the crystal. The signal region will be defined for particles with an energy of $\mathcal{O}(10\,\mathrm{keV})$ and hardly any associated light. Hence a key requirement on the Dark Matter analysis is to ensure that both detectors, and in particular the light detector, are operational.

This monitoring is achieved by injecting control pulses every 3 seconds. These pulses are used to control the operating point of the detectors following online pulse height evaluation. The precision of this control may quickly be estimated: Limiting factor is the baseline noise N of the detector. As an example, Zora has $N \approx 5\,\mathrm{mV}$ corresponding to $E \approx 700\,\mathrm{eV} = 1.1 \times 10^{-16}\,\mathrm{J}$. The (electronic) heat capacity of the tungsten film is readily estimated as $c_\mathrm{e} = \gamma T_\mathrm{C}$ where the Sommerfeld constant for tungsten is $\gamma = 1.0\,\mathrm{mJ\ mol^{-1}\ K^{-2}}$ [283] and $T_\mathrm{C} \approx 15\,\mathrm{mK}$. The tungsten thermometer measures $6\,\mathrm{mm} \times 8\,\mathrm{mm} \times 200\,\mathrm{nm}$, so it is stabilized to a precision of $\Delta T = E/C_\mathrm{e} < 10\,\mu\mathrm{K}$.

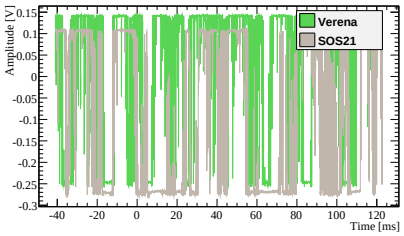

(a): Malfunction of the SQUIDs or DAQ system, often seen simultaneously in multiple channels.

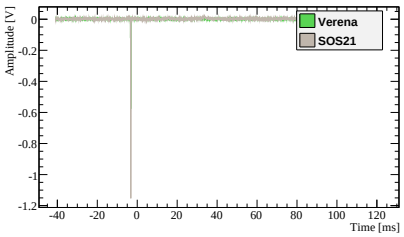

(b): Negative noise spike; often seen simultaneously in multiple channels.

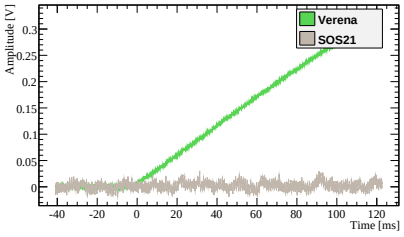

(c): If the SQUID is malfunctioning, this will mostly be cured following the SQUID reset once the output exceeds ±10 V.

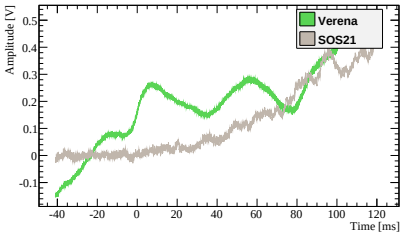

(d): Noisy states like this occur rarely but can last for minutes and are often seen in many detectors at the same time.

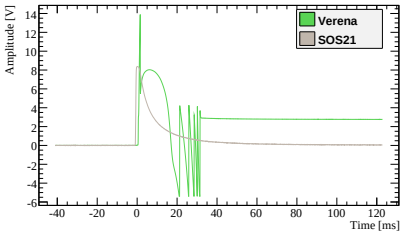

(e): The SQUID of the phonon detector oscillates (it *rings*) after an interaction.

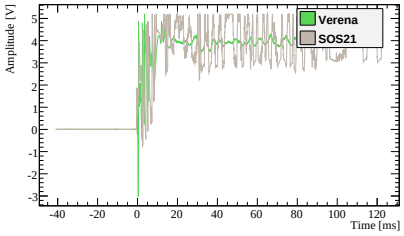

(f): Both SQUIDs oscillate following an interaction. (figure continued next page)

Figure 9.2: Selection of pathological pulses from the detector module VERENA/SOS21. The origin of the electronic problems (a,b) is unclear. Walking baselines (c,d) point toward SQUID problems but can easily be rejected. Flux quantum losses (e,f,g,h) occur if the thermometer resistance changes too quickly for the SQUID to follow, and the detector will change its baseline level (continued next page).

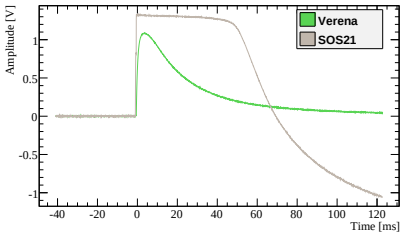

(g): Flux quantum loss following a high-energy interaction that exceeded the slew rate of the light detector SQUID.

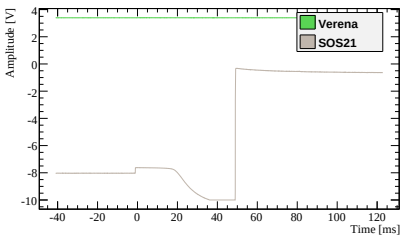

(h): After a flux quantum loss the SQUID output goes below the dynamic range ($-10\,\mathrm{V}$), and resets to $0\,\mathrm{V}$.

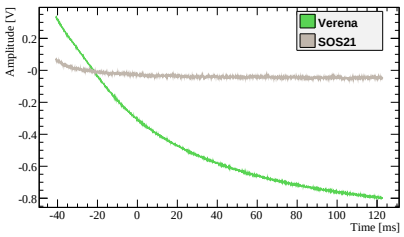

(i): The tail of a high energy interaction that occurred prior to this recorded pulse can still trigger once the trigger is activated.

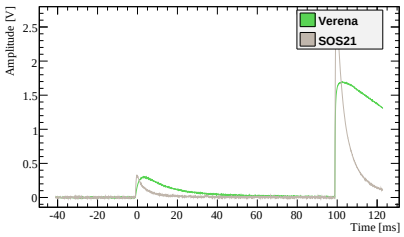

(j): For the Dark Matter analysis, pile-up events like this one can be rejected due to the low trigger rate...

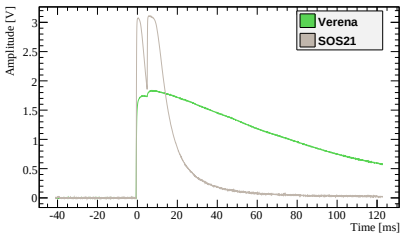

(k): ...but for an analysis of α-events pile-ups need to be considered, since many α decays result in cascades, such as shown here.

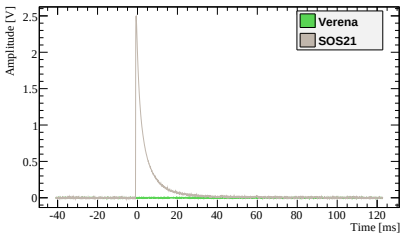

(l): Direct hits of the light detector may (this chapter) or may not (chapter 8) be rejected for a Dark Matter analysis.

Figure 9.2 (continued): Following a high energy interaction, if the readout value is still above trigger threshold upon activation of the trigger, decaying pulses (i) are recorded. Pile-ups (j) are not reconstructed in the search for WIMP interactions since WIMPs are not expected to double scatter and cutting them introduces negligible dead time. Alpha events (g,k) or direct hits of the light detector (l) are irrelevant for the search considered here.

It is easy to see that at this level of temperature stability even small disturbances on the cryostat may cause the detectors to depart from their operating point. Just as an example, despite the cryostat in Gran Sasso resting on air dampers, and the carousel with the detectors being decoupled from the cold finger by springs, ruggedly walking up the stairs on the outside of the hut could disturb the detectors during runs 29 and 30.

Thus a **stability cut** is performed, where the `pulse height` of the control pulses is monitored and times with excursions from the set point are rejected. Figure 9.3 shows an example of the `control pulse height` versus time for detectors VERENA and SOS21, showing an excursion of the operating point for both detectors.

With the heater pulse calibration method at hand, this excursion could be corrected for. However this would prevent a smoothing of the splines as is appropriate for the stable time periods. Eventually, the crucial question to be asked *before* the analysis is: Could one trust a WIMP candidate event if it occurred precisely during the time of this excursion? Probably one would be very tempted to reject this event as a noise glitch. But in doing so one would do a mistake in the calculation of the live time, since one then would have to reject *all* time periods in which such excursions happened, simply because one would have rejected the WIMP candidate event in all such unstable periods. Therefore, these periods are cut away in the **stability cut** prior to any further analysis of the data.

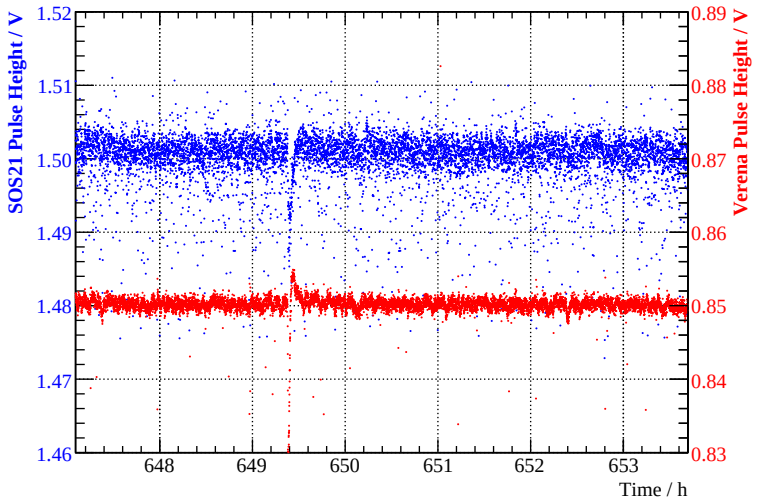

Figure 9.3: Example of an excursion of the detectors VERENA and SOS21 from their operating point.

Two ways are possible for doing this cut. One is to simply histogram the `control pulse height`s for all events. Events are rejected if the neighboring control pulses (or an interpolation between their `pulse heights`) are outside the bulk of this distribution. This works fine if the detector is generally in a stable operating condition, with only occasional excursions such

as the one depicted in figure 9.3.

But the data analyzed here was taken during prototyping (runs 27 and 28) and commissioning (runs 29 and 30) and includes time periods where the detectors are not as stable as desired. In this case, the first variant of the stability cut will keep also such events for which the control pulses are within the main distribution, despite the event occurring during a time of unstable running conditions. Hence a more labor intensive stability cut is done for the data presented here, where the data is plotted just as in figure 9.3 and time spans during which the detectors depart from their set point are cut manually. With proper macros at hand this can be done for a detector module within reasonable time for the whole run. In addition, with this method, the analyst benefits from an in-depth understanding of the working conditions of the detectors. Hence this method is recommended given it prevented the author from the odd shortfall.

9.2.3 Amplitude Cut

As we have seen in figure 5.12 on page 103, the calibration with heater pulses may translate high amplitudes into low energies for pulses where no calibration is available. A simple cut on the `amplitude` of the pulses, far from the energy region of interest, prevents confusion.

9.2.4 Light Detector Cut

Direct hits of the light detector only show a signal there, but none in the phonon detector. They can be cut easily in the `trigger delay` parameter, since this is set to a value larger than the post-trigger length for events that do not trigger in the phonon detector. Sometimes, e.g. during high-noise periods during commissioning, the light detector trigger is not even activated during data taking, rendering this cut surplus. Also, this cut can be skipped if one does not mind a large quantity of events with amplitude in the phonon detector below trigger threshold. However, for the data of run 27 and 28, the trigger rate in the light detector was very high due to a low threshold, making this a convenient cut.

9.2.5 Right-Minus-Left-Baseline Cut

A cut on the robust `right-minus-left baseline` parameter is performed to cut most of the pathological event classes shown in figure 9.2. If high energy events ($\gtrsim 100\,\mathrm{keV}$) are still of interest, this cut may be performed in an energy dependent way. In the example considered here, Zora/SOS23 during run 30, the cut is energy independent and simply $-0.15 <$ `right-minus-left-baseline`$/\mathrm{V} < +0.15$ for Zora, see figures 9.4, 9.5 and 9.6.

During run 30, the alpha activity of the crystal Zora was relatively high, leading to many alpha induced events that are removed by this cut. If this is considered a nuisance, two possibilities may be implemented reduce

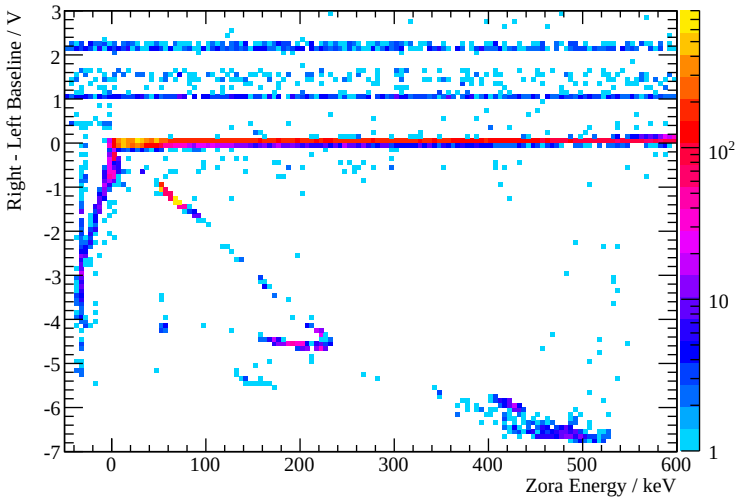

Figure 9.4: Broad histogram for detector ZORA during run 30 of the `right-minus-left-baseline` parameter versus energy. Color coded is number of entries per bin according to the scale on the right. The horizontal line at `right-minus-left-baseline` $\approx 0\,\mathrm{V}$ are the events of interest. Most of the events above zero are high energy events whose pulses cannot relax within the record length (figure 9.2 (k)), and most events below are relaxing pulses that occur before the event but still trigger (figure 9.2 (i)).

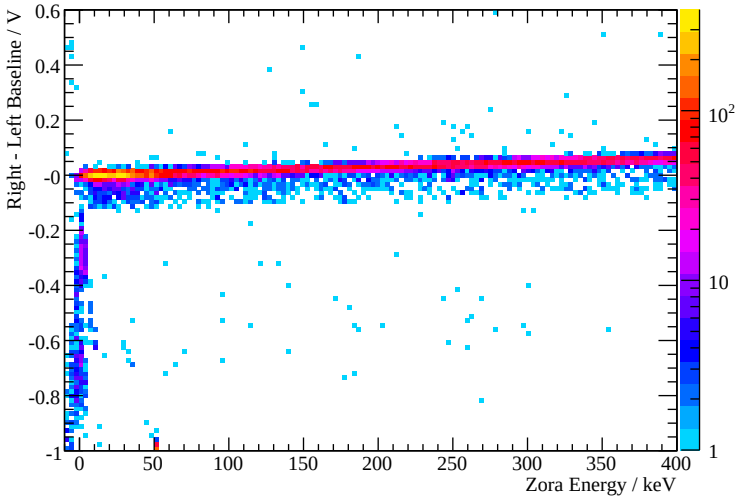

Figure 9.5: Zoom in the distribution of figure 9.4. The events of interest are the dominant band at $\approx 0\,\mathrm{V}$ with events leaking to lower values being due to slightly inclined baselines after a high-energy interaction, and even further below are relaxing pulses that still trigger. Above are a few pile-up events. A cut is placed as $-0.15 <$ `right-minus-left-baseline`$/\mathrm{V} < +0.15$, not affecting in any way the population of well-reconstructed events.

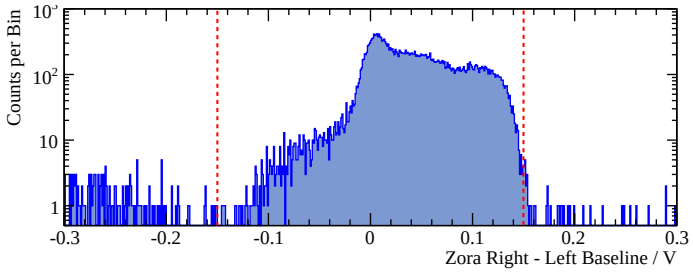

Figure 9.6: Histogram of the `right-minus-left-baseline` distribution in ZORA, with the cuts at $\pm 0.15\,\mathrm{V}$. The cut can be seen to remove basically no well-reconstructed particle interactions at all.

this class of events. One is to prevent a trigger if the input signal is above threshold at the time the trigger becomes activated, and to require that the input signal goes above the threshold from lower values. However this is difficult to realize with slow signals as there are always many threshold crossings caused by the noise.

For run 31 another way was chosen, namely, the record length was doubled, so that most of these high energy pulses will be able to relax to the baseline before the end of the record. Hence, once the trigger becomes active again after readout, the baseline is already flat and most of these events will not appear. This has the additional advantage that even higher pulses can be reconstructed conveniently with the truncated standard event fit.

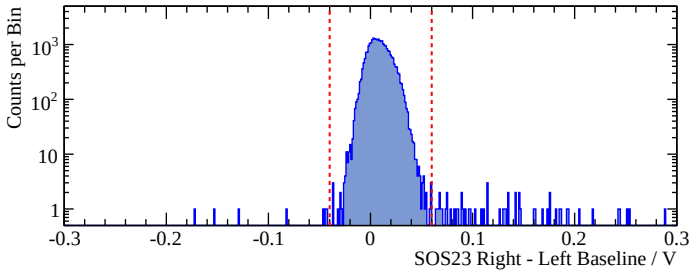

Figure 9.7: Histogram of the `right-minus-left-baseline` distribution for events in SOS23 that survived the previous cut in ZORA. The cut is placed at $-0.04 <$ `right-minus-left-baseline`$/\mathrm{V} < +0.06$, only cutting a few direct hits of the light detector which have an additional signal in the phonon detector (otherwise they would not have triggered it).

A `right-minus-left baseline` cut may also be done for the light detector. Since the light detectors have a much shorter relaxation time, inclined baselines are of no concern here. The only events such a cut will remove are particle interactions that deposit a very high energy in the light detector, such as alphas absorbed there. This prevents the light detector pulse to relax to the baseline within the record length. For the Dark Matter analysis this is of no real concern, however such events may be

mis-reconstructed and appear in the signal region. It is best to perform any cut for the light detector energy independent. This prevents accidental cutting of events with negative amplitude, which may well occur for WIMP candidate events. In the example considered here, the cut is placed at $-0.04 <$ `right-minus-left-baseline`$/\mathrm{V} < +0.06$ for SOS23, see figure 9.7.

9.2.6 Quality of Fit

A final cut is made on the quality of the standard event fit. Some noise events like the one in figure 9.2 (b) or pile-up events can be rejected with this cut. Figures 9.8 and 9.9 show the quality of the fit for the phonon detector, measured by its RMS value. Most events are seen to be fitted very nicely, with the RMS value simply corresponding to the baseline noise of the detector. One might well cut at a value of, say, 0.02 V, this would still keep 95% of the population. Yet to get the most out of the data sample, this analysis cuts much weaker at a RMS value of 0.03 V (98% of the population).

A word of warning is in order when cutting on the quality of the fit. Nuclear recoils are known to have a slightly different pulse shape than electron or photon events, a fact that is even used for discrimination in other Dark Matter direct searches. In case of the CRESST-II detectors, the decay time of the pulses was shown to vary a little [255]. However this difference is already smaller than the width of the distributions for energies around 100 keV, becoming even smaller at lower energies. Hence, as long as the RMS cut is placed well above the distribution, it is well justified.

A cut on the quality of the fit in the light detector has to be done with greatest care, given the light signal is the prime information used for discrimination. Luckily, it is often not needed: Noise events affect mostly both detectors of a module and are hence already rejected at this stage. Events with an additional direct hit of the light detector as a pile-up may be mis-reconstructed, but will have a higher `amplitude` than without the pile-up, and hence do not contaminate the signal region either. For the example considered here, figures 9.10 and 9.11 show the distributions, and a cut is placed at `RMS` < 0.02 V.

9.2.7 Effect of the Cuts

This small set of mild quality cuts suffices to clean the event sample from any spurious event in the nuclear recoil band. Since hardly any signal events are cut, the set maintains a cut efficiency of almost unity. Figure 9.12 shows the equivalent to figure 9.1, now after the above cuts. The nuclear recoil region can be seen to be free from pathological events that were present earlier. The event shown in figure 9.13 remains in the nuclear recoil region, as it should, being a perfectly shaped pulse in the phonon detector.

In the nuclear recoil region, about 4000 events were cut in the data sample taken as an example here. Since one can quickly investigate events per eye, a good portion of these pulses can be looked at. Hence at this stage

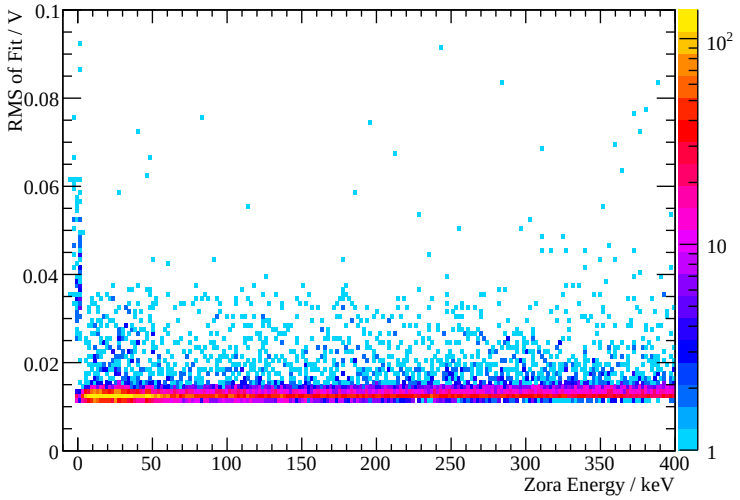

Figure 9.8: Events surviving the previous cuts in a histogram in the RMS-energy plane of the phonon detector ZORA. With a cut at RMS $< 0.03\,\mathrm{V}$ the population of single particle interactions remains basically unaffected. The few events removed by this cut are mostly pile-up events. The population in the vertical band at zero energy are events like the ones in figure 9.2 (b).

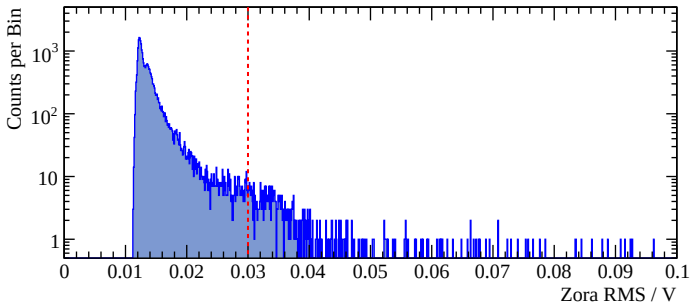

Figure 9.9: Histogram of the events in ZORA that survived the above cuts. Here, the cut is placed at 0.03 V, well in the tail of the distribution (note the logarithmic scaling).

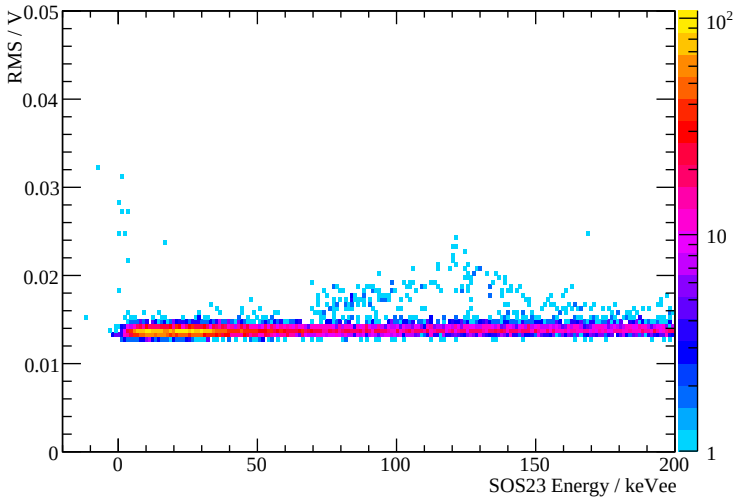

Figure 9.10: Events surviving the previous cuts in a histogram in the `RMS`-energy plane for the light detector SOS23. Placing a cut at `RMS` $< 0.02\,\mathrm{V}$ is well beyond the population of single particle interactions (keeping 99.6% of the events). Again, the few events above that cut are mostly pile-up events, the population in the vertical band at zero energy are events like the ones in figure 9.2 (b), and some of the events that stick out at $\approx 100\,\mathrm{keV}$ will be discussed later in section 9.8.

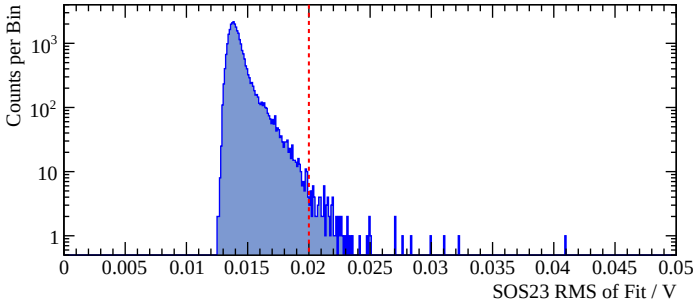

Figure 9.11: Histogram of the events in SOS23 that survived the above cuts. Here, the cut is placed at $0.02\,\mathrm{V}$, again well in the tail of the distribution.

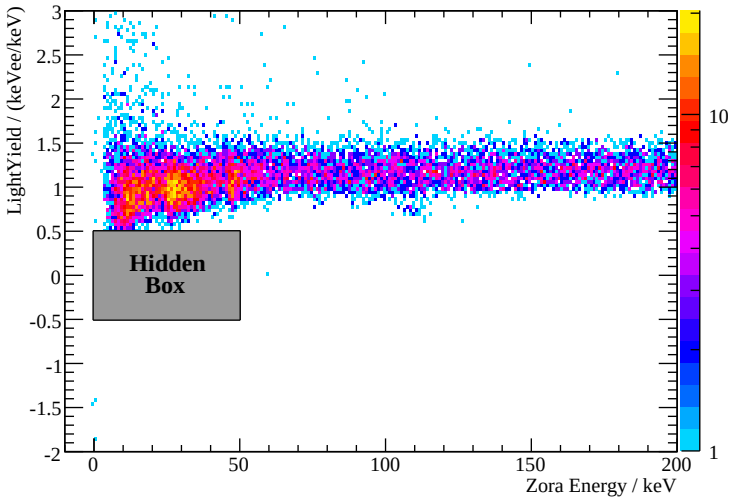

Figure 9.12: Histogram of events from module ZORA/SOS23 during run 30 in the light yield-energy plane after the cuts as described. Color coded is the number of entries per bin according to the palette on the right. Pathological events have been removed.

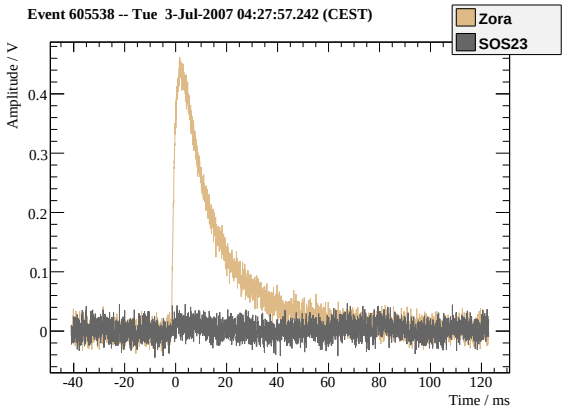

Figure 9.13: This event remains in the nuclear recoil region after the above cuts, before unblinding. The energy is 59.1 keV and the light output 2.3 keV_{ee}, hence the light yield is 0.039 keV_{ee}/keV.

the cut pulses in the nuclear recoil region are investigated by eye to reassure oneself events are removed in the above procedure only for good reason.

As additional cross-check, the cut electron and gamma events within the energy interval $[10, 20]\,\mathrm{keV}$ (and a light yield in $[0.5, 2]\,\mathrm{keV_{ee}/keV}$) are investigated by eye. For the sample considered here, a total of 1610 events in this region survives all cuts, and a total of only 17 events is cut away. Of these 17 events, 9 are of pathological shape. The other 8 cut events piled up on previous high energy events. This again confirms the correctness of the employed cuts.

For proper dead time determination, an important check is whether any of these cuts removes complete time periods. This is by construction true for the stability cut, hence all the live time cut there needs to be accounted for in the dead time. All the other cuts removed events equally throughout time, as can be seen for example from figure 9.14. The vast majority of the cut events are removed by the `amplitude` cut and the `right-minus-left-baseline` cut, and are due to alpha events. Table 9.1 lists the numbers of events that are left after each cut.

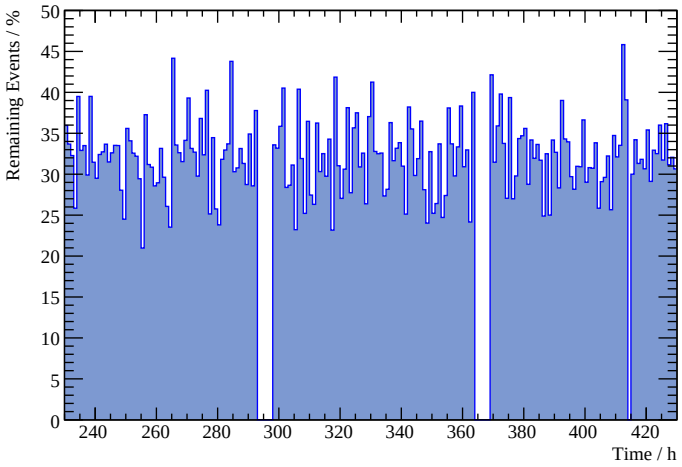

Figure 9.14: Percentage of events remaining after all cuts, in one hour bins, for 200 hours. The two gaps stem from times when the cryostat was refilled with liquid helium and nitrogen, which is necessary every three days.

The fact that the `right-minus-left-baseline` cut mainly removes relaxing baselines following alpha events can also seen when examining the time difference between two events. For radioactive background, the time distribution is expected to follow a Poisson process, so the distribution of time differences should be a simple exponential (see appendix E for the derivation). This is indeed the case, as can be seen in figure 9.15. On the other hand, most of the events that are cut by the `right-minus-left-baseline` cut have a time difference to the preceding pulse close to zero.

Cut	Remaining Triggers	
No Cut	194k	103.7%
Stability	187k	100.0%
Amplitude	128k	68.5%
Zora Trigger	122k	65.1%
Zora Baseline	62k	33.2%
SOS23 Baseline	62k	33.0%
Zora RMS	61k	32.4%
SOS23 RMS	60k	32.2%

Table 9.1: Triggers in Zora for part of run 30 after each cut. The right column gives the numbers normalized to the number of stable triggers. Basically all removed trigger events are alpha events or relaxing baselines and are hence cut by the `amplitude` and `right-minus-left-baseline` cut. For completeness, let it be noted that a total of 123k calibration pulses and 1233k control pulses were injected during the same time period of 1015 hours live time, distributed over 67 days.

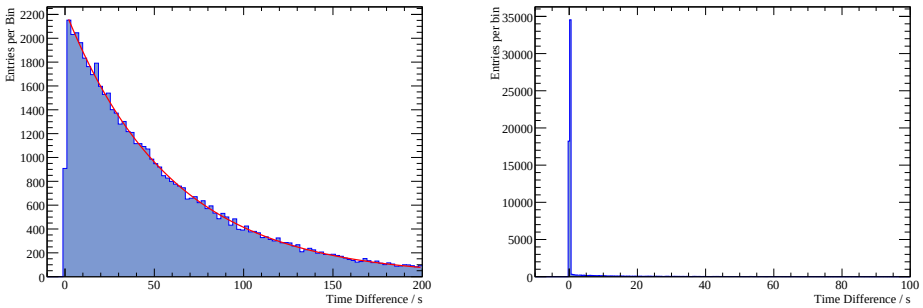

Figure 9.15: Left: The time distribution for the data sample after all cuts nicely fits an exponential (red line) as expected from a Poisson process, with a time constant of (59.3 ± 0.3) s inferred from the fit. This is consistent with the total number of pulses in the histogram, 60k, distributed over a live time of 40 d, hence one event every 57.9 s. Right: Many alpha events cause a second trigger on the relaxing baseline, hence the time distribution of these cut events is sharply peaked at zero.

9.3 Unblinding

With these cuts fixed, module ZORA/SOS23 can now be unblinded: The above cuts are applied to the events in the hidden box. Figure 9.16 shows for the example of this chapter the resulting scatter plot in the light yield-energy plane after each cut, and the final plot is shown as figure 9.17. Three events appear in the nuclear recoil region above 10 keV. Appendix F gives the previous histograms with which the cuts were defined for the complete, unblinded data sample.

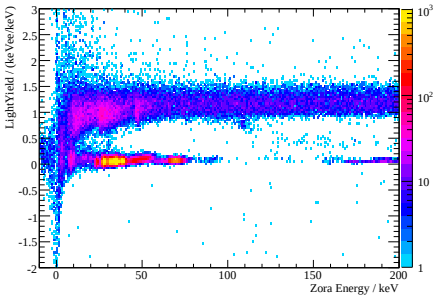

(a): The raw population of all particle events, no cuts are yet applied.

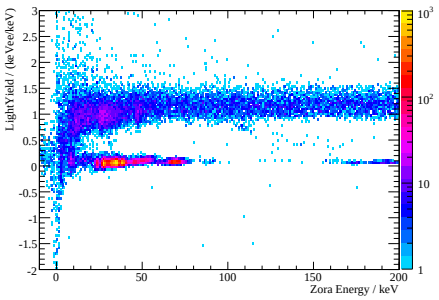

(b): After the stability and amplitude cut.

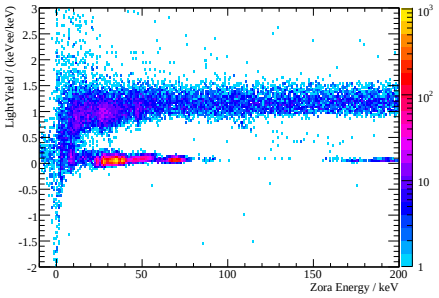

(c): Events close to the ordinate are cut by the trigger cut.

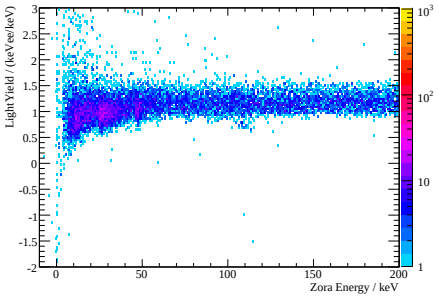

(d): Pathological events are cut on the phonon detector baseline.

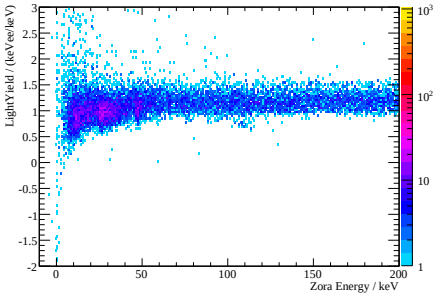

(e): Not much effect after the baseline cut in the light detector.

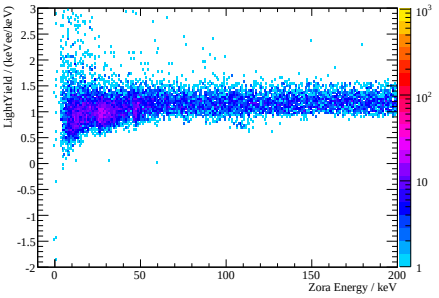

(f): A few mis-reconstructed events are cut on the phonon RMS.

Figure 9.16: Effect of the cuts described in this section; see text for details.

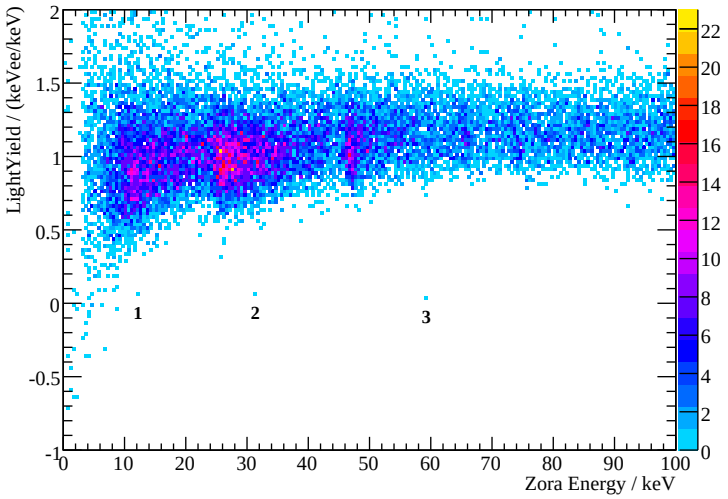

Figure 9.17: Histogram of events in the detector module ZORA/SOS23 after unblinding, now with a linear color scale. Shown is data from 11.888 kg d of exposure during run 30. Three events remain in the most relevant nuclear recoil region above 10 keV, labeled as indicated.

Three of the remaining events are labeled as indicated by the figure. The pulses are shown individually in appendix G. While two of them show no exceptional pulse shape, the event number 1 has a very long decay time. Possible origins of these events are discussed in section 9.5.

9.3.1 Bowler Hats

For technical reasons, the analysis of the background data sample is split in two parts. The analysis presented so far includes about half of the background exposure time used from run 30. The same cuts were applied to the other data set of detector module ZORA/SOS23, and figure 9.18 shows the resulting light yield-energy plot for this second data set.

A surprising number of events in the signal region appears. Inspection of their pulse shapes quickly revealed a few events like the one in figure 9.19. Although the origin of these events is unclear, it is obvious that these events are unphysical and cannot be due to a particle interaction in the target crystal. To make the following discussion easier, these events will be dubbed *bowler* shaped. Their differing pulse shape can already be seen with the naked eye. More importantly, their decay time is much too fast to be due to a true thermal event in the detector: These pulses decay from 0.12 V to 0.02 V in 2 ms which translates into a decay time of ≈ 1 ms. This needs to compared to the thermal relaxation following a particle interaction, which for ZORA happens with a decay time of 16 ms, more than an order of magnitude slower.

Another peculiarity about these events is their timing. A total of ten

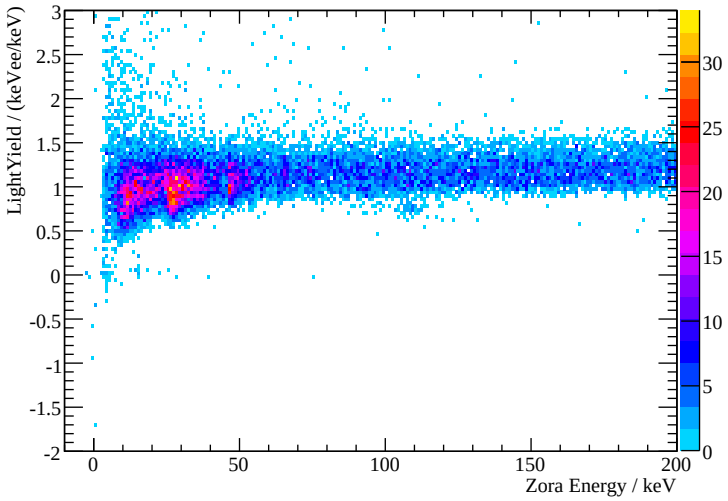

Figure 9.18: Histogram of events in ZORA after unblinding for a second data set during dun 30. Many events are seen in the low energy and low light yield region of the plot.

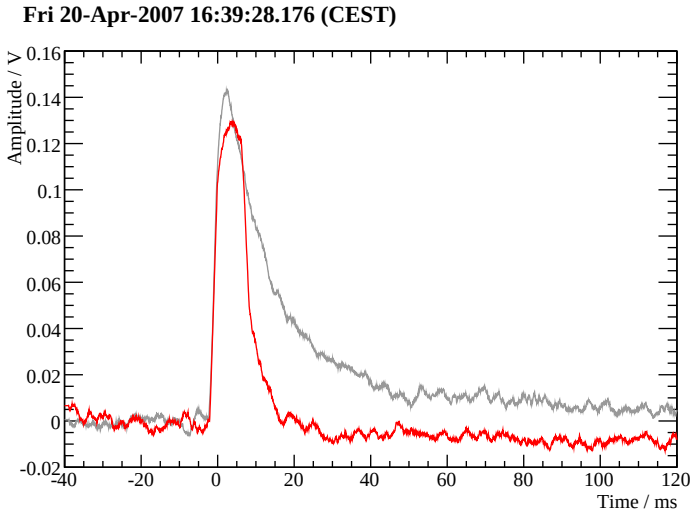

Figure 9.19: One of the events that appeared in the signal region of ZORA after unblinding in red, with a normal event of similar pulse height for comparison (gray). Plotted is the 50 channel average of the pulse to reduce the visual impact of noise. While the rise time of the pulse is consistent with a true particle interaction, the decay is much too fast to be due to a thermal event in the detector.

bowler events was found, out of which seven came within seven minutes on April 20th, 2008, and another two within the next two days. Table 9.2 gives their arrival times and pulse heights.

Number	Arrival Time	Bowler Amplitude	RMS Bowler/ RMS StdEvt
1	March 24th, 15:25:32.156	0.187 V	0.83
2	April 20th, 16:39:28.176	0.136 V	0.65
3	April 20th, 16:39:50.353	0.128 V	0.81
4	April 20th, 16:39:58.029	0.130 V	0.81
5	April 20th, 16:40:02.512	0.128 V	0.80
6	April 20th, 16:45:51.907	0.136 V	0.67
7	April 20th, 16:45:55.583	0.131 V	0.81
8	April 20th, 16:46:29.448	0.132 V	0.79
9	April 21th, 22:35:18.796	0.139 V	0.65
10	April 22th, 23:01:51:841	0.135 V	0.79

Table 9.2: Some parameters of the observed bowler type events in ZORA during run 30. All are very similar except the first one which has a higher amplitude and a pulse shape with a little broader plateau.

If one accepts that these events cannot be due to a particle interaction, they *have to* be discarded for the Dark Matter analysis. Since they were only discovered after unblinding, greatest care has to be taken to design a legitimate cut. Here, we use those events and create a standard bowler event from them, which is fitted to all pulses. In addition to the previously used RMS value of the usual standard event fit, `RMS StdEvt`, this now gives an additional parameter `RMS Bowler` from the fit of these pathological events. The ratio `RMS Bowler/RMS StdEvt` is histogrammed in figure 9.20.

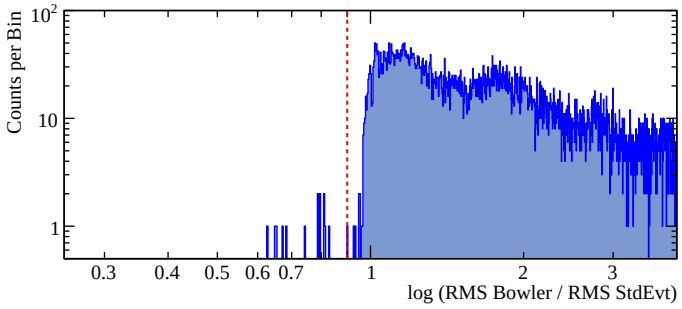

Figure 9.20: Histogram of the ratio of the fit parameters. The logarithm of the ratio is plotted to have equal distortion for values smaller and larger than unity. A non-blind cut requires events to have a ratio > 0.9.

A non-blind cut is enforced that requires pulses to have a ratio `RMS Bowler/RMS StdEvt` > 0.9. This cuts all 10 bowler events, and in addition 4 events which are direct hits of the light detector with a small

associated signal in the phonon detector, as well as one event of the spiky type shown in figure 9.2 (b). All the pulses that are removed by this bowler cut are shown in figure H.1 in the appendix on page 235. The cut is also applied to the event sample of the previous section but removes no events there.

Eventually, figure 9.21 shows the events in the light yield-energy plane for the second data set of ZORA. Again, a few events remain in the area where Dark Matter induced tungsten recoils are expected. They are numbered in the figure and shown individually in appendix G, where relevant parameters are given also. Half of these events have a decay time much longer than expected for particle interactions, yet survive the deliberately lax cuts.

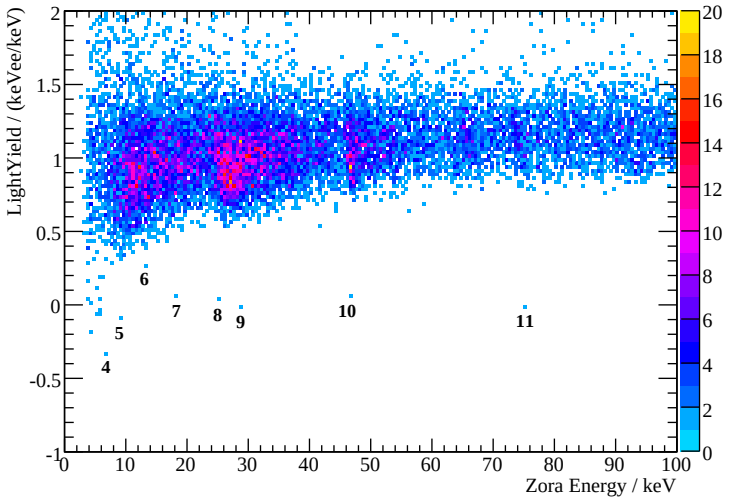

Figure 9.21: Events in the light yield-energy plane for the second data set of ZORA after the bowler cut. The data is accumulated from 10.050 kg d of exposure to background radiation during run 30.

9.4 Other Data Sets

For the data analyzed here, the resolution of the light channel is generally limited by energy independent noise that is already present on the baseline. For the light detector SOS21, paired with VERENA, this is particularly important, as can be seen from figure 9.22. After some modifications to the front-end biasing electronics in April, at around 430 h in figure 9.22 (after data file `bck2_025`), the baseline noise of SOS21 had improved by more than a factor 3. As a technical aside, it is crucial for the data analyst to realize that after data file `bck2_025` the conversion factor for the energy calibration using heater pulses changed for all detectors following an additional modification.

Hence for the Dark Matter analysis, the run is divided into separate

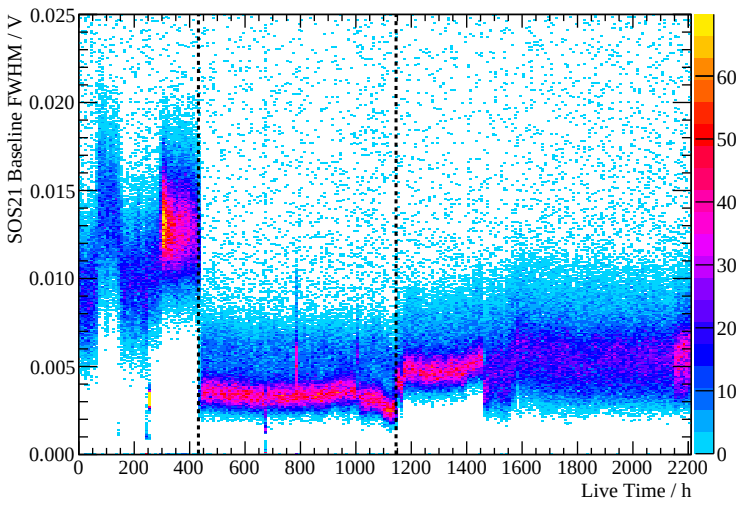

Figure 9.22: FWHM of the baseline noise of light detector SOS21 during run 30. The data is analyzed individually for three time periods separated by the black dashed lines, labeled noise-period high, low, and medium.

data sets which are analyzed individually. This results in a better energy resolution of the light channel for the later data sets, which leads to a better discrimination capability at low energies.

The analysis closely follows the example of detector Zora discussed before, the only relevant difference being that the phonon detector Verena is not linear up to 122 keV, so a standard event was built from the 62 keV tungsten K_α escape peak. Figures 9.23, 9.24 and 9.25 show the resulting events in the light yield-energy plane. A total of about 10 events appear below the electron/gamma band. They are labeled in the figures and shown individually in appendix G together with some relevant parameters. Again, many of them are seen to have an atypically long decay time.

9.5 Discussion of Low Light Yield Events

The origin of the observed dark events is unclear. A few possibilities are considered in the following.

9.5.1 External Neutrons

Given the thickness of the neutron shield we would only expect $\mathcal{O}(10^{-5})$ neutron events per kg d of exposure [215]. However, after this data taking, a weak point in the neutron shield above the radon box was identified, as indicated in figure 4.4 on page 70. One can readily estimate how many neutrons could leak in through this gap: We can approximate the shielding as a cylinder with radius 1.5 m, with a gap that spans at most an angle of 11° as seen from the detectors. This estimate assumes that the shielding

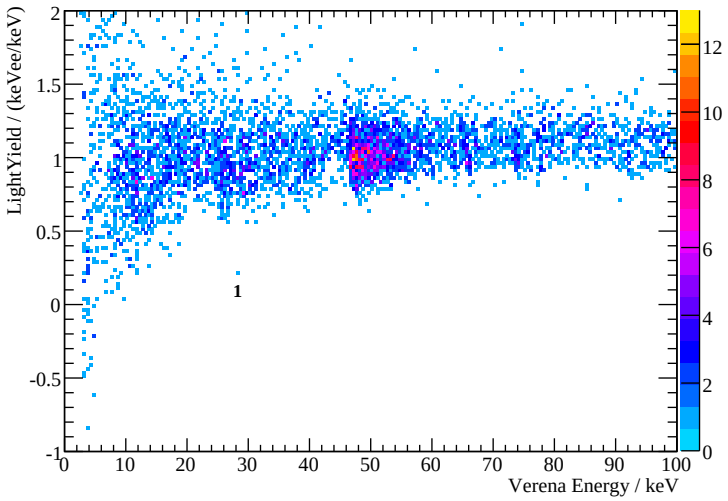

Figure 9.23: Events in the light yield-energy plane for the first data set (high noise) of VERENA after 5.359 kg d of exposure during run 30.

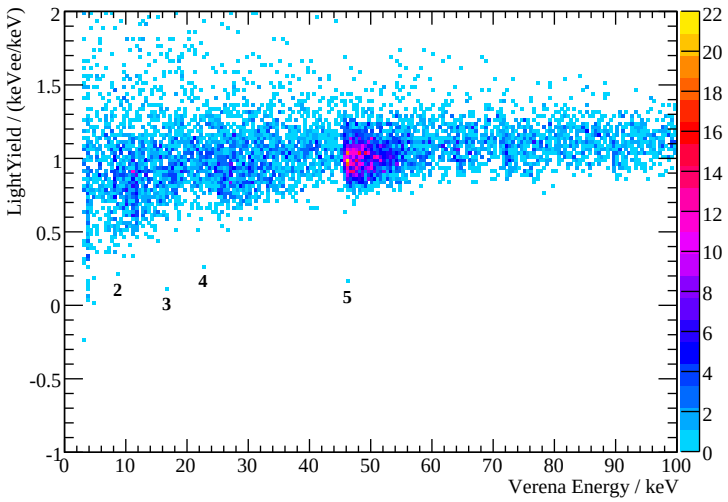

Figure 9.24: Events in the light yield-energy plane for the second data set (low noise) of VERENA after 7.462 kg d of exposure during run 30.

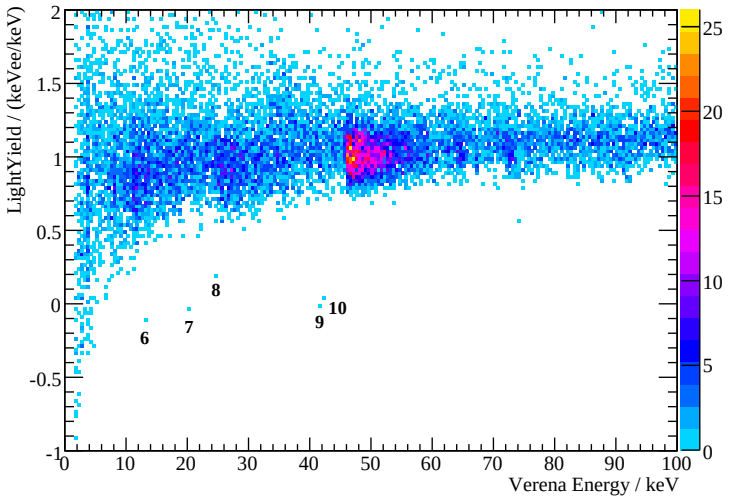

Figure 9.25: Events in the light yield-energy plane for the third data set (medium noise) of Verena after 12.767 kg d of exposure during run 30.

has no effect if the polyethylene is less than ≈ 10 cm thick, so it is a very conservative approximation. This would then correspond to a fraction of 4% of the total surface of the shielding to be uncovered. Given a rate of neutron induced events during run 28 of $0.9\,\mathrm{kg}^{-1}\,\mathrm{d}^{-1}$ [267], this leads us to expect less than 2 events for the combined exposure of 47.525 kg d. Note, however, that neutron induced events should be oxygen recoils due to the kinematics involved and hence be only quenched by a factor $Q \approx 10$.

9.5.2 Other Modules

Radioactive decays in target crystals may lead to neutrons produced within the shielding, mostly from the uranium and thorium chains. If such a decay happens in a crystal that is not operated, such a decay cannot be vetoed. This may therefore contribute to the neutron background. However, given the observed activity of the operational crystals, this background can be estimated to contribute less than $10^{-5}\,\mathrm{kg}^{-1}\,\mathrm{d}^{-1}$ per inactive module [284]. Hence we expect no contribution from this source.

9.5.3 Muon Induced Events

We only expect 3×10^{-3} muon induced events per kg d of exposure [215]. No muon signals in the muon veto were found in coincidence with the observed dark events. This renders this possibility very unlikely as explanation for the observed dark events.

9.5.4 Alpha Decays

An alpha decay in the vicinity may lead to a recoiling nucleus impinging on the crystal. Such events are indeed observed; they are discussed in detail in section 9.8. In order to push these nuclear recoil events out of the acceptance region for WIMP induced events, all surfaces facing the crystal are covered with an efficient scintillator. In this way, the alpha particle produces additional scintillation light. However, if not all surfaces facing the detector are scintillating, this may lead to residual dark events. Yet, given the rather complete coverage of the module with scintillating foil, no dark events from this source can be expected in run 30.

9.5.5 Cracks in the Crystals

Cracks can appear in the crystals following thermal stress if the clamping is too tight (sections 3.3.6 and 4.3.5). Such events are not expected to give any scintillation light and may hence appear in the nuclear recoil band. Cracks in CRESST-I sapphire crystals were observed to have the same pulse shape as particle interactions. However, these cracks should eventually be observable in the crystals with a standard microscope.

9.5.6 Thermal Relaxations

A likely cause for the observed dark events is thermal relaxation in the clamps that hold the crystal. The bad thermal conductivity of the scintillating foil wrapped around them would result in a longer decay constant for the associated phonons. This could then explain the observed long decay times of many of the dark events.

In run 31, a detector module is operational that is clamped without any plastic scintillator between the crystal and the metal clamp. After a preliminary analysis from a small portion of the data from this module, indeed no dark events were observed there. Other modules operated in run 31 have clamps that are covered with a different plastic scintillator, and they might show an even increased rate of dark events. Ongoing work will clarify this point. Given the knowledge at the time of writing, this seems the most likely explanation for the majority of the observed events.

In this case, one would impose an additional cut on the `decay time` of the pulses, rejecting such pulses which decay too slowly. The idea behind this is based on the detector model explained in section 4.3.7, and justified by the observation that will be made in section 9.8.2, namely, that already $\approx 100\,\mathrm{keV}$ pulses from heavy ion recoils hardly differ from electron or gamma induced pulses. The long decay of the pulses would hence be attributed to an energy release e.g. in the clamps holding the crystal, in combination with a bad thermal conductance to the crystal. To this end, figure 9.26 shows the `decay time` versus energy for the second data set of ZORA during run 30. Based on this distribution one could then reject events far from the main

population. In this data set, a cut on `decay time` $< 16\,\mathrm{ms}$ would remove 5 out of the 8 events observed, and no other events at all.

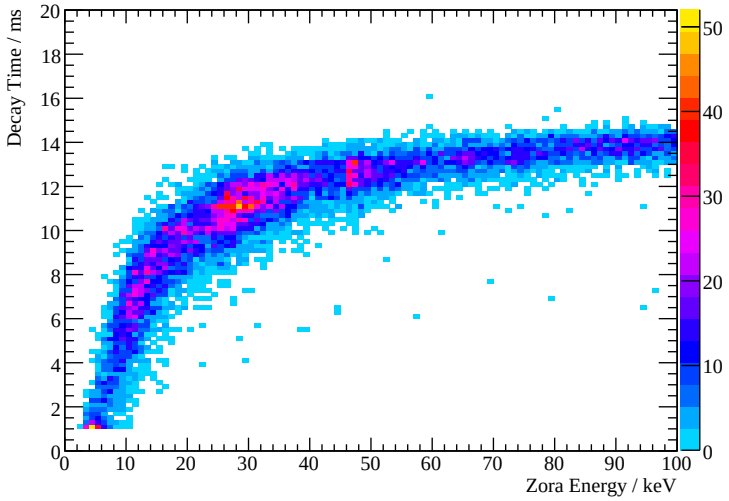

Figure 9.26: Histogram of the decay times of pulses in the phonon detector Zora during run 30. Most of the observed dark events have decay times well above 16 ms.

9.5.7 WIMPs

It seems unlikely that the observed events are WIMP induced. In addition, the observed events show a flat energy spectrum, in contrast to the quasi-exponential spectrum anticipated from WIMPs. Their energies range up to almost 80 keV, well above the energies expected for WIMP induced recoils.

We will therefore use the data to put a limit on the coherent WIMP-nucleus scattering cross section in the next chapter. In order to do so, the phonon and light detector resolutions are extracted from the data in the following two sections.

9.6 Phonon Detector Resolution

The resolution of the phonon detectors is only used to convolve the expected WIMP spectrum. Since this spectrum is rather featureless, the phonon detector resolution is of little relevance as long as it is significantly better than the threshold. For our phonon detectors the resolution can readily be inferred from the observed peaks in the calibration and background runs. Table 9.3 gives measured values for the width (1σ) of peaks at different energies. Figure 9.27 shows this data together with the results from a linear fit, which is sufficient for the purpose needed here.

Energy (Origin)	Detector, Run	Resolution
3.61 keV (^{41}Ca)	VERENA, run 30	(0.13 ± 0.02) keV
8.04 keV (Cu K_α)	VERENA, run 30	(0.17 ± 0.04) keV
	ZORA, run 30	(0.54 ± 0.15) keV
11.5 keV (unknown)	DAISY, run 27	(0.24 ± 0.05) keV
	DAISY, run 28	(0.32 ± 0.08) keV
	VERENA, run 30	(0.28 ± 0.04) keV
46.5 keV (^{210}Pb)	DAISY, run 27	(0.38 ± 0.04) keV
	DAISY, run 28	(0.41 ± 0.08) keV
62.8 keV (^{57}Co-$K_{\alpha1}$)	VERENA, run 30	(0.41 ± 0.03) keV
	ZORA, run 30	(0.79 ± 0.03) keV
64.1 keV (^{57}Co-$K_{\alpha2}$)	VERENA, run 30	(0.43 ± 0.05) keV
65.4 keV (^{179}Ta)	DAISY, run 27	(0.54 ± 0.11) keV
	DAISY, run 28	(0.53 ± 0.14) keV
	VERENA, run 30	(1.19 ± 0.23) keV
	ZORA, run 30	(0.69 ± 0.12) keV
73.7 keV (^{181}W)	DAISY, run 27	(0.39 ± 0.14) keV
	DAISY, run 28	(0.31 ± 0.14) keV
	VERENA, run 30	(0.89 ± 0.13) keV
	ZORA, run 30	(0.43 ± 0.12) keV
122.0 keV (^{57}Co)	DAISY, run 27	(0.89 ± 0.03) keV
	DAISY, run 28	(0.80 ± 0.03) keV
	VERENA, run 30	(0.97 ± 0.04) keV
	ZORA, run 30	(1.07 ± 0.01) keV
136.5 keV (^{57}Co)	DAISY, run 27	(0.96 ± 0.08) keV
	DAISY, run 28	(0.85 ± 0.10) keV
	VERENA, run 30	(1.07 ± 0.12) keV
	ZORA, run 30	(1.08 ± 0.01) keV

Table 9.3: Resolution (1σ) of various detectors from Gaussian fits to suitable peaks. Spectral features that have multiple origins and hence no clear peak signature are excluded from this table.

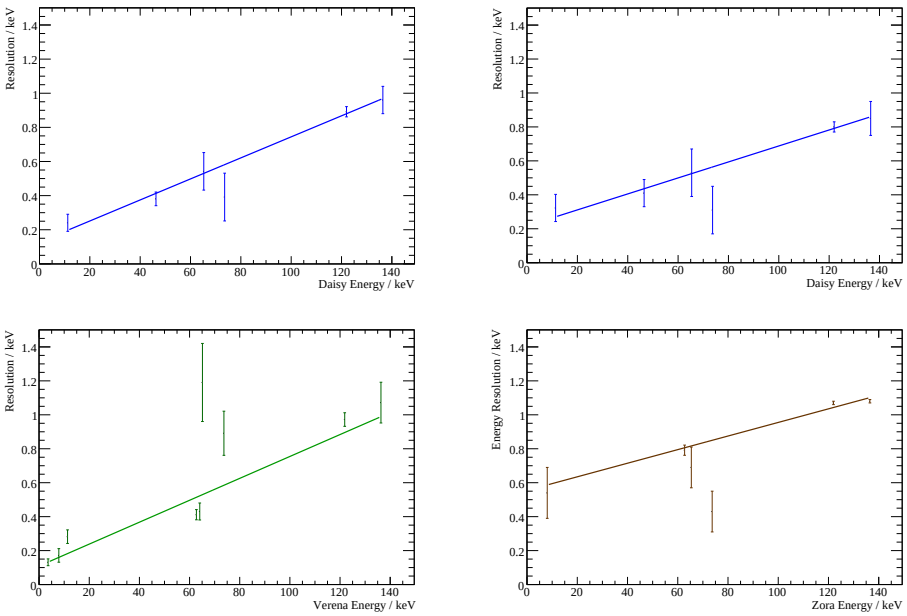

Figure 9.27: Graphs of the 1σ resolution of the different detectors (values in table 9.3) together with a linear fit. The results are, from top left to bottom right, $\Delta E(E) = 0.13\,\mathrm{keV} + 0.0062E$ for Daisy in run 27, $\Delta E(E) = 0.22\,\mathrm{keV} + 0.0047E$ for Daisy in run 28, $\Delta E(E) = 0.11\,\mathrm{keV} + 0.0065E$ for Verena in run 30 and $\Delta E(E) = 0.56\,\mathrm{keV} + 0.0040E$ for Zora in run 30. Given the errors it is not clear whether there is physics behind the ^{179}Ta peak being broader than the ^{181}W peak.

9.7 Light Detector Resolution

The resolution $\sigma(E)$ of the light detectors is much more crucial since it is used to define the acceptance region for WIMP induced recoils. The better the energy resolution, the better the discrimination between electron/gamma events and nuclear recoils. Thus a lower discrimination threshold can be set, which, given the steeply rising recoil spectrum expected from WIMPs, increases the significance of the analysis.

The resolution of interest here is the convolved resolution of the whole detector module. This includes the light output characteristics of the crystal, reflectivity of the foil, possible position dependencies of the light absorber, counting statistics, as well as electronic and thermal noise in the detector:

- The baseline noise of the detector gives an energy independent contribution σ_0. Various sources contribute here, such as noise from the SQUIDs and thermal fluctuations in the thermometer.

- Our light detectors can register events with less than 10 photons [233, 234], so Poissonian counting statistics are relevant. Hence we can expect a term $\sigma_1\sqrt{E}$ to contribute to the resolution of the light detectors.

- We have seen in chapter 7 that there is a position dependence of the light output of the crystal, and in chapter 8 that most low energy events in a background run originate from the surface of the detectors. Also, there may be a dependence of the detector response on the position of the absorption in the light detector [285]. We model these and possible other effects with an additional contribution $\sigma_2 E$ to the resolution.

Since the individual sources of noise are independent from each other, they are added quadratically to give the resolution of the light detector as

$$\sigma^2(E) = \sigma_0^2 + \sigma_1^2 E + \sigma_2^2 E^2. \tag{9.1}$$

A simple way to extract this resolution would be to bin the data in energy (taken from the phonon detector), extract the resolution individually for each energy bin, and then fit these resolutions with equation 9.1. However, there are a couple of drawbacks with this procedure. Most importantly, if the resolution is extracted from the light-energy-plane, it is systematically worsened by the energy dependence of the light output. Hence this procedure systematically overestimates the resolution. If it were extracted from the yield-energy plane, the resolution of the phonon detector would be folded in the extracted resolution, making it cumbersome to extract the true resolution.

These issues can be avoided when working on unbinned data in the light-energy plane, in which functions for both the energy dependence of the band as well as the energy dependence of the resolution are fitted. Such a

method is presented in appendix I, and was used in previous works [234, 286]. However, it suffers from two second order effects: One is the non-linearity of the band as discussed in chapter 7. Although incorporable in principle, the quality of the fit as well as its convergence suffers. The major drawback comes from the non-gaussianity of the electron/gamma band due to **excess light events**. This causes also this method to systematically overestimate the resolution of the light detector. In the following, these excess light events are discussed, and a more appropriate method to determine the light channel resolution is presented.

9.7.1 Excess Light Events

As can be seen in any of the previous light yield-energy histograms (e.g. on page 172), at energies of $\mathcal{O}(10\,\mathrm{keV})$, there is a class of events with high light yield that leak out of the electron/gamma band. This shifts the calculated centroid of the band to higher energies and in addition leads one to deduce a worse resolution at low energies than would be appropriate.

The conjecture was that these excess light events are due to backscattered electrons. Hence they have an interaction directly with the light detector in addition to the interaction with the crystal. If true, this should result in a faster pulse in the light detector, more resembling the pulse shape of a direct hit. To examine this conjecture in more detail, the pulse shapes of these events are compared in figure 9.28, and it can be seen that indeed the excess light events are faster. The individual time constants from a fit of the detector model to these pulses (equation 4.8 on page 82) are given in table 9.4.

Pulse	τ_n	τ_in	τ_t	$A_\mathrm{n}/(A_\mathrm{n}+A_\mathrm{t})$
Direct hit	0.15 ms	3.9 ms	13.3 ms	77%
Excess light	0.13 ms	5.0 ms	21.2 ms	88%
Crystal event	0.43 ms	5.3 ms	29.5 ms	90%

Table 9.4: Parameters from a fit of equation 4.8 to the pulses in the light detector SOS23 that are shown in figure 9.28. Errors of the fits are smaller than the stated precision. The excess light events have a τ_n comparable to the direct hits, and are much faster than scintillation events originating from the crystal.

This observation allows to design a cut to reject these events, which can help to correctly determine the resolution of the light detector (appendix I). This cut works in a very similar manner to the one described in the context of the bowler shaped events, section 9.3.1: In addition to the usual (correlated truncated) standard event fit, a second fit is performed, with **light only events** as template, that is, events that are direct hits of the light detector. Both fits yield the χ^2 or `RMS` as quality parameter. The ratio of these two values is then used to discriminate excess light events as shown in figure 9.29.

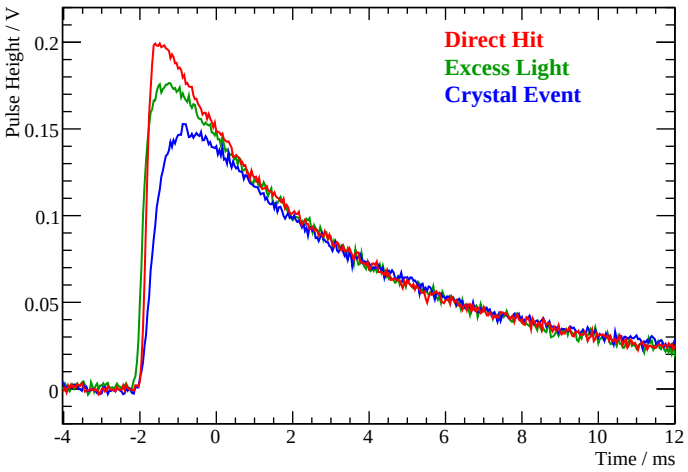

Figure 9.28: Comparison of standard events, each built from 37 pulses in the light detector SOS23 during run 30. Clearly, excess light events (green) are faster than normal events from the electron/gamma band (blue), yet slower than direct hits of the light detector (red). See table 9.4 for a quantitative comparison.

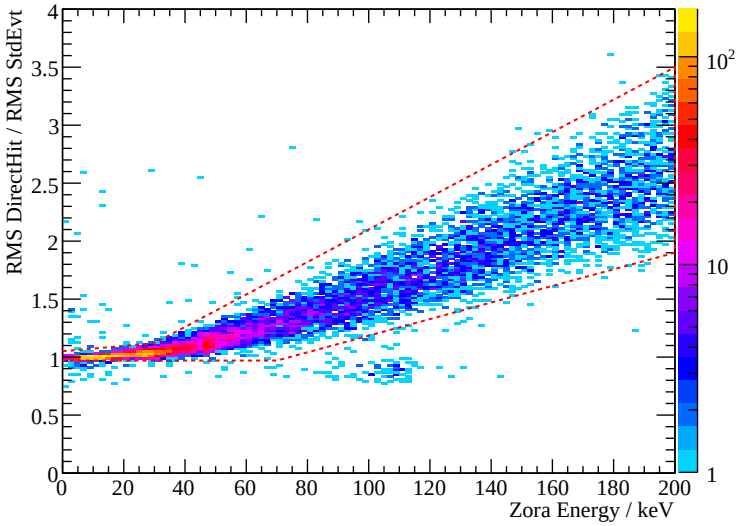

Figure 9.29: In order to ease a correct determination of the light detector resolution, events may be cut if they are out of the main distribution, as indicated by the dashed line. Since efficiency is not much of an issue to define the resolution, the cut may be placed tightly around the population. A similar second cut in a plot against energy in the light detector would yield an even cleaner event sample. The population of events that is seen in the figure below the main band at $\approx 100\,\mathrm{keV}$ will be discussed in section 9.8.

9.7.2 Determination of the Resolution

As an alternative to the previously mentioned methods, a natural and at the same time very accurate method to determine the resolution is as follows. The data is binned in a two-dimensional histogram in the light-energy-plane (L, E). This histogram is then fitted in one step with a two dimensional Gaussian that gives both the dependence $L(E)$ of the electron/gamma band, as well as the resolution $\sigma(E)$.

More precisely, the background density $\varrho_{\mathrm{b}}(L, E)$ is fitted with the Gaussian

$$\varrho_{\mathrm{b}}(L, E) = A(E) \frac{1}{\sqrt{2\pi}\,\sigma} \exp\left(-\frac{1}{2}\frac{(L - L(E))^2}{\sigma^2(E)}\right). \tag{9.2}$$

Since the detectors are linearized with both the truncated standard event fit and the calibration with heater pulses, the energy dependence of the mean $L(E)$ is to first order a simple linear function, $L(E) = l_1 E$. In addition, the non-proportionality of the light yield can be modeled with this procedure. Here, the dependence

$$L(E) = \frac{l_1 E}{1 + \exp(-l_{\mathrm{e}} E)} \tag{9.3}$$

with both $(l_1, l_{\mathrm{e}}) > 0$ is found to model the dependence with high accuracy. The resolution $\sigma(E)$ is modeled with equation 9.1,

$$\sigma(E) = \sqrt{\sigma_0^2 + \sigma_1^2 E + \sigma_2^2 E^2}. \tag{9.4}$$

At this point we still need a parametrization for the amplitude $A(E)$ as an input to the fit. Here, the energy dependence of the amplitude is taken from the observed (one-dimensional) spectrum. One additional scaling parameter a is incorporated which allows the fit to reduce the amplitude as a compensation for discarded excess light events or, more generally, as a compensation for a non-Gaussianity of the band. Hence the amplitude is taken as

$$A(E) = a\ \mathrm{Spectrum}(E). \tag{9.5}$$

If there were a significant nuclear recoil background in the data, this would introduce an error in the fit. Certainly the sound discrimination capability of the CRESST-II detectors exclude this possibility above a few keV, so even if it were present just above threshold, its influence would still be negligible given the range of the fit over 100 keV or so.

Naturally, graphical representations of three dimensional circumstances are limited, yet figure 9.30 is a doomed attempt to visualize the fit. For Zora/SOS23 in run 30, the values obtained from the fit are shown in table 9.5. They are similar to values obtained from alternative methods (appendix I and [234]), but more precise. The fit has an excellent $\chi^2/ndf = 3536/3450 = 1.02$ given only 6 free parameters. In addition, the derived

values are very robust, well within the stated errors, toward variations of the binning of the data histogram or an extension of the fit range. Finally, the influence of excess light events has been suppressed, and the results are stable whether or not these events are taken into account. Table 9.6 gives the parameters for the three noise periods of detector module VERENA/SOS21.

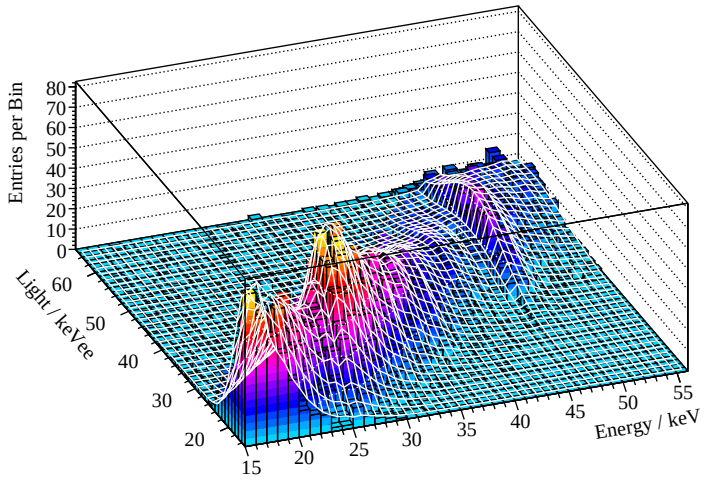

Figure 9.30: Attempt to visualize the fit in two dimensions; For clarity, only a detail is shown. In color the histogram with the data from ZORA during run 30, the white lines is the fit.

Parameter	Fit
a	(0.917 ± 0.009)
l_1	$(1.068 \pm 0.003)\,\mathrm{keV_{ee}/keV}$
l_e	$(0.180 \pm 0.007)\,1/\mathrm{keV}$
σ_0	$(1.1 \pm 0.3)\,\mathrm{keV_{ee}}$
σ_1	$(0.46 \pm 0.03)\,\mathrm{keV_{ee}/keV}$
σ_2	$(0.178 \pm 0.004)\,\mathrm{keV_{ee}/keV^2}$

Table 9.5: Values and associated errors from the two-dimensional fit to the data of ZORA/SOS23 in run 30.

To check in more detail how well the fit describes the true situation, the data is binned in 2 keV energy bins. For each bin, the number of events that are observed within a given sigma around the central line of the band is compared to the number of events expected for a Gaussian distribution. Figure 9.31 is a graphical representation of this ratio, seen to have only small deviations from a fully Gaussian behavior. Consequently, the comparison of the fitted resolution with a binned RMS, shown in figure 9.32, is highly consistent. Finally, figure 9.33 shows the observed data from ZORA/SOS23 together with the fit.

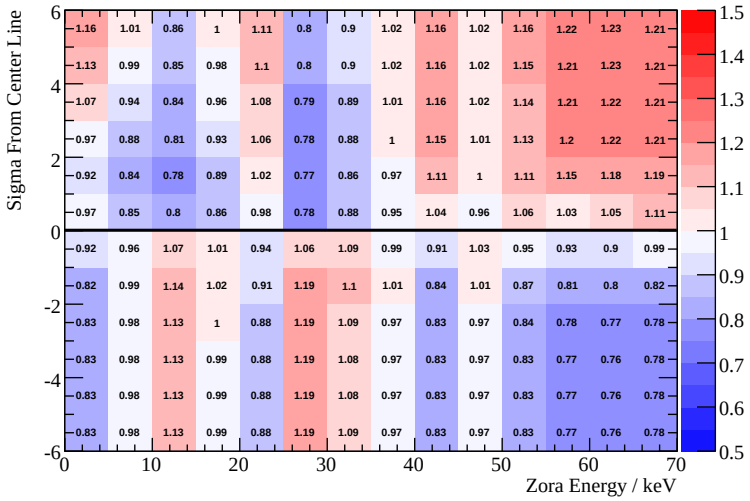

Figure 9.31: Ratio observed entries divided by expected entries within a given confidence around the central band, shown color coded as well as numerically. There are no systematic deviations (there are no large patches of one color or the other). Generally, the method is in excellent agreement with the data and good to about 10%.

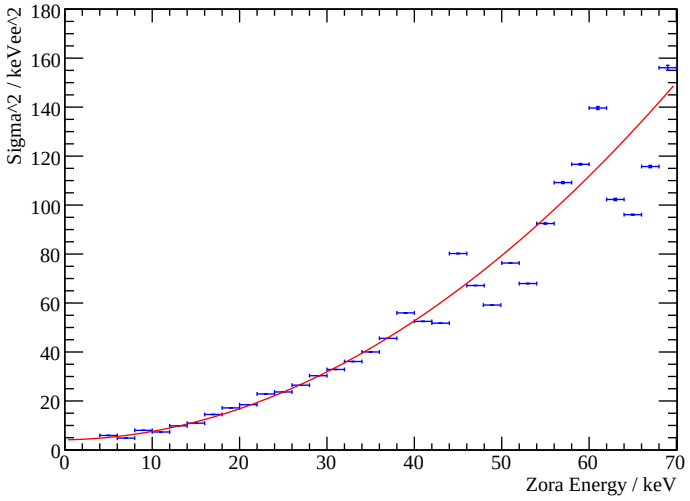

Figure 9.32: Resolution of the light detector SOS23 in the data sample discussed here. The blue line is the resolution σ^2 as inferred from the two dimensional fit. The data points are σ^2 from a Gaussian fit to the data in each 2 keV energy bin. Fit and data are seen to be in excellent agreement.

Parameter	High	Low	Medium
a	0.94 ± 0.02	0.88 ± 0.01	0.85 ± 0.01
l_1/ keV$_{ee}$/keV	1.021 ± 0.005	1.035 ± 0.003	1.036 ± 0.002
l_e/ 1/keV	0.169 ± 0.001	0.171 ± 0.008	0.22 ± 0.01
σ_0/ keV$_{ee}$	3.5 ± 0.6	1.18 ± 0.37	1.26 ± 0.13
σ_1/ keV$_{ee}$/keV	1.00 ± 0.15	0.72 ± 0.07	0.76 ± 0.04
σ_2/ keV$_{ee}$/keV^2	0.03 ± 0.08	0.09 ± 0.01	0.106 ± 0.006

Table 9.6: Values and associated errors from the two-dimensional fit to the data of VERENA/SOS21 in the three noise periods during run 30.

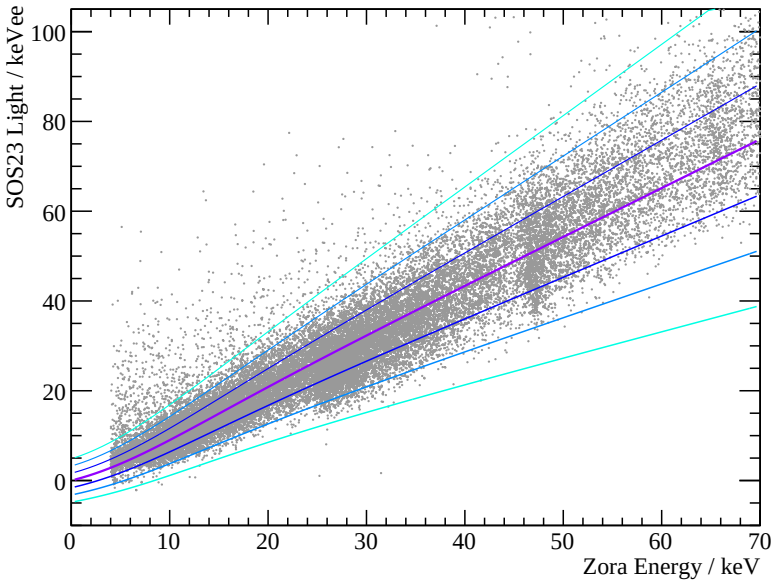

Figure 9.33: Scatter plot of data from ZORA/SOS23, run 30, in the light-energy-plane. Superimposed is the fitted electron/gamma band (thick line) with the one-, two- and three-sigma lines.

Dark Matter interactions are expected to give almost no light, so the energy independent σ_0 term of the resolution is the most important one. It gives the resolution of the light detector itself, mainly due to noise on the baseline, and independent of counting statistics or scintillation effects in the crystal. Its value can be compared to the resolution of heater pulses that are injected directly in the light detector. Figure 9.34 shows the `amplitude` distribution of these pulses for different injected energies. Gaussians are fitted to each distribution individually, yielding consistently a resolution (1σ) of $\sigma_0 = (1.080 \pm 0.006)\,\mathrm{keV_{ee}}$ (where the error is the spread of the individual fits). This agrees with the value inferred above, $\sigma_0 = (1.1 \pm 0.3)\,\mathrm{keV_{ee}}$.

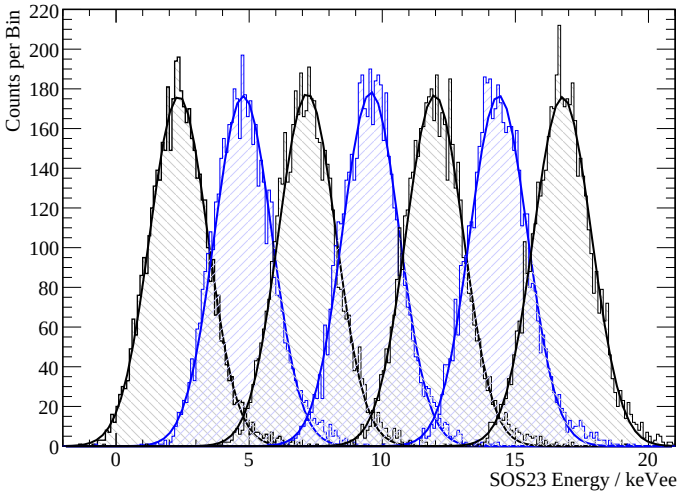

Figure 9.34: Resolution of heater pulses injected on the light detector SOS23 during run 30 with varying energy. Each energy distribution is fitted individually with a Gaussian, yielding consistent results for the energy independent light detector resolution term σ_0 as the method described before.

9.7.3 Validating the Method with Simulation

A small simulation was set up in order to validate the method and to get a feeling for the accuracy that may be expected for a true Gaussian behavior. To this end, events were drawn from the spectrum, and their light simulated according to a Gaussian distribution, equation 9.2, with energy dependent $L(E)$ and $\sigma(E)$. The task is then for the algorithm to reconstruct the simulated values $l_1 = 1.1$, $l_e = 0.2$, $\sigma_0 = 1.5$, $\sigma_1 = 0.4$ and $\sigma_2 = 0.2$. More than 2000 data sets were simulated, and figure 9.35 shows the distributions of the resulting parameters.

As can be seen from this figure, the values of the central band l_1 and l_e are reconstructed with a precision at or below the percent level. The constant term in the resolution σ_0 has a tendency to be slightly overestimated, albeit consistent with the stated error. Fitting results in an erroneous $\sigma_1 = 0$ in

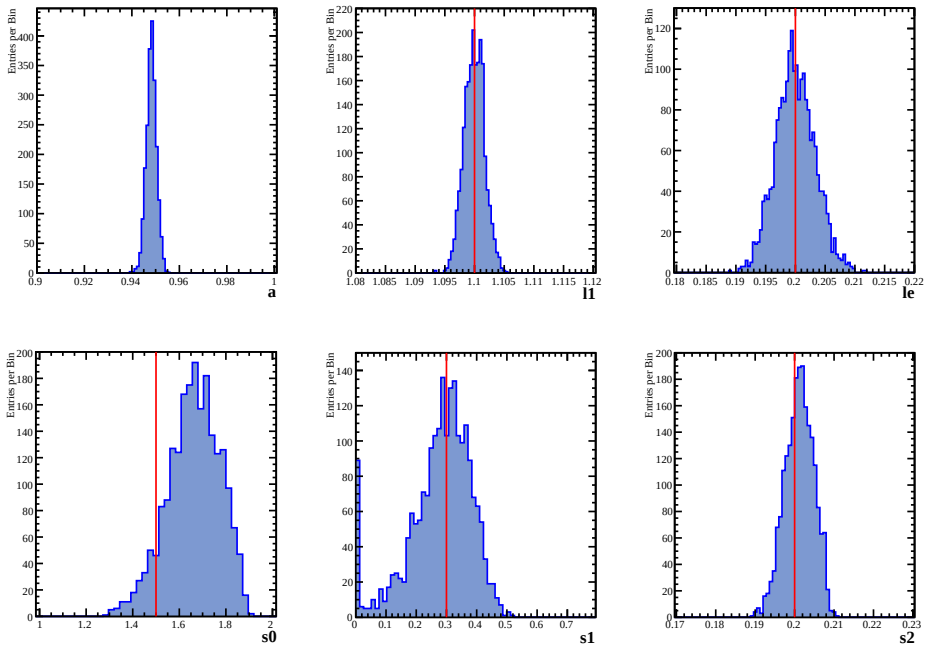

Figure 9.35: Reconstructed values from more than 2000 fits to simulated data, with the simulated parameters shown as red lines. From top left: a, l_1, l_e, σ_0, σ_1 and σ_2.

4% of the simulated cases, but if such a case would happen on data, it could easily be recognized by the unphysical value and a large error associated with it. Slightly changing the binning of the data histogram would find a remedy for this problem. σ_3 is robustly found at the correct value.

Analogous to the previous section, figure 9.36 shows the ratio of observed simulated events over the expected events for a pure Gaussian distribution, and figure 9.37 compares the binned width with the fitted resolution. As expected, both distributions are in excellent agreement, and the observed small deviations can help to put the fit on the data into perspective.

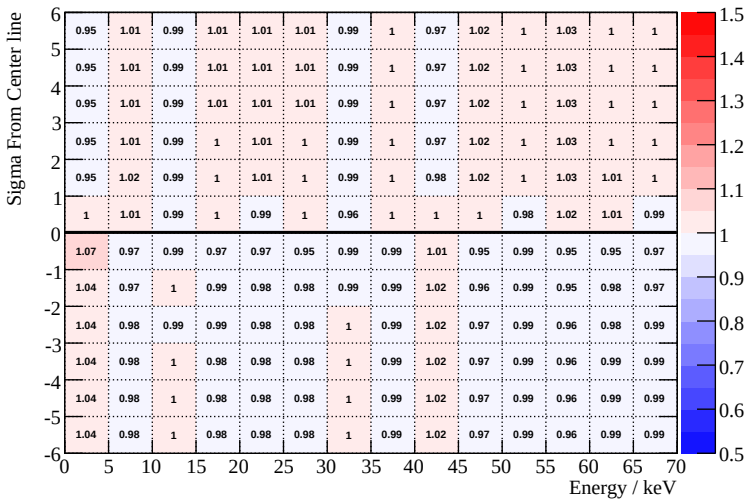

Figure 9.36: Ratio of simulated events per expectation for a pure Gaussian distribution.

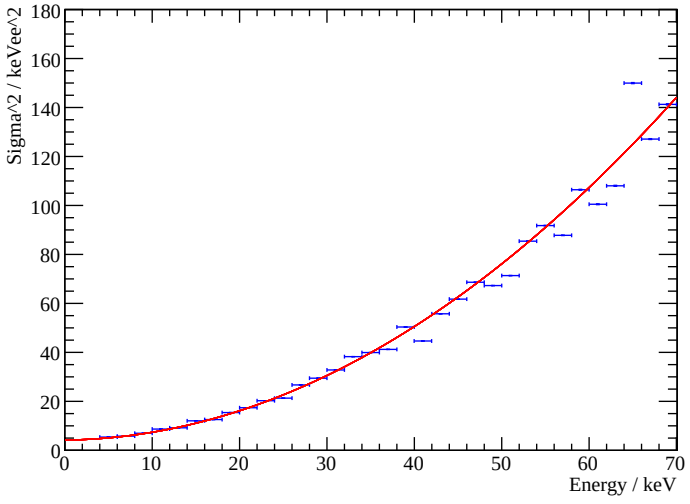

Figure 9.37: Resolution as fitted (red line) as well as inferred from Gaussian fits to the simulated data in 2 keV bins. As expected, the method very nicely reproduces the true (simulated) resolution.

9.8 Po-210 Surface Events

Before we come to the calculation of a limit from these data sets in the next chapter, it is worth discussing a peculiar source of background.

9.8.1 Po-210 in Run 27

Figure 9.38 is a scatter plot of 12 kg d taken with detectors DAISY/BE13 during run 27. Back then, the detectors were enclosed with a non-scintillating silver reflector foil. A population of events in the nuclear recoil band can be seen around 100 keV, and their spectrum is shown in figure 9.39. These events are attributed to the alpha decay of ^{210}Po, which is a step of the natural decay chain of ^{238}U following the decay of radon.

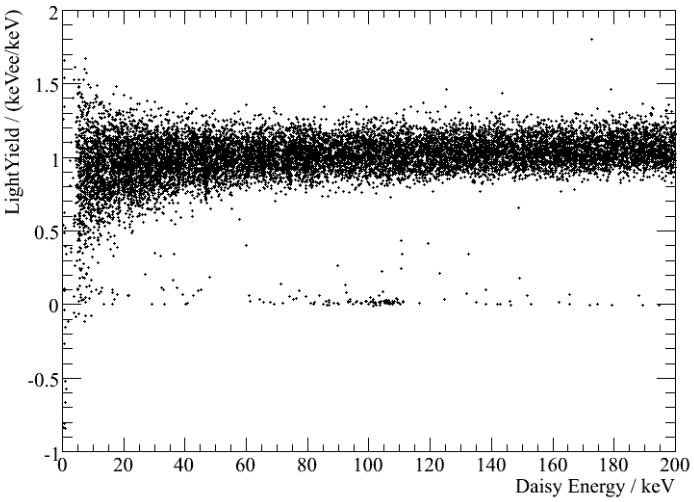

Figure 9.38: Events in the light yield-energy plane of detectors DAISY/BE13 after 12.31 kg d of exposure to background radiation during run 27.

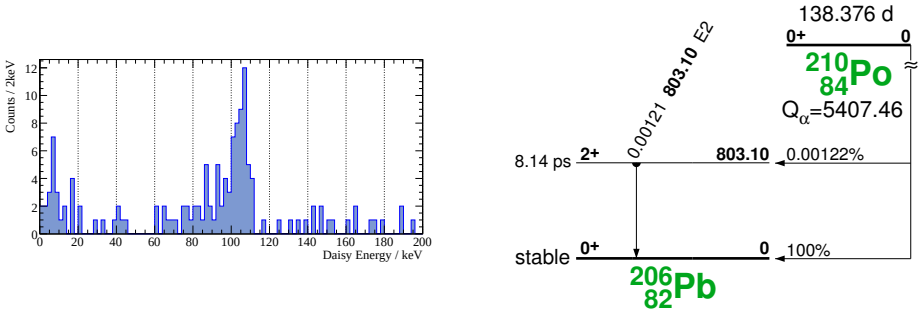

Figure 9.39: The events in the nuclear recoil band of figure 9.38 show a spectrum (left) that would be expecteted from the decay of ^{210}Po (right, from [195]) on and below nearby surfaces.

If ^{210}Po decays, it will eject an alpha, and the remaining ^{206}Pb nucleus will recoil. From momentum conservation we can calculate the energy of this recoiling lead nucleus as $E_{\mathrm{Pb}} = m_\alpha/m_{\mathrm{Pb}} E_\alpha = 4/206 \times 5304\,\mathrm{keV} = 103\,\mathrm{keV}$. If the decay happens on a surface surrounding the detector, the recoiling lead nucleus can hit the crystal and mimic a heavy nuclear recoil. Now, the ^{210}Po itself is a daughter nucleus, produced in preceding alpha decays. Hence it can be implanted in the surface, so upon decay, the ^{206}Pb nucleus may loose energy before reaching the crystal, leading to lower energy recoils. Therefore such **surface alpha contaminations** are a very dangerous background for the Dark Matter search.

We can check for consistency with the decay chain $^{210}\mathrm{Pb} \rightarrow {}^{210}\mathrm{Bi} \rightarrow {}^{210}\mathrm{Po}$. In section 6.2.1 on page 112 we have seen that for Daisy in run 27 we have an external contamination of ^{210}Pb with an activity of $(49 \pm 6)\,\mu$Bq. From figure 9.39 it can be estimated that we have 63 ± 7 ^{206}Pb events in $[80, 120]\,$keV. This translates to an activity of $(18 \pm 2)\,\mu$Bq of ^{206}Pb nuclei hitting the crystal. The relevant difference in the two signals is that the lead nucleus can only come from within a detector module, whereas the 46.5 keV gamma can also come from outside the module. Hence it is no surprise that the activity from recoiling nuclei is only a third of what we have from the ^{210}Pb decay. Dedicated experiments were conducted within the collaboration to study the spectral shape expected from this class of background [287, 288].

In run 28, the detectors were encapsulated with a 3M Radiant Mirror Film VM2000, and since run 29 with a VM2002 foil that is not only reflective foil but also scintillating [233]. Hence these events will have additional light associated from the alpha hitting the foil, which allows to discriminate this source of background. From run 29 on, also the clamps that hold the crystal were covered with the scintillating foil.

9.8.2 Po-210 in Run 30

Figure 9.1 clearly shows a population of events below the electron/gamma band at energies around 100 keV. This population is observed in all data sets analyzed here. The conjecture is that these events are the above ^{210}Po decays, and the foil just happens to shift them up close to the electron/gamma band. If this were true, we can expect these events to have a different pulse shape in the light detector: Whereas plastic scintillators such as the employed foil usually have scintillation light decay constants in the nanosecond range [289], $CaWO_4$ has a reported decay time of $6\,\mu$s at room temperature [290], increasing up to $220\,\mu$s at 77 K [291].

Hence the pulses from the polonium decay should appear faster in the light detector than the usual $CaWO_4$ scintillation events. This is indeed the case, as can be seen from figure 9.40, which confronts the pulse shape of $\approx 100\,\mathrm{keV_{ee}}$ events selected from the electron and gamma band, from direct hits in the light detector, and from events in the ^{210}Po population. Clearly, the pulse shape of the latter events is somewhere in between the other two

classes, supporting the idea of the ^{210}Po decay, with additional scintillation light from the alpha hitting the surrounding foil.

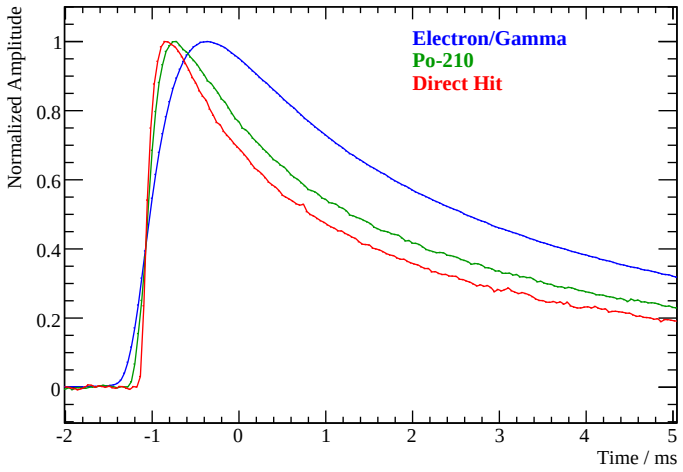

Figure 9.40: Standard events of the light detector SOS21, built from a few events of each class with energies of about 100 keV$_{ee}$: The fastest pulse (red) is a direct hit in the light detector which takes only $\tau_{rise} = 0.16$ ms from 10 to 90% peak height. Blue is a standard pulse from electron/gamma interactions in the crystal, which takes $\tau_{rise} = 0.54$ ms ($(10-90)\%$). The events from the ^{210}Po surface decays (green) are somewhere in between, $\tau_{rise} = 0.28$ ms (errors are less than the stated precision). Also, the decay times ($(90-10)\%$) are different: $\tau_{decay} = 10$ ms for the direct hit, $\tau_{decay} = 13$ ms for the electron/gamma event and $\tau_{decay} = 11$ ms for the polonium event.

One way to isolate these events is given by the ratio of the χ^2 or `RMS` values of two template fits, one with the usual standard event, and one with a standard event from direct hits in the light detector, just as had been done in section 9.7.1 to isolate the excess light events. Since the energy of these ^{206}Pb recoils is higher, there is an even cleaner cut in the plane spanned by the two RMS values. In any case, tagging these events is not difficult given the two RMS values.

Eventually, this cut identifies the events shown in figure 9.41 as being of different origin than the usual electron or gamma events. The population below the band is clearly visible, leaking to both higher (if the polonium is implanted in the crystal) and lower (implanted in the foil) energies in the phonon detector. In addition, a second population appears within the band. The reason for this distinct separation is not clear at this stage. Possible explanations include a position dependence for events on the curved or flat areas, or a different scintillation light yield from foil and plastic scintillator rings used in the module.

The spectrum of these events is shown in figure 9.42. Estimating the activity from the counts in the energy interval $[80, 120]$ keV gives $(60 \pm$

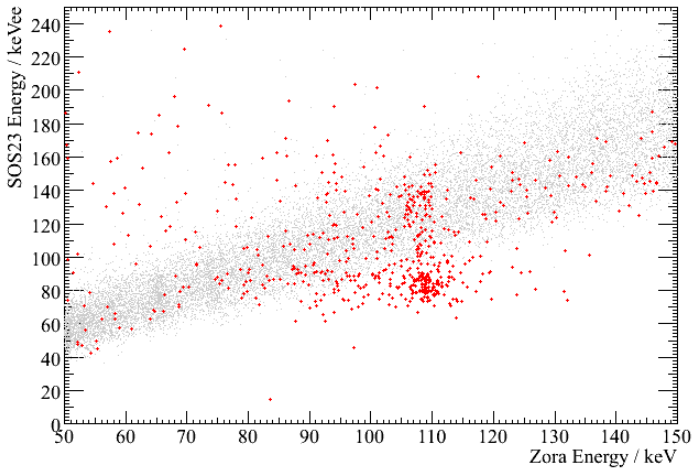

Figure 9.41: Selected Events based on the ratio of the two RMS values in red, plotted together with all other events in gray. Besides the population below the band, another population appears within the band.

4) μBq, a factor of three higher than observed for Daisy in run 27. This underlines the necessity to store all parts that are employed close to the detectors in a radon free environment, e.g. a box that is constantly flushed with nitrogen.

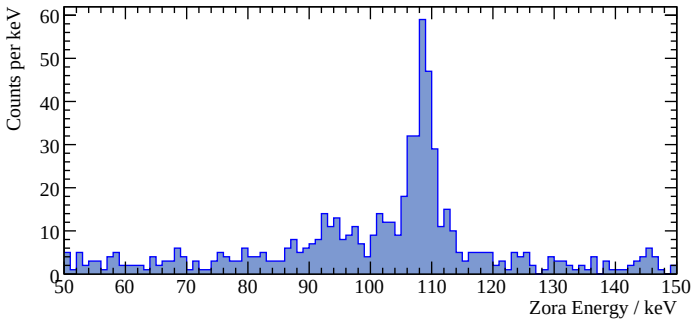

Figure 9.42: ^{210}Po decays close to crystal Zora, selected by a cut on the two available RMS values, for a total exposure of 21.94 kg d. The number of decays can be estimated from this as 371 ± 26 counts above a constant background. Note that the peak is above 103 keV, hence the decay takes place at the surface of the crystal, and the escaping alpha also deposits some energy in it.

Finally, we can examine the pulse shapes in the phonon detector of such lead recoil events. By eye no difference can be seen, and even the parameters from a fit of the pulse shape (section 4.3.7) are not different within errors. Nevertheless, a standard event can be built from the ^{206}Pb recoils, giving a second χ^2 parameter also for the phonon detector. Then, again, the ratio of

the two available RMS values can be built. Figure 9.43 shows this ratio for both lead recoil events and events from the electron/gamma band. The two populations are seen to differ significantly in this parameter! This opens the possibility for an additional discrimination parameter in future analysis for the search of Dark Matter, and demonstrates the power of the new method using two independent standard event fits.

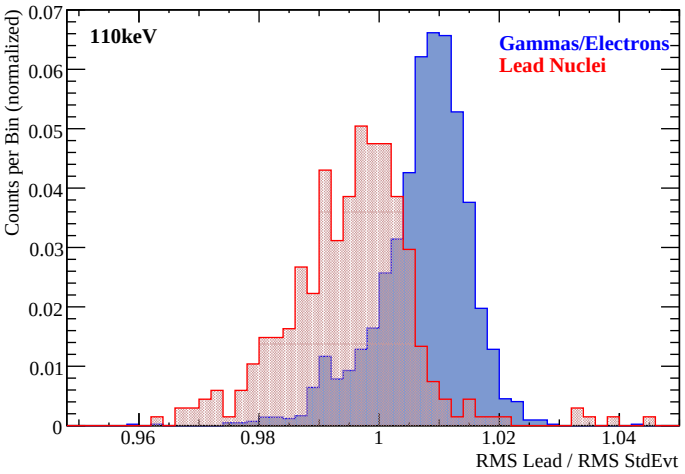

Figure 9.43: The ratio of the quality of two standard event fits in the phonon detector can act as an additional discrimination parameter, as shown here: Red is the ratio `RMS Lead/RMS StdEvt` for the lead recoils following a polonium decay (tagged by the different pulse shape in the light detector), and in blue the ratio for events from the electron/gamma band of similar energy. Both distributions are normalized to unity to ease the comparison. The mean of both distributions are more than 1σ apart from each other.

Chapter 10

Calculating Limits

Intent: Given events analyzed as in the previous chapter, we can now calculate a limit on the coherent WIMP-nucleon scattering cross section. This chapter describes a new method to define the acceptance region where one searches for WIMP induced tungsten recoils. The Yellin methods for the subsequent calculation of a limit are presented, together with an innovative way to combine individual detectors within that framework. To conclude, the limits derived from run 30 data are presented.

Organization: In section 10.1 the calculation of the nuclear recoil band is described. An automated method for the determination of the optimum acceptance region is derived in section 10.2. Section 10.3 comments on methods to calculate a limit, and section 10.4 explains how to combine detectors with different characteristics within the Yellin framework. Limits calculated from run 30 data are given in section 10.5.

10.1 Nuclear Recoil Band

The acceptance region is defined as the area in the light yield-energy-plane in which events are considered to calculate the limit. To this end, it is necessary to define the region of tungsten recoil events, which are the expected signature of a WIMP interaction in the $CaWO_4$ target.

Given the central line of the electron/gamma events $L(E)$, the central line $L_W(E)$ of this tungsten band is simply at

$$L_W(E) = \frac{1}{Q} L(E), \tag{10.1}$$

where Q is the quenching factor for tungsten recoils, $Q = 40.1 \pm 2.7$ (section 7.1.1). As for the resolution, the situation is more involved. The resolution of the light channel $\sigma(E)$ is a function of the light itself, and only an implicit function of the total energy of the interaction. For the quenched band, this σ_W is equal to the unquenched resolution σ at an electron energy E' that would give the same light as is observed in the quenched band:

$$\sigma_W(E) = \sigma\left(E' \,\middle|\, L(E') = L_W(E)\right). \tag{10.2}$$

With equations 10.1 and 9.3 this gives the condition

$$L(E') = L(E)/Q \tag{10.3}$$

$$\frac{l_1 E'}{1+\mathrm{e}^{-l_2 E'}} = \frac{l_1 E/Q}{1+\mathrm{e}^{-l_2 E}} \tag{10.4}$$

for the required energy E'. This equation cannot be solved for E' in a closed form but requires resort to the Lambert W function [292]. In software it is therefore solved numerically for E', which has the additional advantage of being the same implementation for different models in $L(E)$ for the scintillator non-proportionality. Figure 10.1 shows a sample of events with the bands as calculated by this procedure.

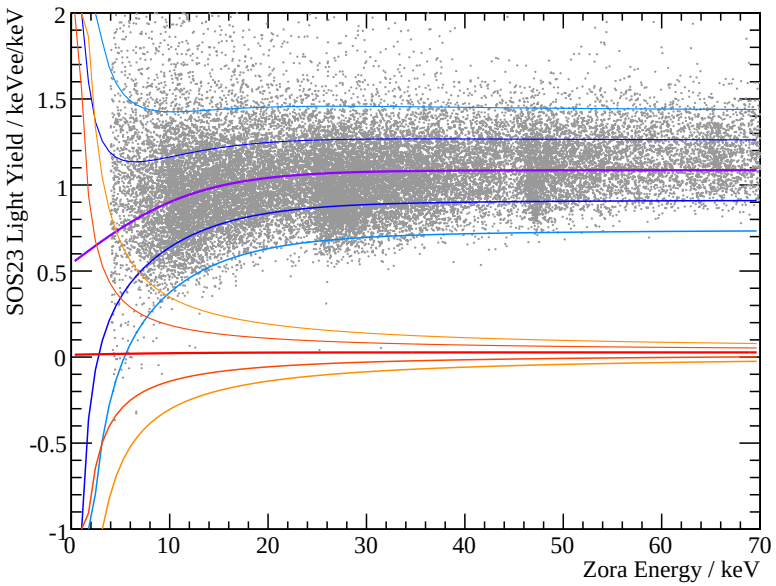

Figure 10.1: Events from run 30, ZORA/SOS23, in the light yield–energy-plane together with the fitted recoil bands. Blue is the electron/gamma band, red the tungsten recoil band (quenching factor of 40.1). Drawn are the central line as well as the 1σ and 2σ widths of the two bands. A one-sided 90% confidence band would be at 1.28σ.

To define the acceptance region, direct Dark Matter search experiments typically start from the signal band defined in such or similar ways. This band is followed along the one-sided 90% confidence for energies above discrimination threshold (where it starts overlapping at some confidence with the electron/gamma band) up to a few tens of keV (above which no WIMP induced recoils are expected); examples include previous CRESST analysis [267, 286].

10.2 Energy Dependent Acceptance

Here, a more impartial method is developed and employed. The acceptance region should be chosen such that it gives the most information about WIMPs, or, in other words, that it gives the most stringent limit in the absence of a signal. Of course this region has to be chosen a priori, that is, independent of the particular statistical realization of the given experiment. Hence the objective function to be optimized is the **expected limit**, or **sensitivity**.

10.2.1 The Objective Function

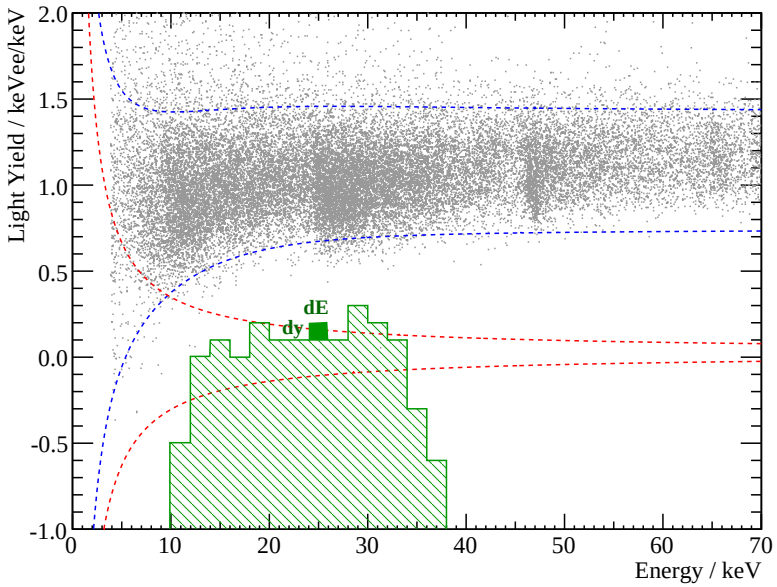

Figure 10.2: Finding the optimum acceptance region: The acceptance region (green) is expanded by a unit of area $(\mathrm{d}y, \mathrm{d}E)$ if this improves the sensitivity, or reduced by this area if the sensitivity is worsened. The algorithm is iterated until convergence.

Consider again events distributed in the light yield–energy-plane (y, E), figure 10.2 shows it once more. In each unit area $(\mathrm{d}y, \mathrm{d}E)$ there is an expected background density $\varrho_\mathrm{b}(y, E)$. To model this, we take the particle spectrum, the position of the electron/gamma band $L(E)$, and the resolution function $\sigma(E)$. In addition, there is an expected signal density $\sigma\varrho_\mathrm{s}(y, E)$ that is proportional to the WIMP-nucleon scattering cross section σ. This density is calculated from the expected WIMP spectrum $\mathrm{d}\Gamma/\mathrm{d}E$ and the tungsten recoil band.

The green hatched area in figure 10.2 is the **acceptance region**: only events within this region are considered to calculate the limit. In the

CRESST case, the acceptance region can conveniently be parametrized by its upper boundary $y_{\max}(E)$, the negative boundary taken to be at $y_{\min} = -\infty \approx -1\,\mathrm{keV_{ee}/keV}$. Given $y_{\max}(E)$, the expectation values for the observed number of signal and background events are

$$\langle n_\mathrm{s} \rangle = \int_0^\infty \mathrm{d}E \int_{-\infty}^{y_{\max}(E)} \mathrm{d}y \;\; \sigma \varrho_\mathrm{s} \tag{10.5}$$

$$\langle n_\mathrm{b} \rangle = \int_0^\infty \mathrm{d}E \int_{-\infty}^{y_{\max}(E)} \mathrm{d}y \;\; \varrho_\mathrm{b}. \tag{10.6}$$

Given $y_{\max}(E)$, a particular experiment will observe a certain number of accepted events $n_\mathrm{obs} \in \mathbb{N}$. This number then allows to calculate some number $n_{\mathrm{s},90}$ of events as being excluded at the stated confidence, here 90%. This is discussed in section 10.3.1. Here, it suffices to note that this exclusion depends on the acceptance region:

$$n_{\mathrm{s},90} = n_{\mathrm{s},90}(n_\mathrm{obs}) = n_{\mathrm{s},90}\left(y_{\max}(E)\right). \tag{10.7}$$

To transfer this number into a limit σ_{90} on the cross section, equation 10.5 is evaluated for an arbitrary σ', yielding $\langle n'_\mathrm{s} \rangle$, and σ_{90} can then be calculated according to

$$\frac{\sigma_{90}}{\sigma'} = \frac{n_{\mathrm{s},90}}{\langle n'_\mathrm{s} \rangle} \tag{10.8}$$

$$\Rightarrow \sigma_{90} = \frac{\sigma'}{\langle n'_\mathrm{s} \rangle}\, n_{\mathrm{s},90}. \tag{10.9}$$

Since $\langle n'_\mathrm{s} \rangle \propto \sigma'$, the primed variables eventually drop out of the equation again.

The limit σ_{90} will of course depend on the particular realization of the events in a given experiment, so it cannot be used as the objective function. However, the **expectation value** $\langle \sigma_{90} \rangle$ is independent of a given experiment, and will be used instead. As a first step, this expectation value simply follows from equation 10.9:

$$\langle \sigma_{90} \rangle = \frac{\sigma'}{\langle n'_\mathrm{s} \rangle}\, \langle n_{\mathrm{s},90} \rangle. \tag{10.10}$$

The excluded number of events $n_{\mathrm{s},90}$ depends on the number of observed events n_obs, which in turn depends on the number of background events n_b. We take n_b to be distributed according to a Poisson process with expectation value $\langle n_\mathrm{b} \rangle$. To calculate $\langle \sigma_{90} \rangle$, we can then simply use the definition of the expectation value:

$$\langle \sigma_{90} \rangle = \frac{\sigma'}{\langle n'_\mathrm{s} \rangle} \sum_{n_\mathrm{obs}=0}^{\infty} n_{\mathrm{s},90}(n_\mathrm{obs})\, P(n_\mathrm{obs}) \tag{10.11}$$

$$= \frac{\sigma'}{\langle n'_\mathrm{s} \rangle} \sum_{n_\mathrm{obs}=0}^{\infty} n_{\mathrm{s},90}(n_\mathrm{obs})\, \frac{\langle n_\mathrm{b} \rangle^{n_\mathrm{obs}}}{n_\mathrm{obs}!}\, \mathrm{e}^{-\langle n_\mathrm{b} \rangle}. \tag{10.12}$$

$\langle \sigma_{90} \rangle$ depends on the acceptance region $y_{\max}(E)$ through equations 10.5 and 10.6 and is the objective function of choice.

10.2.2 Varying the Acceptance Region

The task is now to vary $y_{\max}(E)$ until $\langle\sigma_{90}\rangle$ is minimal. Despite thorough attempts it was not possible to deal with this variational problem analytically, so resort was taken to a computational solution. To this end, the (y, E) plane is binned. Not all possible combinations for the binned acceptance region are tried out (already with e.g. 10 energy bins and 10 relevant yield bins this would be $2^{10^{10}} \approx 10^{30}$ possibilities). Instead, the acceptance region is varied only on its borders: For each energy bin, the acceptance region is increased or decreased as long as it improves the expected limit. The algorithm is iterated until the sensitivity converges.

Some technical remarks on equation 10.12 are in order. Although $\mathrm{e}^{-\langle n_\mathrm{b}\rangle}$ can be drawn out of the sum, this does not mean that $\langle\sigma_{90}\rangle \to 0$ as $\langle n_\mathrm{b}\rangle \to \infty$, since $n_{\mathrm{s},90}$ counteracts. Instead the sum is very well behaved, as can be seen in figure 10.3. However, its calculation is rather computationally intensive. Therefore it is calculated only once, and the values for integer $\langle n_\mathrm{b}\rangle$ are stored in a table, from which the needed $\langle\sigma_{90}\rangle$ are drawn by simple interpolation. $n_{\mathrm{s},90}(n_\mathrm{obs})$ is calculated from Poisson statistics. Had one knowledge of the background, $n_{\mathrm{s},90}$ could also be calculated e.g. from the Feldman-Cousins scheme [293, 294] (red curve in figure 10.3), but this is not employed for CRESST data.

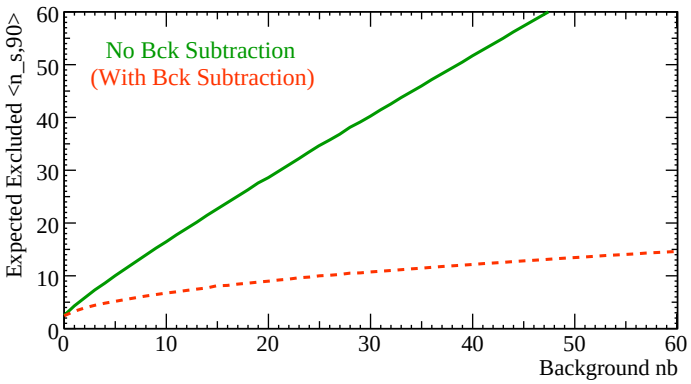

Figure 10.3: The sum $\langle n_{\mathrm{s},90}\rangle$. The green curve gives the employed curve; in orange the (not used) variant in which the background is taken into account using the ordering scheme of Feldman and Cousins.

Given the simple Gaussian behavior of the signal and background densities ϱ_s and ϱ_b, it is not surprising that the objective function is also well behaved. Figure 10.4 shows the sensitivity as a function of the cut $y_{\max}(E = 10\,\mathrm{keV})$ in one 1 keV energy bin. The minimum is obvious.

In some cases, in particular at higher energies above the first dip of the signal spectrum due to the form factor, this minimum in $y_{\max}$ can be degenerate to the double point precision used in software. In addition, the algorithm would have the acceptance going to infinite recoil energies. Hence

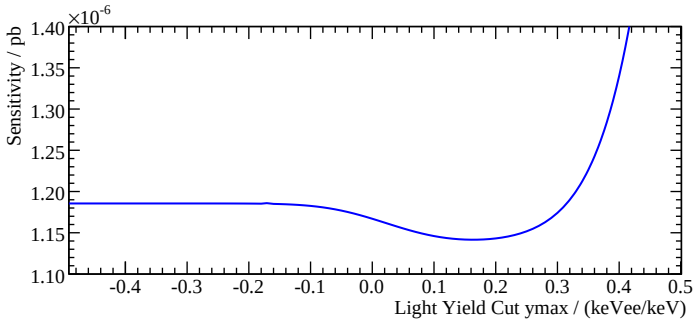

Figure 10.4: Given an acceptance region, this is an example of the sensitivity as a function of the cut $y_{\max}$ in one 1 keV energy bin.

after the overall minimum was found, the acceptance region is reduced such that the signal contained within is reduced to 99.9%, obviously with negligible effect on the sensitivity.

10.2.3 New Frontiers

This method breaks with two traditions in the direct search for Dark Matter. Previously, the accepted fraction of the signal in a search experiment was taken energy independent (or only slightly energy dependent [182]). Here, the fraction of the signal that is accepted is allowed to vary to give the optimum result. In addition, the acceptance region previously was fixed for all WIMP masses and not optimized for the particular model that was to be excluded. Here, the acceptance region is calculated individually and appropriately for each signal expectation. This complicates visualization somewhat, but improves the informative value of the experiment.

Figure 10.5 shows the acceptance region for module ZORA/SOS23 during run 30 for various WIMP masses with expected recoil spectra as laid out in section 3.3.5. At low and intermediate recoil energies, the shape of the acceptance region nicely follows the resolution of the light channel. In came as a surprise that for very low WIMP masses, the algorithm finds it beneficial to *increase* the acceptance toward lower recoil energies. This is due to the recoil spectrum being confined to the lowest energies, and being a sharply rising exponential. Hence the increasing electron/gamma background is being overcompensated for.

The acceptance region is not smoothly bounded but shows some small dents. This is because the background density ϱ_{b} needed to evaluate equation 10.6 was calculated using the observed spectrum, smeared by the calculated resolution of the light channel. Hence, the acceptance is reduced slightly for example at $\approx 25\,\mathrm{keV}$ where the ^{227}Ac feature appears in ZORA. To conclude, figure 10.6 shows as an example the accepted signal for a $100\,\mathrm{GeV/c^2}$ WIMP as function of energy. The absolute number of accepted signal events rises with energy as the acceptance region becomes larger, and

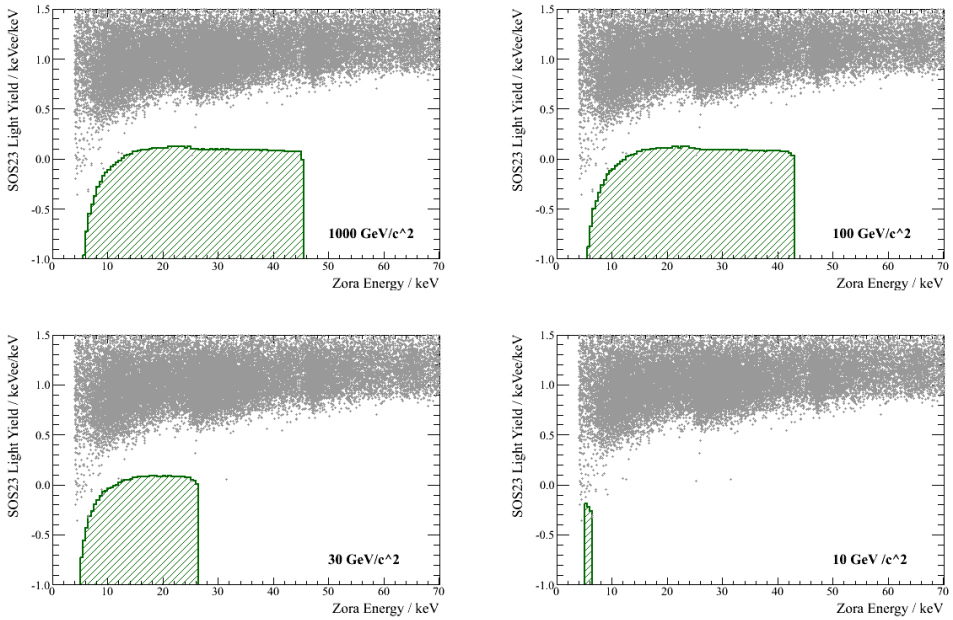

Figure 10.5: Acceptance regions for various WIMP masses. Note the unexpected shape of the acceptance region for very low mass WIMPs.

eventually drops again as the expected recoil spectrum goes to zero. The relative acceptance on the other hand smoothly increases to almost 100% for high energies and is cropped at a value above which hardly any signal is expected anymore.

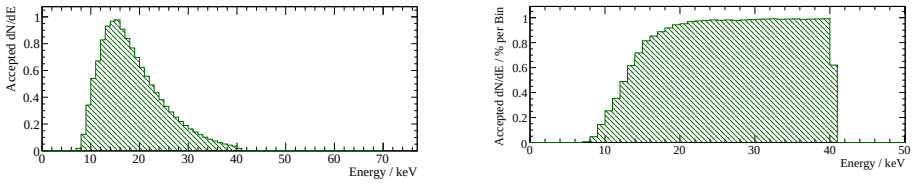

Figure 10.6: Accepted number of signal events shown for the example of a $100\,\mathrm{GeV/c^2}$ WIMP in detector Zora. Left: As (arbitrarily scaled) absolute number, rising up to $\approx 15\,\mathrm{keV}$ due to the increasing acceptance, and decreasing at higher energies due to the expected spectral dependence. Right: Illustrated as percentage of the total number of signal events at a given energy. Previously, acceptances were typically set by requiring this number to have a fixed value.

10.3 Calculating a Limit

10.3.1 Two Parameter Limits

In a counting experiment like CRESST-II, one measures the number of events n_{obs} observed during a given exposure and would like to calculate a number n_{s} from a signal that is compatible with the measurement. If n_{obs} is small or even $n_{\mathrm{obs}} = 0$, or if the observed events could all be from some sort of background, one can give a **limit** on n_{s}: Given a statistical **confidence** one can exclude too high values $n_{\mathrm{s},90}$ above some particular value, the limit, because such processes would produce too many signal events n_{s}. In the easiest case of a Poissonian signal process, $n_{\mathrm{obs}} = 0$, and no background $n_{\mathrm{b}} = 0$, the 90% confidence limit is $n_{\mathrm{s},90} < 2.30$, since

$$P_{\mathrm{n_{obs}}}(n_{\mathrm{s},90}) = \frac{(n_{\mathrm{s},90})^{n_{\mathrm{obs}}}}{n_{\mathrm{obs}}!}\mathrm{e}^{-n_{\mathrm{s},90}} = \frac{(n_{\mathrm{s},90})^{0}}{0!}\mathrm{e}^{-n_{\mathrm{s},90}} \stackrel{!}{=} 0.1 \quad (10.13)$$

$$\Leftrightarrow n_{\mathrm{s},90} = -\ln(0.1) = 2.30. \quad (10.14)$$

In the presence of a completely known background, limits can be treated e.g. in the unified ordering scheme of Feldman and Cousins [293]. Uncertainties on the background can be taken into account e.g. with the method of Rolke et al. [295]. All these methods have in common that the computed limit only depends on the number of observed events n_{obs}, the number of expected background events $\langle n_{\mathrm{b}} \rangle$, and the number of signal events $\langle n_{\mathrm{s}} \rangle$ expected from a given signal process.

10.3.2 The Yellin Methods

In direct Dark Matter searches, backgrounds are never known a priori. This is due to the completely new realm of physics investigated: Nuclear processes at the low energies of relevance here are poorly understood, and instrumental effects are not investigated with the needed precision unless measured in own work. This in turn often requires long exposures to identify rare background processes. Hence **the best measurement of such backgrounds is the measurement to search for Dark Matter itself**. Various examples of such backgrounds have been discussed exhaustively in the previous chapters.

Under these circumstances it is a valid but overly conservative approach to calculate a limit based on one of the above methods, solely using the number of observed events n_{obs} and expected signal events $\langle n_{\mathrm{s}} \rangle$. Instead, in addition to the simple numbers of events, **spectral information** can be taken into account to distinguish a signal, which is of the quasi exponential form, from backgrounds, which in general will have a different spectral shape. Hence basically all direct Dark Matter searches use the Yellin methods [296] that were developed for this purpose.

10.3.3 The Maximum Gap Method

Suppose there is a signal expectation

$$\sigma \frac{\mathrm{d}\Gamma}{\mathrm{d}E}(E) \tag{10.15}$$

and a set of i observed events at energies E_i, distributed as in figure 10.7. The many events shown at high energies are most likely not signal events, since they do not follow the expected spectral dependence. This information should be used in the calculation of the limit.

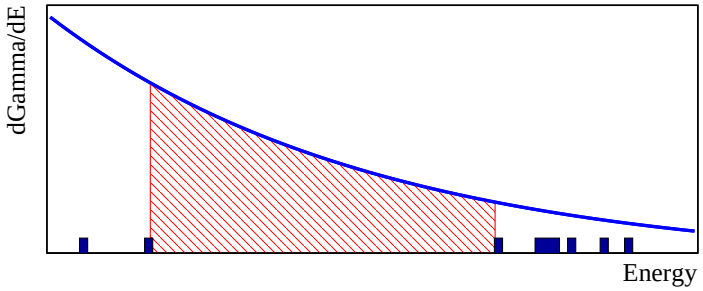

Figure 10.7: Illustrating the Maximum Gap method: Observed events in dark blue, signal expectation in light blue, and the Maximum Gap as red hatched region.

To this end, the integral

$$n_\mathrm{i} := \int_{E_\mathrm{i}}^{E_\mathrm{i+1}} \sigma \frac{\mathrm{d}\Gamma}{\mathrm{d}E}\,\mathrm{d}E \tag{10.16}$$

is calculated between any two events (and the endpoints of the accepted spectral range, E_min and E_max). The **maximum gap** $\hat{n}$ is the largest of these integrals n_i and is used to set the limit. Qualitatively, a cross section σ is excluded as being too high if most random experiments would give smaller maximum gaps. Quantitatively, this is shown in [296] to be that σ for which the function

$$C_0(\hat{n}, N) = \sum_{k=0}^{m} \frac{(k\hat{n} - N)^k\, \mathrm{e}^{-k\hat{n}}}{k!} \left(1 + \frac{k}{N - k\hat{n}}\right) \tag{10.17}$$

equals the desired confidence, usually 0.90. Here,

$$N = \int_{E_\mathrm{min}}^{E_\mathrm{max}} \sigma \frac{\mathrm{d}\Gamma}{\mathrm{d}E}\,\mathrm{d}E \tag{10.18}$$

and m is the greatest integer less or equal to $N/\hat{n}$.

10.3.4 The Optimum Interval Method

Coming back to figure 10.7, suppose the measurement is continued for a small time, and an additional event were observed with an energy right in

the middle of the Maximum Gap. This would disproportionately worsen the limit. Hence the Maximum Gap method is generalized to the **Optimum Interval** method. Not only the largest integral $\hat{n}$ with *no* events inside is considered to calculate the limit. Instead, also integrals with $1, 2, \ldots, n_{\mathrm{obs}}$ events within are calculated. To set the limit, that integral is used that gives most information about the signal, or in other words, that gives the most stringent limit.

Technically, this requires a function C_{n} in analogy to equation 10.17 which can be tabulated by a Monte Carlo program [296]. The maximum of all C_{n} for all possible integrals between any two events is denoted $\hat{C}_{\mathrm{n}}$ and is used to calculate the limit. However, for a given confidence, say 90%, it is not enough to demand $\hat{C}_{\mathrm{n}}$ to reach 0.90. One needs to take into account that *any* integral could have been the optimum one, with any number $0, 1, 2, \ldots, n_{\mathrm{obs}}$ of events within. Hence, $\hat{C}_{\mathrm{n}}$ is required to be equal to a larger value $\overline{C} > 0.90$. The details of this procedure are laid out in [296], where it is shown how to evaluate $\overline{C}$ by a Monte Carlo program. Figure 10.8 shows $\overline{C}$ as a function of the expected events N.

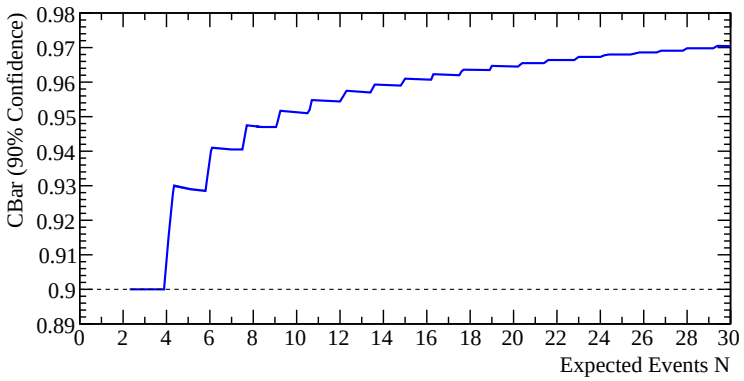

Figure 10.8: The function $\overline{C}$ that is used to calculate a limit with the optimum interval method at 90% confidence.

Since no cross section that gives $N < 2.30$ can be excluded with more than 90% confidence, $\overline{C}$ is not defined for values smaller than 2.30 in the 90% confidence case. In addition, the function spurts upward at certain N. This is the case whenever it becomes possible for an interval with an additional event inside to be the optimum interval itself. For example, as long as $N < 3.9$, the optimum interval is always the maximum gap. Only once N goes above 3.9, the optimum interval can be either the maximum gap or the integral with one event inside. This possibility gives a penalty on the requirement on C_{n}: $\overline{C}$ spurts up. Hence, if $N > 3.9$ but the optimum interval still happens to be the maximum gap, the limit is worse than that from the maximum gap method alone. It is therefore necessary to decide a priory which method is to be used to achieve a true limit with the stated confidence. In typical cases published in the literature, the differences between the two methods are small compared to other uncertainties.

10.4 Combining Detectors

10.4.1 Two-Parameter Limits

Many direct Dark Matter experiments operate segmented detectors. Hence it is necessary to combine different subdetectors to give one limit. If the limit were calculated only using the number of observed and expected events, this would simply mean adding the individual numbers. But if we want to use the additional spectral information as is inherent in the Yellin methods, this path fails.

10.4.2 Frequentist vs. Bayesian

Given data, the Yellin methods return the confidence $C(\sigma)$ with which one can reject a cross section σ as being too high. But the approach is purely **classical**, or **frequentist** (in contrast to **Bayesian** statistics). Thus one makes no a posteriori statement about the true value of σ, e.g. the probability that σ is lower than a certain limit. Instead, the probabilistic statement is about the limit itself, and it is already known prior to looking at the data. Namely, if after looking at the data one states a limit of $\sigma < 10^{-6}\,\text{pb}$ at 90% confidence, this does not mean that σ is lower than this value with a probability of 90%. Instead, it means that one uses a method to find an upper limit such that the limit is correct in 90% of the cases, e.g. given frequently repeated experiments of the same kind. Thus the name frequentist statistics.

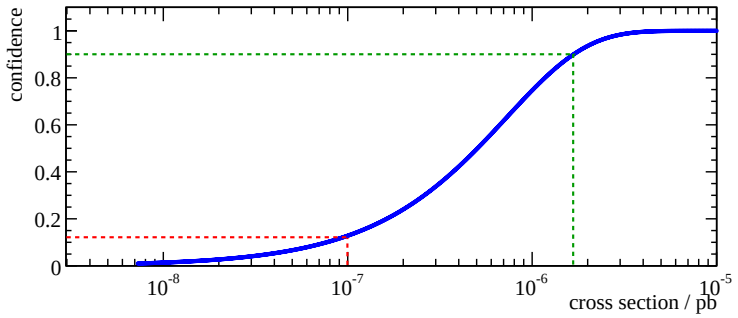

Figure 10.9: Sketch of the result from a Maximum Gap analysis given some experimental data. When looking at this curve e.g. at a cross section of $10^{-7}\,\text{pb}$, it becomes evident that a statement about an exclusion confidence is not a statement about the probability for a given cross section.

This distinction is crucial, and to clarify, here is an example of a pitfall that one can get caught in. Suppose one wants to combine the limits derived from two different experiments, or two different detector modules. From each individual experiment or module one derives, using Yellin's frequentist approach, a confidence $C(\sigma)$ as shown in figure 10.9. The terminology is that a cross section of, say, $10^{-6}\,\text{pb}$ is excluded with a confidence of $C(10^{-6}\,\text{pb})$. Now, in order to combine these curves from individual experiments, one

might be tempted to simply multiply the individual functions to get the combined confidence. This can be done in Bayesian statistics, where one has likelihood functions that can indeed be multiplied. But it is wrong here, because only probabilities about a parameter can be multiplied like this, which is not what we have. Thus combining individual experiments by combining the individual confidence curves is the wrong way to go in frequentist statistics. Instead one must calculate the combined confidence based on a combination of the individual data, as elaborated in the next section.

10.4.3 Energy Transformation

If the detectors that need to be combined are identical, they can be treated as one detector with the added exposure, even in the Yellin framework. If the accepted spectra of the detectors differ, a possible but unfavorable possibility is to *make* different detectors equal e.g. by setting the energy threshold to the same value, namely that of the worst detector. It is clear that this is incompatible with the idea of using the optimum acceptance region for a given detector. Hence a procedure is needed to combine the results from individual detectors in the Yellin framework.

In this framework, the computed limit (see e.g. equation 10.17) depends on integrals of the form 10.16. To facilitate the combination of different detectors, the energy coordinate E is transformed in a new variable η according to the integral transform

$$\eta(E) := \frac{1}{\mathcal{N}} \int_{E_{\min}}^{E} \sigma \frac{\mathrm{d}\Gamma}{\mathrm{d}E'} \, \mathrm{d}E' \tag{10.19}$$

which is a bijective transformation and hence leaves the calculated limit unchanged. The normalization constant $\mathcal{N}$ is chosen such that

$$\begin{aligned} 1 &\stackrel{!}{=} \eta(E_{\max}) && (10.20)\\ &= \frac{1}{\mathcal{N}} \int_{E_{\min}}^{E_{\max}} \sigma \frac{\mathrm{d}\Gamma}{\mathrm{d}E'} \, \mathrm{d}E' && (10.21)\\ &= \frac{1}{\mathcal{N}} N, && (10.22) \end{aligned}$$

so $\mathcal{N} = N$. In this new energy variable η, the expected signal spectrum is flat, which can be most easily seen manipulating differentials:

$$\frac{\mathrm{d}\Gamma}{\mathrm{d}\eta} = \frac{\mathrm{d}\Gamma}{\mathrm{d}E} \frac{\mathrm{d}E}{\mathrm{d}\eta} = \frac{\frac{\mathrm{d}\Gamma}{\mathrm{d}E}}{\frac{\mathrm{d}\eta}{\mathrm{d}E}} = \frac{\frac{\mathrm{d}\Gamma}{\mathrm{d}E}}{\frac{\mathrm{d}}{\mathrm{d}E} \frac{1}{N} \int \frac{\mathrm{d}\Gamma}{\mathrm{d}E} \, \mathrm{d}E} = \frac{\frac{\mathrm{d}\Gamma}{\mathrm{d}E}}{\frac{1}{N} \frac{\mathrm{d}\Gamma}{\mathrm{d}E}} = N. \tag{10.23}$$

With this transformation all possible differences of individual detectors have been mapped into the interval $\eta = [0, 1]$ in which the events are now distributed, and the single number N that is a measure of the exposure and acceptance of the detector. Therefore, for each expected WIMP spectrum, individual subdetectors can now be joined to give the combined limit: Simply add up the individual N and apply the desired Yellin method on the energy interval $[0, 1]$ considering the observed events from all detectors.

10.5 Limit from Run 30

Equipped with this toolbox, we can finally calculate a limit on the coherent WIMP-nucleon cross section. To this end, we use the WIMP expectation presented in section 3.3 and the data analyzed in the previous chapter 9. The two individual data sets from detector module Zora/SOS23 as well as the three sets from Verena/SOS21 are combined in the framework just discussed.

Figure 10.10 shows the improvement in sensitivity given the optimum acceptance region with respect to the previously defined region with a fixed 90% acceptance above 12 keV. At high WIMP masses the new method gives a limit that is about 10% stronger than from the old method. Such a small difference may have been expected, since for such WIMP masses, much of the signal is expected above 12 keV anyway. For low WIMP masses on the other hand, the optimum acceptance region results in significantly improved limits. For example, for a 15 GeV/c^2 WIMP the new limit is more than an order of magnitude stronger than the old one.

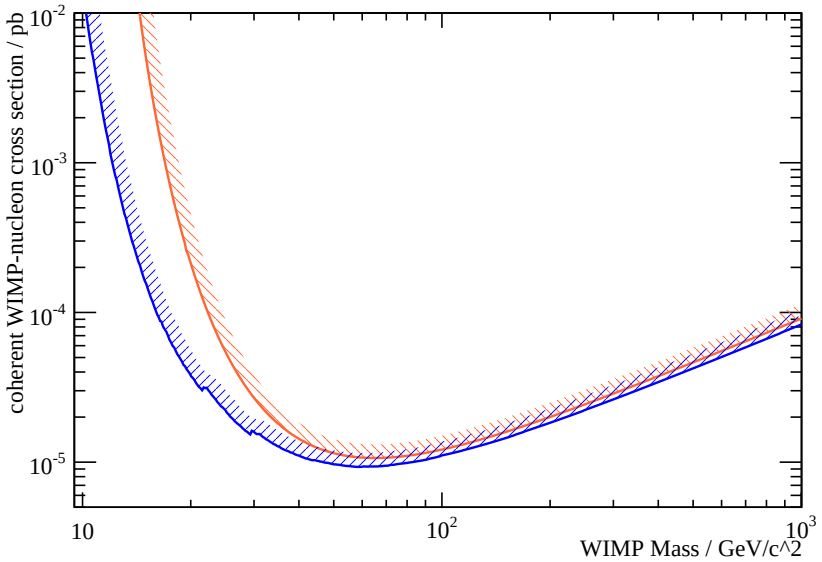

Figure 10.10: Sensitivity for 1 kg d of exposure on a tungsten target and no observed events, given two different acceptance regions: In orange the acceptance is set to 90% of the expected signal in $[12, 40]$ keV. Blue is the acceptance region as calculated using the method presented here, for a detector with resolution typical for run 30.

Figure 10.11 shows the limit calculated from the data sets presented in the previous chapter, namely, a total of 21.938 kg d of exposure on Zora and 25.587 kg d on Verena. Unlike sensitivity curves or previously published limits, those exclusion curves show dents whenever the acceptance

region changes such that observed events drop in or out of it. A second, stronger limit is also shown in which pulses with abnormal pulse shape are not considered.

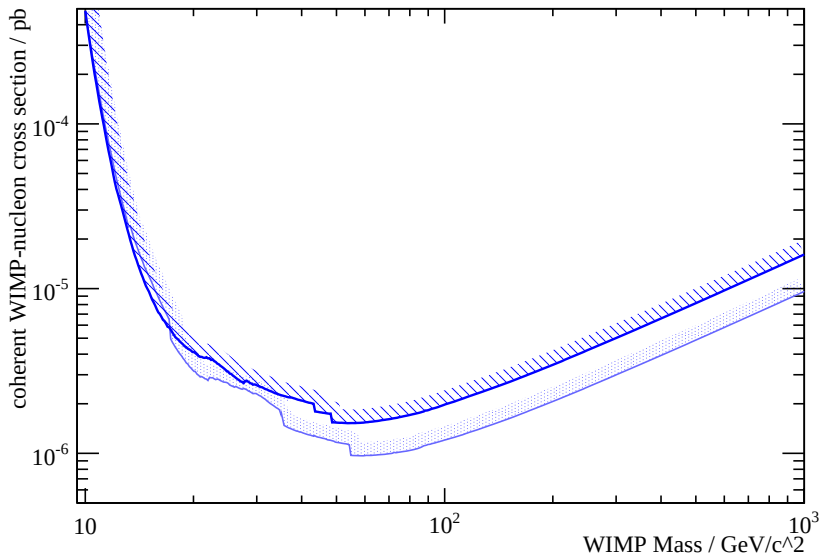

Figure 10.11: Limits on the coherent WIMP-nucleus scattering cross section from the data analyzed in the previous chapter, adding up to a total of 47.525 kg d of exposure. To calculate the limit, only the tungsten exposure of 30.346 kg d was taken into account since the acceptance region is optimized for tungsten recoils only. The dark blue curve includes all events. For the light blue curve events are discarded that have an untypically high decay time and are hence probably due to thermal relaxations rather than particle interactions.

Chapter 11

Outlook

At the time of writing, 17 detector modules are installed in the cold box in Gran Sasso and data taking of run 31 is in progress. This includes crystals where steps have been taken to reduce intrinsic radioactive contaminations, mainly due to strontium. Also, a $ZnWO_4$ crystal is installed. It will be very interesting to analyze the spectra of these detectors and compare them to the ones presented in chapter 6.

At this stage, it is not clear whether nuclear recoils also show the scintillator non-proportionality. Given the low light yield of such recoils, a possible effect is small in any case. However, dedicated experiments or at least a neutron calibration with high statistical significance are required to demonstrate the expected absence of such an effect for nuclear recoils. Given all detectors are operational, this will also allow to conclude about a possible dip in the light yield for photons close to the tungsten K_α energy.

Experiments are under way that aim to a more complete surface coverage of the target by means of a light detector in the form of a cup. This would allow to veto events close to the surface, dominant background at energies below 1 keV.

A thorough analysis of pulse shapes has to be implemented. On the one hand, possible thermal relaxations close to the detector, or cracks in the crystal, need to be distinguishable from particle interactions. In addition, it needs to be examined whether the pulse shape can be used as a meaningful discrimination parameter at the low energies of interest to distinguish electron/gamma events from tungsten recoils.

On the experimental side, it will be of crucial importance to see the detector that has no plastic on its clamps operational in run 31. This will clarify whether the observed dark events can indeed be due to the conjectured thermal relaxations.

To take full advantage of the optimum acceptance region, the Yellin method should be extended to the two dimensional case. Some ideas how this might be done are put forward in [297].

In run 31, X-ray sources are installed that allow the light detectors to be calibrated in terms of absolute energy. This will clarify how much light is really detected with these devices, and show how much room for improve-

ment can be expected in this channel. What is more, the observed small inclination of gamma and alpha lines [298] may be explained by a sharing of available energy on the light and phonon channel. In this case, an absolute calibration of the light detector would allow to correct the energy scale for this effect.

A possible indication of WIMPs in the detector would call for further investigations. One very promising approach is to run the detector with various different target materials. Since the WIMP scattering rate is expected to scale $\propto A^2$, this allows for a cross-check for the WIMP nature of the detected events. For CRESST, a promising material is $CaMoO_4$, where molybdenum has $A \approx 96$, a much lower mass in contrast to tungsten.

Overall, the increase of the CRESST exposure and target mass already in progress now will lead to many new insights in short time, including more information about the nature of Dark Matter.

Appendix A

Inflation and the Cosmic Microwave Background

Intent: There is no necessity to go into details about the theory of inflation within the scope of this thesis. Of course, results such as the observed flatness of the universe are direct consequences of this theory. Nevertheless, two aspects related to the cosmic microwave background are worth mention in an appendix.

The shape of the cosmic microwave background power spectrum is actually very much the same as that of a single note played on an instrument, e.g. a guitar [299], where one also has a strong root and then the harmonics at multiples of the root's frequency. Minor differences are that with the guitar, we deal with a Fourier transform in the time domain and short time scales, while with the microwave background, we have a decomposition into spherical harmonics of an angular signal. A major difference however is the boundary condition, since there are no bound ends in the universe. But there is good reason why one gets peaks and droughts for the microwave background anyway: After inflation, perturbations with different wave numbers re-entered the horizon at various times and since then had different times to oscillate. What we observe today is then the amplitude of these oscillations, given the time difference between the time of their re-entering the horizon and today.

When plotting the power spectrum of the cosmic microwave background, one should keep in mind that for any given multipole, an infinite number of modes contributes, i.e. the same wavelength of the perturbation, but in different directions. Putting it another way, in order to plot the amplitude for a wave number, one needs to average over all wave vectors with that same wavenumber. But then the question is: Why don't these different amplitudes add up to zero? That is, for a given wavenumber, why did all the waves start off with the same phase? And the answer is the same as given above: Because of inflation. Perturbations evolved freely during inflation, but at some point they decoupled from the expansion, and their amplitude was frozen in. Then, at some later time, the perturbations re-entered our event horizon, all with zero velocities, thus adding up in phase.

Appendix B

Surface Treatment

Intent: In order to achieve low background conditions in the experiment, several arrangements have to be made. All materials used in the immediate vicinity of the detector modules are low background materials, mainly very pure copper, thus introducing only little amounts of radioactivity. But it is necessary to minimize surface contaminations of the employed parts. The cleaning processes which are used to do so are described in this chapter in a rather informal way.

B.1 Safety Notices

The surface treatment of metals utilizes dangerous chemicals. Be sure to

- Always wear protective glasses, protective gloves and appropriate clothing. Wash hands and face after working with these chemicals.
- Remember to never ever pour water into acid ("*Erst das Wasser, dann die Säure, sonst geschieht das Ungeheure*"). When diluting sulfuric acid, first supply the water, then pour the acid in real slowly. It will boil if poured in too quickly. In any case, the dilution will heat up to about 80 °C.
- Set up the process in a chemistry lab and make sure to dispose of waste properly.

B.2 Cleaning Copper

Starting point for this procedure are pieces made from copper or bronze as they come from a workshop. The cleaning procedure obeys the following steps, based on an older recipe [300]:

1. If the parts are very dirty or have corners which are difficult to access, they may be dipped in acetone first or even treated in an ultrasonic bath. Remove acetone before the next step e.g. by pressurized air or through a water dip.

2. The first major step is a dip in **Piranha acid**, which is in its concentrated form also known as **Carot's acid**. Piranha acid is a mixture of sulfuric acid H_2SO_4 to pickle the metal, and hydrogen peroxide H_2O_2 to remove organic contaminants. Here, only diluted piranha acid is used: For 1 l of acid, fill a container with 700 ml of de-ionized water. Very slowly add 150 ml of 95% H_2SO_4. This will heat up the mixture to about 80 °C, so wait until it has cooled down again (a few hours or so). Then add 150 ml of 30% H_2O_2.

   This solution will etch copper at a rate of very roughly 1 μm/min, but this value depends strongly on the temperature of the acid, the particular shape of the copper piece, and also on the particular copper alloy.

   For completeness it shall be noted that some people warn that above a concentration of roughly 3 g of copper per liter of acid this may "*catalyze the explosive decomposition of* H_2O_2" [300]. However, other sources give higher values of up to 10 g/l [301] and in my case this did not happen at all — even at higher concentrations. Nevertheless, one should try to stay below such values by estimating the amount etched — the density of copper is 9 g/cm^3.

3. After pickling, the parts are dipped in a few baths of de-ionized water, and afterward rinsed thoroughly. The pieces are now clean but have microscopically rough surfaces. For some parts this may already be sufficient. If the copper has not been rolled, one should even stop here to prevent the electrolyte used for electropolishing from penetrating the metal. In this case, the pieces are flushed in nitrogen until dry. Before packing, storage in vacuum overnight is encouraged to guarantee dry surfaces which will not oxidize.

4. The pickled pieces have rough surfaces which may in the turn of time accumulate lots of dirt, possibly radioactive. **Electropolishing** smoothens the surfaces, thus making it a smaller target for particles to stick to. At the Max-Planck-Institut für Physik, an electropolishing machine by *Poligrat* has been used. Detailed instructions can be found in the manual [301]. Electropolishing works like a galvanic process, the only difference being that here the specimen acts as the anode, and the material is removed from its surface. Since electric fields are strongest near tips, this smoothens the surface of the copper piece. Electrical contact is most easily made by copper hooks (e.g. for rings) or copper baskets (e.g. for screws).

   As with the etching process above, no precise numbers for the applied parameters can be given. With the setup used, a voltage of around 10 V polishes away about 1 μm of copper per minute. No material is removed where the specimen are electrically contacted, so the polishing is done in two (e.g. for rings) or more (e.g. for screws) stages with different contact points to yield a possibly uniform metal removal.

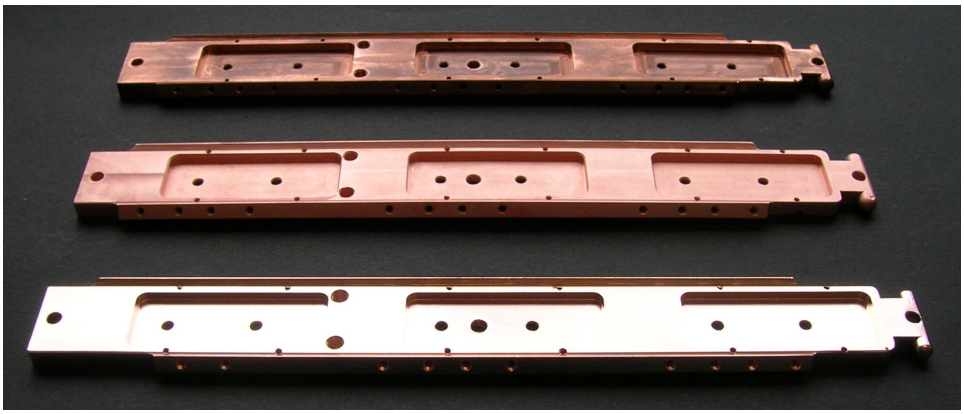

Figure B.1: Effect of the cleaning processes as described. Top: One of the CRESST carousel wings after machining in the workshop. Middle: After pickling, the wing has a clean, pink surface but is rough on a microscopic level. Bottom: After electropolishing, the surface is smooth and shiny. Surface contaminations have been removed.

5. Contrary to what is suggested in the Poligrat process *E 103* [301], after electropolishing the pieces are flushed immediately with de-ionized water. A series of dips in cleaner and cleaner water baths follows. Eventually, a thorough immersion in de-ionized water, vented by nitrogen, follows. Depending on the time of this immersion, the copper comes out in colors ranging from pink (after about 10 minutes) to orange (after more than about 30 minutes). Since the electrolyte is rather sticky and viscous, it is crucial that the water baths are exchanged very often so that the electrolyte cannot accumulate. As a final stage the specimens are rinsed in de-ionized water for more than a minute. Rinsing is a crucial step and has to be done patiently and thoroughly.

6. If packing of the pieces is required, one possibility is to dry them quickly with a highly pressurized inert gas to prevent stain due to water spotting. Then they can be stored in vacuum overnight to prevent any oxidation. Suggested packing is by sealing in foil in a slightly overpressurized inert gas atmosphere.

   For even cleaner surfaces, the drying with pressurized gas should be skipped since it will blow lots of dirt onto the surfaces (remember the Bernoulli effect caused by the pressurized noozle). In this case, the wet parts are put directly into vacuum overnight. Afterward they are only handled under clean room conditions. If the electropolishing process is not set up in a clean room (as was the case here) this is the recommended procedure.

B.3 Cleaning Other Materials

Usually other materials are cleaned with isopropanol or ethanol, if necessary in an ultrasonic bath. However, ethanol is made from sugar cane and is therefore rich in ^{40}C. Thus, for pieces which are very close to the detectors, methanol may used instead: Since methanol is made from mineral oil, it hardly contains radioactive isotopes. As a draw back, methanol is rather poisonous.

Electropolishing for other materials than copper or copper alloys requires different electrolytes. For details the reader is referred to the manuals.

Appendix C

Main Parameters

Intent: Main parameters that are calculated from the raw pulses are described.

Upon loading a file from disk, a set of fast and robust parameters are calculated. They are described in the following.

`Test pulse Amplitude:` In case the event is an injected heater pulse, this parameter stores the injected heater energy in volts. Control pulses have a test pulse amplitude of 10 V. If an empty baseline is recorded, this is treated as a heater pulse with negative amplitude.

`Time since Start:` This is the time of the event, taken from the computer clock, and can be used to retrieve the date and time of an event.

`Trigger Delay:` This parameter is zero for the pulse from a detector that triggers. Detectors on the same (8 channel) digitizer that trigger also within the allowed time window (half of the post trigger region) have their `trigger delay` parameter set to the time difference between their trigger signal and that of the first detector.

`Baseline Offset:` The average height of the baseline of the pulse, sampled from 95% of the pre-trigger region. Typically pulses are shown with their baseline subtracted, which just refers to this parameter.

`FWHM of Baseline:` Evaluated within 95% the pre-trigger region.

`Baseline Sample:` The average amplitude evaluated within the first averaging region, typically 50 samples.

`Baseline Gradient:` A first order polynomial is fitted to 95% of the baseline. The slope is then stored as this parameter.

`Right - Left Baseline:` The average of the baseline taken from the first 50 samples, minus the average of the baseline taken from the last 50 samples. This parameter gives a robust estimation of the inclination of the baseline. Such events occurs for example following a high-energy interaction, after which the detector could not relax back to its operating point within the record length.

`Pulse Height:` The 50-sample average of the pulse is calculated, and this parameter is the maximum of this filtered pulse minus the `baseline offset`. This is a quick and robust parameter, but it is biased and can

therefore not be used for further analysis. Proper pulse height evaluation is described in section 5.3.

`Peak Position:` The position of the position with the maximum amplitude used for the `pulse height` parameter. Due to the 50-sample averaging of the pulse this parameter is only good to this precision.

`Peak Onset:` Going from the peak position to earlier times, the peak onset is when the pulse height relaxes in the noise of the baseline.

`Rise- and Decay time:` Three parameters store the time required for the pulse to go from $(10-50)\%$, from $(10-70)\%$ and from $(1-\mathrm{e}^{-1})$ of the pulse height.

`Integral over Pulse Height:` A simple complete integral over the pulse, divided by the pulse height.

`Dead Time:` This parameter is the summed dead time for this detector since the measurement has started.

`Live Time:` Stores the life time of this detector since the measurement has started.

`Heater Demand:` Voltage applied for the constant heating of the thermometer through the heater structure.

Appendix D

Absorption of Photons

Intent: The attenuation of photons, given for the convenience of the reader.

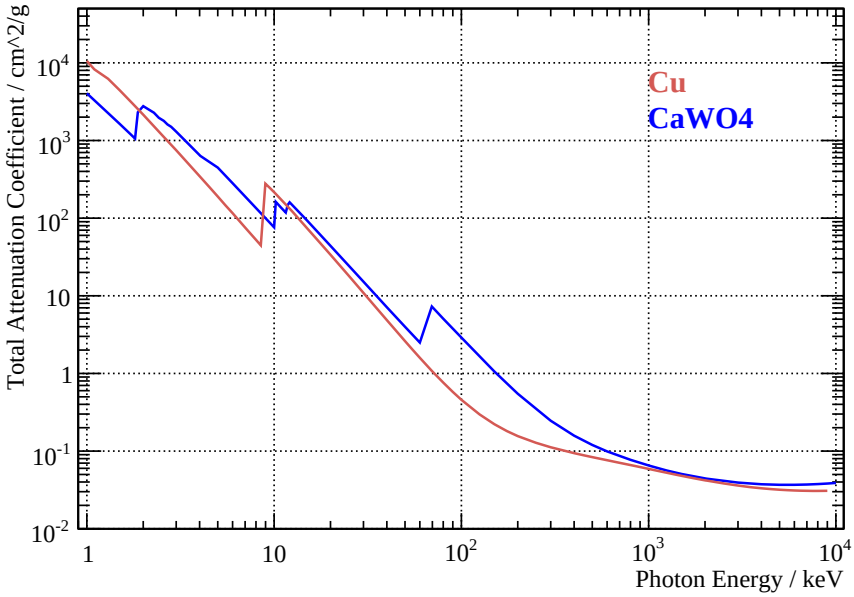

Figure D.1: The photon mass attenuation coefficient μ/ϱ for copper and calcium tungstate, extracted from [302]. The density of copper is $\varrho_{\mathrm{Cu}} = 8.92\,\mathrm{g/cm^3}$ and for calcium tungstate, $\varrho_{\mathrm{CaWO_4}} = [5.8 \ldots 6.1]\,\mathrm{g/cm^3}$. The intensity after a slab of material of thickness d is then given as $I/I_0 = \mathrm{e}^{-(\mu/\varrho)\,\varrho\,d}$.

Appendix E

Time Differences in a Poisson Process

Intent: A simple derivation of the exponential form expected for the time difference of events from a Poisson process that is used in section 9.2.7.

Consider the Poisson process

$$P_{\mathrm{n}}(\lambda) = \frac{\lambda^n}{n!}\mathrm{e}^{-\lambda} \tag{E.1}$$

with expectation value $\lambda = \mu\Delta t$. The distribution of time intervals until the next event is then

$$\begin{aligned} P(t)\,\mathrm{d}t &\equiv P(\text{next event comes in dt after an event at t}) \\ &= P(\text{no event in [0,t] and one event in [t,t+dt]}) && \text{(E.2)} \\ &= P_0(\mu t) \times P_1(\mu\ \mathrm{d}t) && \text{(E.3)} \\ &= \mathrm{e}^{-\mu t} \times \mu\ \mathrm{d}t\,\mathrm{e}^{-\mu\,\mathrm{d}t}. && \text{(E.4)} \end{aligned}$$

For $\mathrm{d}t \to 0$, we have $\mathrm{e}^{-\mu\ \mathrm{d}t} \to 1$, so

$$P(t)\,\mathrm{d}t = \mu\mathrm{e}^{-\mu t}\,\mathrm{d}t \tag{E.5}$$

and thus

$$P(t) = \mu\mathrm{e}^{-\mu t}. \tag{E.6}$$

Appendix F

Cut Defining Histograms

Intent: The histograms of the figures in section 9.2 that are used to define the cuts on the blind data sample are repeated here for the unblinded data. Some new populations appear in the histograms that are cut, but solely due to pathological pulse shapes.

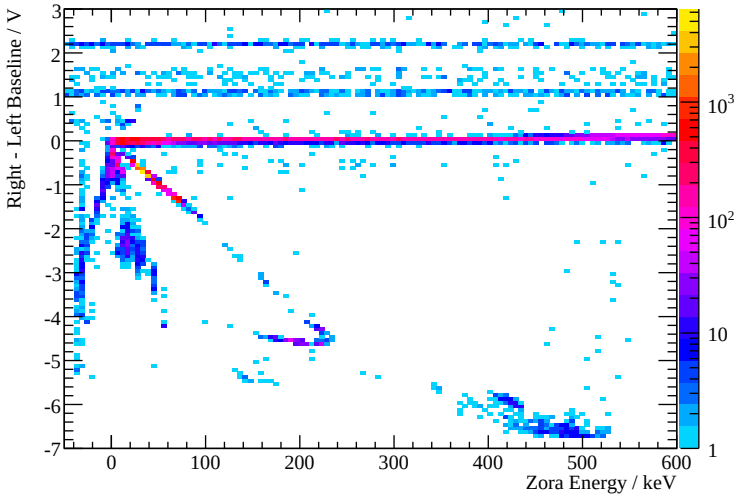

Figure F.1: Equivalent to figure 9.4: Broad histogram for detector ZORA during run 30 of the `right-minus-left-baseline` parameter versus energy, color coded is the number of entries per bin according to the scale on the right. The horizontal line at `right-minus-left-baseline` $\approx 0\,\mathrm{V}$ are the events of interest. The population that appears in addition in this figure below that horizontal line are only relaxing pulses that still triggered (figure 9.2 (i)).

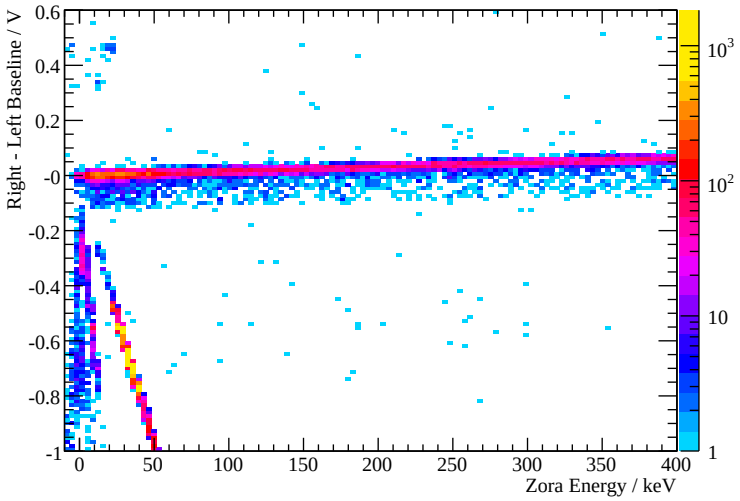

Figure F.2: Equivalent to figure 9.5: Zoom in the distribution of figure F.1. The events of interest are the dominant band at $\approx 0\,\mathrm{V}$ with events leaking to lower values being due to slightly inclined baselines after a high-energy interaction. A new population, going diagonally to the lower right, appears, which is again relaxing baselines like the one in figure 9.2 (i). The cut is placed as $-0.15 < \texttt{right-minus-left-baseline}/\mathrm{V} < +0.15$.

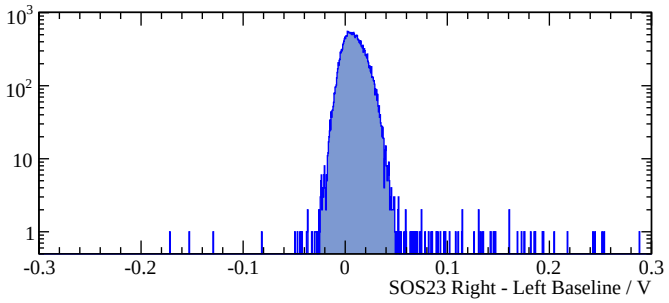

Figure F.3: Equivalent to figure 9.7: Histogram of the `right-minus-left-baseline` distribution for events in SOS23 that survived the previous cut in ZORA. The cut is placed at $-0.04 < \texttt{right-minus-left-baseline}/\mathrm{V} < +0.06$.

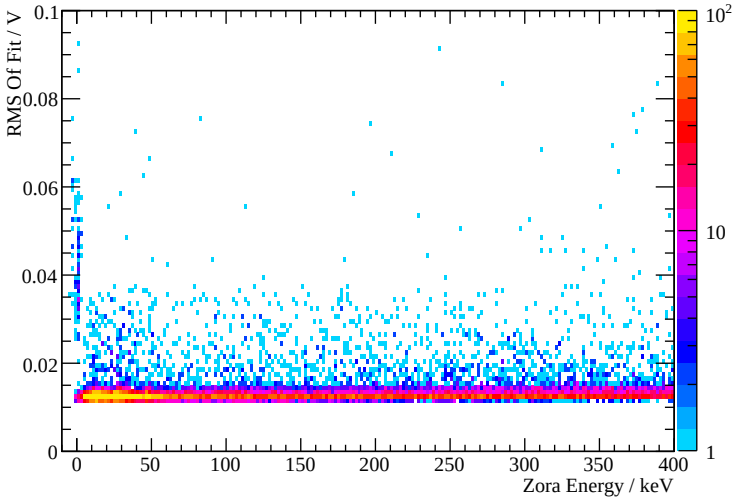

Figure F.4: Equivalent to figure 9.8: Events surviving the previous cuts in a histogram in the RMS-energy plane for the phonon detector. The cut is placed at RMS $< 0.03\,\mathrm{V}$, leaving the population of single particle interactions unaffected.

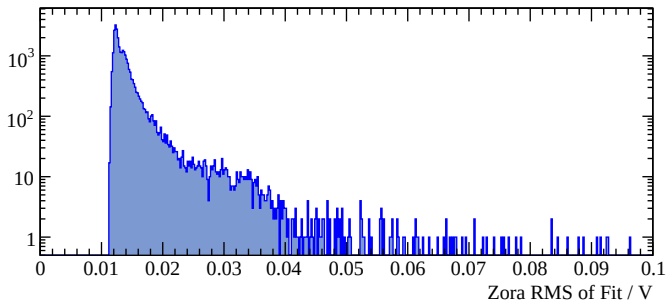

Figure F.5: Equivalent to figure 9.9: Histogram of the events in Zora that survived the above cuts. The cut is placed at $0.03\,\mathrm{V}$.

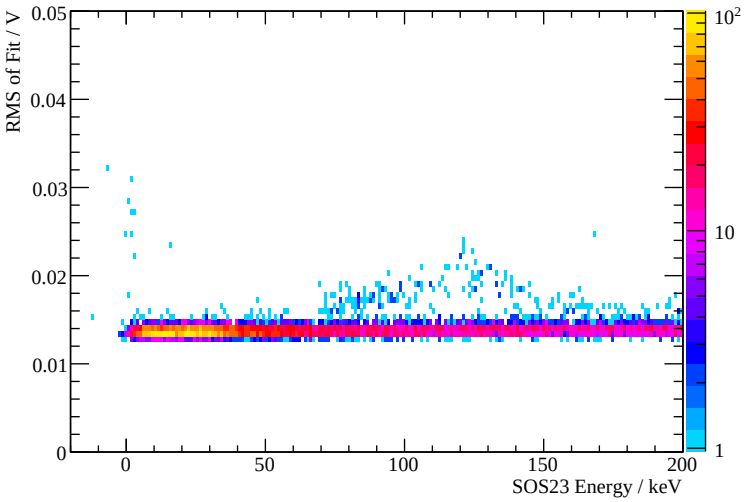

Figure F.6: Equivalent to figure 9.10: Events surviving the previous cuts in a histogram in the `RMS`-energy plane of the light detector, where the cut is placed at `RMS` $< 0.02\,\mathrm{V}$. No additional population above the main one appears from the hidden box.

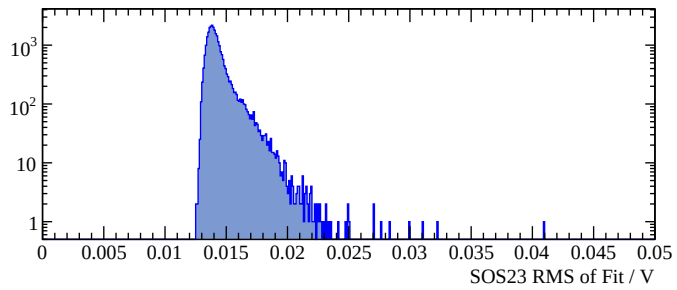

Figure F.7: Equivalent to figure 9.11: Histogram of the events in SOS23 that survived the above cuts. Here, the cut is placed at $0.02\,\mathrm{V}$.

Appendix G

Dark Events

Intent: Events that are observed well below the electron/gamma band following the analysis of chapter 9 are shown here. Parameters of the pulses in the phonon detector are also given.

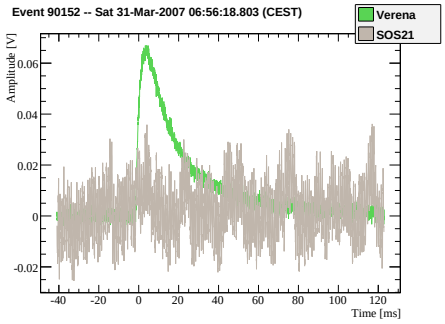

Figure G.1: The observed dark event of detector VERENA in the first data set (with high noise on the light detector SOS21) has a prolonged decay time.

Event	Date	File	Energy (keV)	Light Yield (keV_{ee}/keV)	RMS of Fit (V)	Decay time (ms)
Verena 1	31.03, 06:56:19	`bck2_007`	28.2	0.2121	0.00192	16.3

Table G.1: Parameters of an observed dark event of detector VERENA from the first data set with high noise on the light detector SOS21.

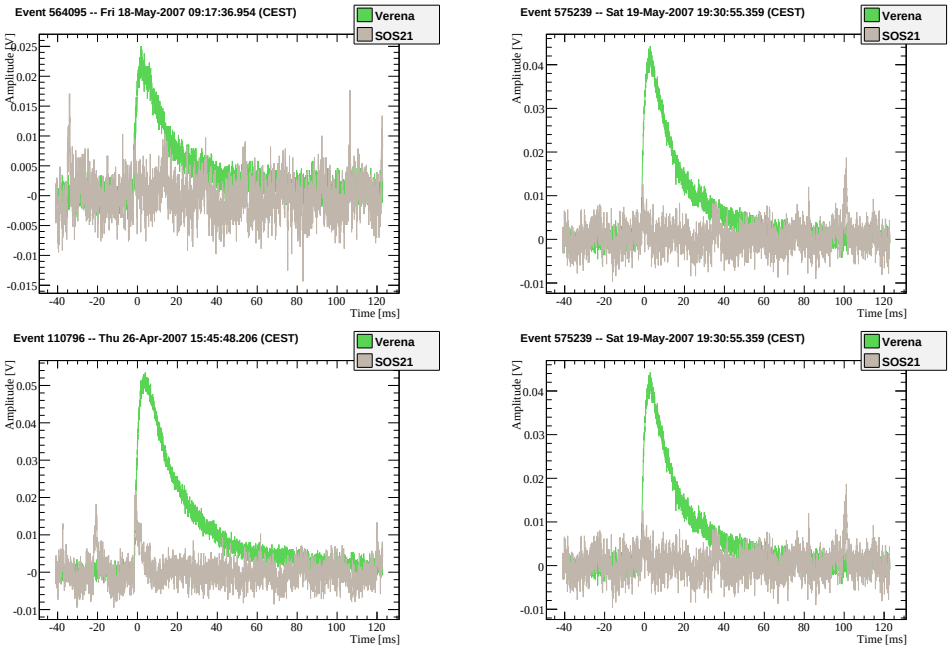

Figure G.2: The four observed dark events in the second data set (low noise) of detector VERENA.

Event	Date	File	Energy (keV)	Light Yield (keV_{ee}/keV)	RMS of Fit (V)	Decay time (ms)
Verena 2	18.05, 09:17:37	bck2_059	8.8	0.2145	0.00131	13.3
Verena 3	19.05, 19:30:55	bck2_062	17.0	0.1177	0.00131	13.0
Verena 4	26.04, 15:45:48	bck2_031	22.7	0.2559	0.00185	18.2
Verena 5	02.05, 23:53:23	bck2_039	46.5	0.1505	0.00134	15.7

Table G.2: Parameters of the four observed dark event in the second data set (low noise on the light detector) of detector VERENA/SOS21.

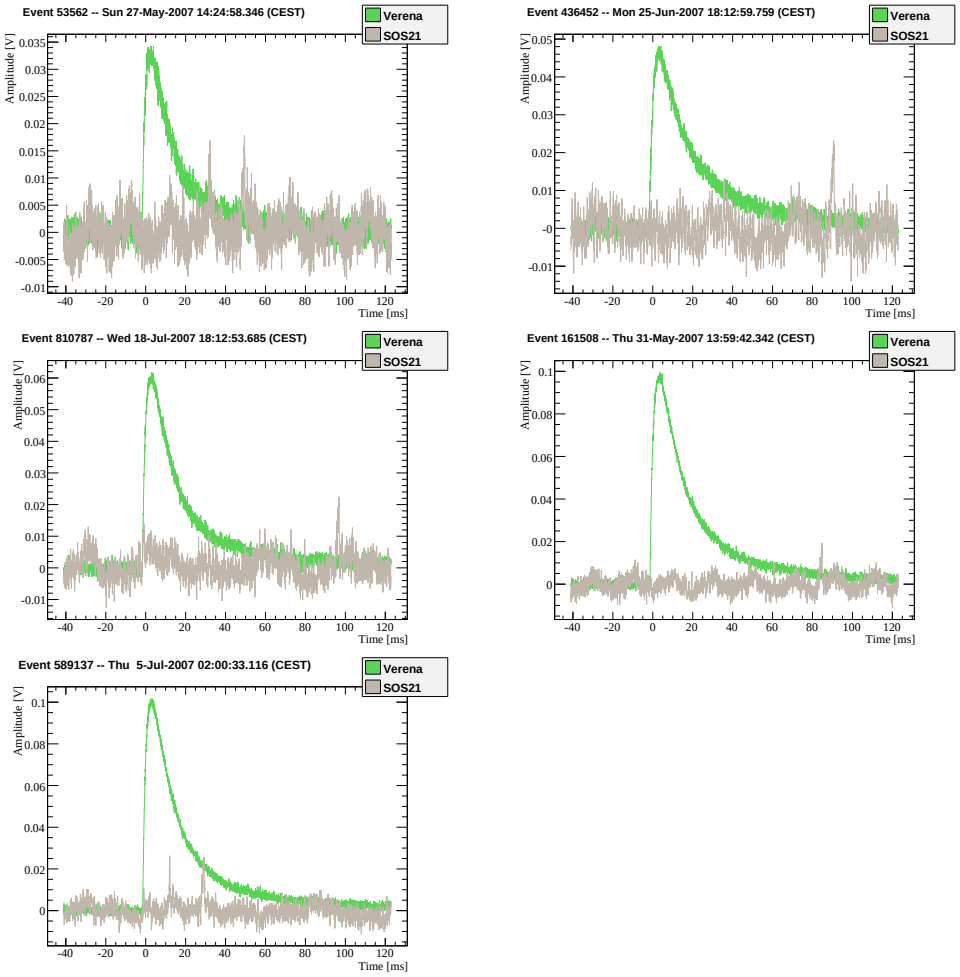

Figure G.3: The five observed dark events in the third data set of detector VERENA.

Event	Date	File	Energy (keV)	Light Yield (keV_{ee}/keV)	RMS of Fit (V)	Decay time (ms)
Verena 6	27.05, 14:24:58	bck2_068	13.4	-0.1106	0.00137	13.4
Verena 7	25.06, 18:13:00	bck3_003	20.0	-0.0418	0.00169	18.3
Verena 8	18.07, 18:12:54	bck3_030	24.9	0.1756	0.00129	14.4
Verena 9	31.05, 13:59:42	bck2_075	41.8	-0.0235	0.00138	16.4
Verena 10	05.07, 02:00:33	bck3_014	42.3	0.0397	0.00128	15.1

Table G.3: Parameters of the five observed dark event in the third data set (with medium noise on SOS21) of the phonon detector VERENA.

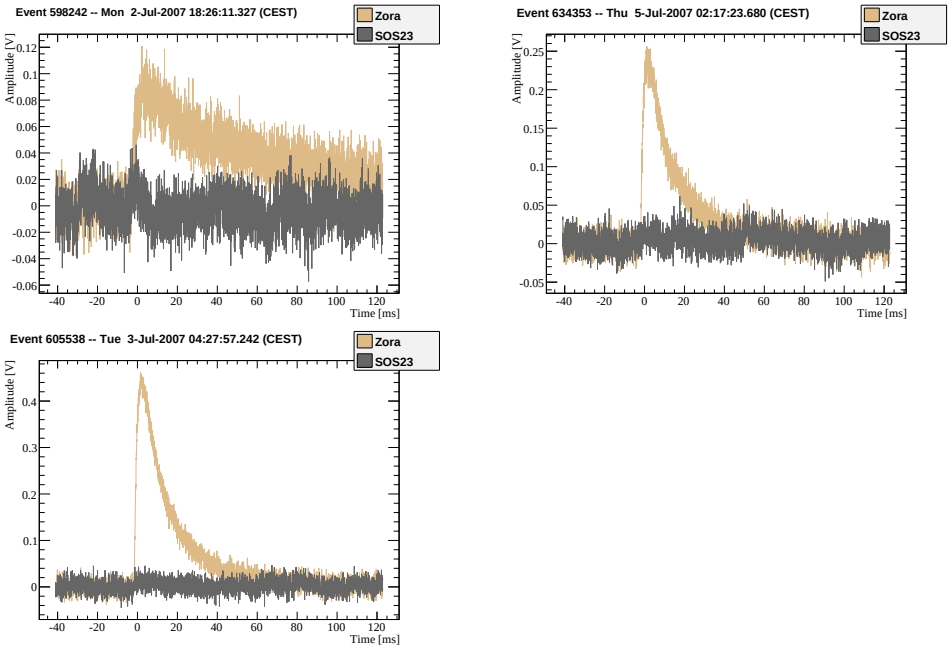

Figure G.4: The three observed dark events in the first data set of detector ZORA, from top left numbered 1, 2, and 3.

Event	Date	File	Energy (keV)	Light Yield (keV_{ee}/keV)	RMS of Fit (V)	Decay time (ms)
Zora 1	02.07, 18:26:11	bck3_011	12.0	0.0651	0.0188	22.6
Zora 2	05.07, 02:17:23	bck3_014	31.5	0.0526	0.0117	10.2
Zora 3	03.07, 04.27:57	bck3_011	59.1	0.0392	0.0125	12.8

Table G.4: Parameters of the three observed dark events in the first data set of detector ZORA. Event 1 has a much prolonged decay time.

Event	Date	File	Energy (keV)	Light Yield (keV_{ee}/keV)	RMS of Fit (V)	Decay time (ms)
Zora 4	07.04, 09:53:48	bck2_016	6.6	-0.3277	0.0131	23.0
Zora 5	30.03, 12:18:50	bck2_005	9.2	-0.0971	0.0129	21.3
Zora 6	18.05, 03:47:00	bck2_059	13.0	0.2521	0.0141	8.2
Zora 7	16.04, 04:34:24	bck2_023	18.1	0.0684	0.0121	10.0
Zora 8	30.03, 19:17:32	bck2_007	25.2	0.0411	0.0231	21.5
Zora 9	26.04, 10:54:42	bck2_031	28.6	-0.0023	0.0274	32.7
Zora 10	09.04, 17:54:12	bck2_017	46.9	0.0507	0.0118	12.2
Zora 11	26.03, 07:35:19	bck1_007	75.2	-0.0028	0.0269	20.6

Table G.5: Parameters of the eight observed dark events in the second data set of detector ZORA. Decay times and RMS values can be seen to be unusual for most of these events.

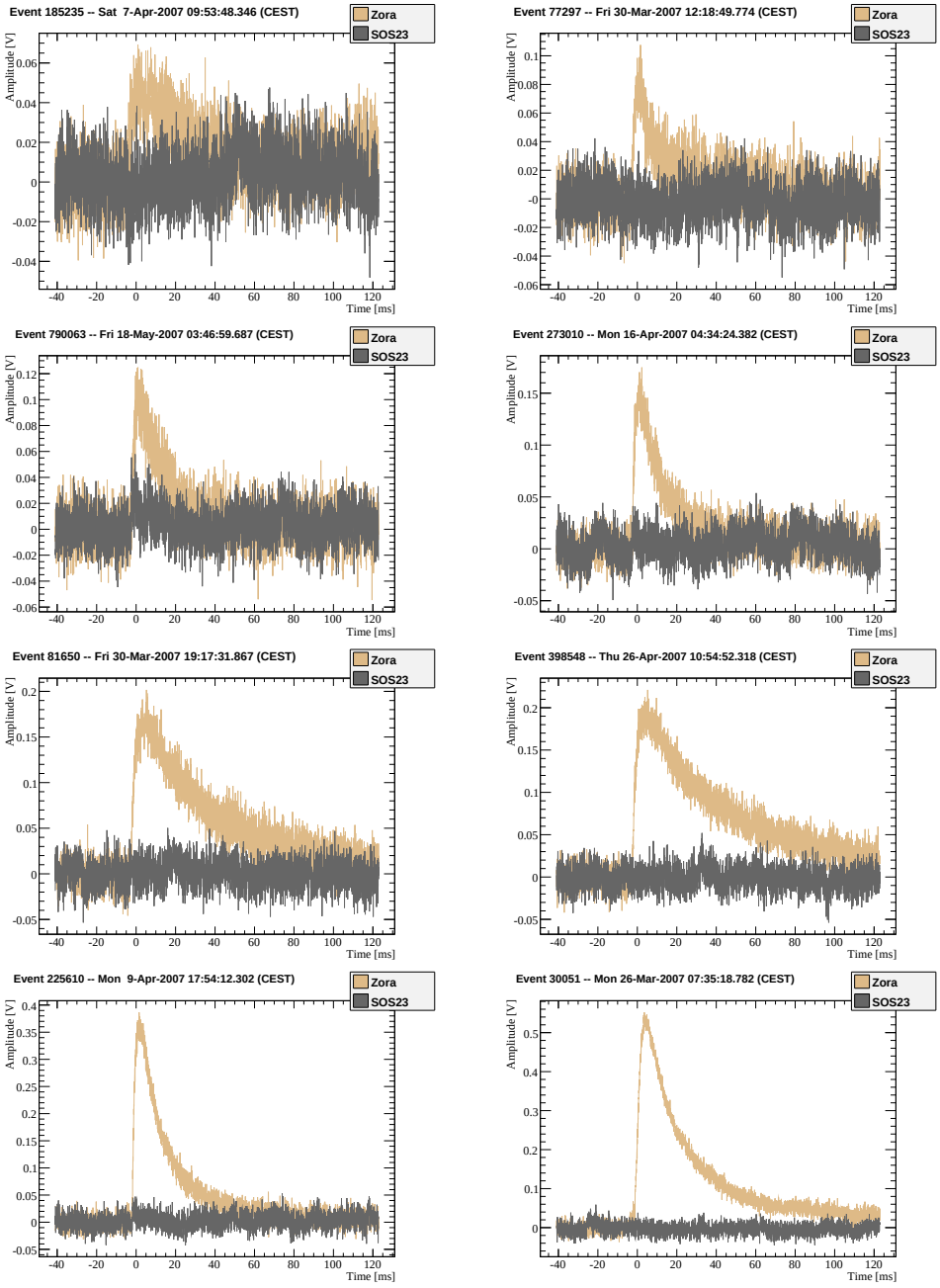

Figure G.5: The eight observed dark events in the second data set of detector Zora, from top left numbered 4 to 11.

Appendix H

Bowler Events

Intent: To avoid confusion, all the events that are cut by the bowler cut (section 9.3.1) are shown here. Only pulses with pathological shapes are removed by this cut.

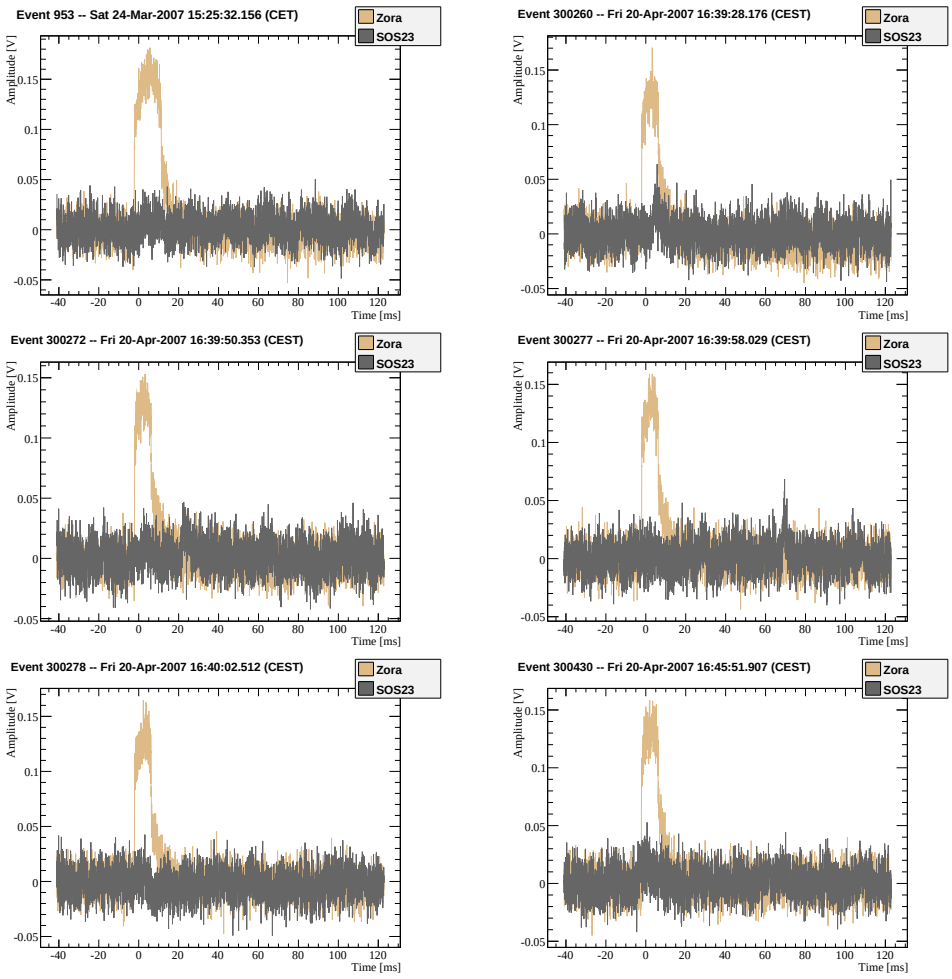

Figure H.1: All events removed by the bowler cut (continued next page).

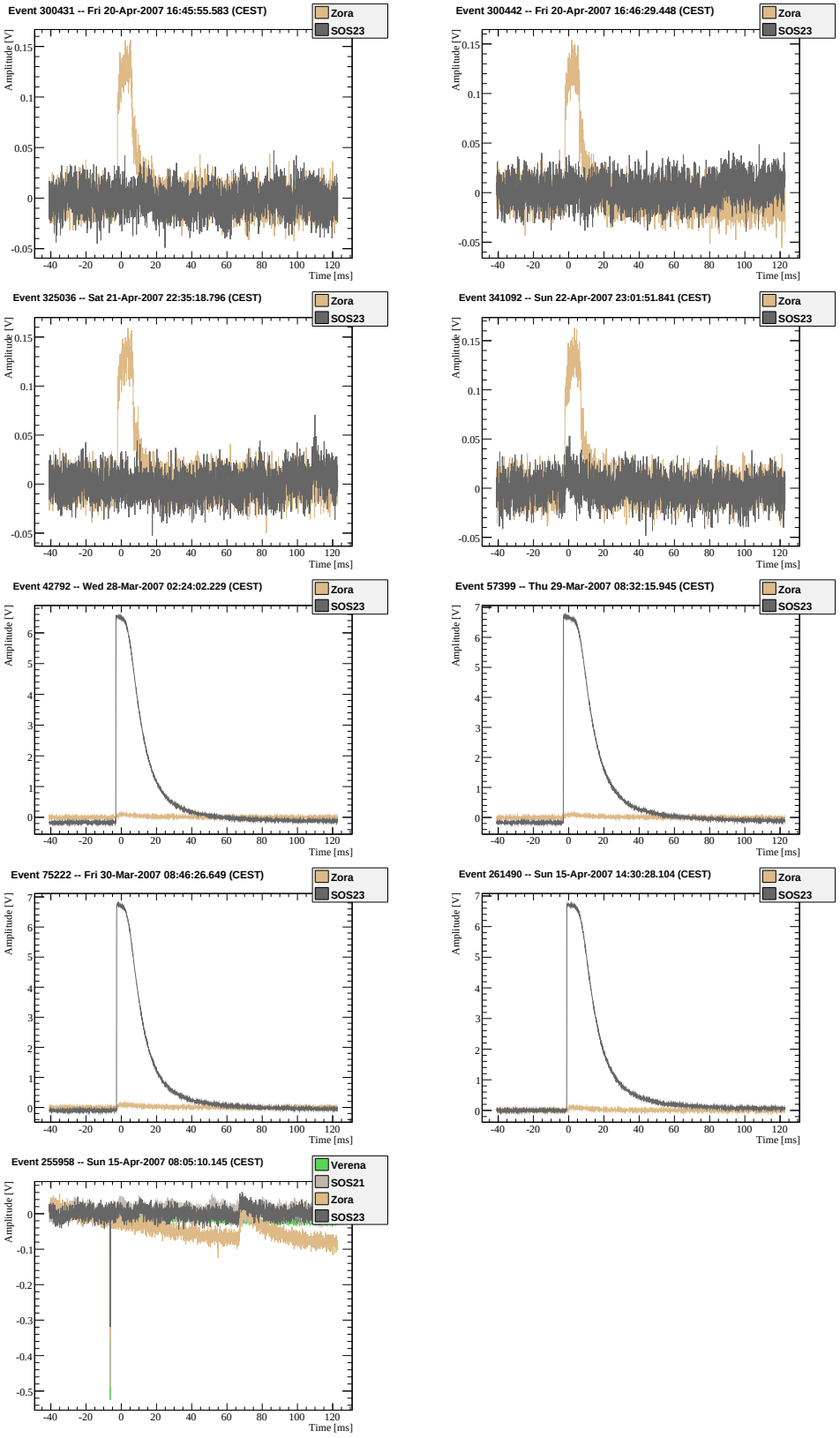

Figure H.1 (continued).

Appendix I

Alternative Resolution Extraction

Intent: An alternative method is discussed that can be used to extract the resolution of the light channel from the electron/gamma band. However, due to the non-gaussianity of the band, this method is found to perform worse than the one discussed in section 9.7. The method is described, and reasons for its failure are given.

I.1 The Method

I.1.1 Extracting the Band

As a first step, the light output L_i (in $\mathrm{keV_{ee}}$) for all events i is plotted versus energy E (in keV), and a polynomial is fitted to the band, see figure I.1 (a), yielding a fit $L(E)$. Since the light output L has to be zero for vanishing energy E, and since the light detector response is highly linear over the full energy range of interest, the simple function

$$L(E) = l_1 E + l_2 E^2 \tag{I.1}$$

is appropriate. Already the second term can mostly be neglected: In the example considered here, module Zora/SOS23 during run 30, the fit gives $L(E) = (1.19 \pm 0.01)\,\mathrm{keV_{ee}/keV}\ E + 7 \times 10^{-15}\,\mathrm{keV_{ee}/keV^2}\ E^2$.

However, the large squared residuals at large energies tend to be overweighted in a standard χ^2 fit with uniform weights, where the energy dependent resolution of the light detectors is not yet built into the method. Hence, each data point i needs to have an error ΔL_i attributed to it, which is of course the missing resolution.

I.1.2 Extracting the Resolution

Now, for each data point i at $(L_\mathrm{i}, E_\mathrm{i})$ the residual

$$\Delta L_\mathrm{i} = L_\mathrm{i} - L(E_\mathrm{i}) \tag{I.2}$$

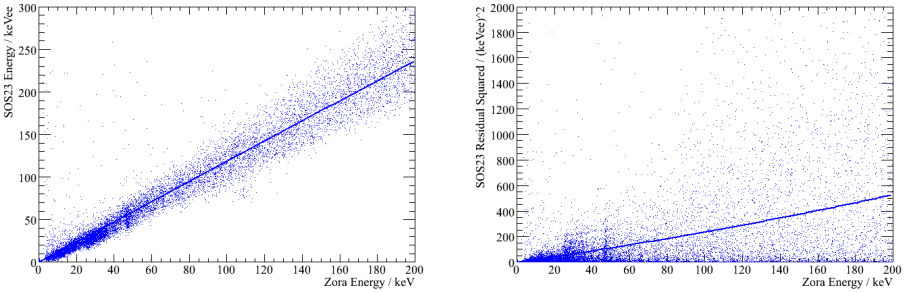

(a): Fitting a polynomial to the light response.

(b): Fitting a polynomial to the squared residuals.

Figure I.1: Picturing the method for calculating the light detector resolution with the example of module ZORA/SOS23 in run 30.

is calculated. These are squared,

$$(\Delta L_\mathrm{i})^2 \equiv S_\mathrm{i}(L_\mathrm{i}) \tag{I.3}$$

and the resulting distribution is fitted with a polynomial

$$(\Delta L)^2(E) \equiv S(E) = \sum_k s_k E^k, \tag{I.4}$$

see figure I.1 (b). $\Delta L(E)$ is of course already a first estimate of the energy resolution.

To define the band of events properly, the method is iterated: $L(E)$ is fitted again, with the errors ΔL_i considered for each point. In the example, $L(E)$ hardly changes but the fit parameters become better defined, $L(E) = (1.187 \pm 0.002)\,\mathrm{keV_{ee}/keV}\ E + 4 \times 10^{-14}\,\mathrm{keV_{ee}/keV^2}\ E^2$.

Since we now have a fit of the electron/gamma band, we can extract the resolution from the squares of the residuals $S(E)$ (figure I.1 (b)). Fitting requires once more that each data point has an error associated with it. This error is given by a straight forward error propagation:

$$\begin{aligned} \Delta S_\mathrm{i} &= \frac{\partial S_\mathrm{i}(L_\mathrm{i})}{\partial L_\mathrm{i}} \Delta L_\mathrm{i} \\ &= \frac{\partial (L_\mathrm{i}^2 - 2L_\mathrm{i}L + L^2)}{\partial L_\mathrm{i}} \Delta L_\mathrm{i} \\ &= 2(\Delta L_\mathrm{i})^2 \end{aligned} \tag{I.5}$$

$$\tag{I.6}$$

with the definitions I.2 and I.3. Fitting the distribution S_i with the errors ΔS_i yields the desired resolution of the light detectors.

I.2 Validating the Method

We can resort to simulation in order to validate this method and test its accuracy. To do so, 10000 data points are simulated, distributed equally in energy, and with light according to a Gaussian which mean and sigma both vary with energy according to defined polynomials. The task is then for the method to reconstruct these coefficients. For the slope of the electron/gamma band, the mean is simulated to be $L(E) = 1E + 10^{-10}E^2 = l_1E + l_2E^2$, and the width is simulated as $S^2(E) = (1^2 + (0.3\sqrt{E})^2 + (0.01E)^2 = s_0^2 + s_1^2E + s_2^2E^2$.

The fit rapidly converges. Already after the first iteration (that is, after fitting $L(E)$ and $S(E)$, calculating the errors on L_i and S_i, and fitting $L(E)$ and $S(E)$ again) the obtained values are close to the original values within the quoted error. A second iteration gives further convergence toward the simulated parameter for the important constant term of the resolution. In very few cases (less than 0.2%), it was observed in the simulation that s_0 was found to be zero, but after a third iteration, and with more than 34000 data samples simulated, no such flawed fits were observed.

Hence, one can be confident that after three iterations, the method yields the correct resolution parameters within the stated errors. Figures I.2 and I.3 illustrate this point.

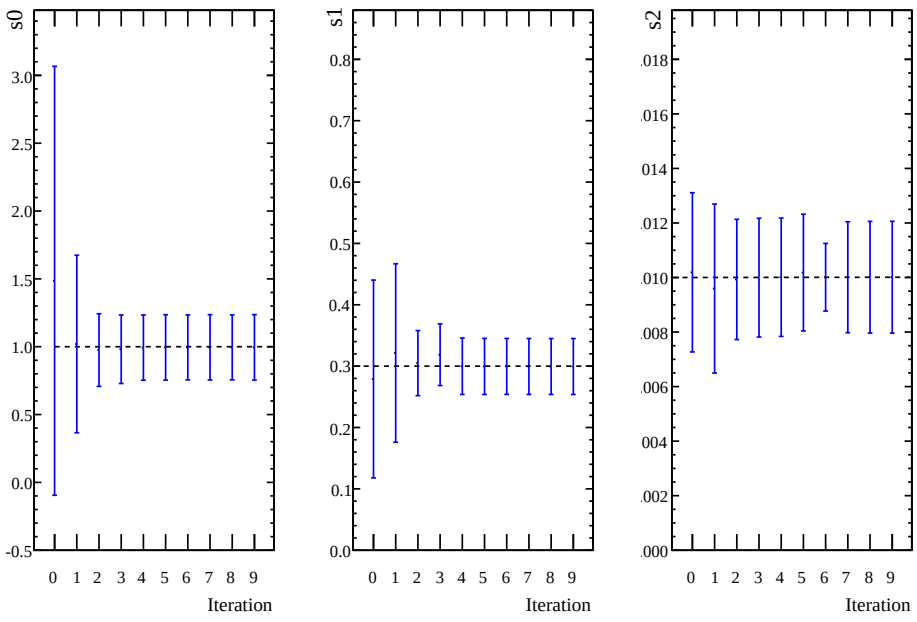

Figure I.2: Convergence of the resolution parameters σ_i^2, equation 9.1. Shown are mean and RMS of the distribution from 34329 individual simulations. After three iterations the results are stable.

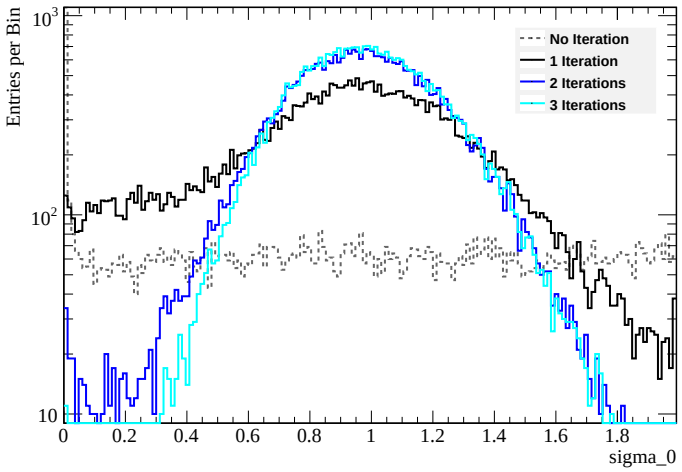

Figure I.3: The constant resolution term σ_0^2 inferred from simulation benefits from the method to be iterated three times.

I.3 Applying the Method

Unfortunately the data is not Gaussian but contaminated with the excess light events. These excess light events weigh heavily in the fit of the resolution (figure I.1 (b)) and cause the fitted resolution to be much worse than is actually the case.

Removing the excess light events with the help of the second fit quality criterion (section 9.7.1) drastically improves the situation. However, the observed band is still not symmetric, but has a few events leaking out toward high values: Remaining excess light events that could not be cut. These events still cause the calculated resolution at low energies to be worse than is actually the case. To cope with this problem, one can now use only the lower half of the band to calculate the light detector resolution. For the fit of S this simply means that only those events i are used which obey $L_\mathrm{i} < L(E_\mathrm{i})$. Figure I.4 shows the results of this method, applied as described to the data from module ZORA/SOS23 during half of run 30.

This complicates the method, but still does not give very satisfying results. The polynomial fit for $L(E)$ was also given an additional term $l_3 E^{3/2}$. This would give an term $\propto \sqrt{E}$ in the light yield plot to model a possible non-linearity of the light yield (chapter 7). However, the resulting fit left l_1 and l_2 as well has the resolution parameters σ_i unchanged within the stated errors, and in addition found $l_3 \approx 0$ within the error of the fit. Hence no such dependence could be modeled, and it is no surprise to see large systematic deviations in figure I.5.

Finally, figure I.6 helps to understand the limitation of this procedure, and why a direct fit in two dimensions as discussed in section 9.7 works much better. In the fit of the resolution to the squared residuals, outliers contribute with a strong weight, namely with their distance to the central

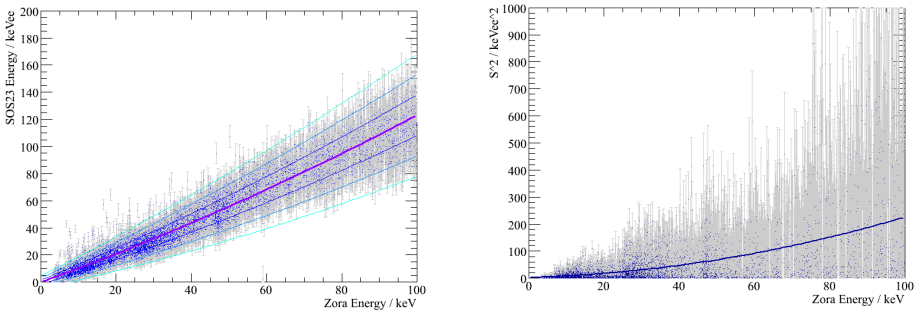

(a): The fitted polynomial to the light response, together with the 1σ, 2σ and 3σ widths of the derived band.

(b): The fit of a polynomial to the squared residuals of events below the central line $L(E)$.

Figure I.4: Results of the method for calculating the light detector resolution with the example of module Zora/SOS23 in run 30. The central line is at $L(E) = (0.999 \pm 0.004)\,\mathrm{keV/keV_{ee}}E + (0.00231 \times 10^{-10} \pm 0.00008)(\,\mathrm{keV/keV_{ee}})^2E^2$ and the derived resolution is $\sigma^2 = (2.5 \pm 1.3) + (0.38 \pm 0.14)E + (0.019 \pm 0.003)E^2$.

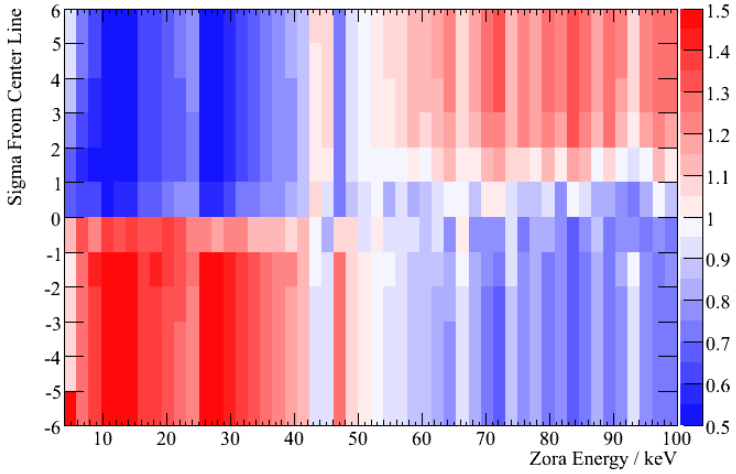

Figure I.5: Ratio observed entries divided by expected entries within a given confidence around the central band, shown color coded. At low energies, there are large systematic deviations due to the non-proportionality of the light yield. Just by looking one may even guess that this is data from detector Zora with its pronounced ^{227}Ac features and a rather sharp ^{210}Pb line. But even at high energies, the fit is not satisfactory.

line, which can be very large. Since the squares of the residuals are restricted to positive values, this causes the fitted resolution to be systematically overestimated. In the two dimensional fit on the other hand, these events do not contribute with their distance to the central line, but simply as a single event, which is negligible given the large population of normal behaving events. More generally, and this is also shown in figure I.6, the RMS value of a distribution with long tails is larger than the sigma inferred from a (Gaussian) fit to the distribution.

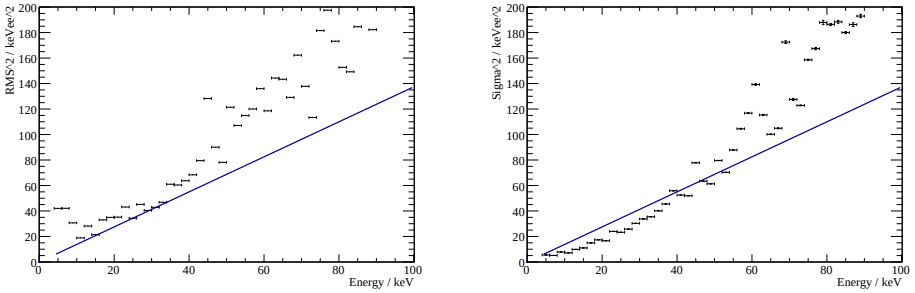

Figure I.6: Resolution of the light detector SOS23 in the data sample discussed here. The blue line is the resolution as inferred from the fit, even with excess lights removed and only considering the lower half of the band. (a): The RMS^2 of the residuals, binned in 2 keV bins. (b): The σ^2 of the residuals, from a Gaussian fit to the data in each 2 keV bin. $\sigma^2 < \mathrm{RMS}^2$ most prominently at low energies. The fit can be seen to resemble more the RMS values rather than the desired σ at least at low energies. Also toward higher energies the fit is unsatisfactory.

Acknowledgments

This thesis was written in the group of Dr. Franz Pröbst, whose liberal views made this work possible in the first place. His expertise was of inestimable value, and discussions with him always very fruitful. I am grateful to Prof. Lothar Oberauer for his spontaneous agreement to referee my thesis back when I had not even started on it, as well as to Prof. Allen Caldwell for his availability on short notice.

The atmosphere in the group is very pleasant. I am grateful to Wolfgang for many practical insights in hardware related issues, and for being a well of good ideas. Leo is a fantastic mentor, and discussions with him greatly contributed to the success of this thesis. Thanks go to Dieter for profound proofreading and intelligent questions. I am grateful to Federica, Bela and Antonio for countless discussions and comments. My gratitude to Hans not only for his availability to solve tricky problems. Many thanks to my office mate Irina. To my fellow colleagues Emilija, Jens, Patrick, Michael and Karo many thanks for proofreading, discussions, and the odd distraction.

I am thankful to Peter, Walter and Heinrich from the workshops who always were always available, also on short notice, and contribute a great deal with their high quality work and expertise to the success of the experiment. Thanks go to Mr. Vogt and Mr. Braun for a pleasant working environment, to Uwe and Denis for their computing support, and to Katharina and Eddi for a pleasant atmosphere.

I am indebted to my colleagues from Oxford, above all Hans, Barnaby and Richard. Thanks go to Wolfgang for numerous helpful remarks and discussions, and to Marcel for good times here and there.

Last but not least my gratitude goes to my parents who always were and still are the foundation of this work. I am deeply thankful to Franziska for so many things, be it only mentioned here, for her patience in the last months of writing this thesis.

Rafael Lang, München, Oktober 2008

Bibliography

[1] V. M. Slipher, *The Radial Velocity of the Andromeda Nebula*, Lowell Observatory Bulletin **II** (1913), no. 58, 56–57.

[2] V. M. Slipher, *Spectrographic Observations of Nebulae*, Popular Astronomy **23** (1915), 21–24.

[3] E. Hubble, *A Relation between Distance and Radial Velocity among Extra-Galactic Nebulae*, Proceedings of the National Academy of Science **15** (1929), 168–173.

[4] J. Lesgourgues, *An overview of Cosmology*, arXiv:astro-ph/0409426, 2004.

[5] A. Einstein, *Die Feldgleichungen der Gravitation*, Sitzungsberichte der Königlich Preußischen Akademie der Wissenschaften zu Berlin (1915), 844–847, also available from http://nausikaa2.mpiwg-berlin.mpg.de/cgi-bin/toc/toc.x.cgi?dir=6E3MAXK4.

[6] A. Friedman, *Über die Krümmung des Raumes*, Zeitschrift für Physik **10** (1922), no. 1, 377–386.

[7] E. Komatsu et al., *Five-Year Wilkinson Microwave Anisotropy Probe (WMAP) Observations: Cosmological Interpretation*, Astrophysical Journal Supplement Series (2008), accepted; arXiv:0803.0547.

[8] S. Dodelson, *Modern Cosmology*, Academic Press, San Diego, 2003.

[9] G. Steigman, *Primordial Nucleosynthesis in the Precision Cosmology Era*, The Annual Review of Nuclear and Particle Science **57** (2007), 463–491, arXiv:0712.1100.

[10] A. A. Penzias and R. W. Wilson, *A Measurement of Excess Antenna Temperature at 4080 Mc/s*, Astrophysical Journal **142** (1965), no. 1, 419–421.

[11] R. H. Dicke et al., *Cosmic Black-Body Radiation*, Astrophysical Journal **142** (1965), no. 1, 414–419.

[12] D. J. Fixsen et al., *The Cosmic Microwave Background Spectrum from the Full COBE1 FIRAS Data Set*, Astrophysical Journal **473** (1996), 576–587.

[13] *Wilkinson Microwave Anisotropy Probe*, homepage of the experiment at http://map.gsfc.nasa.gov/, 2008.

[14] G. F. Smoot et al., *First Results of the COBE Satellite Measurement of the Anisotropy of the Cosmic Microwave Background Radiation*, Advances in Space Research **11** (1991), no. 2, 193–205.

[15] G. Hinshaw et al., *Five-Year Wilkinson Microwave Anisotropy Probe (WMAP) Observations: Data Processing, Sky Maps, & Basic Results*, Astrophysical Journal Supplement Series (2008), accepted; arXiv:0803.0732.

[16] R. K. Sachs and A. M. Wolfe, *Perturbations of a Cosmological Model and Angular Variations of the Microwave Background*, Astrophysical Journal **147** (1967), no. 1, 73–90.

[17] J. Dunkley et al., *Five-Year Wilkinson Microwave Anisotropy Probe (WMAP) Observations: Likelihoods and Parameters from the WMAP data*, Astrophysical Journal Supplement Series (2008), accepted; arXiv:0803.0586.

[18] M. R. Nolta et al., *Five-Year Wilkinson Microwave Anisotropy Probe (WMAP) Observations: Angular Power Spectra*, Astrophysical Journal Supplement Series (2008), accepted; arXiv:0803.0593.

[19] P. de Bernardis et al., *A flat Universe from high-resolution maps of the cosmic microwave background radiation*, Nature **404** (2000), 955–959, arXiv:astro-ph/0004404.

[20] D. J. Eisenstein, W. Hu and M. Tegmark, *Cosmic Complementarity: Joint Parameter Estimation from Cosmic Microwave Background Experiments and Redshift Surveys*, Astrophysical Journal **518** (1999), no. 1, 2–23, arXiv:astro-ph/9807130.

[21] M. Tegmark et al., *Cosmological constraints from the SDSS luminous red galaxies*, Physical Review D **74** (2006), 123507, arXiv:astro-ph/0608632.

[22] V. Springel et al., *Simulations of the formation, evolution and clustering of galaxies and quasars*, Nature **435** (2005), 629–636, arXiv:astro-ph/0504097.

[23] D. G. York et al., *The Sloan Digital Sky Survey: Technical Summary*, Astronomical Journal **120** (2000), no. 3, 1579–1587, arXiv:astro-ph/0006396.

[24] C. Blake et al., *Cosmological baryonic and matter densities from 600000 SDSS luminous red galaxies with photometric redshifts*, Monthly Notices of the Royal Astronomical Society **374** (2007), no. 4, 1527–1548, arXiv:astro-ph/0605303.

[25] K.-H. Chae, *Cosmological Parameters from the SDSS DR5 Velocity Dispersion Function of Early-Type Galaxies through Radio-selected Lens Statistics*, Astrophysical Journal Letters **658** (2007), no. 2, L71–L74, arXiv:astro-ph/0611898.

[26] W. J. Percival et al., *The Shape of the Sloan Digital Sky Survey Data Release 5 Galaxy Power Spectrum*, Astrophysical Journal **657** (2007), no. 2, 645–663, arXiv:astro-ph/0608636.

[27] T. Padmanabhan, *Structure Formation in the Universe*, Cambridge University Press, Cambridge, 1993.

[28] M. Davis et al., *The Evolution of Large-Scale Structure in a Universe Dominated by Cold Dark Matter*, Astrophysical Journal **292** (1985), no. 2, 371–394.

[29] F. W. Bessel, *On the Variations of the Proper Motions of Procyon and Sirius*, Monthly Notices of the Royal Astronomical Society **6** (1844), 136–141.

[30] F. W. Bessel, *Ueber Veränderlichkeit der eigenen Bewegungen der Fixsterne*, Astronomische Nachrichten **22** (1844), no. 514, 145–160.

[31] N. S. Hetherington, *Sirius B and the gravitational redshift - an historical review*, Royal Astronomical Society, Quarterly Journal **21** (1980), no. 3, 246–252.

[32] J. C. Adams, *An Explanation of the observed Irregularities in the Motion of Uranus, on the Hypothesis of Disturbance caused by a more distant Planet*, Monthly Notices of the Royal Astronomical Society **7** (1846), 149–157.

[33] T. J. J. See, *Leverrier's Letter to Galle and the Discovery of Neptune*, Popular Astronomy **18** (1910), 475–476.

[34] C. L. Cowan et al., *Detection of the Free Neutrino: A Confirmation*, Science **124** (1956), 103.

[35] F. Reines and C. L. Cowan, *The Neutrino*, Nature **178** (1956), 446.

[36] R. Schödel et al., *A star in a 15.2-year orbit around the supermassive black hole at the centre of the Milky Way*, Nature **419** (2002), 694–696.

[37] E. W. Kolb and M. S. Turner, *The Early Universe*, Addison-Wesley, Redwood City, 1989.

[38] M. Taoso, G. Bertone and A. Masiero, *Dark Matter Candidates: A Ten-Point Test*, Journal of Cosmology and Astroparticle Physics **0803** (2008), 022, arXiv:0711.4996.

[39] G. Jungman, M. Kamionkowski and K. Griest, *Supersymmetric dark matter*, Physics Reports **267** (1996), 195–373, arXiv:hep-ph/9506380.

[40] J. D. Barrow, *Cosmology and Elementary Particles*, Fundamentals of Cosmic Physics **8** (1983), 83–200.

[41] K. Griest and D. Seckel, *Three exceptions in the calculation of relic abundances*, Physical Review D **43** (1991), no. 10, 3191–3203.

[42] J. E. Gunn et al., *Some Astrophysical Consequences of the Existence of a Heavy Stable Neutral Lepton*, Astrophysical Journal **223** (1978), no. 3, 1015–1031.

[43] *Dwarf Galaxies in Coma Cluster*, Courtesy NASA/JPL-Caltech/GSFC/SDSS, http://photojournal.jpl.nasa.gov/catalog/PIA09561, 2008.

[44] F. Zwicky, *Die Rotverschiebung von extragalaktischen Nebeln*, Helvetica Physica Acta **6** (1933), 110–127.

[45] M. J. Geller, A. Diaferio and M. J. Kurtz, *The Mass Profile of the Coma Galaxy Cluster*, Astrophysical Journal **517** (1999), no. 1, L23–L26, arXiv:astro-ph/9903305.

[46] E. L. Lokas and G. A. Mamon, *Dark matter distribution in the Coma cluster from galaxy kinematics*, Monthly Notices of the Royal Astronomical Society **343** (2003), 401–412, arXiv:astro-ph/0302461.

[47] C. S. Kochanek et al., *Clusters of Galaxies in the Local Universe*, Astrophysical Journal **585** (2003), no. 1, 161–181, arXiv:astro-ph/0208168.

[48] D. Clowe et al., *A Direct Empirical Proof Of The Existence Of Dark Matter*, Astrophysical Journal Letters **648** (2006), L109–L113, arXiv:astro-ph/0608407.

[49] F. D. Kahn and L. Woltjer, *Intergalactic Matter and the Galaxy*, Astrophysical Journal **130** (1959), no. 3, 705–717.

[50] C. S. Kochanek, *The Mass of the Milky Way*, Astrophysical Journal **457** (1996), 228–243, arXiv:astro-ph/9505068.

[51] J. Binney and S. Tremaine, *Galactic Dynamics*, 2nd ed., Princeton Series in Astrophysics, Princeton University Press, Princeton, 1994.

[52] *The Digitized Sky Survey POSS-II*, homepage of the survey at http://archive.stsci.edu/dss/index.html, 2008.

[53] E. Corbelli and P. Salucci, *The extended rotation curve and the dark matter halo of M33*, Monthly Notices of the Royal Astronomical Society **311** (2000), 441–447, arXiv:astro-ph/9909252.

[54] E. Corbelli, *Dark matter and visible baryons in M33*, Monthly Notices of the Royal Astronomical Society **342** (2003), 199–207, arXiv:astro-ph/0302318.

[55] G. Gentile et al., *NGC3741: the dark halo profile from the most extended rotation curve*, Monthly Notices of the Royal Astronomical Society **375** (2007), 199–212, arXiv:astro-ph/0611355.

[56] H. W. Babcock, *Spectrographic Observations of the Rotation of the Andromeda Nebula*, Publications of the Astronomical Society of the Pacific **50** (1938), no. 295, 174–175.

[57] V. C. Rubin and W. K. Ford, *Rotation of the Andromeda Nebula from a Spectroscopic Survey of Emission Regions*, Astrophysical Journal **159** (1970), no. 2, 379–403, and images on plates 1–3.

[58] V. C. Rubin, N. Thonnard and W. K. Ford, *Extended rotation curves of high-luminosity spiral galaxies. IV - Systematic dynamical properties, SA through SC*, Astrophysical Journal Letters **225** (1978), no. 3, L107–L111.

[59] M. Persic, P. Salucci and F. Stel, *The universal rotation curve of spiral galaxies - I. The dark matter connection*, Monthly Notices of the Royal Astronomical Society **281** (1996), no. 1, 27–47, arXiv:astro-ph/0604496.

[60] P. Salucci et al., *The Universal Rotation Curve of Spiral Galaxies. II. The Dark Matter Distribution out to the Virial Radius*, Monthly Notices of the Royal Astronomical Society **378** (2007), no. 1, 41–47, arXiv:astro-ph/0703115.

[61] R. A. Benjamin et al., *First GLIMPSE Results on the Stellar Structure of the Galaxy*, Astrophysical Journal Letters **630** (2005), no. 2, L149–L152, arXiv:astro-ph/0508325.

[62] J. P. Ostriker and P. J. E. Peebles, *A Numerical Study of the Stability of Flattened Galaxies: or, can Cold Galaxies Survive?*, Astrophysical Journal **186** (1973), no. 2, 467–480.

[63] D. Lynden-Bell, *Statistical Mechanics of Violent Relaxation in Stellar Systems*, Monthly Notices of the Royal Astronomical Society **136** (1967), no. 1, 101–121.

[64] R. Kippenhahn and A. Weigert, *Stellar Structure and Evolution*, 1st ed., Springer, Berlin, 1994.

[65] J. F. Navarro, C. S. Frenk and S. D. M. White, *The Structure of Cold Dark Matter Halos*, Astrophysical Journal **462** (1996), no. 2, 563–575, arXiv:astro-ph/9508025.

[66] J. F. Navarro, C. S. Frenk and S. D. M. White, *A Universal Density Profile from Hierarchical Clustering*, Astrophysical Journal **490** (1997), no. 2, 493–508, arXiv:astro-ph/9611107.

[67] B. Moore et al., *Cold collapse and the core catastrophe*, Monthly Notices of the Royal Astronomical Society **310** (1999), no. 4, 1147–1152, arXiv:astro-ph/9903164.

[68] Kravtsov et al., *The Cores of Dark Matter-dominated Galaxies: Theory versus Observations*, Astrophysical Journal **502** (1998), no. 1, 48–58, arXiv:astro-ph/9708176.

[69] L. Bergström, P. Ullio and J. H. Buckley, *Observability of γ rays from dark matter neutralino annihilations in the Milky Way halo*, Astroparticle Physics **9** (1998), no. 2, 137–162, arXiv:astro-ph/9712318.

[70] E. Daw, *PHY-323, Lecture 3, The Isothermal Sphere Model*, available from http://www.shef.ac.uk/physics/teaching/phy323, 2004.

[71] M. Fich, L. Blitz and A. A. Stark, *The Rotation Curve of the Milky Way to $2R_0$*, Astrophysical Journal **342** (1989), no. 1, 272–284.

[72] M. Honma and Y. Sofue, *Rotation Curve of the Galaxy*, Publications of the Astronomical Society of Japan **49** (1997), no. 4, 453–460, arXiv:astro-ph/9611156.

[73] J. Brand and L. Blitz, *The velocity field of the outer Galaxy*, Astronomy and Astrophysics **275** (1993), 67–90.

[74] E. S. Levine, C. Heiles and L. Blitz, *The Milky Way Rotation Curve and its Vertical Derivatives Inside the Solar Circle*, Astrophysical Journal **679** (2008), no. 2, 1288–1298, arXiv:0802.2714.

[75] W. B. Burton and M. A. Gordon, *Carbon Monoxide in the Galaxy, III. The Overall Nature of its Distribution in the Equatorial Plane*, Astronomy and Astrophysics **63** (1978), 7–27.

[76] M. Fich and S. Tremaine, *The mass of the Galaxy*, Annual Review of Astronomy and Astrophysics **29** (1991), 409–445.

[77] K. Kuijken and G. Gilmore, *The mass distribution in the galactic disc - I. A technique to determine the integral surface mass density of the disc near the Sun*, Monthly Notices of the Royal Astronomical Society **239** (1989), no. 3, 571–603.

[78] K. Kuijken and G. Gilmore, *The mass distribution in the galactic disc - II. Determination of the surface mass density of the galactic disc near the Sun*, Monthly Notices of the Royal Astronomical Society **239** (1989), no. 3, 605–649.

[79] K. Kuijken and G. Gilmore, *The mass distribution in the galactic disc - III. The local volume mass density*, Monthly Notices of the Royal Astronomical Society **239** (1989), no. 3, 651–664.

[80] M. Crézé et al., *The distribution of nearby stars in phase space mapped by Hipparcos. I. The potential well and local dynamical mass*, Astronomy and Astrophysics **329** (1998), 920–936, arXiv:astro-ph/9709022.

[81] B. Moore et al., *Dark matter in Draco and the Local Group: Implications for direct detection experiments*, Physical Review D **64** (2001), 063508, arXiv:astro-ph/0106271.

[82] R. A. Flores, *Dynamical Estimates of the Local Density of Dark Matter*, Physics Letters B **215** (1988), no. 1, 73–80.

[83] C. Flynn, J. Holopainen and J. Holmberg, *White dwarfs and Galactic dark matter*, Monthly Notices of the Royal Astronomical Society **339** (2003), 817–824, arXiv:astro-ph/0202244.

[84] L. Iorio, *Solar System planetary orbital motions and dark matter*, Journal of Cosmology and Astroparticle Physics **05** (2006), 002, arXiv:gr-qc/0602095.

[85] I. B. Khriplovich and E. V. Pitjeva, *Upper Limits on Density of Dark Matter in Solar System*, International Journal of Modern Physics D **15** (2006), no. 4, 615–618, arXiv:astro-ph/0601422.

[86] J. D. Anderson et al., *Indication, from Pioneer 10/11, Galileo, and Ulysses Data, of an Apparent Anomalous, Weak, Long-Range Acceleration*, Physical Review Letters **81** (1998), no. 14, 2858–2861, arXiv:gr-qc/9808081.

[87] J. D. Anderson et al., *Study of the anomalous acceleration of Pioneer 10 and 11*, Physical Review D **65** (2002), 082004, arXiv:gr-qc/0104064.

[88] J.-M. Frère, F.-S. Ling and G. Vertongen, *Bound on the dark matter density in the Solar System from planetary motions*, Physical Review D **77** (2008), 083005, arXiv:astro-ph/0701542.

[89] J. D. Anderson et al., *Anomalous Orbital-Energy Changes Observed during Spacecraft Flybys of Earth*, Physical Review Letters **100** (2008), 091102.

[90] S. L. Adler, *Can the flyby anomaly be attributed to earth-bound dark matter?*, arXiv:0805.2895v1, 2008.

[91] T. Damour and L. M. Krauss, *A New Solar System Dark Matter Population of Weakly Interacting Massive Particles*, Physical Review Letters **81** (1998), no. 26, 5726–5729, arXiv:astro-ph/9806165.

[92] T. Damour and L. M. Krauss, *New WIMP population in the solar system and new signals for dark-matter detectors*, Physical Review D **59** (1999), 063509, arXiv:astro-ph/9807099.

[93] X. Xu and E. R. Siegel, *Dark matter in the Solar System*, Physical Review D (2008), submitted; arXiv:0806.3767.

[94] A. H. G. Peter, S Tremaine, *Dynamics of WIMPs in the solar system and implications for detection*, arXiv:0806.2133, 2008.

[95] J. L. Feng, S. Su and F. Takayama, *Lower Limit on Dark Matter Production at the CERN Large Hadron Collider*, Physical Review Letters **96** (2006), 151802, arXiv:hep-ph/0503117.

[96] A. De Roeck (ed.), *CMS Physics Technical Design Report, Volume II: Physics Performance*, 2006, ISBN 978-92-9083-269-0, CERN/LHCC2006-021. See in particular section 4.2.2.

[97] E. A. Baltz et al., *Determination of Dark Matter Properties at High-Energy Colliders*, Physical Review D **74** (2006), 103521, arXiv:hep-ph/0602187.

[98] A. Heister et al. (The ALEPH Collaboration), *Absolute mass lower limit for the lightest neutralino of the MSSM from e^+e^- data at $\sqrt{s}$ up to* 209 GeV, Physics Letters B **583** (2004), 247–263.

[99] J. Diemand et al., *Clumps and streams in the local dark matter distribution*, Nature **454** (2008), 735–738, arXiv:0805.1244.

[100] J. Lavalle et al., *Full calculation of clumpiness boost factors for antimatter cosmic rays in the light of ΛCDM N-body simulation results*, Astronomy and Astrophysics **479** (2008), 427–452, arXiv:0709.3634.

[101] Zackrisson et al., *Strong lensing by subhalos in the dwarf-galaxy mass range I: Image separations*, Astrophysical Journal **684** (2008), no. 2, 804–810, arXiv:0806.2149.

[102] D. Hooper, *Indirect Searches For Dark Matter: Signals, Hints and Otherwise*, arXiv:0710.2062, 2007.

[103] G. Bertone, D. Hooper and J. Silk, *Particle dark matter: evidence, candidates and constraints*, Physics Reports **405** (2005), no. 5–6, 279–390, arXiv:hep-ph/0404175.

[104] D. P. Finkbeiner, *Microwave Interstellar Medium Emission Observed by the Wilkinson Microwave Anisotropy Probe*, Astrophysical Journal **614** (2008), no. 1, 186–193, arXiv:astro-ph/0311547.

[105] D. Hooper, D. P. Finkbeiner and G. Dobler, *Possible evidence for dark matter annihilations from the excess microwave emission around the center of the Galaxy seen by the Wilkinson Microwave Anisotropy Probe*, Physical Review D **76** (2007), 083012, arXiv:0705.3655.

[106] D. Hooper at al., *Prospects for detecting dark matter with GLAST in light of the WMAP haze*, Physical Review D **77** (2008), 043511, arXiv:0709.3114.

[107] P. Jean et al., *Early SPI/INTEGRAL measurements of 511 keV line emission from the 4th quadrant of the Galaxy*, Astronomy and Astrophysics **407** (2003), L55–L58, arXiv:astro-ph/0309484.

[108] C. Boehm et al., *MeV Dark Matter: Has It Been Detected?*, Physical Review Letters **92** (2004), no. 10, 101301, arXiv:astro-ph/0309686.

[109] D. P. Finkbeiner and N. Weiner, *Exciting Dark Matter and the INTEGRAL/SPI 511 keV signal*, Physical Review D **76** (2007), 083519, arXiv:astro-ph/0702587.

[110] G. Weidenspointner et al., *An asymmetric distribution of positrons in the Galactic disk revealed by γ-rays*, Nature **451** (2008), 159–162.

[111] W. de Boer et al., *EGRET excess of diffuse galactic gamma rays as tracer of dark matter*, Astronomy and Astrophysics **444** (2006), no. 1, 51–67, arXiv:astro-ph/0508617.

[112] W. de Boer et al., *The supersymmetric interpretation of the EGRET excess of diffuse Galactic gamma rays*, Physics Letters B **636** (2006), 13–19, arXiv:hep-ph/0511154.

[113] I. V. Moskalenko et al., *Understanding limitations in the determination of the diffuse Galactic gamma-ray emission*, Nuclear Physics B (Proceedings Supplement) **173** (2007), 44–47, arXiv:astro-ph/0609768.

[114] D. Elsässer and K. Mannheim, *Supersymmetric Dark Matter and the Extragalactic Gamma Ray Background*, Physical Review Letters **94** (2005), 171302, arXiv:astro-ph/0405235.

[115] F. W. Stecker, S. D. Hunter and D. A. Kniffen, *The likely cause of the EGRET GeV anomaly and its implications*, Astroparticle Physics **29** (2008), 25–29, arXiv:0705.4311.

[116] S. Ando and E. Komatsu, *Anisotropy of the cosmic gamma-ray background from dark matter annihilation*, Physical Review D **73** (2006), 023521, arXiv:astro-ph/0512217.

[117] S. Ando, *Can Dark Matter Annihilation Dominate the Extragalactic Gamma-Ray Background?*, Physical Review Letters **94** (2005), 171303, arXiv:astro-ph/0503006.

[118] A. W. Strong, I. V. Moskalenko and O. Reimer, *A New Determination of the Extragalactic Diffuse Gamma-Ray Background from EGRET Data*, Astrophysical Journal **613** (2004), no. 2, 962–976, arXiv:astro-ph/0406254.

[119] L. Bergström et al., *Gamma Rays from Kaluza-Klein Dark Matter*, Physical Review Letters **94** (2005), 131301, arXiv:astro-ph/0410359.

[120] D. Horns, *TeV γ-radiation from Dark Matter annihilation in the Galactic center*, Physics Letters B **607** (2005), 225–232, arXiv:astro-ph/0408192. Erratum ibid., **611** (2005), 297.

[121] F. Aharonian and A. Neronov, *High energy gamma rays from the massive black hole in the Galactic Center*, Astrophysical Journal **619** (2005), 306–313, arXiv:astro-ph/0408303.

[122] R. M. Crocker et al., *The AGASA/SUGAR Anisotropies and TeV Gamma Rays from the Galactic Center: A Possible Signature of Extremely High-energy Neutrons*, Astrophysical Journal **622** (2005), 892–909, arXiv:astro-ph/0408183.

[123] F. Aharonian et al. (The H.E.S.S. Collaboration), *HESS Observations of the Galactic Center Region and Their Possible Dark Matter Interpretation*, Physical Review Letters **97** (2006), 221102, arXiv:astro-ph/0610509 (and an erratum for the pedant: Physical Review Letters **97** (2006) 249901).

[124] S. W. Barwick et al. (The HEAT Collaboration), *Measurements of the Cosmic-Ray Positron Fraction From 1 to 50 GeV*, Astrophysical Journal Letters **482** (1997), no. 2, L191–L194, arXiv:astro-ph/9703192.

[125] I. V. Moskalenko and A. W. Strong, *Production and Propagation of Cosmic-Ray Positrons and Electrons*, Astrophysical Journal **493** (1998), no. 2, 694–707, arXiv:astro-ph/9710124.

[126] T. Delahaye et al., *Positrons from dark matter annihilation in the galactic halo: Theoretical uncertainties*, Physical Review D **77** (2008), 063527, arXiv:0712.2312.

[127] F. Donato et al., *Antiprotons in cosmic rays from neutralino annihilation*, Physical Review D **69** (2004), 063501, arXiv:astro-ph/0306207.

[128] J. Ellis et al., *Prospects for Detecting Supersymmetric Dark Matter at Post-LEP Benchmark Points*, European Physical Journal C **24** (2002), no. 2, 311–322, arXiv:astro-ph/0110225.

[129] L. Bergström et al., *Is the dark matter interpretation of the EGRET gamma excess compatible with antiproton measurements?*, Journal of Cosmology and Astroparticle Physics **0506** (2006), 006, arXiv:astro-ph/0602632.

[130] I. Gebauer, *Uncertainties of the antiproton flux from Dark Matter annihilation in comparison to the EGRET excess of diffuse gamma rays*, in: Proceedings of SUSY07, arXiv:0710.4966, 2008.

[131] F. Donato, N. Fornengo and D. Maurin, *Antideuteron fluxes from dark matter annihilation in diffusion models*, arXiv:0803.2640, 2008.

[132] H. Fuke et al. (The BESS Collaboration), *Search for Cosmic-Ray Antideuterons*, Physical Review Letters **95** (2005), 081101, arXiv:astro-ph/0504361.

[133] F. Donato, N. Fornengo and P. Salati, *Antideuterons as a signature of supersymmetric dark matter*, Physical Review D **62** (2000), 043003, arXiv:hep-ph/9904481.

[134] J. Edsjö, M. Schelke and P. Ullio, *Direct versus indirect detection in mSUGRA with self-consistent halo models*, Journal of Cosmology and Astroparticle Physics **0409** (2004), 004, arXiv:astro-ph/0405414.

[135] V. Barger, W. -Y. Keung and G. Shaughnessy, *Monochromatic Neutrino Signals from Dark Matter Annihilation*, Physics Letters B **664** (2008), no. 3, 190–193, arXiv:0709.3301.

[136] P. Natarajan et al., *Constraints on the Collisional Nature of the Dark Matter from Gravitational Lensing in the Cluster A2218*, Astrophysical Journal Letters **580** (2002), no. 1, L17–L20, arXiv:astro-ph/0207045.

[137] G. D. Starkman et al., *Opening the window on strongly interacting dark matter*, Physical Review D **41** (1990), no. 12, 3594–3603.

[138] R. H. Cyburt et al., *Constraining strong baryon–dark-matter interactions with primordial nucleosynthesis and cosmic rays*, Physical Review D **65** (2002), no. 12, 123503, arXiv:astro-ph/0203240.

[139] G. D. Mack, J. F. Beacom and G. Bertone, *Towards closing the window on strongly interacting dark matter: Far-reaching constraints from Earth's heat flow*, Physical Review D **76** (2007), 043523, arXiv:0705.4298.

[140] H. Nelson, *Searches For Dark Matter (the Quest), Lecture 1*, given at the SLAC Summer Institute, available from http://www.slac.stanford.edu/econf/C0307282/lec_notes/nelson.html, 2003.

[141] I. F. M. Albuquerque and L. Baudis, *Direct Detection Constraints on Superheavy Dark Matter*, Physical Review Letters **90** (2003), no. 22, 221301, Erratum ibid., **91** (2003), 229903, arXiv:astro-ph/0301188.

[142] A. Drukier and L. Stodolsky, *Principles and applications of a neutral-current detector for neutrino physics and astronomy*, Physical Review D **30** (1984), no. 11, 2295–2309.

[143] M. W. Goodman and E. Witten, *Detectability of certain dark-matter candidates*, Physical Review D **31** (1985), no. 12, 3059–3063.

[144] F. Giuliani, *Are Direct Search Experiments Sensitive to All Spin-Independent Weakly Interacting Massive Particles?*, Physical Review Letters **95** (2005), 101301, arXiv:hep-ph/0504157.

[145] F. Donato, N. Fornengo and S. Scopel, *Effects of galactic dark halo rotation on WIMP direct detection*, Astroparticle Physics **9** (1998), 247–260, arXiv:hep-ph/9803295.

[146] R. H. Helm, *Inelastic and Elastic Scattering of 187-MeV Electrons from Selected Even-Even Nuclei*, Physical Review **104** (1956), no. 5, 1466–1475.

[147] J. Engel, *Nuclear form factors for the scattering of weakly interacting massive particles*, Physics Letters B **264** (1991), no. 1,2, 114–119.

[148] J. D. Lewin and P. F. Smith, *Review of mathematics, numerical factors, and corrections for dark matter experiments based on elastic nuclear recoil*, Astroparticle Physics **6** (1996), 87–112, see also *Detector response corrections: correction* and *Spin factors - revised tables*, available from http://hepwww.rl.ac.uk/UKDMC/pub/publications.html.

[149] P. J. T. Leonard and S. Tremaine, *The Local Galactic Escape Speed*, Astrophysical Journal **353** (1990), no. 2, 486–493.

[150] B. W. Carroll and D. A. Ostlie, *An Introduction to Modern Astrophysics*, 2nd ed., Pearson Education, 2007.

[151] F. J. Kerr and D. Lynden-Bell, *Review of galactic constants*, Monthly Notices of the Royal Astronomical Society **221** (1986), 1023–1038.

[152] A. K. Drukier, K. Freese and D. N. Spergel, *Detecting cold dark-matter candidates*, Physical Review D **33** (1986), no. 12, 3495–3508.

[153] K. Griest, *Effect of the Sun's gravity on the distribution and detection of dark matter near the Earth*, Physical Review D **37** (1988), no. 10, 2703–2713.

[154] A. Gould, *Resonant Enhancements in Weakly Interacting Massive Particle Capture by the Earth*, Astrophysical Journal **321** (1987), no. 1, 571–585.

[155] A. Bottino et al., *Exploring the supersymmetric parameter space by direct search for WIMPS*, Physics Letters B **402** (1997), no. 1-2, 113–121, arXiv:hep-ph/9612451.

[156] J. Åström et al., *Fracture processes studied in CRESST*, Nuclear Instruments and Methods A **559** (2006), 754–756.

[157] J. Åström et al., *Fracture processes observed with a cryogenic detector*, Physics Letters A **356** (2006), no. 4-5, 262–266, arXiv:physics/0504151.

[158] J. Åström et al., *Comment on "Universal Distribution of Interearthquake Times"*, arXiv:physics/0612081, 2006.

[159] J. Åström et al., *Brittle fracture down to femto-Joules — and below*, arXiv:0708.4315, 2007.

[160] K. Freese, J. Frieman and A. Gould, *Signal modulation in cold-dark-matter detection*, Physical Review D **37** (1988), no. 12, 3388–3405.

[161] C. Enss (ed.), *Cryogenic Particle Detection*, ch. *Dark Matter Direct Detection* by G. Chardin, Springer, Heidelberg, 2005, arXiv:astro-ph/0411503.

[162] R. J. Gaitskell, *Direct Detection of Dark Matter*, Annual Review of Nuclear and Particle Science **54** (2004), 315–359.

[163] S. P. Ahlen et al., *Limits on cold dark matter candidates from an ultralow background germanium spectrometer*, Physics Letters B **195** (1987), no. 4, 603–608.

[164] D. O. Caldwell et al., *Searching for the cosmion by scattering in Si detectors*, Physical Review Letters **65** (1990), no. 11, 1305–1308.

[165] P. S. Barbeau, J. I. Collar and O. Tench, *Large-Mass Ultra-Low Noise Germanium Detectors: Performance and Applications in Neutrino and Astroparticle Physics*, Journal of Cosmology and Astroparticle Physics **09** (2007), 009, arXiv:nucl-ex/0701012.

[166] C. E. Aalseth et al. (The CoGeNT Collaboration), *Experimental constraints on a dark matter origin for the DAMA annual modulation effect*, arXiv:0807.0879, 2008.

[167] R. Bernabei et al., *First results from DAMA/LIBRA and combined results with DAMA/NaI*, European Physical Journal C (2008), submitted; arXiv:0804.2741.

[168] R. Bernabei et al., *The DAMA/LIBRA apparatus*, Nuclear Instruments and Methods A (2008), submitted; arXiv:0804.2738.

[169] R. Bernabei et al., *Possible implications of the channeling effect in NaI(Tl) crystals*, European Physical Journal C **53** (2008), 205–213, arXiv:0710.0288.

[170] R. Foot, *Mirror dark matter and the new DAMA/LIBRA results: A simple explanation for a beautiful experiment*, 2008, arXiv:0804.4518.

[171] E. Behnke et al., *Spin-Dependent WIMP Limits from a Bubble Chamber*, Science **319** (2008), 933–936, arXiv:0804.2886.

[172] H. S. Lee et al. (The KIMS Collaboration), *Limits on Interactions between Weakly Interacting Massive Particles and Nucleons Obtained with CsI(Tl) Crystal Detectors*, Physical Review Letters **99** (2007), 091301, arXiv:0704.0423.

[173] V. Sanglard et al. (The EDELWEISS Collaboration), *Final results of the EDELWEISS-I dark matter search with cryogenic heat-and-ionization Ge detectors*, Physical Review D **71** (2005), 122002, arXiv:astro-ph/0503265.

[174] S. Scorza, *The EDELWEISS-II Experiment*, arXiv:0806.3147, 2008.

[175] D. S. Akerib et al. (The CDMS Collaboration), *First Results from the Cryogenic Dark Matter Search in the Soudan Underground Laboratory*, Physical Review Letters **93** (2004), no. 21, 211301, arXiv:astro-ph/0405033.

[176] D. S. Akerib et al. (The CDMS Collaboration), *Exclusion Limits on the WIMP-Nucleon Cross-Section from the First Run of the Cryogenic Dark Matter Search in the Soudan Underground Laboratory*, Physical Review D **72** (2005), 052009, arXiv:astro-ph/0507190.

[177] D. S. Akerib et al. (The CDMS Collaboration), *Limits on Spin-Independent Interactions of Weakly Interacting Massive Particles with Nucleons from the Two-Tower Run of the Cryogenic Dark Matter Search*, Physical Review Letters **96** (2006), 011302, arXiv:astro-ph/0509259.

[178] D. S. Akerib et al. (The CDMS Collaboration), *Limits on spin-dependent WIMP-nucleon interactions from the Cryogenic Dark Matter Search*, Physical Review D **73** (2006), 011102, arXiv:astro-ph/0509269.

[179] Z. Ahmed et al. (The CDMS Collaboration), *A Search for WIMPs with the First Five-Tower Data from CDMS*, Physical Review Letters (2008), submitted, arXiv:0802.3530.

[180] E. Aprile et al., *Scintillation response of liquid xenon to low energy nuclear recoils*, Physical Review D **72** (2005), 072006, arXiv:astro-ph/0503621.

[181] E. Aprile et al., *Simultaneous Measurement of Ionization and Scintillation from Nuclear Recoils in Liquid Xenon for a Dark Matter Experiment*, Physical Review Letters **97** (2006), 081302, arXiv:astro-ph/0601552.

[182] J. Angle et al. (The XENON Collaboration), *First Results from the XENON10 Dark Matter Experiment at the Gran Sasso National Laboratory*, Physical Review Letters **100** (2008), 021303, arXiv:0706.0039.

[183] G. Bertone et al., *Identification of Weakly Interacting Massive Particles Through a Combined Measurement of Axial and Scalar Couplings*, Physical Review Letters **99** (2007), 151301, arXiv:0705.2502.

[184] G. Sciolla et al., *DM-TPC: a new approach to directional detection of Dark Matter*, arXiv:0805.2431, 2008.

[185] D. Dujmic et al. (The DM-TPC Collaboration), *Observation of the "head-tail" effect in nuclear recoils of low-energy neutrons*, Nuclear Instruments and Methods A **584** (2008), no. 2–3, 327–333, arXiv:0708.2370.

[186] S. Burgos et al. (The DRIFT Collaboration), *Studies of neutron detection and backgrounds with the DRIFT-IIa dark matter detector*, Astroparticle Physics **28** (2007), no. 4–5, 409–421, arXiv:0707.1488.

[187] T. K. Gaisser, *Cosmic Rays and Particle Physics*, Cambridge University Press, Cambridge, 1990.

[188] W.-M. Yao et al., *Review of Particle Physics*, Journal of Physics G **33** (2006), 1, chapter 24: *Cosmic Rays*, available from http://pdg.lbl.gov.

[189] *Canfranc underground laboratory (LSC)*, webpage at http://www.unizar.es/lfnae/ipaginas/ip0200.html, 2008.

[190] *Deep Science*, webpage at http://www.deepscience.org/, 2008.

[191] *Cryogenic Rare Event Search with Superconducting Thermometers*, homepage of the experiment at http://www.cresst.de/, 2008.

[192] G. Angloher et al. (The CRESST Collaboration), *Cresst-II: dark matter search with scintillating absorbers*, Nuclear Instruments and Methods A **520** (2004), 108–111.

[193] *LNGS - Gran Sasso National Laboratory*, homepage of the laboratory at http://www.lngs.infn.it/, 2008.

[194] M. Aglietta et al. (The LVD Collaboration), *Muon "depth-intensity" relation measured by the LVD underground experiment and cosmic-ray muon spectrum at sea level*, Physical Review D **58** (1998), 092005, arXiv:hep-ex/9806001.

[195] R. B. Firestone et al., *Table of Isotopes (CD ROM Edition)*, 1st ed., John Wiley & Sons, New York, 1996.

[196] A. Bassignani et al., *Review of Long Term Radon Studies at the Gran Sasso Underground Laboratory*, Radiation Measurements **25** (1995), no. 1–4, 557–560.

[197] A. Bassignani et al., *Measurements of Radon Concentration and Gamma Ray Activity in Hall B of the Gran Sasso Laboratory*, Radiation Measurements **28** (1997), no. 1–6, 609–612.

[198] M. Laubenstein, *WP1: Measurement of the backgrounds in the EU underground sites*, www.unizar.es/ilias/JRA1/Paris0207/J1_WP1_laubenstein_paris2007.ppt, see also http://www.unizar.es/ilias/docs/internal/JRA1_2nd_techreports.pdf, 2007.

[199] J. Kisiel, *Gamma ray background measurements in the underground labs*, http://ilias.in2p3.fr/ilias_site/meetings/documents/ILIAS_3rd_Annual_Meeting/Parallel_ULA_Kisiel.pdf, 2006.

[200] For example, the author read a value of 75 $\mathrm{Bq/m^3}$ in hall A at 17:30 o'clock on August 7th, 2008.

[201] C. Arpesella, *Background Measurements at Gran Sasso Laboratory*, Nuclear Physics B (Proceedings Supplement) **28A** (1992), 420–424.

[202] C. Arpesella, *Background Measurements at Gran Sasso Laboratory*, Applied Radiation and Isotopes **47** (1996), no. 9–10, 991–996.

[203] G. Pfennig et al., *Karlsruher Nuklidkarte*, 6th edition 1995, revised reprint 1998, Marktdienste Haberbeck Lage/Lippe, 1998.

[204] A. Zastawny, J. Bialoń and T. Sosiński, *Migration of* ^{210}Po *in Lead to the Surface*, Applied Radiation and Isotopes **43** (1992), no. 9, 1147–1150.

[205] T. Nakamura and M. Nakamura, *Radioactivity measurement of materials for OPERA experiment*, http://flab.phys.nagoya-u.ac.jp/~takunaka/radioactivity.html, 2000.

[206] A. Alessandrello et al., *Measurements of internal radioactive contamination in samples of Roman lead to be used in experiments on rare events*, Nuclear Instruments and Methods B **142** (1998), 163–172.

[207] E. Fiorini, *Measurements on low Radioactivity: From Fundamental to Environmental Physics*, www.presid.infn.it/er/er04fiorini.ppt, 2004.

[208] *NA-CAST – Die Marke für Stranggussprodukte*, Norddeutsche Affinerie AG, Hamburg, 1998.

[209] *Weihenstephan — älteste Brauerei der Welt*, http://www.brauerei-weihenstephan.de/.

[210] G. Angloher et al. (The CRESST Collaboration), *Limits on WIMP dark matter using sapphire cryogenic detectors*, Astroparticle Physics **18** (2002), 43–55.

[211] M. Sisti, *CRESST – a Cryogenic Experiment for Dark Matter Search*, Ph.D. thesis, Ludwig-Maximilians-Universität München, 1999.

[212] H. Wulandari et al., *Neutron flux at the Gran Sasso underground laboratory revisited*, Astroparticle Physics **22** (2004), 313–322, arXiv:hep-ex/0312050.

[213] P. Belli et al., *Deep underground Neutron Flux Measurement with Large* BF_3 *Counters*, Il Nuovo Cimento **101A** (1989), no. 6, 959–966.

[214] F. Arneodo et al., *Neutron background measurements in the Hall C of the Gran Sasso Laboratory*, Il Nuovo Cimento **112** (1999), no. 8, 819–831.

[215] H. Wulandari et al., *Neutron Background Studies for the CRESST Dark Matter Experiment*, arXiv:hep-ex/0401032, 2004.

[216] H. R. T. Wulandari, *Study On Neutron-Induced Background in the Dark Matter Experiment CRESST*, Ph.D. thesis, Technische Universität München, 2003.

[217] G. Heusser, *Low-Radioactivity Background Techniques*, Annual Review of Nuclear and Particle Science **45** (1995), 543–590.

[218] B. Majorovits et al., *Production of Low-Background CuSn6-Bronze for the CRESST Dark-Matter-Search Experiment*, Applied Radiation and Isotopes (2008), accepted.

[219] F. Pobell, *Matter and Methods at Low Temperatures*, 1st ed., Springer, Berlin, 1992.

[220] J. W. Gibson and R. A. Hein, *Superconductivity of Tungsten*, Physical Review Letters **12** (1964), no. 25, 688–690.

[221] C. Cozzini, *CRESST Dark Matter Search with Cryogenic Calorimeters*, Ph.D. thesis, Ludwig-Maximilians-Universität München, 2003.

[222] L. Gonzalez-Mestres and D. Perret-Gallix, *Detection of low energy solar neutrinos and galactic dark matter with crystal scintillators*, Nuclear Instruments and Methods A **279** (1989), no. 1–2, 382–387.

[223] J. B. Birks, *Theory and Practice of Scintillation Counting*, Pergamon, 1967.

[224] C. Bucci et al., *Proposal to the Gran Sasso Laboratory for a Second Phase of the CRESST Dark Matter Search*, MPI-PhE/2000-04, 2000.

[225] C. Bucci et al., *Update of the Proposal to the LNGS for a Second Phase of the CRESST Dark Matter Search*, MPI-PhE/2001-02, 2001.

[226] T. Edison, *Note*, Nature **53** (1896), no. 1377, 470.

[227] M. Paganoni (The CMS collaboration), *The CMS electromagnetic calorimeter*, Nuclear Instruments and Methods A **535** (2004), no. 1–2, 461–465.

[228] A. Askin, *Light Yield Investigation of Titanium Doped Al2O3 Crystals for CRESST Dark Matter Search*, 2006, master thesis, Universität Siegen.

[229] I. Bavykina, Ph.D. thesis, Ludwig-Maximilians-Universität München, in preparation.

[230] T. Frank, *Development of Scintillating Calorimeters for Discrimination of Nuclear Recoils and Fully Ionizing Events*, Ph.D. thesis, Technische Universität München, 2002, available from http://www.d-nb.de/ or directly from http://tumb1.biblio.tu-muenchen.de/publ/diss/ph/2002/frank.html.

[231] K.-T. Wilke and J. Bohm, *Kristallzüchtung*, 2nd ed., Deutsch, Frankfurt/Main, 1988.

[232] C. D. Brandle, *Czochralski growth of oxides*, Journal of Crystal Growth **264** (2004), no. 4, 593–604.

[233] F. Petricca, *Dark Matter Search with Cryogenic Phonon-Light Detectors*, Ph.D. thesis, Ludwig-Maximilians-Universität München, 2005.

[234] E. Pantić, *Performance of Cryogenic Light Detectors in the CRESST-II Dark Matter Search*, Ph.D. thesis, Technische Universität München, 2008.

[235] P. Meunier, *Discrimination between nuclear recoils and electron recoils by simultaneous detection of phonons and scintillation light*, Applied Physics Letters **75** (1999), no. 9, 1335–1337.

[236] J. Ninković, *Investigation of CaWO4 Crystals for Simultaneous Phonon-Light Detection in the CRESST Dark Matter Search*, Ph.D. thesis, Technische Universität München, 2005, available via http://www.d-nb.de/ or directly from http://tumb1.biblio.tu-muenchen.de/publ/diss/ph/2005/ninkovic.html.

[237] F. Pröbst et al., *Model for cryogenic particle detectors with superconducting phase transition thermometers*, Journal of Low Temperature Physics **100** (1995), no. 1–2, 69–104.

[238] M. Gluyas, F. D. Hughes and B. W. James, *The elastic constants of calcium tungstate, 4.2–300 K*, Journal of Physics D: Applied Physics **6** (1973), no. 17, 2025–2037.

[239] R. Orbach and L. A. Vredevoe, *The Attenuation of High Frequency Phonons at Low Temperatures*, Physics **1** (1964), no. 1, 19.

[240] S. Henry et al., *The 66-channel SQUID readout for CRESST II*, Journal of Instrumentation **2** (2007), 11003.

[241] J. B. Johnson, *Thermal Agitation of Electricity in Conductors*, Physical Review **32** (1928), no. 1, 97–109.

[242] H. Nyquist, *Thermal Agitation of Electric Charge in Conductors*, Physical Review **32** (1928), no. 1, 110–113.

[243] H. Haken and H. C. Wolf, *Atom- und Quantenphysik*, 8th ed., Springer, Berlin, 2004.

[244] J. H. Hubbell and S. M. Seltzer, *Tables of X-Ray Mass Attenuation Coefficients and Mass Energy-Absorption Coefficients*, http://physics.nist.gov/PhysRefData/XrayMassCoef/cover.html, 1996.

[245] C. Cozzini et al., *Detection of the natural α decay of tungsten*, Physical Review C **70** (2004), 064606, arXiv:nucl-ex/0408006.

[246] G. Eska and K. Neumaier, *A carbon resistance thermometer with fast response below* 10 mK, Cryogenics **23** (1983), no. 2, 84–86.

[247] W. C. Black Jr., W. R. Roach and J. C. Wheatley, *Speer Carbon Resistors as Thermometers for Use Below* $1^\circ K$, The Review of Scientific Instruments **35** (1964), no. 5, 587–591.

[248] G. N. Kim, 2008, private communication.

[249] X. Zhang et al., *Excitation Functions for* $^{\mathrm{nat}}\mathrm{W}(\mathrm{p},\mathrm{xn})^{181}\mathrm{Re}$ *Reactions and Production of No-Carrier-Added* $^{186}\mathrm{Re}$ *via* $^{186}\mathrm{W}(\mathrm{p},\mathrm{n})^{186}\mathrm{Re}$ *Reaction*, Radiochimica Acta **86** (1999), 11–16.

[250] M. U. Khandaker et al., *Excitation functions of proton induced nuclear reactions on* $^{\mathrm{nat}}\mathrm{W}$ *up to* 40 MeV, Nuclear Instruments and Methods B **266** (2008), 1021–1029.

[251] M. H. Mortensen, R. R. Betts and C. K. Bockelman, *W(p,t) reactions. II. Odd target*, Physical Review C **21** (1980), no. 6, 2288–2292, see also ibid., 2275–2287.

[252] W. Bambynek et al., *Orbital electron capture by the nucleus*, Review of Modern Physics **49** (1977), 77–221, and errata: ibid., 961–962.

[253] R. B. Firestone and L. P. Ekström, *WWW Table of Radioactive Isotopes*, http://ie.lbl.gov/toi/, 2004.

[254] M. J. Weber, *Scintillation: mechanisms and new crystals*, Nuclear Instruments and Methods A **527** (2004), no. 1–2, 9–14.

[255] M. Stark, *Detektoren mit effizienter und schneller Phononensammlung für das CRESST-Experiment*, Ph.D. thesis, Technische Universität München, 2005, available via http://www.d-nb.de/ or directly from http://tumb1.biblio.tu-muenchen.de/publ/diss/ph/2005/stark.html.

[256] C. Coppi et al., *Quenching factor measurement for* $CaWO_4$ *by neutron scattering*, Nuclear Instruments and Methods A **559** (2006), 396–398.

[257] T. Jagemann, *Measurement of the Scintillation Light Quenching for Nuclear Recoils induced by Neutron Scattering in Detectors for Dark Matter Particles*, Ph.D. thesis, Technische Universität München, 2004, available via http://www.d-nb.de/ or directly from http://tumb1.biblio.tu-muenchen.de/publ/diss/ph/2004/jagemann.html.

[258] T. Jagemann, J. Jochum and F. v. Feilitzsch, *Neutron scattering facility for the measurement of nuclear recoil quenching factors*, Nuclear Instruments and Methods A **551** (2005), 245–260.

[259] T. Jagemann et al., *Measurement of nuclear recoil quenching factors in* $CaWO_4$, Astroparticle Physics **26** (2006), no. 4–5, 269–281.

[260] C. Coppi, Ph.D. thesis, Technische Universität München, in preparation.

[261] C. Ciemniak, Ph.D. thesis, Technische Universität München, in preparation.

[262] J.-C. Lanfranchi et al., *Neutron Scattering Facility for Characterization of CRESST and EURECA Detectors at mK Temperatures*, arXiv:0810.0132, 2008.

[263] J. Ninković et al., *New technique for the measurement of the scintillation efficiency of nuclear recoils*, Nuclear Instruments and Methods A **564** (2006), 567–578, arXiv:astro-ph/0604094.

[264] P. Huff, *Messung der Lichtausbeute von Rückstoßkernen in* $CaWO_4$, 2006, Diplomarbeit, Technische Universität München, available via http://publications.mppmu.mpg.de/.

[265] I. Bavykina et al., *Interpretation of light-quenching factor measurements*, Astroparticle Physics **28** (2007), no. 4–5, 489–493, arXiv:0707.0766.

[266] M. Moszyński et al., *Characterization of* $CaWO_4$ *scintillator at room and liquid nitrogen temperatures*, Nuclear Instruments and Methods A **553** (2005), no. 3, 578–591.

[267] G. Angloher et al. (The CRESST Collaboration), *Limits on WIMP dark matter using scintillating* $CaWO_4$ *cryogenic detectors with active background suppression*, Astroparticle Physics **23** (2005), 325–339, arXiv:astro-ph/0408006.

[268] D. Wahl, *Optimisation of light collection in inorganic scintillators for rare event searches*, Ph.D. thesis, University of Oxford, 2005.

[269] M. Furst and H. Kallmann, *Fluorescent Light yield with Alpha, Beta and Gamma Radiations*, Physical Review **91** (1953), 766–767.

[270] W. W. Moses et al., *Scintillator Non-Proportionality: Present Understanding and Future Challenges*, IEEE Transactions on Nuclear Science **55** (2008), no. 3, 1049–1053.

[271] B. D. Rooney and J. D. Valentine, *Scintillator light yield nonproportionality: calculating photonresponse using measured electron response*, IEEE Transactions on Nuclear Science **44** (1997), no. 3, 509–516.

[272] E. J. Sternglass, *Backscattering of Kilovolt Electrons from Solids*, Physical Review **95** (1954), no. 2, 345–358.

[273] W. S. M. Werner, I. S. Tilinin and M. Hayek, *Angular distribution of electrons reflected elastically from noncrystalline solid surfaces*, Physical Review C **50** (1994), no. 7, 4819–4833.

[274] R. J. Gaitskell and J. Filippini, *SUSY Dark Matter/Interactive Direct Detection Limit Plotter*, http://dmtools.berkeley.edu/limitplots/, 2008.

[275] J. I. Collar, *Solar-bound weakly interacting massive particles: A no-frills phenomenology*, Physical Review D **59** (1999), 063514, arXiv:astro-ph/9808058.

[276] I. Langmuir, *Pathological Science*, talk at the General Electrics research laboratories, available from http://www.cs.princeton.edu/~ken/Langmuir/langmuir.htm, 1953.

[277] S. Stone, *Pathological Science*, arXiv:hep-ph/0010295, 2000.

[278] C. Amsler et al., *The Review of Particle Physics*, Physics Letters B **667** (2008), no. 1, section *History Plots*, available from http://pdg.lbl.gov/.

[279] J. G. Heinrich, *Benefits of Blind Analysis Techniques*, CDF public memo on statistics 6576, available from http://www-cdf.fnal.gov/publications/cdf6576_blind.pdf, 2003.

[280] P. F. Harrison, *Blind analysis*, Journal of Physics G: Nuclear Particle Physics **28** (2002), 2679–2691.

[281] A. Roodman, *Blind Analysis in Particle Physics*, talk from PhyStat2003, arXiv:physics/0312102, 2003.

[282] J. R. Klein and A. Roodman, *Blind Analysis in Nuclear and Particle Physics*, Annual Review of Nuclear and Particle Science **55** (2005), no. 1, 141–163.

[283] C. Kittel, *Einführung in die Festkörperphysik*, 12th ed., Oldenbourg, München, 2002.

[284] S. Scholl, 2008, private communication.

[285] A. C. S. M. Bento, *Aspects of the performance of low temperature calorimeters for X-ray spectroscopy with high detection efficiency*, Ph.D. thesis, University of Oxford, 2004.

[286] G. Angloher et al. (The CRESST Collaboration), *Commissioning Run of the CRESST-II Dark Matter Search*, Astroparticle Physics (2008), submitted, arXiv:astro-ph/0408006.

[287] W. Westphal, *Characterization of the Response of CaWO4 on Recoiling Nuclei from Surface Alpha Decays*, Journal of Low Temperature Physics **151** (2008), 824–829.

[288] W. Westphal, *Development and Characterization of Cryogenic Detectors for the CRESST Experiment*, Ph.D. thesis, Technische Universität München, 2008, available from http://www.e15.physik.tu-muenchen.de/fileadmin/downloads/thesis/phd/2008_Wolfgang_Westphal.pdf.

[289] G. F. Knoll, *Radiation Detection and Measurement*, 3rd ed., John Wiley & Sons, New York, 2000.

[290] S. E. Derenzo and W. W. Moses, *Experimental Efforts and Results in Finding New Heavy Scintillators*, Proceedings of the CRYSTAL 2000 International Workshop on Heavy Scintillators for Scientific and Industrial Applications, 1993, available from http://breast.lbl.gov/~wwwinstr/.

[291] R. Grasser, A. Scharmann and K.-R. Strack, *On the intrinsic nature of the blue luminescence in* $CaWO_4$, Journal of Luminescence **27** (1982), no. 3, 263–272.

[292] R. M. Corless et al., *On the Lambert W function*, Advances in Computational Mathematics **5** (1996), 329–359.

[293] G. J. Feldman and R. D. Cousins, *Unified approach to the classical statistical analysis of small signals*, Physical Review D **57** (1998), no. 7, 3873–3889, arXiv:physics/9711021.

[294] U. Schwanke and T. Lohse, *Calculation of Upper Limits and Measurement Errors for Small Signals*, http://www-hess.physik.hu-berlin.de/public/limits.pdf, 2004.

[295] W. A. Rolke, A. M. López and J. Conrad, *Limits and confidence intervals in the presence of nuisance parameters*, Nuclear Instruments and Methods A **551** (2005), 493–503, arXiv:physics/0403059.

[296] S. Yellin, *Finding an upper limit in the presence of an unknown background*, Physical Review D **66** (2002), 032005, arXiv:physics/0203002.

[297] S. Yellin, *Extending the optimum interval method*, arXiv:0709.2701, 2008.

[298] M. Jelen, *The CRESST Dark Matter Search - Background Considerations and Data Analysis*, 2006, Diplomarbeit, Technische Universität München, available via http://publications.mppmu.mpg.de/.

[299] S. Dodelson, *Cosmology for Particle Physicists, Lecture 3*, given at the SLAC Summer Institute, movie available from http://www-conf.slac.stanford.edu/ssi/2007/talks/ssi31am2.ram, 2007.

[300] M. Sisti and Y. Ramachers, *Monica and Yorck's Etching Recipe for Copper*, informal note, Max-Planck-Institut für Physik.

[301] Poligrat GmbH München, *Betriebsanleitung Poligrat Laborant Typ L60/20-EP60* ***and*** *Gebrauchsanweisung Poligrat-Elektrolyt E 103 PG GA 9.3.1.001*, 1998.

[302] M. J. Berger et al., *XCOM: Photon Cross Sections Database*, http://physics.nist.gov/PhysRefData/Xcom/html/xcom1.html, 1998, ver. 3.1.